universiteit
hasselt

2013 | Faculteit Wetenschappen

DOCTORAATSPROEFSCHRIFT

Controlled synthesis of substrate supported TiO_2 nanostructures with different/interesting morphologies

Proefschrift voorgelegd tot het behalen van de graad van doctor
in de wetenschappen, chemie, te verdedigen door

Bertie Souvereyns

Promotor: prof. dr. M.K. Van Bael
Copromotoren: prof. dr. A. Hardy en prof. dr. Pegie Cool

D/2013/2451/47

Dankwoord

'Doelen zijn dromen met een deadline.' Met deze spreuk sta ik aan het einde van een lange weg met als doel het behalen van de doctoraatstitel. Deze weg was niet altijd zo straight forward maar kende behoorlijk wat dalen en diepten, langs omleidende en ingewikkelde wegen met zo nu en dan een steile helling die leidde naar een hogere top. Het heeft me dan ook bloed, zweet en tranen, van het ene wat meer als van het andere, gekost om te staan waar ik nu sta. Toen ik 4 jaar geleden aan dit doctoraat begon, werd ik geleid door een grote portie onzekerheid, over mezelf, mijn capaciteiten en mijn toekomst. Ik ben dan ook zeer fier om vandaag te mogen zeggen dat ik gegroeid ben tot de persoon die ik altijd wilde zijn, en dit mede door de weg die ik heb moeten afleggen om mijn doctoraat op een goede manier af te werken. Onderweg zijn er dan ook een tal van mensen geweest die mij hun steun en vertrouwen hebben gegeven om deze deadline te bereiken. Ieder van hun heeft op hun eigen manier mij sterker gemaakt, als wetenschapper maar ook als persoon. Het schrijven van dit dankwoord is dan ook iets waarnaar ik jaren heb uitgekeken. Niet alleen omdat het betekent dat ik aan het einde van de weg sta maar ook om bepaalde mensen specifiek te bedanken.

In de eerste plaats richt ik een dankwoord tot de personen die me de kans hebben gegeven dit doctoraat te beginnen, mijn (co)promotoren. Marlies en An, jullie hebben 4 jaar geleden in mij geloofd ondanks ik zelf toen nog niet in mezelf geloofde dat ik dit kon, dat doctoreren iets voor mij is. Ik wil jullie hier dan ook hartelijk voor bedanken en vooral voor de momenten dat jullie tijd hebben gemaakt voor mij om me een hart onder de riem te steken en me te motiveren als het onderzoek even vast zat en de druk zijn tol eiste. Deze momenten zijn een enorme hulp voor mij geweest waaruit ik steeds de kracht en de steun heb gevonden om er opnieuw voor te gaan en te geloven in mijn kunnen. Dikke merci hiervoor!

Pegie en Vera, ook jullie geloofden in mijn kunnen en ondanks ik niet gekozen heb voor een doctoraat in Antwerpen, zijn jullie me toch niet uit het oog verloren. Met Pegie als copromotor en via een gemeenschappelijk project, zijn jullie steeds nauw betrokken geweest met bij mijn onderzoek. De oprechte interesse alsook de input en feedback, heb ik steeds weten waarderen. Bedankt voor alles!

Ik zou liegen mocht ik zeggen dat ik collega's niet belangrijk vind. Integendeel, ze bepalen de werksfeer en de ontspanning tijdens de (middag)pauzes. De groep van doctorandi en post docs hebben zich zo uitgebreid dat ik kan zeggen dat ik in die vier jaar meer mensen heb zien komen dan gaan. Enkel Kevin, Daan en Linny hebben na het beëindigen van hun doctoraatsbeurs andere oorden opgezocht. Ik wil jullie bedanken voor de fijne momenten en wens jullie veel succes in jullie verdere loopbaan. Aan Kevin wil ik nog een extra bedankje uiten daar hij na 5 jaar samen studeren, mij nog niet beu was en me terug is gevolgd van Antwerpen naar Hasselt om te doctoreren. Gedurende 9 jaar waren we collega's en zijn onnozeliteiten hebben steeds gezorgd voor vele lachmomenten (cfr. dokter Hibbert) en de nodige ontspanning. Ik wens je veel succes in je verdere beroepsleven en dat KRC Genk nog veel mag winnen tegen Brugge ;)

De postdocs Christopher en Ken, jullie hebben me zoveel bijgeleerd over onderzoek en jullie feedback op de vele versies van manuscripten hebben me steeds vooruit geholpen. Hiervoor wil ik jullie bedanken! Christopher, naast de vele AFM sessies die je voor mij gedaan hebt, wil ik je nog bedanken voor je eerlijkheid en de persoon te zijn wie je bent. Ik heb zeer veel geleerd uit onze gesprekken en ben blij dat jij er was tijdens mijn doctoraat! Verder nog, en dat zullen de anderen ook bevestigen, ik ben blij dat jij in ons team zit!

De twee andere post docs Alexander en Nick, het siert jullie dat jullie nog steeds tussen het 'plebs' (=doctorandi) willen zitten, hoewel Alexander sinds kort (verplicht?) is verhuisd naar een éénmans kantoortje. Weg dus met de sociale controle, hopelijk is het nu niet het seizoen van het poolen ;). Misschien wordt darts je nieuwe sport voor tussen de middag… Nick, nog veel succes met het afwerken van je doctoraat en de bouw van jullie huis.

Dan de meiden Hanne, Lize, Ellen en Giulia, bedankt voor de leuke momenten, de middag uitstapjes en de gezellige wandelingen die onze soms lange werkdagen onderbraken en ons de nodige nieuwe energie gaven. Het ga jullie goed!

Verder wil ik ook nog de andere collega's bedanken voor hun gesprekken, hulp en vriendelijkheid: Thomas (onze onmisbare IT specialist ;)), Giedrius, Maarten, Nikolina, Anke, Sven, Jonathan. De nieuwelingen Wouter, Boaz en Gilles, welkom op het eiland en laat ook voor jullie de komende vier jaar een bron van inspiratie zijn voor al hetgeen je wil bereiken in de toekomst.

Dan de 'mensen van het IMO', die natuurlijk onmisbaar zijn geweest bij het tot stand brengen en uitvoeren van relevant onderzoek. Jan, wanneer ik op maandagochtend met een bang hartje mijn stalen voor analyse kwam brengen, stelde je me steeds die ene vraag die me zo onzeker maakte: " Wat wil je nu eigenlijk bereiken met deze analyse ?". Jij hebt me door de jaren heen geleerd eerst kritisch na te denken vooraleer ik (tot bij jou kwam om) een staal liet analyseren. Bedankt hiervoor! Ook bedankt Bart, voor de vele en snelle metingen, Christel en Hilde voor de staalpreparatie.

Binnen de printgroep (ONE), wil ik dr. Ir. Wim Deferme bedanken voor de samenwerking en Jeroen Stryckers voor de vele screen print testjes (tussen de drukke onderwijsgerelateerde periodes in).

Natuurlijk verdienen de collega's van de andere onderzoeksgroepen een welgemeende dank je wel. Van bij TANC/organische wil ik Prof. Dr. Robert Carleer en Jan Czech bedanken voor de Headspace metingen, Huguette voor de UV-Vis metingen, Elsy voor de ICP-AES analyse maar vooral de persoonlijke gesprekken ;), Ivo die steeds paraat stond me weer iets te lenen uit het labo, Greet voor de last minute ICP-AES metingen, Guy voor alle praktische TGA vragen, Koen voor de snelle herstellingen van al het materiaal dat weer juist op het meest ongepaste moment even niet correct 'wilde' werken en Martien voor de hulp bij het fotograferen van mijn stalen.

Van bij de onderzoeksgroep morfologie wil ik als eerst prof.dr. Ivo Lambrichts bedanken voor de vruchtvolle samenwerking. Het was me een eer en genoegen samen te werken met een persoon die zo gefascineerd is in zijn onderzoek en dit ook kan overbrengen naar mensen die niet in het vakgebied werken. Bedankt voor deze inspirerende samenwerking. Verder wil ik dan ook Annelies Bronckaers en Wendy Martens bedanken

voor de uitvoering en interpretatie van de experimenten en resultaten en het nalezen van de wetenschappelijke output. Marc Jans wil ik zeker niet vergeten te bedanken voor zijn werk met het inbedden van de vele stalen. Dank je wel.
Er mag zeker geen dankwoord vergeten worden voor de collega's bij didactiek. Hilde, Gene en Rita, door jullie harde werk zijn de didactische labo's steeds goed voorbereid waardoor het als begeleider zeer aangenaam is om een praktisch labo met de studenten te begeleiden. Bedankt hiervoor.
Dan nog enkele personen die ik zeker wil bedanken voor hun bijdrage zijn Johan Soogen van de werkplaats voor het uitdenken en realiseren van het semi-automatisch druksysteem voor de soft lithografische experimenten en Marc Withofs, voor de succesvolle foto's van mijn dispersie voor mijn eerste publicatie.

Ook buiten onze universiteit, heb ik de mogelijkheid gekregen samen te werken met andere instellingen. Binnen de onderzoeksgroep Adsorptie en Katalyse van de universiteit van Antwerpen, zou ik graag Monika Kus willen bedanken voor de vele fotokatalytische experimenten die ze voor mij gedaan heeft. Ook al bleken de meeste experimenten niet reproduceerbaar, ik hoop dat ze voor jou niet geheel tijdverlies waren. Nog veel succes met jouw doctoraat! Cynthia Van Oers en Sebastiaan Herregods wil ik bedanken voor de sorptiemetingen en succes met het beëindigen van jullie doctoraat.
Van de universiteit van Gent wil ik prof.dr. José C. Martins en Freya Van den Broeck voor de samenwerking omtrent de NMR analyses.

Zoals de meeste weten, was het publiceren van mijn eerste artikel geen senicure. Toen mijn manuscript vlak voor kerstmis vorig jaar voor de tweede maal werd geweigerd, zonk de moed me geheel in de schoenen. Gelukkig heb ik toen kunnen rekenen op collega's uit niet-universitaire instellingen. Daarom wil ik dan ook Jan Gilleir en Kurt Bellemans van Umicore bedanken voor de snelle en succesvolle hulp bij het analyseren van de dispersie, en dit nog voor de feestdagen. Binnen VITO, wil ik Myrjam Mertens bedanken voor de snelle quantitatieve XRD analyses en Steven Mullens voor de 17 daags durende viscositeitsmeting, tot grote frustratie van andere onderzoekers op het VITO. Ook bedankt voor de kritische input bij het verwerken van de resultaten en de verwerking in het uiteindelijk gepubliceerde manuscript. Heidi van den Rul wil ik bedanken voor haar tijd en interesse in mijn onderzoek en het bespreken van mijn onderzoeksaanpak. Ook Brigitte Schade van Particles Solutions wil ik bedanken voor de analyse op de dispersie en de vlotte samenwerking.

Als laatste maar daarom niet het minst belangrijke, wil ik het thuisfront bedanken. Vooreerst richt ik mijn dank tot mijn ouders. Zij hebben mij 9 jaar geleden de mogelijkheden gegeven om verder te studeren. Ze zijn me blijven steunen en motiveren, hoewel dit niet altijd even makkelijk was, maar door hen heb ik een doorzettingsvermogen opgebouwd waar ik best fier op mag zijn. De dag dat ik mijn master diploma behaalde moet voor hun ook het moment geweest zijn waarop ze beseften hoe belangrijk die vele oppeppende gesprekken zijn geweest. Ik heb hun daar nooit voor bedankt maar bij deze… Dank je wel!

Mariska, Heidi en Lindsey, jullie beseffen maar half zoveel hoe belangrijk jullie zijn voor mij. Zo vaak hebben jullie mijn tranen kunnen vegen, als ik weer eens zo door emoties werd overrompeld omdat het in het labo niet lukte, of aan mijn eigen kunnen twijfelde. Jullie hebben steeds in mij geloofd en hiervoor wil ik jullie bedanken. Natuurlijk ook voor de gezellige en ontspannende avonden die we samen, de afgelopen 8 jaar, samen hebben doorgebracht.

Kenny, mijn allerliefste ventje, jou zou ik eigenlijk in het begin moeten bedanken want wat jij voor mij betekent, daar kan ik wel een heel hoofdstuk aan wijden . Ondanks jij in een heel andere sector werkt, heb je me wel steeds weten steunen en motiveren. Zeker de laatste maanden, tijdens het schrijven van mijn thesis, heb ik zo weinig tijd voor jou gemaakt maar toch bleef je begripvol en motiverend. Bedankt hiervoor! Je wordt een geweldige papa! Want ja, terwijl anderen de schrijfperiode ervaren als vervelend en stresserend, heb ik dit meer ervaren als de zaligste periode van heel mijn doctoraat. Niet alleen om dat ik eens alle resultaten in een verhaal mocht gieten maar ook omdat ik deze periode samen heb mogen beleven met het nieuwe leven in mijn buik. Zijn aanwezigheid heeft me een zodanige positieve energie en relativeringsvermogen gegeven waardoor ik mijn thesis heb geschreven met een efficiency dat ik nooit voor mogelijk had gehouden. Wij kijken zo uit naar jouw komst, lieverd!

Als laatste wil ik mijn dankwoord afsluiten met een spreuk die me zeer veel inzicht heeft bijgebracht:

Laat wat u niet kunt,
niet in de weg staan
van wat u wel kunt.

Bertie

Outline

PART II

Conclusions and outlook

List with output

Appendix

A. Hamaker software for the prediction of dispersion stability: theory and use
B. Applied characterization techniques

Aim of research

The research topic of this thesis concerns the development of titanium dioxide (TiO_2) films with different/interesting nanostructured morphologies for a wide range of applications. TiO_2 gains interest due to its specific properties such as its photocatalytic activity, photovoltaic effect, medium dielectric permittivity, high chemical stability and low toxicity, which offers a versatile potential in different applications to this metal oxide. In this work, the focus lies on the potential of the developed films in heterogeneous photocatalysis, as growth layers for human cells, and to a limited extent on superhydrophobic self-cleaning materials. Although the use of the deposited films in these applications will be described, the **main challenge** of this thesis consists of the development of a **stable dispersion** of very **small TiO_2 nanoparticles** in **aqueous medium**, which is suitable as a precursor for the deposition of **films with different nanostructures**.

Notwithstanding, the sol-gel technique has emerged one of the most promising techniques for the deposition of TiO_2 films, a huge drawback lies in the need for subsequent thermal treatment at relatively high temperatures to crystallize the films. On the one hand, the application of high temperatures is unfavorable when using substrates of thermally low resistant materials such as plastics and untreated glass. On the other hand, high temperature treatments may introduce undesired phase transformation, particle growth and agglomeration. Since the performance of the films in the above applications depends on the interaction between the oxide layer and the interacting media, a high specific surface area is beneficial in this context, which can dramatically be decreased by particle agglomeration. In general, besides specific surface area and particle agglomeration, also phase composition, pore size distribution, particle morphology, surface defects and surface hydroxyl groups, play a crucial role in determining the efficiency in specific applications. These characteristics are directly associated to the synthesis and processing routes. The study of the influence of the characteristics of different kinds of nanostructured films on their activity in specific applications, is only meaningful when the various nanostructured films are prepared using comparable synthesis and deposition conditions. Therefore, in this work, an aqueous precursor is developed and applied for the deposition of different nanostructured films, making it possible to compare their performance in the selected applications.

For the aqueous precursor, a low temperature, **hydrothermal synthesis** route is selected as a first step toward the control over phase composition and particle size and a better understanding of the influence of different parameters on the material performances. In this work, the aimed crystal phase of TiO_2 is anatase since this phase promises the highest activity in photocatalytic and photovoltaic applications. Besides the synthesis of highly crystalline nanoparticles, hydrothermal synthesis is also used for the synthesis of very small (<10 nm) nanoparticles in a controlled and reproducible manner. The reason for the synthesis of very small nanoparticles in this work derives, on the one side, from the increased surface-to-volume ratio, and thus the specific surface area, of these nanoparticles. On the other side, particles smaller than 10 nm are known to obtain enhanced optical parameters due to a quantum size effect.

To disperse nanoparticles in water, mostly sonication is applied, with or without additives. Nevertheless, sonication can deteriorate the stability of the nanoparticles against sedimentation in function of time, influencing the preparation of homogeneous films. In this thesis, the use of an **alternative dispersing method** for the preparation of a stable dispersion is evaluated toward the deposition of homogeneous films via traditional deposition techniques.

The thesis consists of an introduction chapter and 4 experimental chapters divided in two parts:

Chapter 1 gives an introduction on TiO_2 as oxide material, the different methods to prepare powders and nanostructured films and the use of TiO_2 in most of the above mentioned applications. As the most important part of the research concerns the synthesis of a stable dispersion, some aspects of colloid chemistry are described in a more theoretical way.

Part I is the main part and concerns the synthesis of a stable and aqueous TiO_2 dispersion and the deposition of different substrate supported nanostructures.

In **chapter 2**, the development of a two-step hydrothermal synthesis route for the preparation of a stable, aqueous dispersion of small nanoparticles is described. Besides the discussion of the characteristics of the nanoparticles themselves, the stability of the particles in the dispersion is discussed more extensively. Furthermore, the synthesis conditions are studied in more detail in order to gain insight into the mechanism of dispersion and stabilization of the particles in the presented colloidal system.

The use of the TiO_2 dispersion synthesized in chapter 2 in combination with different (more traditional) deposition techniques is described in **chapter 3**. This chapter demonstrates that the TiO_2 dispersion can be used as a starting material for the deposition of different substrate supported morphologies. Here, the focus lies on the optimization of the process parameters of the deposition techniques in order to enhance the properties such as thickness and homogeneity of the nanostructured films. Besides nanostructures from the TiO_2 dispersion, the synthesis of anatase nanorods via hydrothermal growth is discussed.

Part II handles the preliminary study of the influence of the different nanostructures in photocatalytic and biomedical applications.

In **chapter 4**, the different morphologies prepared in chapter 3, are applied in heterogeneous photocatalysis. This study is focused on the topographical effect of the nanostructured layers on the photocatalytic performance and is seen as a first step in obtaining more insight into the factors determining the photocatalytic activity of the nanostructured TiO_2 films rather than obtaining high efficiencies. Furthermore, the potential use of the nanostructured films as superhydrophobic coatings are studied briefly.

The effect of topography (of the different morphologies) on the growth of human cells is studied in **chapter 5**. The different nanostructured films are studied towards the growth, profileration and differentiation of stem cells to bone forming cells. Furthermore, the cytotoxicity of TiO_2 is investigated via the evaluation of the viability of the cells in contact with the very small TiO_2 nanoparticles, prepared in chapter 2.

List of abbreviations and symbols

µTM	Microtransfer Moulding
AFM	Atomic Force Microscopy
CM	Control Medium
CPS	Centrifugal Particle Sizing
CSD	Chemical Solution Deposition
DLS	Dynamic Light Scattering
DSSC	Dye Sensitized Solar Cell
EDX	Energy –dispersive X-ray Spectroscopy
EtOH	Ethanol
fwhm	Full with at half maximum
hDPSC	Human Dental Pulp Stem Cells
HPC	Hydroxypropylcellulose
IS	Ionic Strength
MIMIC	Micromoulding in capillaries
NIST	National Institute of Standards and Technology
ODM	Osteogenic Differentiation Medium
PCS	Photon Correlation Spectroscopy
PDMS	Polydimethylsiloxane
PSD	Particle Size Distribution
PVA	Polyvinylalcohol
Rh6G	Rhodamine 6G
SAED	Selected-Area Electron Diffraction
SEM	Scanning Electron Microscopy
SPM/APM	Sulphuric Peroxide Mixture/Ammonia Peroxide Mixture
TEAH	Tetraethylammonium hydroxide
TEM	Transmission Electron Spectroscopy
TOC	Total Organic Compound
TTIP	Titanium(IV)tetraisopropoxide
UV	Ultraviolet
WCA	Water Contact Angle
XRD	X-ray Diffraction

Chapter 1: Introduction

This introduction chapter begins with the description of the general properties of TiO_2 as metal oxide. Then, the synthesis of TiO_2 nanopowders via aqueous methods and the dispersion of nanoparticles are discussed. In the next, the deposition of TiO_2 films from dispersions and the synthesis of patterned TiO_2 films are described. As a final point, the application of TiO_2 in photocatalysis, photovoltaics and biomedical applications is shortly reviewed.

1.1 TiO_2 in general

Titanium dioxide (TiO_2) has been commercially produced since the early twentieth century, showing a wide range of applications from pigments [1] to sunscreens [2, 3] and toothpaste [4]. In 1972, the phenomenon of photocatalytic splitting of water on a TiO_2 electrode under ultraviolet light was discovered by Fuijshima and Honda [5-8]. Since then, the research of TiO_2 materials has increased enormously, leading to a wide range of promising applications, from photovoltaics and photocatalysis to photo-/electrochromics and sensors [9-12].

In nature, TiO_2 occurs in three **polymorphs: rutile** (tetragonal), **anatase** (tetragonal) **and brookite** (orthorhombic). All three crystalline structures consist of deformed TiO_6 octahedra connected differently by corners and edges, as represented in Figure 1.1. In each octahedron the Ti^{4+} ion is surrounded by six O^{2-} ions.

In the rutile structure, two octahedral edges are shared to form linear chains along the c-axis and the TiO_6 chains are linked to each other through corner-shared bonding. In anatase, each octahedron shares four edges with other four octahedra, resulting in a zigzag structure. In brookite, each octahedron shared three edges and the octahedral arrangement produces a crystalline structure with tunnels along the c-axis.

These differences in lattice structures result in different mass densities and electronic band structures between the three forms, as listed in Table 1.1.

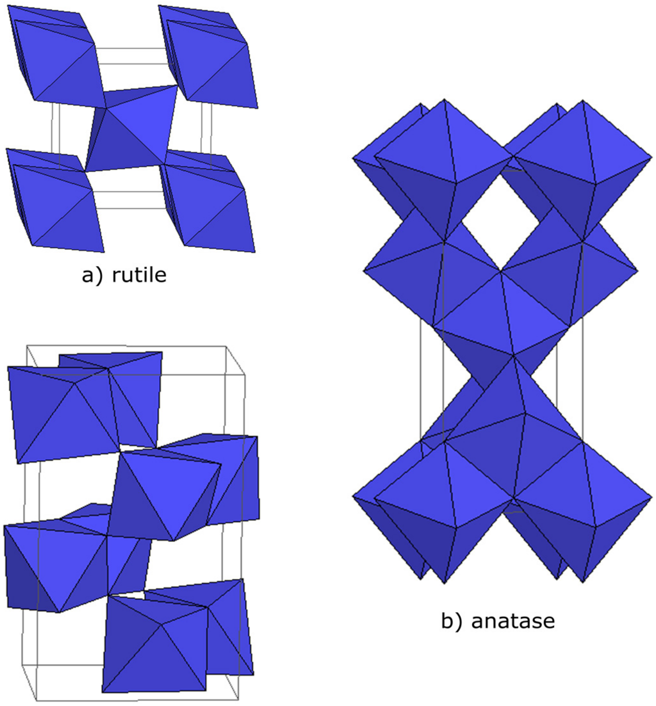

a) rutile

b) anatase

c) brookite

Figure 1.1 The three different crystal structures of TiO_2: rutile, anatase and brookite [13].

	Rutile	Anatase	Brookite
Wt (g/mol)	79.890	79.890	79.890
Z	2	4	8
Crystal system	Tetragonal	Tetragonal	Orthorhombic
Point group	2/mmm	4/mmm	mmm
Space group	$P4_2/mnm$	$I4_1/amd$	Pbca
Unit cell:			
a (Å)	4.5845	3.7842	9.184
b (Å)			5.447
c (Å)	2.9533	9.5146	5.145
Vol ($Å^3$)	62.07	136.25	257.38
MolarVol (cm^3/mol)	18.693	20.156	19.377
Density (g/cm^3)	4.2743	3.895	4.123
Eg (eV)	3.0	3.2	3.1-3.4

Table 1.1 Overview of some properties of the three polymorphs of TiO_2 [13].

Thermodynamically, rutile is the most stable phase while anatase and brookite, being kinetically stable, transform to rutile under heating accompanied with coarsening. The following (irreversible) transitions are all seen: anatase to brookite to rutile [14], brookite to anatase to rutile [15], anatase to rutile [16], brookite to rutile [16]. Banfield et al. found that the anatase and/or brookite nanoparticles start to transform into rutile after reaching a certain particle size [17, 18] and once rutile was formed, it grew more faster than anatase. Further, they found that the sequence of transformation and the thermal phase stability also depends on the particle size of anatase and brookite [14]. It was concluded that for equally sized nanoparticles, anatase was thermodynamically stable for sizes <11 nm, brookite for sizes between 11 and 35 nm, and rutile for sizes > 35 nm. In aqueous solutions, the phase stability depends on the solution pH. At small sizes, rutile is stabilized relative to anatase in very acid solutions, whereas in very alkaline solutions anatase is stabilized relative to rutile and brookite [19, 20].

With the exponentially growth of the research in nanoscience and nanotechnology [21-24], new physical and chemical properties has arisen when decreasing the size of the material to the nanoscale. Pronounced effects on the spectral properties arise specially when the size of the nanoparticle is comparable with the size of the exciton, inducing a blue shift in the absorption band edge. This effect, known as the **quantum confinement**, governs the movement of electrons and holes in semiconductor nanomaterials and becomes important in nanoparticles with sizes between 1-12 nm [25-27].

As a high band gap, n-type semiconductor, TiO_2 only **absorbs UV light** (10-400 nm), creating holes in the valence band and electrons in the conduction band. The higher band gap of anatase and the lower effective electron mass result in a higher mobility of the charge carriers in anatase than in rutile, enhancing the activity of anatase in photo-induced applications. To extend the absorption of TiO_2 toward the visible light region, doping or sensitizing titania is frequently applied [28-31].

1.2 Synthesis of TiO_2 nanopowders

The synthesis methods for powders can be classified in physical and chemical methods. Among the chemical methods, water-based methods are discussed in this section.

1.2.1 Water-based methods

TiO_2 nanopowders can be synthesized via different methods such as: chemical precipitation [32-35], sol-gel [36, 37], hydrothermal [38, 39], solvothermal processes [40, 41], combustion method [42], micro-emulsion mediated processes [43], electrochemical synthesis [44, 45], chemical vapour deposition [46], flame-made processes [47, 48], plasma-enhanced process [49] etc.

Rutile nanocrystals are commonly synthesized from the transformation of the metastable phases anatase and brookite, under elevated temperatures (mostly above 650°C). While anatase nanocrystals are mostly prepared via sol-gel synthesis, brookite is often observed as a by-product when precipitation is carried out in an acid medium under low temperature. Anatase-brookite nanocrystals could be successfully synthesized by a sonochemical sol-gel method [50] while pure brookite, without the rutile or anatase, is rather difficult to prepare [51].

Commercial TiO_2 (P25 Degussa) is an example of a powder prepared by flame-made synthesis. This powder contains anatase and rutile in a ratio of 4/1 and is frequently used in comparative studies concerning TiO_2 powders prepared from other methods.

Methods such as sol-gel, precipitation and hydrothermal synthesis, mostly include the **hydrolysis** of titanium alkoxides in order to produce amorphous or crystalline TiO_2 nanopowders. The reactions are represented as follows [52]:

Hydrolysis: $Ti(OR)_4 + xH_2O \rightarrow Ti(OH)_{4-x}OH_x + xROH$

Condensation: $Ti(OH)_{4-x}OH_x + Ti(OR)_4 \rightarrow (OR)_{4-x}TiO_xTi(OR)_{4-x} + xROH$

With R ethyl-, propyl-, i-propyl, n-butyl etc.

High hydrolysis rates result in a large quantity of $Ti(OH)_4$., while a low hydrolysis rate together with a low water content and an excess of titanium alkoxide, favors the Ti-O-Ti chains which develop further into 3D polymeric skeletons via condensation. The size and morphology of the final TiO_2 nanoparticles depend on factors such as alkoxy groups of the used alkoxides, concentration of reactants, pH of the solution, temperature of hydrolysis and the addition of electrolytes [53-55]. The average TiO_2 nanoparticle radius increases linearly with time, in agreement with the Lifshitz-slyozov-Wagner model (or Ostwald ripening) for coarsening [56]. Furthermore, TiO_2 nanocrystals with a high surface area and different ratios of anatase/rutile can be obtained by varying the parameters in the sol-gel method such as hydrolyzing agents, molar ratio, aging time and calcination temperatures [57].

Calcination is required when the hydrolysis and condensation result in amorphous powders and is meant to induce oxide formation and crystallization. The main disadvantage of sol-gel methods is that the required calcination treatment gives rise to particle agglomeration and grain growth and may induce (undesired) phase transformation [58]. Therefore, to promote crystallization at milder temperatures, the hydrothermal synthesis represents an alternative route to calcination.

1.2.2 Hydrothermal synthesis

The term hydrothermal is purely of geological origin, first described by the Britisch geologist Sir R. Murchison (1792-1871) as the action of water at elevated temperature and pressure leading to the formation of various rocks and minerals. **Hydrothermal processing** is defined as any homogeneous (nanoparticles) or heterogeneous (bulk materials) reaction in the presence of aqueous solvents or mineralizers under high pressure (100 kPa -1.5 MPa) and temperature (25 -200°C). Under these conditions, materials that are relatively insoluble under ordinary conditions can dissolve and recrystallize (recover). Syntheses are usually conducted under autogeneous pressure, which corresponds to the vapor pressure above the solution at the specified temperature and composition of the hydrothermal solution. However, in the case of hydrothermal growth of single crystals, additional pressure adjustment is done to control solubility and growth [59, 60]. Upper limits of hydrothermal synthesis extend to over 1000°C and 500 MPa pressure [61].

The hydrothermal synthesis method is generally conducted in steel pressure vessels called **autoclaves** with or without Teflon liners, and is widely used for the production of small particles in the ceramics industry. A great **variety of materials** like native elements, metal oxides, hydroxides, silicates, carbonates etc both as spheres and nanostructures like nanotubes, nanowires, nanorods and so on, have been obtained using the hydrothermal method.

The reactants used in hydrothermal synthesis are generally called **precursors**, which are administrates in the form of solutions, gels and suspensions. Mineralizers are either inorganic or organic additives that are often used to control pH and at high concentrations they promote the solubility. Other **additives**, also organic or inorganic, are used to serve other functions such as promoting particle dispersion or control crystal morphology.

Many papers have been published on the synthesis of crystalline TiO_2 nanoparticles using the hydrothermal route [19, 62-64]. Frequently additives are used to induce **peptization** prior[1] to the hydrothermal treatment in order to control the particle size [65-68]. Peptization is defined as the dispersion of agglomerates to form a colloidal stable suspension or emulsion[2]. It is the process that is responsible for the formation of a stable dispersion of colloidal particles, starting from a freshly prepared precipitate in the presence of a suitable electrolyte, known as peptizing agent. The ions of the peptizing agent can adsorb onto the particles of the precipitate which get dispersed due to electrostatic repulsion. Furthermore, peptizing agents have the ability to influence the physical properties of titania, such as particle size, shape and ratio of anatase to rutile phase [69]. The peptization starts from the deoxolation of the TiO_6 octahedral units in amorphous TiO_2. When an acid peptizing agent is used, the electrophilic proton attacks the oxygen atom in the Ti-O-Ti bridge and withdraws the electron density from the Ti

---

[1] Peptization is not always followed by a hydrothermal treatment thus not inherent to hydrothermal synthesis (cfr Cassaignon, et al. (2007), Journal of material science 42).

[2] Definition according to IUPAC (International Union of Pure and Applied Chemistry)

atom. Then, the Ti atom attracts the electron density from the oxygen of the water molecule which lead to the breakage of the oxolation bond [19]. With increasing H^+ concentration, HO-Ti-OH are the dominating species which are not stable due to the following condensation among these species. The reduced Ti-O-Ti bonds lead to structural rearrangements, forming corner sharing octahedral chains which are characteristic of the rutile phase. Under basic conditions, no breakage of oxolation bonds occurs as the nucleophilic OH^- groups attack the Ti-atom, replacing weaker ligands. The increasing number of OH^- species that is coordinated with the Ti-atom, allows an increasing possibility of forming edge-shared octahedra, representative for the anatase phase.

Under hydrothermal conditions, the phase transformation occurs through a **dissolution-precipitation** process [70, 71]. Dissolution of amorphous titania is a first step in the reaction pathway [72] followed by a decrease of the solubility of the titania TiO^{2+} species in relation to the increased condensation rate.

Using hydrothermal processing for **ceramic powder production**, high temperature calcinations, mixing and milling steps are not necessary or minimized, resulting in less time- and energy consuming process steps. Moreover, the ability to precipitate the powders directly from solutions regulates the rate and uniformity of nucleation, growth and aging, which affords size, morphology and aggregation control that is not possible with many synthesis processes [73, 74]. The elimination/reduction of aggregates combined with narrow particle size distributions in the starting powders leads to optimized and reproducible properties of ceramics because of better microstructure control. Other advantages of the hydrothermal synthesis over other methods are the lower operation temperature and a higher rate of reaction.

1.2.3 State of the art of TiO_2 nanopowders via hydrothermal synthesis

As a result of the unique pressure-temperature interaction, hydrothermal methods allow the preparation of phases which are difficult to prepare with other synthetic methods, such as brookite. Kobayashi demonstrated the synthesis of brookite by the hydrothermal treatment of water-soluble titanium complexes under basic conditions in the presence of an additive (ammonia or ethylenediamine) [77]. Phase pure anatase, rutile and brookite nanoparticles were prepared via hydrothermal synthesis starting from the same amorphous TiO_2 [71]. The formation of anatase is proposed to be dominated by surface energy effects while the formation of brookite and rutile follows a dissolution-precipitation mechanism. This mechanism includes the arrangement of the chains of sixfold-coordinated titanium complexes into different crystal structures depending on the reactant chemistry.

High crystalline **anatase** and rutile nanoparticles were synthesized by hydrothermal treating with tetraalkylammonium hydroxides or HNO_3 peptized titania sols respectively [68, 78]. Tetraalkylammonium hydroxides are mostly used as peptizing agents and it was found that the particle size decreased with increasing alkyl chain length [68]. The peptizer with the longest carbon chain exhibits the weakest alkalinity, decreasing the formation of anatase nuclei and thus lowering the growth rate of anatase nanocrystals. Moreover, the choice of peptizer and its concentration influenced the morphology of the particles [79]. In the presence of tetramethylammonium hydroxide, different sizes and shapes of anatase nanoparticles could be obtained via polycondensation of titanium alkoxides [56, 80].

Beside nanospheres, **other nanostructures** such as TiO_2 nanorods, nanotubes and nanowires have been successfully obtained via the hydrothermal method [81-84], as represented in Figure 1.2 . Nanorods are mostly synthesized in the presence of acid or inorganic salts while nanotubes and nanowires are typically prepared in NaOH aqueous solutions.

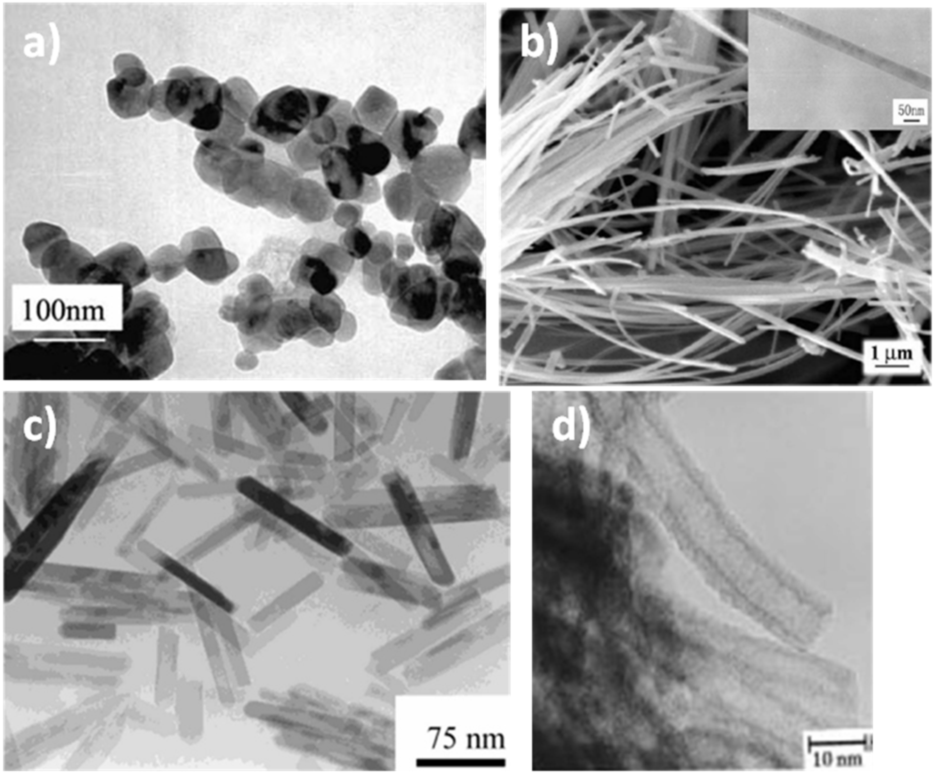

Figure 1.2 Different TiO_2 morphologies prepared by hydrothermal synthesis: a) nanospheres [68], b) nanowires [85], c) nanorods [81], and d) nanotubes [86].

1.2.4 Characterization of the crystal phase and particle size

In this section, the techniques applied in this thesis to determine the crystal phase and the dimension of the nanoparticles are described.

For the determination of the **crystal structure and crystallinity**, commonly **X-ray diffraction** (XRD) is applied. Using the Scherrer equation, this technique also allows to estimate the crystal grain size using the Scherrer equation, derived from the Bragg's law (nλ=2d sinθ, illustrated in Figure 1.3):

$$D = \frac{K\lambda}{\beta \cos\theta} \qquad \text{(Equation 1)}$$

where K is the dimensionless constant (shape factor to include the actual shape of the crystallite) [87], 2θ is the diffraction angle, λ the wavelength of the X-ray radiation and β the full width at half-maximum (fwhm) of the diffraction peak [88].

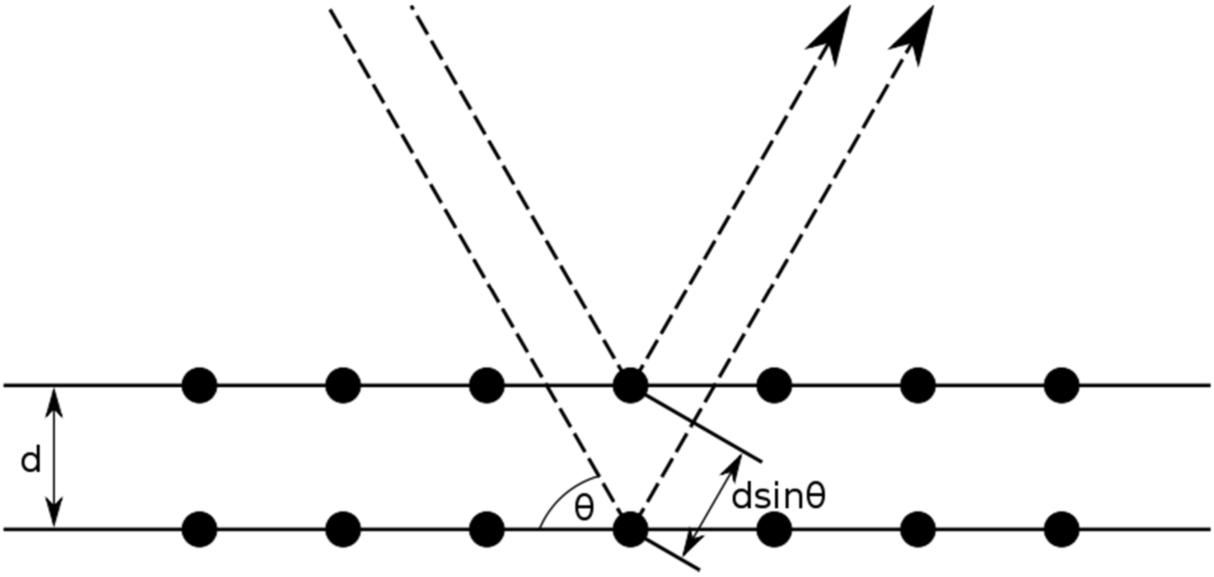

Figure 1.3 Illustration of the Bragg's diffraction occurring in a crystalline solid, with d the spacing between the planes in the atomic lattice.

Crystallite size (D) is actually determined by measuring the broadening of a particular peak in a diffraction pattern associated with a particular planar reflection from within the crystal unit cell. The crystallite size is inversely related to the fwhm of an individual peak- the narrower the peak, the larger the crystallite size. The diffraction of the X-ray beam is reinforced by the periodicity of the individual crystallite domains and results in an intense, narrow peak. Crystals which are randomly arranged or have a low degree of periodicity result in a broader peak.

Since TiO_2 is also Raman active, the crystal phase can also be determined by **Raman Spectroscopy**. This technique is based on the inelastic scattering of monochromatic light, containing photons which are absorbed and reemitted by the material. The change in frequency of the reemitted photons provides information about the vibrational, rotational and other low frequency transitions in the molecules, which are characteristic to the material. While XRD analysis only can be applied on solids, Raman Spectroscopy can be used to study both solid and liquid (and even gaseous) samples. With decreasing particles size, the Raman peaks show increased broadening and systematic frequency shifts [89].

Via **Transmission Electron Spectroscopy (TEM),** the **size and the morphology** of the particles can be analyzed by displaying the particles due to their interaction with a beam of electrons. The most common mode of operation in TEM is the **bright field** imaging mode. In this mode, the contrast formation is directly formed by occlusion and absorption of electrons in the sample leading to regions with a higher density or higher atomic number appearing black, while the absence of sample in the beam path appears bright.

In crystalline samples, the electrons undergo Bragg scattering inducing diffraction contrast in the sample. The desired Bragg reflections can be selected leading to a **dark field image** where the regions with no sample appear dark. By tilting the sample, high contrast images can be obtained. From this measuring mode, also a **diffraction pattern** can be generated, called as selected-area electron diffraction (**SAED**) from which the crystal phase of the sample can be identified, using the specific Miller (hkl) indices.

The size of the particles can be determined based on the bright field images, while the crystallite sizes can be calculated via import of the dark field image in an image processing program such as Image J. In this work, the Feret's diameter is determined, defined as the overall length of the particle, from 'top-to-tail'. Further information about this method is given in the Appendix.

To determine the **specific surface** of a powder, **gas adsorption** can be applied. This technique is based on the addition of a known volume of gas (mostly N_2 for powders and Kr for films) to a solid material in a sample vessel at cryogenic temperatures. At these temperatures, weak molecular attractive forces cause the gas molecules to adsorb (attach) onto the surface of the powder. The pressure in the sample vessel after each (dosed) added volume of gas is measured, which shows a direct relation between the pressure and the volume of gas in the sample vessel. Via the decrease of pressure due to absorption and the ideal gas law, the volume of gas adsorbed by the sample can be determined. The resulting relationship of volume of gas adsorbed versus the relative pressure at constant temperature is known as an adsorption isotherm. At a certain time, a small increase of relative pressure induces a high increase in adsorbed volume, referred as capillary condensation. The higher the relative pressure at which the capillary condensation occurs, the larger the size of the pores in the powder. The total pore volume is mostly determined at a relative pressure of 0.98, from which the surface area can be calculated (knowing the cross-sectional area of the adsorbate gas molecule).

1.3 Dispersion of TiO_2 nanoparticles in aqueous medium

In view of the application of TiO_2 as substrate supported materials (films), nanoparticles need to be dispersed in a liquid, preferably water from ecological viewpoint water. Due to the spontaneous agglomeration of TiO_2 nanoparticles when brought in water, the amount of accessible surface is reduced, which plays an important role in the surface related applications such as photo-induced applications [90]. Therefore, one of the most important and controllable properties of colloidal suspensions is their **stability**.

In the **macroscopic** sense this term expresses an even distribution of components throughout the whole volume and resistance of the phases to separate from each other with time (sedimentate) [91]. In the **microscopic** sense, the stability of the particles is determined by the degree of and the tendency to particle agglomeration.

1.3.1 Basic concepts of colloid chemistry

This section aims the overview of some concepts of colloid chemistry [92] [93] used in this research such as the DLVO theory, electric double layer, light scattering, stability etc. It is not attempted to go in detail on every aspect and only the concepts and theories which are applied in this work are discussed in more detail.

Definition of a colloid

A colloid is a substance that is microscopically dispersed throughout another substance. Two separate phases exist in a colloidal system, also called **colloidal dispersion**: a **dispersed phase** and a continuous phase (**dispersion medium**) in which the colloid is dispersed. The dispersed particles have at least one dimension between 1 and 1000 nm. The three forms in which all matter exists are solid, liquid or gas and colloidal systems can be any combination of these states resulting in a.o aerosols, emulsions, foams, solid dispersions, as listed in Table 1.2.

Disperse phase	Dispersion medium	Technical name	Examples
Solid	Gas	Aerosol	Smoke
Liquid	Gas	Aerosol	Hairspray, mist, fog
Solid	Liquid	Sol or dispersion	Printing ink, paint
Liquid	Liquid	Emulsion	Milk, mayonaise
Gas	Liquid	Foam	Beer, soap
Solid	Solid	Solid dispersion	Rubby glass, some alloys
Liquid	Solid	gel	Butter, cheese
Gas	Solid	Solid foam	Insulating foam

Table 1.2 Various types of colloidal dispersion with some common examples.

The term 'colloid' is derived from the Greek '*Kolla'* which means 'glue', and refers to some original organic colloidal solutions which were glues. This term first appeared in 1862 to distinguish colloids from crystalloids such as sugar and salt. In the early 19th century, Michael Faraday showed that when a strong beam of light is passed through a colloidal solution, it is scattered. This method to study colloids was further developed by John Tyndall and is known as the *"Tyndall effect".* The Tyndall scattering is visible in colloids and only occurs when the dimensions of the particles that are causing the scattering are larger than the wavelength of the radiation that is scattered.

Formation and properties of a colloid

There are two ways of forming a colloid: reduction of larger particles to colloidal size or condensation of smaller particles, e.g. molecules, into colloidal particles. The latter makes use of chemical reactions such as hydrolysis or displacement[3].

Colloidal particles are generally aggregates of numerous atoms or molecules. They pass through most filters but can be detected by light scattering, sedimentation and osmosis. The most interesting properties of colloids are caused by their dimensions, which is between atomic and 'bulk' level. Colloids contain enormous surface areas and energies which increase when decreasing the particle sizes. **Surface tension** becomes important and the **specific surface area** is inversely proportional to the diameter of the spherical particles.

Robert Brown, an English botanist, made the first observation of the rapid and erratic motion of small particles in his study of pollen grains. This observation, the **Brownian motion** called, was thought to be caused by the bombardment of the particles by the surrounding molecules of the solvent.

The movement of the particles can be described by the **Random walk** which is a mathematical formalization of a path, consisting of a succession of random steps. The

---

[3] IUPAC: "The process in which expulsion of a previously adsorbed component from the interfacial layer is effected by subsequent stronger adsorption of another component".

probability that a particle is a certain distance, *x*, away from the origin after a time, t, taking random steps with length l every τ seconds (t>>τ) is expressed as

$$\mathcal{P}(x,t) = (\frac{\tau}{2\pi l^2 t})^2 \exp(\frac{-\tau x^2}{2tl^2}) \qquad \text{(Equation 2)}$$

Due to a possible gradient in the chemical potential of a substance, diffusion occurs throughout the phase. From the diffusion force (F_d) per molecule of a substance i, an apposed viscous force (f_v) and a material flux (J_i), the diffusion D, known as the **Einstein-Stokes relation**, is derived as summarized below:

The driving force for the diffusion (F_d): $F_d = -\frac{d\mu_i}{dx}$ (Equation 3)

Diffusion force per molecule, with concentration of substance c_i:

$$f_d = -\left(\frac{kT}{c_i}\right)\frac{dc_i}{dx} \qquad \text{(Equation 4)}$$

An opposed viscous force : $f_v = Bu$ (Equation 5)

With the friction factor B, which measures how strongly the surrounding fluid resists the motion of the particle, equal to $6\pi\eta R$ with η the viscosity of the external phase (Pa.s) and R the radius of a spherical particle.

Flux of material given by *Fick's first law of diffusion:* $J_i = -D\frac{dc_i}{dx}$ (Equation 6)

The **diffusion coefficient D** becomes $\boldsymbol{D = \frac{kT}{6\pi\eta R}}$ (Equation 7)

This equation, as will be discussed later, is used to calculate the particle size by measuring the diffusion coefficient.

For **concentrated suspensions**, the Brownian motion, more specifically the gradient diffusion, which refers to the motion of particles as a consequence of a concentration gradient, need to be revised. The diffusive flux in an inhomogeneous concentrated suspension can be calculated by an extension of the argument used by Einstein in his original study of dilute suspensions. The argument is only adopted in the case of a suspension in equilibrium under an applied field. The field is assumed to act only on the particles, giving rise to a force f(x), where x denotes the position of the particle centre. As a result of this field the equilibrium particle density n(x) will not be uniform, inducing a flux due to Brownian motion. This flux is balanced by the sedimentation flux which is proportional to the sedimentation velocity (for non-concentrated suspensions)

$$< V > = < V_0 > (1 - 6{,}55\phi) \qquad \text{(Equation 8)}$$

with V_0 the sedimentation velocity of an isolated particle and φ the volume fraction of the substance in the suspension. Applying the Fick's first law and taking into account that *D* depends on the local particle volume fraction, the **diffusivity** in a concentrated suspension is derived:

$$\frac{D}{D_0} = 1 + 1{,}45\phi \qquad \text{(Equation 9)}$$

where D_0 is the diffusivity in a dilute suspension (equation 7).

Forces between colloidal particles

One of the most important forces in the surface and colloid chemistry is the **van der Waals force** between atoms, molecules or particles. Van der Waals forces arise from the induced or permanent polarities created in molecules by the electric fields of the neighboring molecules or due to the instantaneously dipoles originating by the positions of the electrons around the nucleus. Three categories of van der Waals forces exist:

- Keesom forces: forces between two permanent dipoles
- Debye forces: forces between a permanent dipole and a corresponding induced dipole
- London dispersion force: forces between two instantaneously induced dipoles

The **London dispersion forces** are always present and therefore represent a major role in colloid chemistry. The London force not only influences the physical adsorption and surface tension, is important in the adhesion and structure of macromolecules but also determines the stability and coagulation of colloidal systems. Van der Waals forces (0.4-4 kJ/mol) are always **attractive** and its influence can work from 0,2 till more than 10 nm. In the presence of only van der Waals forces, particles will form agglomerates because of the continuous collisions due to Brownian motion.

Two mechanism can prevent **aggregation** during a collision. Either the particles can be given an electrical charge (positive or negative) and particles with the same charge will repel each other. This mechanism is called **electrostatic stabilization**. In this kind of stabilization, the **electrical double layer forces** play an important role, as they influence the stability of many colloids: food colloids, farmaceutical dispersions, paints, water contaminants. The electrical charge which particles carry in aqueous media, can be originated from:

- Ionisation of the surface groups (due to variation in pH)
- Different solubility behavior of the ions on the surface of a bad soluble crystal
- Adsorption of specific ions

When the charged particle is immersed in an electrolyte solution, it is surrounded by ions of the opposite charge, in order that the particle appears to be neutral at a certain distance. The electrical charge together with the opposite charge in the solution is called the **electrical double layer**, as presented in Figure 1.4. The ions that induce the charge on the surface are the potential determining ions. As the potential vary with the distance in the formed double layer, two charged surfaces, separated by a dielectricum, have a potential variation Δψ, according to the model of parallel plate capacity. The inner region of the liquid layer surrounding the particles, where the ions are strongly bonded to the particle, is called the Stern layer. In the outer, diffuse region where the ions are less firmly attached, there is a notional boundary inside where the particles and ions form a stable entity. This boundary is called the slipping plane and only the ions within this plane travel with the particle as the particle moves. The potential at this slipping plane, is defined as the **zeta potential** which can be affected by the pH (Figure 1.5). The pH at which the surface carries no net electrical charge, is called the **isoelectrical point** and is considered as the point where the colloidal system is the least stable.

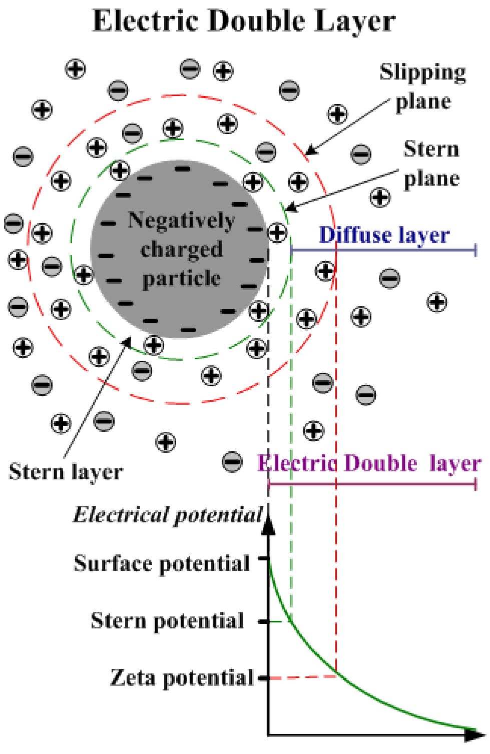

www.substech.com

Figure 1.4 Representation of an electrical double layer: a charged material immersed in an electrolyte solution, and the definition of the different planes with the corresponding potentials.

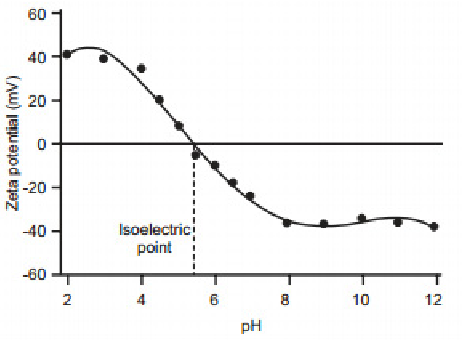

Figure 1.5 A typical plot of zeta potential versus pH.

A second way to prevent aggregation is coating the particles with an adsorbed layer of a polymer which itself prevents their close approach and this is called **steric stabilization.**

For a specific system, the relative magnitude of the attractive and the repulsive forces between the particles determines the coagulation behavior of the system. Conventional, the potential energy of attraction is defined as negative while the repulsion is positive, as represented in Figure 1.6. The combination of repulsion and attraction results in potential energy curves with energy barriers and energy minima. Both the attractive as the repulsive forces decrease with increasing distance between the particles.

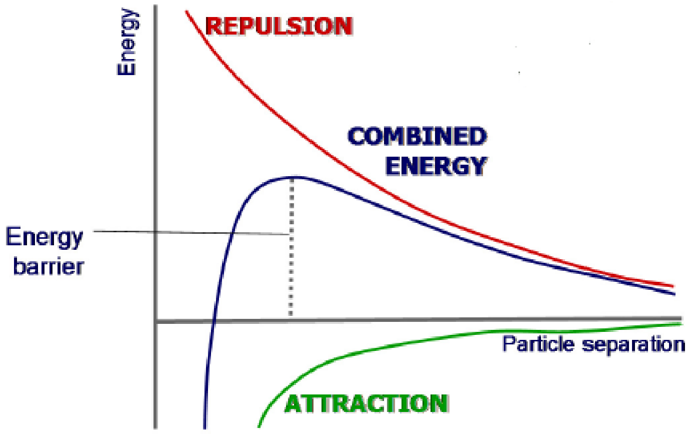

Figure 1.6 General potential energy curve indicating the combined curve of the repulsive forces and the attractive forces.

In fact, the stability of particles in solution is dependent upon its **total potential energy** function V_T. A theory was developed by the scientists Derjaguin, Verwey, Landau and overbeek, known as **the DLVO theory**, which recognizes that the total potential energy is the balance of several competing contributions:

$$V_T = V_A + V_R + V_s \qquad \text{(Equation 10)}$$

Where V_s is the potential energy of the solvent, but usually negligible. The attractive and repulsive contributions, V_A and V_R, are larger and operate over a much larger distance.

The balance between these two contributions is important, representing the combined effect by

$$V = 4\varepsilon\left[(\frac{\sigma}{r})^{12} - (\frac{\sigma}{r})^{6}\right] \quad \text{(Equation 11)}$$

which is known as **the Lennard-Jones potential,** illustrated in Figure 1.7. The first part of equation describes the repulsive forces between particles while the latter part denotes attraction. For colloidal particles, being macroscopic bodies, the molecular interactions are additive.

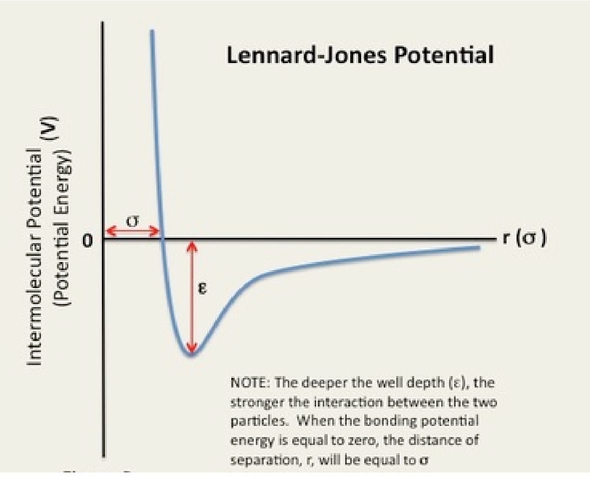

Figure 1.7 Ilustration of the Lennard-Jones potential representing the combined effect of attraction and repulsion [94].

The pairwise combination of the intermolecular attractions between two bodies was applied by Hamaker for different geometries. The potential energy for two blocks is given by

$$V_A = -\frac{A}{12\pi d^2} \quad \text{(Equation 12)}$$

With the Hamaker constant A

$$A = (\frac{\rho N_A \pi}{M})^2 \beta \quad \text{(Equation 13)}$$

with β the interaction parameter. The **Hamaker constant** (~10^{-20}J) is a material property that represents the strength of the van der Waals attraction between macroscopic bodies.

The repulsive potential is more complex:

$$V_R = 2\pi\varepsilon a\, \zeta^2 \exp(-\kappa D) \quad \text{(Equation 14)}$$

with *a* the particle radius, ε the solvent permeability, κ function of the ionic composition and ζ the zeta potential.

DLVO theory suggests that the stability of a colloidal system is determined by the sum of these van der Waals attractive and electric double layer repulsive forces that exist between the particles as they approach each other due to the Brownian motion. According to this theory, an energy barrier that results from the repulsive forces between the particles, prevents them to approach each other. But if the particles collide with sufficient energy to overcome this barrier, they will have contact by the attractive forces where they will adhere strongly and irreversibly. If the particles have sufficiently high repulsion, the dispersion will resist flocculation and the colloidal system will be stable. However, if there is no repulsion, flocculation or coagulation will eventually take place. So to maintain the stability of the colloidal system, the repulsive force need to be dominant. This can be achieved by steric repulsion or electrostatic stabilization, as described above.

In practice, dispersing agents or other additives (like surface acting agents) are added to enhance the dispersity of the particles in the medium. The addition of ionic additives can either stabilize the particles by the introduction of charges onto the nanoparticles which then repulse each other by electrostatic interactions. On the other hand, the additive itself can interact electrostatically with the charged nanoparticle and in that way prevents the particles to approach each other and to form agglomerates.

The different states and configurations that particles can have when in dried or in dispersed state are illustrated in Figure 1.8. In dry state, nanoparticles can be either aggregated (hard bonds between primary particles due to sintering) or agglomerated (held by weaker van der Waals forces). When dispersing, the particles can remain as singlets or form agglomerates, surrounded by an electric double layer. Agglomerated particles in a liquid can be separated by overcoming the weaker attractive forces by several methodologies, whereas the aggregated nanoparticles can not be separated.

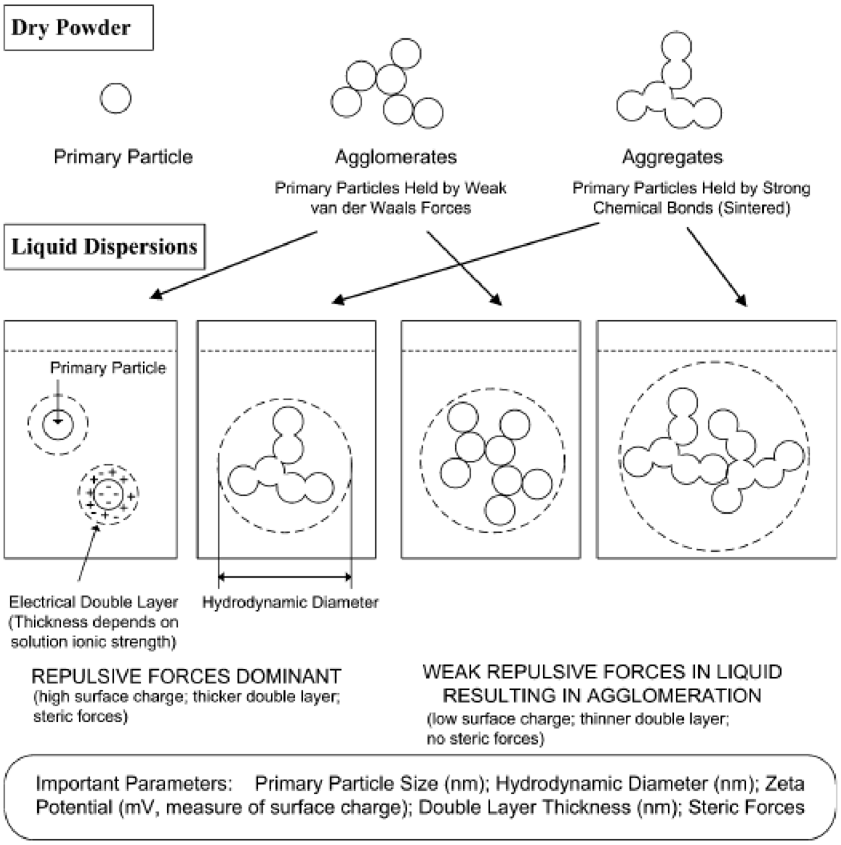

Figure 1.8 Various states of nanoparticles when in dried and dispersed state [95].

It is clear that the process of "dispersion", i.e. peptization, entails overcoming these different binding forces by use of both physicochemical and mechanical means. Physicochemical means include the use of **dispersion aids**. To maintain the highest degree of dispersion, *first* the solid must be wetted by the liquid, frequently followed by the use of surface-active materials, such as surfactants and peptizing agents, which have a strong affinity for interfaces because of having both hydrophobic (water repelling) and hydrophilic (water attractive) parts. According to the NIST[4] definition, surfactants are surface acting agents, substances which lowers the interfacial tension between the solution in which it is dissolved and other phases which are present. Four types of surfactants exist: non ionic, anionic, cationic and ampholytic (positive or negative charged depending on solution conditions). *Secondly*, electrostatic forces of repulsion should be as high as possible for example by addition of electrolytes. If a too high concentration is used, the double layer thickness will decrease, promoting aggregation. Zeta potential measurements are an ideal way to determine the optimum concentration of electrolyte for the dispersion. *Third*, the van der Waals attraction energy between the particles should be kept as low as possible. The smaller the energy of attraction the more

---

[4] National Institute of Standards and Technology

similar are the Hamaker constants for the particle and the liquid. Using surfactants, polyelectrolytes and proteins, which have all have a Hamaker constant close to water, can mask the unfavorable Hamaker constant of the material by an adsorption layer. A further effect of an adsorbed layer of macromolecules is the formation of a steric barrier which can provide very long term stabilization even under extreme solution conditions.

If the dispersion aids doesn't result in a high degree of dispersion, **mechanical dispersion** treatments can be applied. For maximum stability, the total energy of interaction should have a high repulsion barrier. Even with a high energy barrier, aggregation can reoccur because of the use of excess thermal or mechanical agitation during the dispersing process. An increase in thermal or mechanical energy increases the possibility of the collision of particles. Low power ultrasonic baths are therefore recommended. High power sonicators (over 400 W) generate heat which can exceed the critical coagulation temperatures at which the additive molecule can become insoluble. Nevertheless, sonication can be advantageous to disperse the particles before adding the dispersion aids, to provide a maximum interaction surface by deagglomeration of the particles. Therefore, when applying sonication, it is recommended to use the absolute minimum amount of mechanical agitation and preventing thermal agitation by using an ice bath.

Response of colloids to gravitational and centrifugal fields

Under **influence of gravity**, a particle of mass m, settles through a fluid while it is subjected to three forces: the gravitational force, mg, the up thrust due to the displaced fluid, m'g, and the frictional force, fv, due to the (viscous) drag of the surrounding fluid. From **Newton's Law**, the net force is given by:

$$mg - m'g - f_v = m\frac{du}{dt} \qquad \text{(Equation 15)}$$

with g the acceleration due to gravity and u the velocity at time t. The frictional force $f_{v,}$ equal to 6пηr $u_{t,}$ increases with the particle velocity and for colloidal particles settling in a dense medium (like water), the net downward force is balanced resulting in a zero acceleration. Equation 15 becomes

$$(\rho_s - \rho_l).\frac{4\pi r^3 g}{3} = 6\pi\eta r u_t \qquad \text{(Equation 16)}$$

with ρ_s and ρ_l the densities of the solid particles and the liquid respectively (Kg/m^3) and r the **Stokes** settling radius (m), g the acceleration gravity (9.807 m/s^2). From this equation, the sedimentation rate, u_t (m/sec), can be determined:

$$u_t = \frac{2}{9}\frac{(\rho_s - \rho_l)gr^2}{\eta} \qquad \text{(Equation 17)}$$

By measuring u$_t$, the sedimentation can be studied in function of time, as all particles will have settled beyond a certain depth. By following the concentration in function of time, a particle size distribution can be obtained.

As the Stokes equation is only valuable for diluted suspensions, a factor which depends on the phase volume ϕ is added [96]:

$$u_t = \frac{2}{9}\frac{(\rho_s - \rho_l)gr^2}{\eta}(1-\phi)^{5\pm0,25} \qquad \text{(Equation 18)}$$

However, due to the time required for a colloidal particle to settle through a reasonable distance under the influence of gravity alone, this procedure is rather limited.

In most cases, it is necessary to increase the sedimentation rate by subjecting the particles to a **centrifugal field**. This is not only time saving, also the danger of convection currents influencing the results is less and the distance moved by sedimentation can be much greater than the Brownian motion.

The forces that work on a particle in a centrifugal tube are presented in Figure 1.9. The outward force is an apparent (virtual) force invoked to explain the motion of the particle with respect to a coordinate frame attached to the rotor and moving with it.

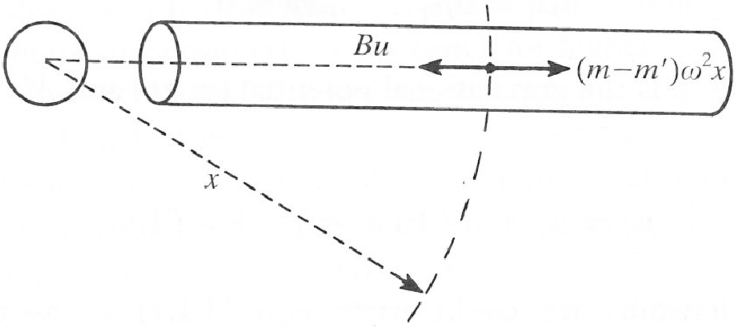

Figure 1.9 Forces on a particle in a centrifuge tube [92].

To keep a particle immersed in a liquid at a distance x from the axis of the centrifuge head (or rotor), a centripetal force acts directed towards the center of the rotor and force the particles to travel in a circle. The magnitude of that force is equal to

$$(m - m')\omega^2 x \qquad \text{(Equation 19)}$$

Where ω is the angular velocity (radians s^{-1}) of the rotor, $(m - m')$ the apparent mass (corrected by buoyancy).

The centripetal force is again retarded by a frictional force that is proportional to its velocity and after a short time these two forces are balanced:

$$(m - m')\omega^2 x = Bu(x) = B\frac{dx}{dt} \qquad \text{(Equation 20)}$$

The velocity is not constant but increases as the particle moves towards the outer end of the tube.

The quantity

$$S = \frac{u(x)}{\omega^2 x} = (m - m')/B \qquad \text{(Equation 21)}$$

is called the sedimentation coefficient and is an important characteristic of the material. S is obtained by integration of equation

$$\frac{dx}{x} = S\omega^2 dt \qquad \text{(Equation 22)}$$

Which results in

$$\ln\left(\frac{x_2}{x_1}\right) = S\omega^2\,(t_2 - t_1) \qquad \text{(Equation 23)}$$

Plots of lnx as function of time at known rotation speeds can be used to determine S. The radius can then determined by

$$r = \left(\frac{9\eta S}{2(\rho_s - \rho_l)}\right)^{1/2} \qquad \text{(Equation 24)}$$

Which can be used to obtain a particle size distribution, as will be discussed in Chapter 2, section 2.4.

Response of colloids to electromagnetic (light) waves

When electromagnetic radiation strikes a particle, it may be absorbed, transmitted, scattered, refracted, or diffracted, illustrated in Figure 1.10. As earlier mentioned, the scattering of beam light by colloidal particles, immersed in a fluid is known as the **Tyndall effect**. The scattering pattern represents the intensity of the scattered light as function of θ, the angle between incident and scattered beam, and depends strongly on the particle size and the wavelength of the light.

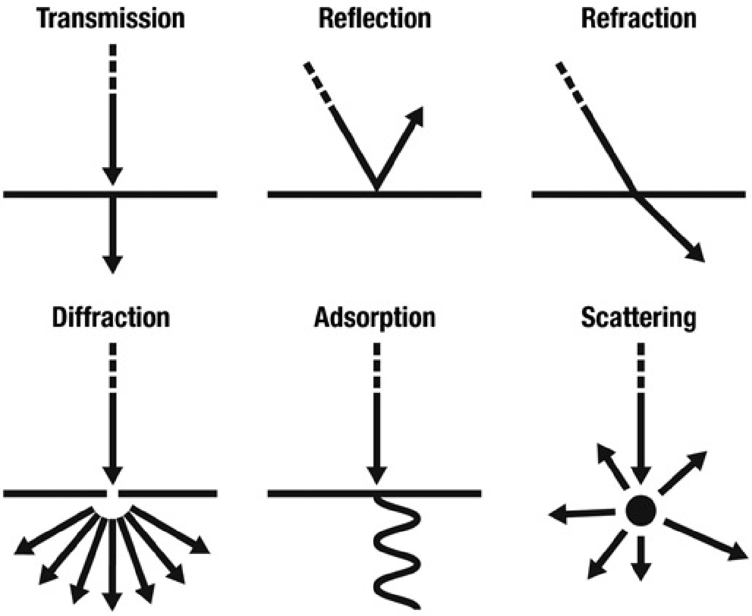

Figure 1.10 Different interactions of light with a surface .

The interaction between an electromagnetic wave of wavelength λ and a particle consisting of thousand of atoms is approached by **Rayleigh** (1871). His analysis concerned the scattering from a collection of **very small**, non-conducting, and non-absorbing particles acting independently of each other and is only valid when β<< 1 where β is defined by

$$\beta = \frac{2\pi a}{\lambda} \text{ and } n\beta \ll 1 \qquad \text{(Equation 25)}$$

with $n=n_p/n_0$ the refractive index of the particles relative to that of the surrounding medium. This first condition ensures the difference in the phases of the scattered wave from the different regions of the particles negligible, since the whole particle is subjected to the same electrical field strength.

The amount of Rayleigh scattering that occurs for a beam of light is proportional with the sixth power of the particle size and the fourth powder of wavelength of the light. according to following equation:

$$I = I_0 \frac{1+cos^2\theta}{2R^2} (\frac{2\pi}{\lambda})^4 (\frac{n^2-1}{n^2+2})^2 (\frac{d}{2})^6 \qquad \text{(Equation 26)}$$

Which is only valid for diluted dispersions.

For **larger particles**, Rayleigh suggested a different strategy which was further developed by Debye and Gans (**RGD theory**). When following conditions are met, it implies that the incident light beam is not affected by the particles.

$$|n-1| \ll 1 \text{ and } 2\beta|n-1| \ll 1$$

Larger particles result in asymmetrical scattering patterns, shown in Figure 1.11, which imply a difference in the amount of forward scattering (0°C<θ<90°C) and backward scattering (90°C<θ<180°C). Not all parts of the particle are subjected to the same electrical field and so the scattered light interferes, changing the intensity of the scattering. Therefore, in the RGD theory, the Rayleigh intensity I_R is adapted with a correction factor P(θ), also geometrical factor, to correct for the interference effects which are not considered in the Rayleigh theory:

$$I_{RGD} = I_R P(\theta) \qquad \text{(Equation 27)}$$

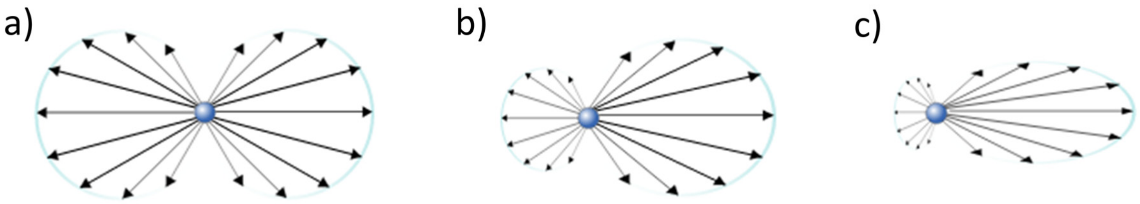

Figure 1.11 Representation of the Rayleigh scattering (a) and the Mie scattering (b and c).

As the particle size increases, the scattering pattern becomes more complicated as the spherical waves from each scattering center in the particle increasingly interfere with one another so that the intensity shows pronounced maxima and minima at particular angles, θ, determined by the size parameter β and particle refractive index. To properly describe the scattering pattern, the **Mie scattering** theory must be used, in the region where a~λ. Actually, Mie solved the general problem for a **sphere** of any size when the refractive indices of both the particle and the medium can be complex (for example when light is absorbed and scattered, the real part describes the absorption and the imaginary part accounts for scattering).

As this theory is also limited to low concentrated dispersions due to the occurrence of multiple scattering in more concentrated systems, the Mie theory is not further discussed here but we can refer to [97] for a general description.

Response to mechanical stress- the rheology of colloid materials

Rheology is frequently used to describe and explain the flow and deformation of matter, subjected to stress. Stress (force per unit area) can be applied in various ways: as a compression, as a tension, or as a shearing process. While dilute dispersions behave very much like simple liquids, highly concentrated dispersions encounter unusual behavior under tension but it is often these very unusual deformation properties that are sought after in the application of a colloidal dispersion. Consider, for example, the way the ‘apparent viscosity’ of a paint changing during it application: it is high when the paint is held on the brush but flows freely when sheared against the surface to be painted; it must quickly increase in viscosity so that it does not run down (drip or sag) under gravity but must flow sufficiently to eliminate the brush marks. The dependence of the viscosity on time and the shearing stress to which it is subjected determine the success of the paint. Also for other coating processes, stringently controlled flow characteristics are required. So it is clear that for many kind of situations, the rheological character of a colloidal dispersion is important.

Furthermore, rheology has become a well-established tool nowadays, for monitoring structural transitions and molecular interactions is solutions, blends, dispersions, emulsions, gels, etc

Considering a simple shearing regime, where a lower plate is held stationary and the upper plate is pulled by a force, *F,* acting in the *x* direction over an area *A*. The force per unit area or shearing stress (also called traction) applied to the material between the plates will cause a deformation (or strain), γ. When the force is removed, the material can return to its original shape (=elastic recovery), or remain in the new position (=flow state) or some partial recovery occurs.

The tensile (stretching) stress S_T is described by the Hooke's Law (for an ideal elastic solid):

$$\frac{F}{A} = S_T = Y_\gamma \qquad \text{(Equation 28)}$$

Where Y is called the **Young's modulus** of the material.

Ideal liquid-like behavior is described as **Newtonian behavior** for which the applied shearing stress is directly proportional to the time rate of strain or rate of shear (ẏ=dγ/dt):

$$S \sim \dot{y} \; or \; S = \eta \dot{y} \qquad \text{(Equation 29)}$$

with η the viscosity.

As for many colloidal dispersions the viscous behavior is the most important, it is sufficient to investigate the relationship between shear stress and shear rate to obtain a more general equation in which the viscosity is no longer a constant. An apparent viscosity, η_{app}, which is independent on time in a long experimental measurement, is defined as

$$\eta_{app}(\dot{y}) = \frac{S}{\dot{y}} \qquad \text{(Equation 30)}$$

Or a differential viscosity

$$\eta_{diff}(\dot{y}) = \frac{dS}{d\dot{y}} \qquad \text{(Equation 31)}$$

The study of colloidal dispersions (including the more concentrated systems described as slurries or pastes) reveals that ideal behavior (either solid-like or liquid-like) is the exception rather than the rule. The viscosity of dispersion is first of all controlled by the continuous phase liquid which might itself be Newtonian or non-Newtonian, and secondly by the added dispersed phase. The size, shape, amount and deformability of the particles of dispersed material can vary considerably, as also the interaction between the individual dispersed particles. Increasing the concentration of the dispersed particles, the viscosity of the mixture increases, going from a free-flowing liquid to a paste, and eventually to a soft liquid, as more and more particles are added.

The first important theoretical work in the study of dispersions was done by **Albert Einstein**, who developed an equation for the dependence of the amount of material φ on the viscosity of a dispersion, given by:

$$\eta = \eta_0(1 + [\eta]\Phi) \qquad \text{(Equation 32)}$$

with η the measured viscosity, η_0 the Newtonian continuous phase viscosity, $[\eta]$ the intrinsic viscosity (equal to 5/2 for spheres), Φ the phase volume, representing that volume of the dispersion occupied by the dispersed phase. The equation of Einstein is independent on the size of the particles but dependent on the shape, since the increase in viscosity comes from the diversion of streamlines in the flow as they are redirected around particles. Moreover, the presence of electrical charges on the surface of the particles leads to extra energy dissipation due to flow distorting the surrounding charge cloud. Von Smouluchowski accounted for this effect mathematically as

$$\eta = \eta_0\left(1 + 2{,}5\phi\left\{1 + (\frac{\varepsilon\zeta}{2\pi})^2\left\{\frac{1}{2\sigma\eta_0 a^2}\right\}\right\}\right) \qquad \text{(Equation 33)}$$

Where ε is the relative permittivity of the continuous phase, ζ the zeta potential potential, σ the specific conductivity of the continuous phase and *a* is the radius of the spherical particles. The effect on electrical charges onto the particles surface can easily double the effective phase volume [98]. To increase the concentration range of these equation to a more practical region, the Kreiger-Dougherty (K-D) equation, was developed which indicate that Φ_m is an important variable to manipulate when we want to control or understand the viscosity of concentrated dispersions:

$$\eta = \eta_0(1 - \frac{\Phi}{\Phi_m})^{-[\eta]\Phi_m} \qquad \text{(Equation 34)}$$

When shear is applied on a dispersion, the change in spatial arrangement decreases the viscosity. This decrease manifests in the K-D equation by a small but significant increase in the value of Φ_m as the shear rate increases. Typical values of Φ_m are about 0,63 for a dispersion of monodisperse, spherical particles at very low shear rates and about 0,71 at very high shear rates.

The change in spatial arrangement of the particles between a dispersion at rest and a dispersion under shear, is caused by the co-operative movement of the randomly dispersed particles, under shear stress, toward a situation where they form strings and layers, as illustrated in Figure 1.12. The decrease in viscosity is induced by the decrease in average distance between the nanoparticles along the flow direction, while the average distance between the nanoparticles increases in a direction orthogonal to the flow direction. The decrease of viscosity in function of the shear rate is given in Figure 1.13, including the factors that influence the viscosity at low and high shear rate. Although the decrease in viscosity mostly seems small, it can produce large effects at high concentrations of particles resulting in a large amount of shear thinning in concentrated suspensions.

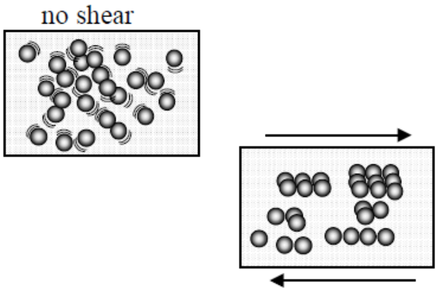

Figure 1.12 The formation of strings and layers in a suspension of non-interacting Brownian spheres under the action of shear flow [99].

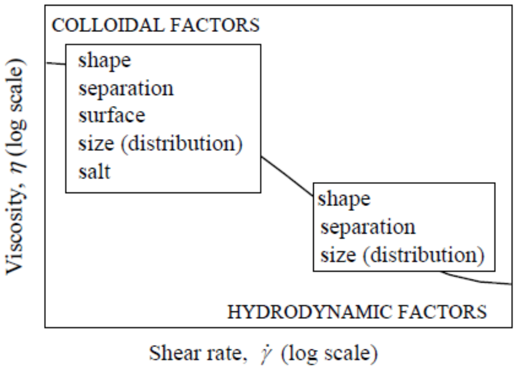

Figure 1.13 Flow curve of a suspension of colloidal particles [99].

1.3.2 Characterization

When preparing a dispersion of nanoparticles, it is necessary to characterize the state of the nanoparticles (such as particle size, particle size distribution, surface charge and degree of agglomeration) in an attempt to investigate the parameters (such as ionic strength, pH and particle surface chemistry) that control the nanoparticle dispersion. Two basic notions exist for characterizing dispersed systems: " **particle size distribution**" (PSD) and "**zeta potential**". There are several methods for determining these characteristics, mostly based on light as micro-electrophoresis, light scattering, light diffraction etc.

Characterizing the particle size distribution of nano- (and submicron-) liquid dispersions is not easy since some 'criticalities' need to be taken into account that may affect the reliability (i.e. accuracy) of the generated analytical data. Figure 1.14 schematically explains that in general the PSD characterization of a liquid dispersion is most straightforward for homogeneous suspensions, that consist of a narrow distribution of spherical particles that are well dispersed, present in a suitable concentration, and being stable in function of time. However, this ideal situation is often far from reality. Therefore, other PSD technologies are necessary, which are presented in Table 1.3.

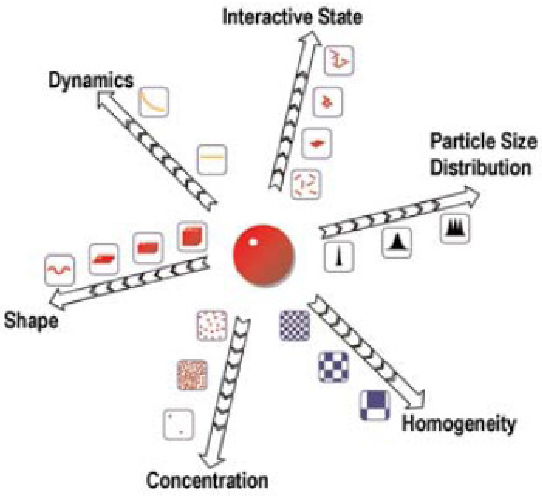

Figure 1.14 Criticalities in the PSD analysis of nano- and submicron liquid dispersions [100].

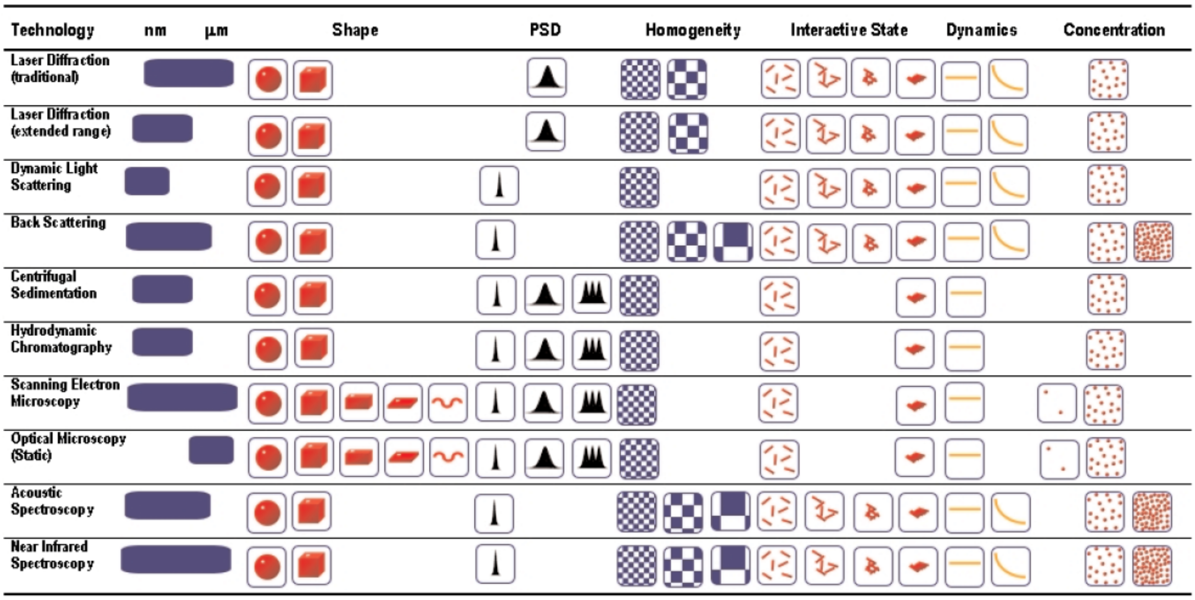

Table 1.3 Schematic evaluation of some common technologies for particle size distribution analysis [100].

From a historical perspective, the most common technology for **particle size distribution** characterization of dispersions is by Dynamic Light Scattering (DLS), also known as Photon Correlation Spectroscopy (PCS).

In Dynamic Light Scattering, a monochromatic beam of laser light illuminates the sample and is scattered into a detector placed at an angle θ with respect to the transmitted beam. Due to the presence of particles in the sample, the transmitted beam is scattered, as represented in Figure 1.15.

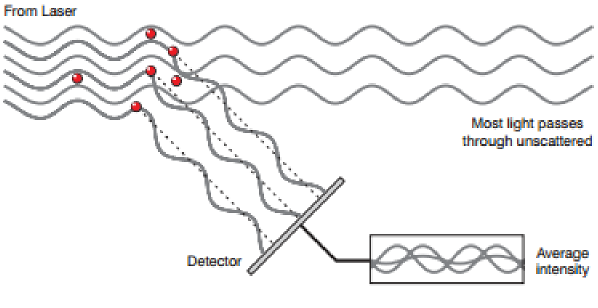

The scattered light falling on the detector.

Figure 1.15 Schematic representation of a light scattering system [101]

The scattered light fluctuates in time because of the Brownian motion of particles in the solution. These temporal fluctuations in scattered light intensity are autocorrelated in DLS and evaluated to determine the intensity weighted average diffusion coefficient D of the particles, for spherical particles. The average hydrodynamic diameter can be calculated from the diffusion coefficient via the Stokes-Einstein equation (equation 7). The hydrodynamic diameter represent the diameter of the sphere that has the same diffusion coefficient as the solvated particles. Since from DLS the hydrodynamic particle size of the suspended particles is calculated, which is larger than the primary particle size, an additional particle size analysis via Transmission Electron Microscopy is recommended to obtain complementary information about the primary particle size. The difference in the particle size obtained via DLS and TEM analysis, not only gives information about the hydrodynamic volume but can also give an indication whether the particles are agglomerated in the medium.

By fitting the correlation curve to a multiple exponential form, the intensity size distribution can be determined which is necessary to describe a system containing multiple particle size groups, leading to a bimodal particle size distribution. By using the Mie theory, the intensity distribution can be converted to a volume distribution and further to a number distribution. However, number distributions are of limited use as small errors in gathering data for the correlation function will lead to huge errors in distribution by number. Nevertheless, as the intensity of the scattered light is proportional to the sixth power of the particles diameter (from Rayleigh's approximation, equation 30), this technique is also very sensitive to the presence of larger particles.

As the physical stability of the particles in dispersion is a function of time, instability phenomena may occur which can be difficult to evaluate due to the sample manipulation. Particularly, for flocculated systems sample preparation and analysis may cause rupture of the clustered particles thereby leading to incorrect information on the actual dispersion state of the product. In addition to this, sample preparation and analysis may induce flocculation of the primary particles. When electrostatic repulsion is the mechanism for stabilization, for stability evaluation purposes, the zeta-potential of the particles may give a better indication of their stability[102].

The optical method used for zeta potential analysis is called **Laser Doppler Electrophoresis** where an applied electric field moves the charged particles, together with the ions of the opposite charge, consisting in the electric double layer, towards the electrode of opposite polarity. The particles undergoing this electrophoresis will scatter light and the frequency is shifted due to the movement of the particles. From the measurement of this frequency shift, the electrophoretic mobility (μ_e) can be determined which is used to calculate the zeta potential (ζ) using the **Henry equation**:

$$\mu_e = \frac{2\varepsilon\zeta f(\kappa a)}{3\eta} \qquad \text{(Equation 35)}$$

with f(κα) the Henry's function, which can be 1,5 (Smoluchowski approximation) or 1.0 (Hückel approximation) depending on the electrolyte concentration (and double layer thickness κ).

The measurement of the mobility can be carried out with the same equipment as for the DLS measurement, with the additional software (ZETAPALS) and the electrode which is shown in Figure 1.16.

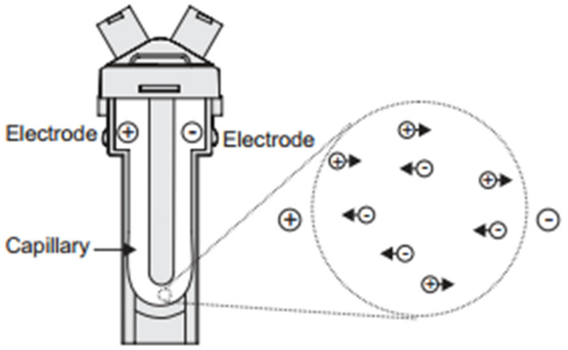

Figure 1.16 Set up for electrophoresis measurement: electrode in the sample cell [103].

Understanding the zeta potential is of critical importance in controlling the dispersion and determining the stability of a nanoparticle suspension i.e. to what degree aggregation will occur over time. A high positive or negative zeta potential indicates that the particles will repel each other and there is no tendency to flocculate. If the particles have a low zeta potential, they have a high tendency to come together and to flocculate. The general dividing line between stable and unstable suspensions is generally taken at either + 30 mV (for positively charged particles) or -30 mV (for negatively charged particles).

The zeta potential of a system does not only depends upon the particle surface but also on its environment. It can be affected by small changes in the pH or ionic strength of the medium which limits the use of concentrated dispersions, as discussed later.

Besides the prediction of the stability, zeta potential determination can also be used to identify the isoelectric point (or point of zero zeta potential) of colloids and for the identification of particle surface adsorption.

The limitations of both light scattering (optical) techniques are addressed to the concentration of the particles in the dispersion and the associated turbidity. Aiming the characterization of the nanoparticles and the stability in diluted systems, these techniques can be widely applied. However, aiming the analysis of a **concentrated dispersion** (> 1 wt%), other techniques are recommended, as in a concentrated dispersion the phenomenon of multiple scattering can lead to e.g. an underestimated hydrodynamic particle radius. Elimination of dilution is especially critical for zeta potential characterization because this parameter is a property of both the particle and the surrounding liquid; diluting changes the suspension medium and, as a result, the zeta potential.

In order to analyze the particle size and the zeta potential in more concentrated dispersions, other techniques are available.

The technique applied in this thesis, which allows the measurement of particles in a concentrated dispersion, is based on **Centrifugal Sedimentation** [104]. This kind of technique measures the particle size based on centrifugal forces and absorbance of light. Furthermore, it allows a much more quantitative monitoring of multimodal distributions. Figure 1.17 shows the design of a **Centrifugal Particle Sizing (CPS)** disc centrifuges which separates the particles by size using centrifugal sedimentation in a liquid medium. The sedimentation is stabilized by a slight density gradient within the liquid and the particles sediment within an optically clear, rotating disc. From the sedimentation velocity of the particles, the diameter of the particles can be calculated using the Stokes' equation (equation 17).

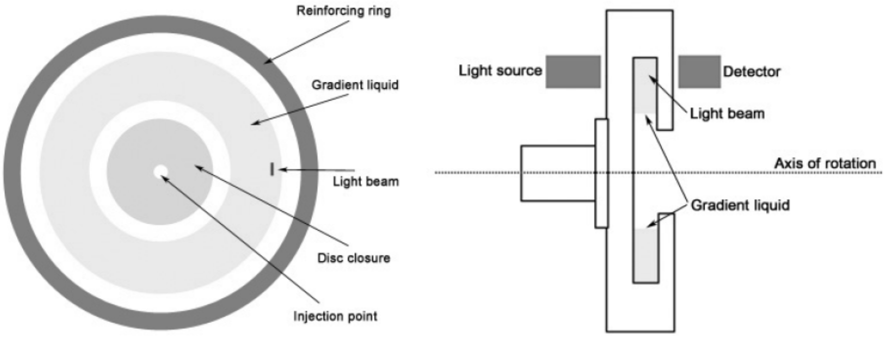

Figure 1.17 Hollow disc centrifuge design of the disc centrifuge with the front view (left) and the cross section view (right) of the disc.

Approaching the outside of the edge, the particles pass through the detector light and block/scatter a portion of the beam. The intensity of the beam that reaches the detector is reduced by the particles and consequently reducing the voltage produced by the detector. Then, the operating software converts the voltage signal into an absorption value and generates a particle size distribution.

Actually, the turbidity (reduction of intensity of light) is measured by absorption of the light source beam (mostly with a wavelength of 405 nm) being scattered. As the beam traverses a solution, this fraction of light, T, is (on average) being scattered at each point in the path. The fraction of light transmitted through a path length l is expressed by

$$\frac{I_t}{I_0} = \exp(-Tl) \qquad \text{(Equation 36)}$$

Thus a measure of the turbidity (which is analogous to the extinction in Beer's Law) can be used to measure molar mass and is converted into a weight distribution using Mie theory light scattering calculations. The theory of sedimentation and detection of particles in fluids is well described in the literature [105].

Another centrifugal sedimentation method for both the analysis of the particle size distribution and the stability in a concentrated dispersion is via de **Lumisizer**, which uses an analytical centrifuge to establish space- and time-resolved extinction/transmission profiles, shown in Figure 1.18 The sample is illuminated with parallel infrared or blue light, and the transmitted light is used to calculate the particle concentration (after conversion into extinction). The principle of this method is illustrated in Figure 1.19. The light source (1) sends out parallel near-IR light (2) which passes through the sample cell (3) lying on the rotor (4). The distribution of local transmission is recorded over the entire sample length by a CCD-line detector (5).

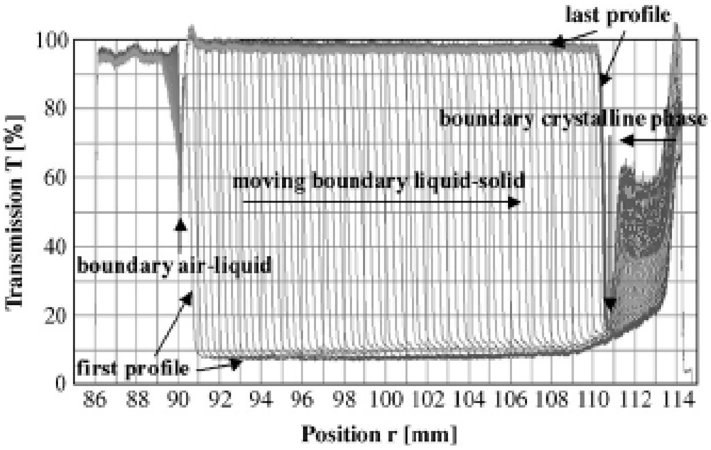

Figure 1.18 Transmission profiles obtained during centrifugation of monodisperse SiO_2 [106]

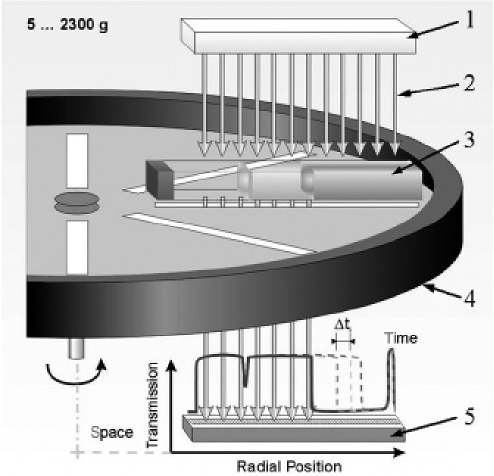

Figure 1.19 Measurement scheme of the multisample analytical photocentrifuge [106].

From the kinetics of transmission/extinction profiles, the demixing behavior and/or dispersion stability can be determined [107]. As the measurement occurs under centrifugal field, the stability test can be performed in such a short period of time (5000 times faster than under gravity) and the obtained results correlate well with the sample behavior at normal gravity.

Furthermore, the transmission profiles can be used to calculate the volume weighted particle size distribution. First, the particle size is determined from the sedimentation velocity using the Stokes law (equation 18) and secondly, the extinction/transmission is transformed into concentration with Lambert-Beer law:

$$- ln\frac{I}{I_0} = \varepsilon \, l \, c \qquad \text{(Equation 37)}$$

With ε the extinction coefficient, l the path length and c the molar concentration of the absorbing species.

The Stokes and Lambert-Beer law are limited to low concentrations due to hindered settling and multiple scattering respectively. At higher volume concentrations, hindered sedimentation occurs due to hydrodynamic interaction between particles and disturbance of the stream lines, which result in a sedimentation velocity which is dependent on the volume concentration φ and the apparent viscosity η.

$$u_t = \frac{1}{18}\frac{\Delta\rho . x^2}{\eta}\omega^2 . r . f_{hind}(\phi) \qquad \text{(Equation 38)}$$

1.3.3 State of the art of aqueous TiO_2 dispersions

The most reports about aqueous TiO_2 nanodispersions show the preparation of the dispersions by mixing crystalline (either commercial or laboratory synthesized) TiO_2 powders with electrolytes [95, 108, 109], surfactants [110, 111] or polymers [112, 113]. The mixing procedure itself includes the use of an orbital shaker [108], stirring (with or without heating) [110, 114] or the use of ultrasonication (horn and/or bath) [95, 108, 109].

Several studies on TiO_2 dispersions have been carried out to evaluate the influence of particle surface area, primary particle size and crystal phase on the TiO_2 nanoparticle dispersion properties. Recent studies on the dispersion properties are mainly carried out in view of toxicology studies since nanoparticles could have the potential to be harmful due to their high specific surface area and unique physicochemical properties [115]. Suttiponparnit [109] studied the hydrodynamic size, zeta potential and isoelectric point of ten laboratory synthesized TiO_2 samples with different phases and particle sizes, and one commercial TiO_2 powder (Degussa) in different solutions using different electrolytes. It was demonstrated that increasing the particle surface area result in a decrease in solution **pH** while at fixed pH, an increase in titania mass concentration enhances the collision frequency between the particles, leading to a higher degree of agglomeration. In addition to the synthesis method, the **isoelectric point** was found to be inversely related to particle size but insensitive to the crystal phase. The obtained results have important implications both in developing nanomaterials for environmental applications as in performing nanotoxicological studies as dispersion properties affect delivery and transport efficiencies. Jiang et al. [95] characterized the state (such as the hydrodynamic size, surface charge, and the degree of agglomeration) of titania (anatase and rutile) and other nanoparticle suspensions and tested the effect of solution pH and **ionic strength** (IS) on dispersion properties. It was found that an increase of ionic strength from 0,001M to 0,1M led to a 50-fold increase in the hydrodynamic diameter and the variation of pH resulted in significant change of particle surface. Moreover, different **ultrasonication** techniques (horn and bath) have been applied indicating the horn as a more effective way to disperse the agglomerates, although bath sonication didn't result in an enhanced agglomeration. Nevertheless, it was concluded that the combination of probe sonication and electrostatic stabilization works very well in dispersing nanoparticle agglomerates. Moreover, this technique can be used to determine the presence of aggregates, which do not disperse in contrast to agglomerated nanoparticles.

Most studies concerning the dispersion and stability of TiO_2 dispersion have been carried out on micrometer and commercial TiO_2 nanopowders. To use these dispersions in subsequent processing steps, a high stability and high solid load are envisioned. Concerning the solid load, aqueous dispersions of TiO_2 particles (30-50 nm) with Triton X as non-ionic surfactant and a maximum solid load of 6,7 wt%. were reported, in view of transparent, photocatalytic coatings [110]. Using commercial titania (P25), colloidal stable aqueous dispersion with a solid load of 35 wt% have been prepared by adding a high amount of polycarboxylic acid dispersant [114]. Using pre-synthesized nanoparticles, stable dispersions with a solid content of only 1wt% in water and ethanol were obtained [116, 117].

Although the dispersion of nanosized titania powders has received some attention in the last years, the understanding of the relationship between nanoparticles and their toxicities in specific test systems is still limited and require more work [118, 119].

1.3.4 Challenges

For the use of TiO_2 in various (environmental) applications, the nanoparticles are desired to be applied in the form of thin, porous and mechanically stable layers, with homogeneous thickness. Such films can only be fabricated from nanoparticle dispersions which are colloidal stable, both macroscopically and microscopically, in a suitable solvent preferably in water. Furthermore, some applications demand for transparency of the films which requires the use of very small nanoparticles with sizes **below 50 nm**, without any significant agglomeration.

Although numerous strategies for the controlled synthesis of TiO_2 nanoparticles of different sizes and shapes have evolved within the last decade, the preparation of highly stable aqueous dispersions of very small nanoparticles (with high specific surface areas) remains still a challenge that need to overcome in order to realize the targeted applications. Moreover, to reduce the volume of applied dispersion and the time needed to obtain films with a certain thickness, dispersions with a **high solid load** are aimed. Previous studies report dispersions with a solid load as high as 35 wt% in aqueous medium, mostly starting from commercial TiO_2, although they lack the study of stability in function of time or the application of the dispersions in layer deposition.

Finally, to approach the ecological demands, aqueous dispersion of nanoparticles prepared via an **aqueous method** is preferred above nanoparticles from non aqueous syntheses.

1.4 Deposition of TiO_2 crystalline films from aqueous dispersions

As the goal of this thesis is to synthesize substrate supported films, the different available deposition techniques are summarized here. Two broad categories can be distinguished, depending on whether the process is primarily physical or chemical [120]. The physical deposition techniques use mechanical, electromechanical and thermodynamic means to produce a film and are further categorized into physical vapor deposition techniques such as sputtering [121] and pulsed laser deposition [122]. Chemical deposition procedures include chemical solution deposition (CSD)[123], chemical vapor deposition [46] and atomic layer deposition [124].

In this work, an aqueous dispersion is applied for film deposition, thus only chemical solution deposition techniques are described in the following. Many advantages are prescribed to CSD techniques, such as low investment costs, controllable film composition and large area deposition which offers a large throughput rate. In general, liquid deposition processes are very versatile methods to produce homogeneous coatings through the spreading of a precursor solution onto a substrate and evaporation of volatile compounds (solvent). The flow chart of a typical chemical solution deposition process is presented Figure 1.20.

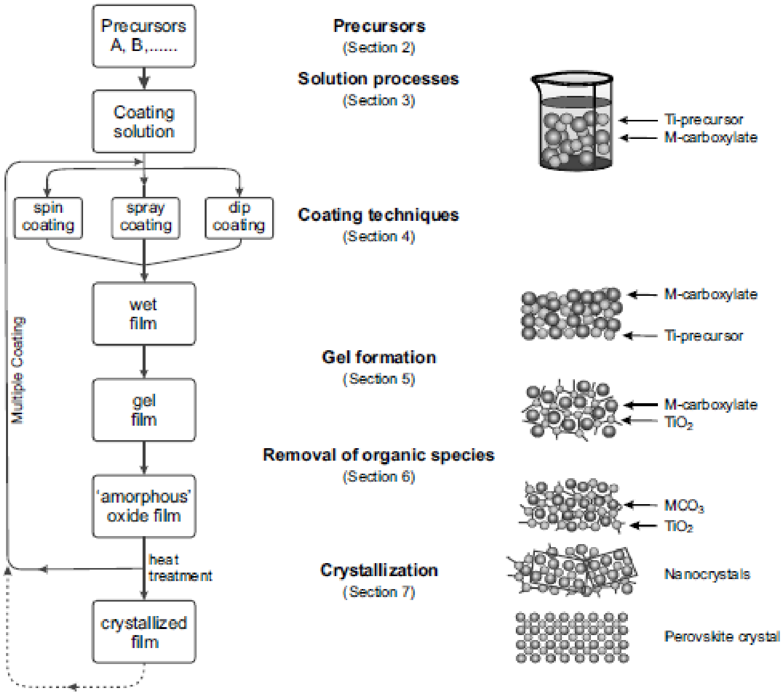

Figure 1.20 Flow chart of a typical chemical solution deposition (CSD) process starting from a sol-gel precursor [125].

The precursors used for chemical solution deposition can be divided into non-aqueous (organic solvent based) and aqueous precursors, from which the aqueous precursors gain more interest from ecological stand point. Aqueous precursors can further be divided in two types: a homogeneous precursor solution or a particulate based precursor. Homogeneous precursor solutions consist of the (desired) metal ions, stabilized in organometallics or by complexing agents (sol-gel synthesis route) in the solution [126, 127]. As for these precursors, the oxide formation and the crystallization occurs in a post thermal treatment, the use of high temperatures could introduce cracking and/or peeling of the film due to shrinkage during the crystallization of the deposited amorphous films. Furthermore, the heating process precludes the fabrication of films on substrates with low thermal stability such as polymers [128].

In contrast, particle based precursors are dispersions/suspensions consisting already of crystalline metal oxide nanoparticles. Although particle based precursors show advantages concerning the applied temperatures and used substrates, the deposition of homogeneous precursors are most studied and understood. A broad overview of the technologies and the applications of films deposited via CSD are given, for example, in [129].

Dip and spin coating are the most common CSD techniques, illustrated in Figure 1.21, each with its advantages and drawbacks, and are usually used in electronics and optics industries.

At the laboratory scale, **spin deposition** [130] is usually achieved with a photoresist spinner holding the substrate on its place by applying a vacuum to the backside of the substrate. After flooding the wafer (substrate) with precursor, the wafer is accelerated rapidly to 1000-8000 rpm. The thickness of the wet film is controlled by the angular velocity and the spinning time, together with the solution viscosity, while the solute concentration influences the thickness of the final ceramic film. One of the great advantages of spin-coating of colloidal dispersions is the production of resultant morphologies at a short span of time [131-133]. When applying a suspension onto the substrate, most of the suspension is flung off through centrifugal forces, leaving behind a film that continues to thin by radial outflow and solvent evaporation. As the suspension becomes more concentrated, its viscosity rises and then eventually becomes so large that radial outflow effectively stops. The film continues to thin, however, until the solvent has evaporated thoroughly and a "dry" film of the suspended material is left [134].

Via **dip coating**, the substrate is successively dipped into the precursor and withdrawn at a constant speed. The solvent evaporates and drainage is continued as the substrate is completely removed from the liquid bath [125]. Besides producing minimal waste, the dip coating process offers a good control of thickness which is related to the rate of substrate withdrawal and solvent volatility.

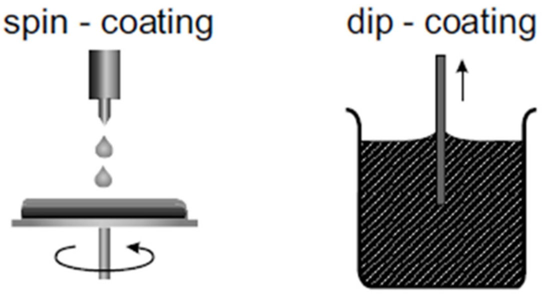

Figure 1.21 Illustration of commonly used coating techniques [125].

Another frequently used deposition technique in combination with dispersions, as aimed in this thesis, is **tape casting** (known as doctor blading) which is applied in the electronic industry, for the preparation of solid fuel cells and laminated composites [135]. Tape casting involves the dispersion of inorganic ceramic powder in a liquid medium, followed by addition of organic binders and plasticizers to increase the strength and flexibility of the tapes after casting and drying [136, 137]. The role of dispersant, binder and plasticizer in tape casting processing are well studied and documented [136, 138].The most critical and challenging step in achieving dense films by tape casting is the colloidal processing of tape casting slurries which should be a well dispersed homogenous stable system with low viscosity, good shear thinning behavior, and high solid loading [139, 140].

Although the above described techniques are frequently used for the preparation of oxide films including TiO_2 films [128, 141, 142], only few reports concern the application of aqueous TiO_2 dispersions in combination with the above described techniques (spin coating, dip coating and tape casting). Table 1.4. gives a short overview, indicating that the preparation of thin, dense films of anatase, deposited from a dispersion of pre-synthesized nanoparticles, via the above techniques, still remains a challenge.

Dispersion synthesis	***Conditions of deposition***	***Properties of film***	***Aimed application***	***Ref***
spin coating				
Synthesized sol-gel dispersion + triton X	2000 rpm, 120s 20 min @450°C 3 spin coat cycles	Transparent films d= 140 nm D =100-400 nm	Photovoltaic cells	[143]
TiO_2 powders (as synthesized and P25), mixing-grinding with H_2O, acetylaceton, Triton X, stirring+ sonication	1000 rpm 15 min @100°C 30 min @450°C	anatase/rutile Dparticle= 16 and 30 nm d= 10-20 μm	Photovoltaic cells	[144]
TiO_2 nanoparticles, via sol-gel, dispersed in water	1500 rpm	D=2 nm d=15 nm	Photovoltaic cells and light emitting diode	[145]
TiO_2 (up to 50 wt% of PVA) +H_2O +PVA (≠conc)+Triton X	spin coated	D= 60-500 nm	Organic thin film transistors	[146]
Dip coating				
60 wt% commercial TiO_2 in H_2O	withdrawn at 6 mm/s 1h @110°C 2h @900°C	d= 15 μm	Catalysis	[147]
anatase TiO_2 + diethylene glycol as complexing solvent, 1,8 wt%	200°C 500°C		Photocatalysis	[110]
Tape casting				
as-obtained TiO_2 powder + HNO_3 solution+ HPC as thicking agent	80 mm/s 60°C 30 min @ 450°C	anatase, porous films d= 2 μm	Photovoltaic cells	[148]

Table 1.4 Overview of the reports using aqueous TiO_2 dispersion combined with spin coating, dip coating and tape casting for film preparation. D= diameter of the nanoparticles, d= thickness of the film, PVA= polyvinylalcohol, HPC= hydroxypropylcellulose.

1.5 Synthesis of substrate supported TiO_2 nanostructures

Besides smooth and dense films, **nanostructured** coatings have attracted a lot of attention due to their interesting optical, electronic, and catalytic properties and their applications including photovoltaics [149, 150], photocatalysis [151, 152], and superhydrophobic/superhydrophilic materials [82] [153] For these applications, TiO_2 coatings with a high specific surface area and tailored pore size show a lot of potential [11, 154] as the pore size and the specific surface area greatly impact the physical properties of these materials, playing a relevant role in their activity. For instance, catalytic applications require a **tunable porosity** to optimize the diffusion rate of reactants towards and reaction products away from the adsorption sites, and a **high surface area** to maximize the interface between the reactant flow and the catalyst surface.

Nanostructured TiO_2 coatings (substrate supported nanostructures) with well controlled morphologies may be synthesized by several methods, all aiming structured arrays with high **aspect ratio**[5] nanoarchitectures. The same morphologies as can be prepared via powder synthesis can be prepared as films, such as nanowires, nanotubes, nanorods etc. Some methods for the preparation of arrays (= films) of these morphologies on substrate simply use the nanostructured powders, dispersed in a medium, to deposit by spin or dip coating, or other deposition methods. While other methods deposit the nanomorphologies directly onto the substrate via hydrothermal growth [155, 156], template assisted synthesis [157, 158] lithographic techniques [159, 160] or a combination [161]. The collection of nanostructured films not only includes nanotube arrays and nanorod arrays but also patterned TiO_2 arrays, which will be discussed more extensively below.

The synthesis of nanoarchitectures can be divided into two categories: top-down and bottom-up. Top down refers to the gradual reduction of size from the macroscale to the nanoscale, while bottom up involves the assembly of larger structures from molecular building blocks. One of the **top down** techniques applied in this thesis will be described in next section.

1.5.1 Patterned nanostructures

The increasing demand of miniaturization of objects and materials down to the micron- and nanoscale have leaded to the development of patterning techniques . In the electronic industry, photolithography have been used and developed for many decades. This technique uses photons or electrons (light) to transfer geometric shapes present on a mask to the surface of a silicon wafer. Although feature sizes << 100 nm can be

---

[5] Ratio of length to width of the nanostructure

patterned with this technique, it shows a lot of drawbacks such as high cost, high-end equipment, clean room conditions and limited application of materials. To overcome these restrictions, Prof. Whiteside developed a family of related patterning techniques in the 1990s, the so called **soft-lithography techniques** [162, 163]. These techniques are mainly parallel patterning methods to pattern large areas in a relatively short period of time and can generate high quality patterns and structures with feature sizes ranging from 30 nm to 100 µm [164]. Besides providing cheap alternatives for the much more costly photolithographic processes, they are able to be used on nonplanar surfaces and to process a wider range of materials, including polymers, biomaterials, ceramics, hybrids and composites.

All soft lithography techniques require an **elastomeric mould or stamp** which is patterned with a relief structure on its surface. One of the steps in the patterning process includes the conformal contact of the elastomer with a substrate. The patterned elastomer is prepared by casting a liquid prepolymer onto a 3D patterned master structure [165] followed by polymerization of the prepolymer. The final result is an elastomeric negative replica of the master structure with 3D patterns. The patterned elastomer can be utilized for patterning in two different ways:

1. The protruding patches of the patterned elastomer can be employed to carry a precursor ink to the substrate (= printing approach)
2. The precursor material is contained in the recessed regions between the protruding patches (= moulding approach)

The soft lithography techniques that can be applied to ceramics and hybrid materials are divided into moulding-based approaches and surface modification-based approaches. The moulding based patterning approaches are presented in Figure 1.22 and include conventional micromoulding, microtransfer moulding (µTM) and micromoulding in capillaries (MIMIC)(Figure 1.22 a-c). All employ physical confinement of a liquid precursor solution or suspension to define the shape of the final pattern. Other micromoulding related techniques are replica moulding and solvent-assisted micromoulding. These surface modification-based patterning techniques (Figure 1.22 d-e) consist of the selective deposition of material on those patches of the substrate which are previously surface modified by chemical contrast (hydrophobic-hydrophilic, charge,…). In principle, higher aspect ratios can be achieved using moulding techniques compared to surface modification methods.

In the following, only the micromoulding technique is discussed in more detail since this type of soft lithography is used in this thesis to prepare patterned films.

Micromoulding, also called embossing or even replica molding, involves imprinting a patterned mould into a continuous wet film by application of some pressure. Both soft (polydimethylsiloxane [166], perfluoropolyester [167]) as rigid (glass, poly(methyl methacrylate) [168] materials have been employed for the moulds. Inherent to this technique is the formation of a residual layer between the desired features wherefore this techniques is only interesting for applications in which the presence of a residual layer presents no problem. Nevertheless, when this layer hinders for the application, a post etching step can be applied.

The term nanoimprint lithography (NIL) is often confused with micromoulding. The NIL process is very similar although it more focuses on nanopatterning of polymers and is often done at elevated temperature (to reduce the viscosity) and involves an optional final UV curing step.

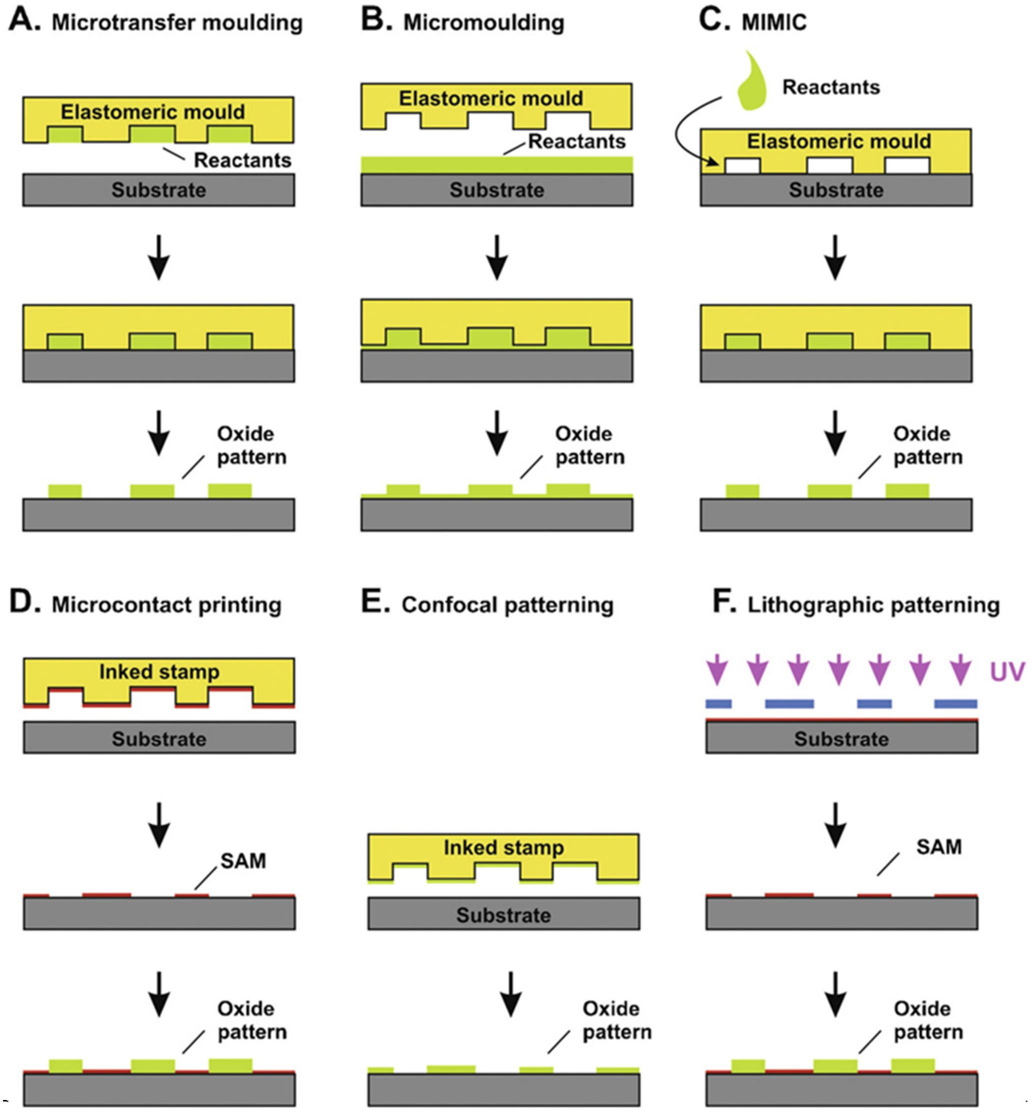

Figure 1.22 Overview soft lithographic (a-e) and photolithographic-aided patterning techniques [160].

In general, the micromoulding process consist of several steps, which are further discussed below:

a) Preparation of the master

The time consuming and expensive methods such as photolithography, e-beam lithography and ion beam milling, are still applied for the preparation of a patterned master, as they result in high quality patterns and reusable stamps. Other available relief structures are diffraction grating, TEM grids, polymer beads assembled on solid supports and relief structures etched in metals or silicon.

b) Preparation of the mold or stamp

The most popular elastomeric material that is widely used for the stamp is polydimethylsiloxane (**PDMS**). PDMS stamps are most frequently made from commercial Sylgard 184 (Dow Corning Inc) which consists of a silicone prepolymer and a curing agent. They are mixed in a certain ratio and poured over the patterned side of the master, followed by a curing step. This process is called cast molding [169] and the curing exists of the cross-linking of the silicone resin by a mixture of vinyl-terminated PDMS and trimethylsiloxy-terminated poly(methylhydro-siloxane) polymers. The obtained elastomeric, rubber-like stamp can then be easily peeled off the master due to its low surface energy [162].

Several properties of PDMS are responsible for the high quality patterns and structures that can be deposited using this elastomer. To achieve intimate contact of the stamp with the substrate, the stamp requires two conflicting properties with respect to the **Young's modulus**. On the one hand, the stamp need to be soft enough to enable good conformal contact with the substrate (flexibility). To adapt elastically to substrate roughness without leaving voids, a low Young's modulus and high work of adhesion is required. On the other hand, precise defined micropatterns require a rigid material which implies a high Young's modulus. The conflict between these properties limits the resolution of the patterns prepared by soft elastomeric stamps. Therefore, the softness of the stamps can lead to various types of deformation. The various types of collapse of patterns are illustrated in Figure 1.23 [170].

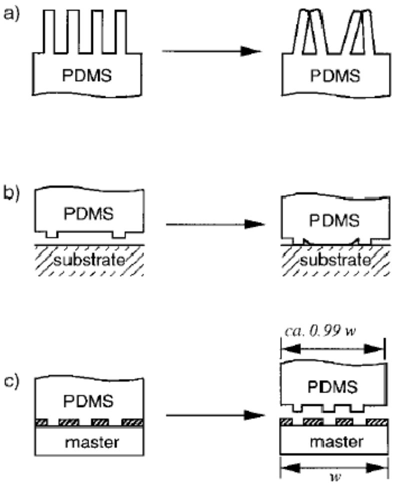

Figure 1.23 Schematic illustration of possible deformations and distortions of microstructures in the surfaces of elastomers such as PDMS; a) pairing, b) sagging and c) shrinking [163].

Besides its **low surface energy** (0.0216 N/m), another essential property is the nature of any present functional group which determines the **wetting and dewetting** behavior of the used precursor solutions in the mould. As the PDMS stamp is hydrophobic, water will not spread on the surface which may be advantageous for the debonding step in micromoulding and microtransfer moulding but disadvantageous applying the MIMIC method.

Other properties of PDMS are a high elongation at break (> 100%) and a good chemical and thermal (up to 186°C) stability.

c) Choice of precursor 'ink'

Both homogeneous precursor solutions as particle suspensions can be applied for patterning although higher volume fractions of solids can be reached using suspensions. Furthermore, the use of suspension-based precursors is preferred when high aspect ratios are required or the chemical transformation from liquid precursor to final ceramic phase has to be avoided. The following is mainly focused on the use of particle based suspensions, as this kind of precursor is applied in this work.

The key physical properties of suspensions are:

- *A* high **solid content** (and thus high metal concentration) is favorable since it is related to the solids volume in the final oxide and it suppresses shrinkage upon drying and post thermal treatment, which can lead to loss of pattern details (80-95%) and severe cracking.
- Low **viscosities** enables fast penetration in the channels of the pattern.
- Low **surface tension** promotes wetting of a relief patterned stamp and is required when water-based solutions are used, but good wetting may hamper the debonding step in which the stamp and ink are separated [171].

- The concentration and volatility of **solvent**s determines the drying rate and drying time. A compromise is necessary as fast evaporation lead to faster solidification of a precursor which can increase the throughput in industrial processes, while a slower drying process improves the packing efficiency of the particle based suspensions [172].

d) Embossing, drying and curing

The actual pattern is formed by embossing the stamp into a wet film of the dispersion with the application of a pressure, followed by a drying step at elevated temperatures which solidifies the dispersion confined by the mould [173]. PDMS is permeable to many solvents but not to polymers or nanoparticles and physical drying of a moulded suspension is possible by the diffusion of the solvent into the PDMS mould. However, using PDMS in combination with certain solvents induces swelling of the stamp [173]. The least swelling solvents are water, glycerol and ethylene glycol while the highest swelling solvents are the apolair solvents such as pentane and xylene.

The final resolution of the patterned material is determined by the surface energies of the components, and the ability of the mould to detach from the patterned material after drying, as mentioned earlier. High resolution requires the selection of a mould material that has significantly lower adhesion energy with the pattern material than the substrate has with the material. It has been shown theoretically that relatively large contact angles between mold and precursor are required to facilitate debonding after moulding based patterning, ideally >90°. Under such conditions, the debonding energy is very large which promotes the release of the dried precursor from the mould. When the contact angle is smaller than 90°, the concave surfaces inhibit the debonding.

The dewetting process, which is driven by both the applied pressure and the differences in interfacial tensions i.e. substrate-elastomer (SE), substrate-liquid (SL), and liquid elastomer (LE) is proportional to the dewetting speed S, is expressed by following equation:

$$S = \gamma SL + \gamma LE - \gamma SE \qquad \text{(Equation 39)}$$

A residual layer can be avoided when the liquid dewet spontaneously from the elastomer surface so that the protruding parts of the mould make conformal contact with the substrate [174]. Except when the stamp is modified, residual layers are very hard to avoid [175].

When using precursor solutions, the formed patterns mostly require a post-patterning heat treatment step after removal of the stamp, in order to convert the dried precursor into the desired crystalline phase, remove organics and/or densify the thin film. The post-treatment crystallization step is avoided using dispersion of crystalline nanoparticles.

1.5.2 State of the art

Many kinds of ceramics and hybrids, such as $Pb(Zr, Ti)O_3$, TiO_2, $BaTiO_3$, ZrO_2, ZnO, SnO_2 and many more [167, 176, 177], have been patterned on micrometer and submicrometer scale, as well as nanoscale (<500 nm). Figure 1.24 shows various micro- and nanostructured deposited by soft lithography. Especially with micromoulding, very small features can be made with high fidelity. The smallest features obtained have diameters of approximately 0.2 µm [167, 178], but are usually 0.5 µm [171] or more [176] in diameter. The smallest **line patterned films** are prepared by Göbel, with widths of 2-20 µm [175]. These conductive Al-doped zinc oxide patterns were prepared from a polymeric solution by applying simply micromoulding.

Recently, several studies have been published on the soft-lithographic patterning of TiO_2, most commonly using micromoulding in capillaries [176, 177], micro-transfer moulding [171], micromoulding and nanoimprinting [178, 179].

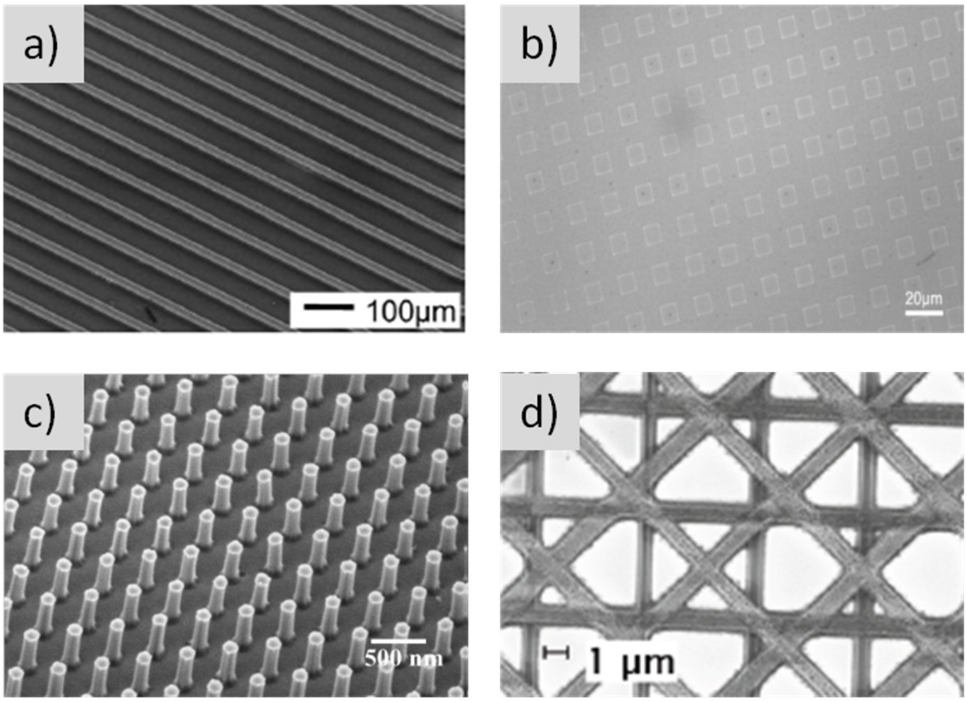

Figure 1.24 Examples of micro and nanostructures with a) TiO_2 lines (23 µm) via MIMIC [180], TiO_2 lattices (10 µm) via embossing [168], c) TiO_2 features (200 nm x600 nm) via embossing [167] and d) hierarchical structure consisting of one Y-stabilized ZrO_2 layer (vertical line) and three $BaTiO_2$ layers via micromoulding [181].

Nonetheless, the fabrication of truly high-aspect ratio structures still remains a challenge. Well-defined submicrometer-scale objects with aspect ratio > 1 are rarely reported. The aspect ratio of the structures depends on the aspect ratio of the relief features in the PDMS, which was shown to be optimal between 0.2 and 2 in order to obtain defect-free stamps or molds [163]. Also shrinkage of the structure after drying and possible post-patterning treatment can decrease the aspect ratio enormously. Less shrinkage was observed using dispersion in combination with MIMIC, compared to the use of solution gel precursors [179]. Nevertheless, the solid load influences the adhesion and the uniformity of the patterns. Low uniformity patterns were obtained from a high solid loaded dispersion while uniform patterns over a wide area were demonstrated using low-solids loading suspensions of different solvents in combination with the MIMIC process [180].

So far, mostly two-dimensional (2D) patterns have been reported, i.e. patterns consisting of a single layer of TiO_2 on a flat substrate. Another experimental challenge is the fabricating of hierarchically ordered structures at multiple length scales. Such materials are important both for the systematic fundamental study of structure-property relations as for their technological promise in applications such as catalysis, selective separations, miniaturized electronic and many more. Yang et al. [182] developed a simple procedure for preparing hierarchically ordered structures by concurrently or sequentially combining micromoulding, latex sphere templating, and cooperative assembly of hydrolyzed inorganic species (sol-gel) and amphiphilic block copolymers. Patterns with different dimensions (10, 100 and 1000 nm) and different compositions, such as niobia, silica and titania, could be obtained. Using the MIMIC technique, Khan [183] developed a method for the fabrication of layer-by-layer structured patterns. One of the limitations of soft-lithographic patterning in general concerns the registry of the formed patterns [184]. Therefore it remains problematic to fabricate hierarchical structures with a more complex function by combining several patterning steps in sequence. Nevertheless, Göbel et al. succeeded in stacking up to five relief patterned functional oxide (YSZO and $BaTiO_3$) thin films and obtained an hierarchical structure with an aspect ratio of 0,10- 0,13.
Based on the aforementioned reports, it is concluded that the preparation of hierarchical structures with high aspect ratios still remains a challenge, which justifies the research carried out in this thesis.

1.6 Applications of TiO_2 in

1.6.1 Photocatalysis

The field of photocatalysis can be traced more than 80 years ago, when the chalking of titania-based paints had been observed for the first time and the darkening of metal oxides in contact with organic compounds in sunlight had been studied. Photocatalysis is generally thought of as the catalysis of a photochemical reaction at a solid surface, usually a semiconductor [7, 185, 186]. The applications of photocatalysis are quite broad, including sterilization, air and water purification, self-cleaning and H_2 generation.

For the degradation of organic compounds, **titanium dioxide** nanoparticle photocatalysts are generally believed to be the most reliable materials due to their non-toxicity, low cost, physical and chemical stability [6, 9]. Furthermore, TiO_2 is the most active photocatalyst under the photon energy of 300 nm $<\lambda<$ 390 nm and remains stable after the repeated catalytic cycles.

In this thesis, the focus only lies on the application of photocatalysis for the degradation of organic pollutants into harmless inorganic substances such as CO_2, H_2O etc. and for self-cleaning materials.

1.6.1.1 Photocatalysis for the photodegradation of pollutants

Most of the aqueous contaminants such as haloalkanes, aliphatic alcohols, carboxylic acids, aromatics, polymers, surfactants, pesticides, and dyes, can be mineralized at the surface of UV-excited TiO_2 photocatalysts [187]. However some issues (which are discussed later) limit their quantum yield, which is in the range of 0,1-10 % for water-solid photocatalytic reactions. Nevertheless, especially for the remediation of dye-contaminated water, the use of semiconductor photocatalysis is a major research area which is not surprising as it is known that 15% of the ca 0.9 million ton of organic dyes produced annually is lost in the environment during the synthesis and production resulting the dyestuff industry as a major source of pollution [188].

The mechanism of the photocatalytic process, presented in Figure 1.25 and listed in Figure 1.26, involves the absorption of light, with energy equal or larger than the bandgap[6] of the semiconductor particle generating delocalized electrons in the conduction band and delocalized holes in the valance band which are uniformly distributed throughout the particle [186]. Within a few picoseconds after photon absorption, these free delocalized carriers migrate to the particle surface and get trapped at various surface sites or annihilate via electron-hole recombination (step 1). When not recombined, the electron and holes react with adsorbed electron acceptors (A) (step 6) and electron donors (D) (step 4), respectively. Reaction of the electrons and holes with adsorbed H_2O, OH^- and O_2 result in the production of hydroxyl radicals (•OH) (step 2 and 3), superoxide radical anions ($O_2^{\bullet-}$)(step 7) and H_2O_2 (step 9). These oxidative species contribute further to the decomposition of organics at the TiO_2 surface (step 5) [7].
The complete photodegradation of pollutants involves two processes: photobleaching and photomineralization. Photobleaching is the photochemical destruction of the dye into intermediate products, while photomineralization concerns the total degradation of the

---

[6] For a bandgap of 3,2 eV (anatase), the wavelength of the photons should be 388 nm or less to induce the excitation of electrons

dye, or its intermediates, into CO_2 and H_2O. The adsorption and the degradation of the dye into intermediates is studied by UV-Vis analysis. As the intermediates can also be toxic or harmfull, the efficiency of the catalyst is actually determined by the ability to completely photoxidize the degradation products to CO_2, which is determined by measuring the Total Organic Compound (TOC). Studying the photocatalytic degradation by both techniques provides complementary information about the activity of the material, as some catalysts are good photobleachers but bad photomineralizers or visa versa. For example, the photodegradation of Rhodamine 6G (Rh6G) by P25 (from Evonik®) was followed by parallel micro volume TOC analysis and UV-vis, at short intervals [189]. It was shown by an immediate decrease in absorbance that the degradation of the dye (photobleaching[7]) starts immediately after the UV-light has been switched on. After 60 min, the amount of dyes decreased to only 16% and after 120 min, the photobleaching was almost complete. In contrast, the TOC results showed that the total amount of organic carbon in the solution was almost constant during the first 20 min. After longer irradiation times, the oxidation to CO_2 started to take place but at a much lower rate. This indicated that at the starting point of the CO_2 removal, the concentration of the initial dye already reached very low values. After 60 minutes of UV irradiation, 36% of the initial amount of carbon was oxidized to CO_2 while 91% of the initial dye molecule photodegraded into smaller compounds, indicating a longer lifetime of the intermediates.

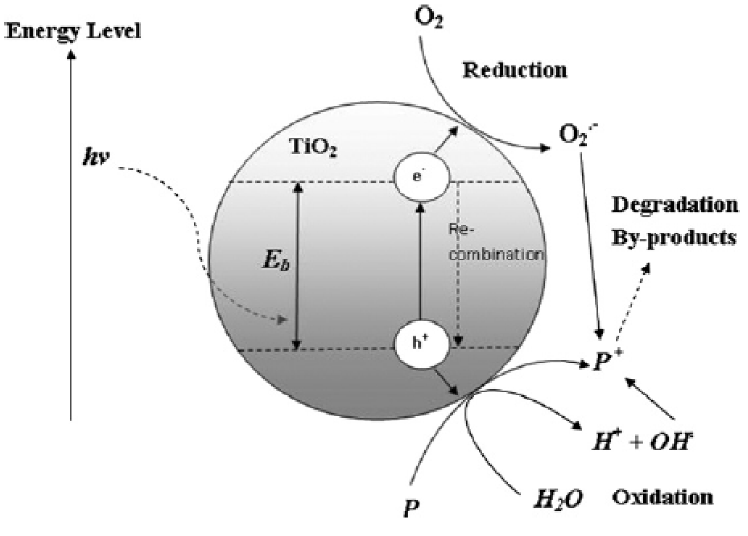

Figure 1.25 Photoinduced formation mechanism of electron hole pairs in a semi-conductor TiO_2 nanoparticle with the presence of water pollutant P [190].

---

[7] Breaking of the conjugated system

$$\mathrm{TiO_2} \xrightarrow[E \geq E_g]{h\nu} \mathrm{TiO_2}(\mathrm{e^-_{cb}},\ \mathrm{h^+_{vb}}) \rightarrow \text{recombination} \qquad (1)$$

$$\mathrm{TiO_2}(\mathrm{h^+_{vb}}) + \mathrm{H_2O_{ads}} \rightarrow \mathrm{TiO_2} + \mathrm{HO^{\bullet}{}_{ads}} + \mathrm{H^+} \qquad (2)$$

$$\mathrm{TiO_2}(\mathrm{h^+_{vb}}) + \mathrm{HO^-_{ads}} \rightarrow \mathrm{TiO_2} + \mathrm{HO^{\bullet}{}_{ads}} \qquad (3)$$

$$\mathrm{TiO_2}(\mathrm{h^+_{vb}}) + \mathrm{D_{ads}} \rightarrow \mathrm{TiO_2} + \mathrm{D^+_{ads}} \qquad (4)$$

$$\mathrm{HO^{\bullet}} + \mathrm{D_{ads}} \rightarrow \mathrm{D_{oxid}} \qquad (5)$$

$$\mathrm{TiO_2}(\mathrm{e^-_{cb}}) + \mathrm{A_{ads}} \rightarrow \mathrm{TiO_2} + \mathrm{A^-_{ads}} \qquad (6)$$

$$\begin{aligned} &\mathrm{TiO_2}(\mathrm{e^-_{cb}}) + \mathrm{O_{2\,ads}} + \mathrm{H^+} \\ &\quad \rightarrow \mathrm{TiO_2} + \mathrm{HO_2{}^{\bullet}} \rightleftarrows \mathrm{O_2{}^{\bullet -}} + \mathrm{H^+} \end{aligned} \qquad (7)$$

$$\mathrm{HO_2{}^{\bullet}} + \mathrm{TiO_2}(\mathrm{e^-_{cb}}) + \mathrm{H^+} \rightarrow \mathrm{H_2O} \qquad (8)$$

$$\mathrm{2HO_2{}^{\bullet}} \rightarrow \mathrm{H_2O_2} + \mathrm{O_2} \qquad (9)$$

Figure 1.26 List of initial photocatalytic reactions (A and D are referred to adsorbed acceptor and donor molecules respectively) [191].

According to the above mechanism, the critical process for photocatalytic reactions is mainly determined by the competition between charge transfer (steps 2, 3, 4, 6 and 7) and recombination of electrons and holes (step 1). To suppress the recombination and increase the probability of interfacial charge transfer, **charge carrier trapping** is needed [11]. Surface and bulk irregularities, which are dependent on the chemical preparation method, can serve as carrier traps and help to suppress the recombination or may increase the lifetime of the electron-hole pairs. The recombination can be delayed, with a lifetime on the scale of µs in nanocrystalline TiO_2 films.

Another way of decreasing the electron-hole recombination rate and to improve the photocatalytic activity is by **modifications of the surface** with other materials such as co-adsorbants (active carbon, porous silica and metallic nanoparticles (Pt, Au, Ag or other doping materials (Au,Fe, Li, S, …) [187, 192].

The application of **nano**structured semiconductor materials in photocatalysis have promoted the photocatalytic efficiency by the **growth of the specific surface area**. Quantum-sized particles (<10 nm) are potential candidates for enhancing the photoefficiency even more due to its high ratio of surface area to volume. The quantum size effect leads to a widening of the band gap and thus the enhancement of redox ability of photogenerated electron-hole pairs since photons with a lower wavelength can be easily absorbed. Also the charge carrier trapping process occurs faster in Q-sized than in bulk by accelerating the migration of electron and holes from inside the particles to the outer surface, as this distance is shorter in smaller particles. The recombination process is then overwhelmed by the charge carrier trapping process.

By reduction of particle size also the number of **surface active sites** are increased which not only improves the surface charge carrier transfer rate in photocatalysis but also favors the adsorption of hydroxyl groups. Moreover, a decrease in particle size results in a redistribution of the planar, edge, and corner sites in a crystal structure. These structural changes are also expected to affect the activity of the photocatalyst.

Besides the surface area, impurities and density of surface groups, the photocatalytic activity of TiO_2 also depends on the crystallinity, more specifically the **crystal form** [193]. Between the rutile and antase, **anatase** is considered as more active while pure rutile phases has limited photocatalytic activity.

In the study for the potential factors in determining the different activity between these phases [76], it has been suggested that the increased photoreactivity of anatase is due to its slightly higher Fermi level, lower capacity to adsorb oxygen and higher degree of hydroxylation[8] [194]. The existence of a certain relationship between the crystallite phase and surface adsorbed water and hydroxyl groups is considered to be important in trapping charge carriers [195]. Furthermore, the difference in lattice structure between rutile and anatase is the distortion of each octahedron and the assembly pattern of the octahedra chains. Commercial TiO_2 P25 (Degussa)[9] has frequently been used as a benchmark for photocatalysts as its activity exceeds that of pure anatase in several reaction systems. Nonetheless, reactions in which both crystalline phases have the same photoreactivity or rutile a higher one are also reported [[196, 197]. The lack of well-defined anatase and rutile samples restrict the attempt in comparing the photocatalytic activity and the determining the factors that influence their activity difference. The disagreement of the results may lie in the intervening effect of various coexisting factors, such as specific surface area, pore size distribution, crystal size, crystal shape and preparation methods, or in the way the activity is measured and expressed.

In fact the two **main challenging issues** in titania photocatalysis are (i) the relatively low quantum efficiencies of the catalysts and (ii) the requirement of near-UV light for photo-activation. The quantum efficiency (the efficiency with which light is utilized to drive redox reactions) is inherently low in TiO_2 because the processes of electron–hole generation and recombination are much faster than the rates at which the electrons and holes are trapped and participate in redox reactions on the surface of the TiO_2 particles , as discussed before. The second challenging issue in titania photocatalysis is the requirement of UV light for the activation of the photocatalyst. Due to its relatively high band gap (3–3.2 eV), currently, only a small fraction (<5%) of the solar radiation can be

---

[8] i.e., number of hydroxy groups on the surface

[9] consist of anatase and rutile in a ratio 4/1

used to activate titania [198]. To expand the spectral response of pure TiO_2 material (mainly anatase TiO_2) towards the visible light region, techniques such as doping TiO_2 with metal impurities or non metal atoms and coupling with narrow band-gap semiconductors can be applied [7].

Although **TiO_2 powder catalysts** have been studied extensively during the years, there appeared some drawbacks, encountering the use of powder suspensions in photocatalysis. These drawbacks are (1) the difficult separation TiO_2 particles from the dispersion (2) the tendency of suspended TiO_2 particles to aggregate especially at high concentrations, and (3) the difficult application of suspensions in continuous flow systems

In an attempt to solve the separation issue, **heterogeneous photocatalysis** was introduced (by Fujishima and Honda)as alternative type of photocatalysis. This type consists of the immobilization (deposition) of TiO_2 particles onto supporting materials such as glass, zeolite, membranes [147, 187]. By immobilization of TiO_2 onto the support material, the stability of TiO_2 is improved, the special morphology is retained and the catalyst can be easily separated from the aqueous solution [199].
Nevertheless, the immobilization of TiO_2 usually leads to significant decrease in photocatalytic activity due to an inherent **decrease in the surface area** available for reaction and **limited immobilization amount** compared to the suspended TiO_2 nanoparticles. Moreover this configuration is considered to suffer from mass transfer limitations of the pollutants to the surface of the catalyst which reduced the photocatalytic activity. Furthermore, the accessibility of the catalytic surface to photons is significantly reduced which in turn influences the degradation rate making it less efficient than the slurry system [200]. Some other inherent problems created by immobilization of the photocatalyst are potential loss of TiO_2 and decreased adsorption of organic substances on the decreased TiO_2 surface [201]. Therefore it is not surprising that studies performed to date have not yet identified an immobilized catalyst system that performs as efficiently as the slurry systems [202]. Nevertheless, the immobilized system is considered as the solution to the problem encountering in suspension systems. Especially for air purification, the only practical way in which the catalyst can be used is as a film.

State of the art

Both TiO_2 powders and thin films for catalytic purposes have been investigated by a wide range of researchers. Although **anatase** phase of TiO_2 is generally accepted as a more efficient photocatalyst, due to the high amount of hydroxyl groups, than rutile and brookite, a good photoactivity has been shown by samples containing anatase, brookite and rutile [203] and even an improved photocatalytic activity is demonstrated for pure rutile [51, 204, 205]. Although only a few studies have examined the photocatalytic activity of pure **brookite** TiO_2 powders or films, brookite showed a good photocatalytic activity for different organic pollutants [206]. Not only the difference in crystal phase, which is also related to the crystal size, makes it difficult to comprehend the factors that determine the photocatalytic efficiency, also the studied pollutants for the degradation experiments which varies from dyes as methylene blue [207], methyl orange [208], Rhodamine 6G [205] to organic solvents [209] and alcohols [210, 211]. Since each pollutant has a different interaction with the catalyst, the degradation rate and diffusion kinetics are influenced, producing less or more harmfull intermediate products.

It has been shown that TiO_2 particles within the sub-micron sizes exhibit improved photocatalysis in the UV region due to the improved redox ability. Conversely, the photocatalytic efficiency decreases for sizes smaller than 5 nm [212], which is attributed to the higher frequency of electron and hole recombination on smaller particles. It was shown that **doping** TiO_2 powders [213] as well as films [214] enhanced the activity of TiO_2 in the visible light region. Furthermore, increasing the surface reaction area per unit outer surface area in TiO_2 films by introducing **porosity**, increased the quantum efficiencies, approaching that of P25 [215]. It was demonstrated that highly porous and interconnected structures are beneficial to rapid diffusion and adsorption of the dye [216]. From the observation that porous films showed higher photocatalytic activity compared to the dense films, it was concluded that the photocatalytic activity is predominantly related to the **specific surface area** and not the crystal size [217]. It is clear that different surface morphologies, such as **nanostructured** and **nanopatterned** films, lead to different photocatalytic activities of TiO_2. [218-220].

Despite various efforts in fabricating and optimizing TiO_2 films for commercial photocatalytic technologies, the correlation between photocatalytic efficiency and film physical morphology such as **grain size**, **surface roughness** and **packing density**, is not well understood.

Since in chapter 4, the focus lies on the photocatalytic activity of dyes on different nanostructured TiO_2 films, the most relevant reports are overviewed in Table 1.5, indicating the variations in either the film properties (synthesis method, crystal phase, particle size, morphology) and photocatalytic experiments (organic compound, test conditions, expression of activity). These variations make it difficult to study the influence of film morphology on the photocatalytic efficiency. Furthermore, as most studies investigate patterned **micro**structures, the study on **nano**patterns is quite new and high expectations exist towards a further increase in photocatalytic activity and the understanding of the photocatalytic process.

Morphology or type of the film	Synthesis method	Characteristics	Photocatalytic analysis	Reference
Porous films	sol-gel (+PEG) + spin coating	A, crystalite size: ca. 12 nm	Decomposition of methyl orange, 7h measurement, promoted due to PEG	[142]
Dense films	sol-gel + dip coating	A	degradation of brilliant red under aerated conditions[10]: 0,6-2,5.10^{-2} min^{-1}	[221]
Films	P25 immobilized on blades via resin-bonded technique	A/R	Degradation MB(10^{-5}M): 93%, Reactive Red 195: 85% and Reactive Yellow 145: 71% after 6h experiment	[222]
Mesoporous TiO_2 on different substrates	sol-gel+ spin coating	A	Photodegradation of MB (10^{-5}M), 210 min experiment, half life= 74 min	[219]
Micro-square patterned TiO_2	**sol-gel +contact pattern transfer with PDMS**	**A, µ-patterns of 100, 200, 400 µm, d= ca 600 nm**	**Degradation rate of MB (10^{-5}M): 0,9-1,7%/min^{-1}, 120 min experiment, activity increased by decreasing pattern feature**	[220]
Mesoporous film with ultrafine anatase nanocrystallites	non-acidic sol-gel + Tween 20+ dip coating	A, BET= 120 m^2/g, pore size 5 nm, crystallites 7 nm	Photocatalytic activity of creatine increases by increase of Tween load, 150 min reaction time, sample area[11] of 1000 mm^2	[225]
Thin film	$TiCl_4$ hydrolysis + spraying	particle size= 7 nm, d=ca. 0,2 µm	5*10^{-5}M Rh6G under UV, degradation of 19% after 5 min	[226]
Thin films with various nanostructures: rods, tubes and particle aggregates	immersion (rods), anodic oxidation+ sol-gel+ dipping (tubes) and P25 ethanolic suspension+ dip coating	predominantly A	Photodegradation of Rhodamine, MB and methyl orange	[227]
Films	TiO_2 suspensions in ethanol or H_2O with EG or PEG+ spraying	A	Degradation of MB: 0,5-1,3 10^{-3} min^{-1} and phenol: 0,8-2,8 10^{-3}min^{-1}	[229]
Dense and porous films	Hydrolysis with citric acid or triethanol amine + inktjet printing	A/R, films with more elongated grains: 90-100 nm, d=85 nm and porous films: 45-50 nm, d= 650 nm	Degradation of methylorange (4,7.10^{-4} min^{-1}), reaction time > 5000 min, compared to P25 (60.10^{-4} min^{-1}	[230]
Dense + columned layers	Glancing angle deposition	A, d= 500 nm, D (colums)= 30-60 nm	Degradation of 10^{-6}M Methyl orange	[218]
Smooth and homogeneous films	TiO_2 sol (+PEG) + dip coating	A/R, more A when PEG added	Degradation > 50% of Congo Red, 120 min, higher degradation when PEG added (more A)	[231]

---

[10] Oxygen is supplied as an electron acceptor to prolong the recombination of electron-hole pairs during the photocatalytic oxidation.

2

Thin porous films	microwave hydrothermal synthesis (+EG)+ inktjet printing	A, d: 130-160 nm, 10-20 nm pores	Photocatalytic degradation of MB: 11.10^{-4} min^{-1}, compared with commercial glass: 5.10^{-4} min^{-1}, ISONORM 2010 applied, 300 min reaction time	[232]
Porous films	P25 based coating solution + dip coating	A/R	Degradation of MB: 98% after 3h, rate $0,043min^{-1}$, identical to slurry system	[233]
TiO_2 on microstructured silicon	sol-gel+ dip coaten	A	Degradation of MB ($3.10^{-5}M$): 70% after 10h, 100% after 30 h	[216]

Table 1.5 Chronological overview of the most relevant reports concerning the study of unmodified TiO_2 nanostructured films on the photocatalytic activityof dyes. (Legend of abbreviations: A=Anatase, B=Brookite, R= Rutile, d= thickness of the film, D= diameter of tube or rod, Rh6G= Rhodamine 6G, MB= methylene blue, EG= ethylene glycol, PEG= polyethylene glycol.

6.1.1.2 Photocatalysis for self-cleaning/water repelling materials

In recent years, photocatalytic TiO_2 coatings have received considerable interest as cleaning, antifogging, and both superhydrophilic and superhydrophobic surfaces [234-236]. Wettability, i.e. the degree of spreading of a liquid onto a solid surface, is not only governed by the chemical properties of the surface but also by its geometry.

The starting point of a wetting model is defined by the **Young's equation**:

$$\cos\theta = \frac{(\gamma_{SV}-\gamma_{SL})}{\gamma_{LV}} \qquad \text{(Equation 40)}$$

derived from a sessile drop on a ideal rigid homogeneous, flat and inert surface. The liquid joins the surface at a **contact angle** θ, illustrated in Figure 1.27a, and the **surface tension** γ indicates the energy per unit surface area of the interface (S=solid, V=vapor, L=liquid).

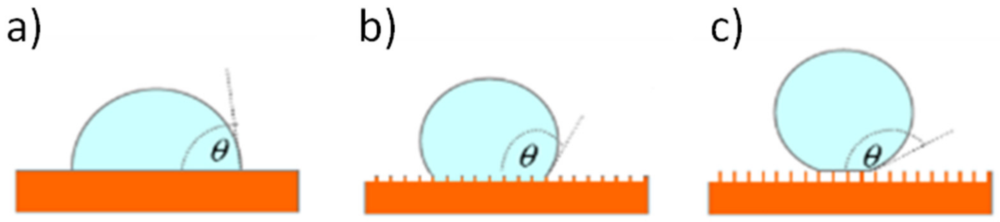

Figure 1.27 Illustration of the behavior of a droplet on a smooth (a) and a rough surface (b) and a surface with topography (c).

Controlling the surface microstructure towards low roughness is a way to improve their hydrophilic properties [237]. Photoinduced[12] superhydrophilic surfaces (θ=0°) can either photomineralize the contaminants or wash them away by water which can be used for

---

[12] Induced by illumination of UV

many applications ranging from self cleaning windows (Figure 1.29) to anticlouding bathroom mirrors, car windows and fender mirrors [238][36].

The mechanism of **photoinduced superhydrophilicity**, illustrated in Figure 1.28, involves the reduction of Ti(IV) cations to Ti(III) by generated electrons and the simultaneous trapping of holes at lattice sites (usually bridging oxygen) or close to the surface of the semiconductor. The trapped holes weaken the bond between the associated titanium and lattice oxygen, allowing oxygen atoms to be liberated, thus creating oxygen vacancies. The subsequent dissociative adsorption of water increases the amount of chemisorbed –OH, leading to an improved reaction between H_2O and –OH and an enhancement of the spreading of water across the surface [239]. Water adsorption does not occur uniformly but produces an amphiphilic surface with alternating hydrophilic and oleophilic regions at the scale of several nanometers (usually <10 nm in size) [240]. The hydrophilic domains align along the bridging oxygen sites. The reduced sites can be reoxidized by air and the weakly bound hydroxyl groups reactively desorb (over some time, typically days in the dark) from the surface that returns to a more hydrophobic form.

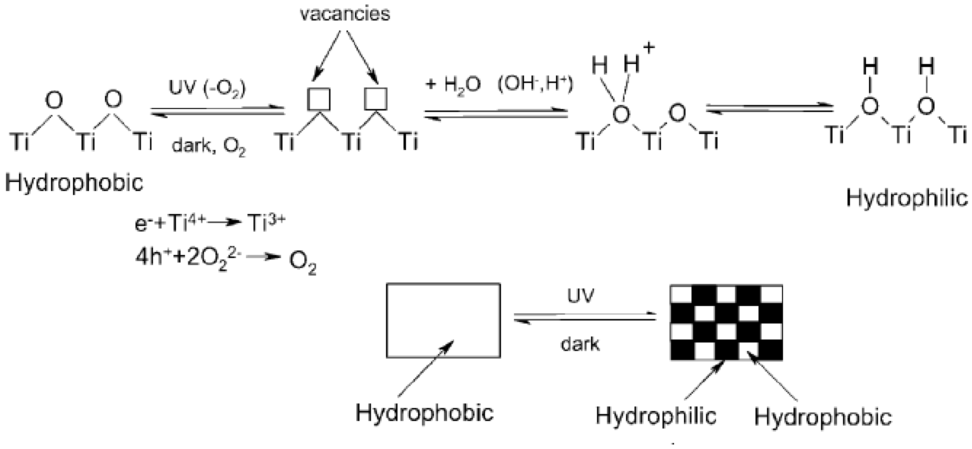

Figure 1.28 Mechanism of photoinduced hydrophilicity of TiO_2 [36]

Besides superhydrophilic surfaces, also **superhydrophobic** surfaces (θ> 150°) gain high interest as they show promising results for self-cleaning applications [241, 242]. These surfaces are inspired by the surface-topography-induced superhydrophobicity of lotus leaves [243] (Figure 1.29) and water striders' legs [244].
]]>

Figure 1.29 Image of a superhydrophilic surface (top) and superhydrophobic lotus leave (bottom)

Since real surfaces usually vary in surface conditions, most scenarios regarding contact angles in practice cannot be fully explained by the Young's equation and other models are developed.

The influence of **roughness** (factor r(x)) on the contact angle is implemented in the **Wenzel equation**

$$cos\theta_W\,(x) = r(x)cos\theta \qquad \text{(Equation 41)}$$

and assumes the penetration of water into grooves caused by surface roughness. Since the equation is related to the homogeneous wetting regime (Figure 1.30), the wettability can be improved by the surface roughness for a hydrophilic surface, but might get worse for a hydrophobic one. This means that when you start from a hydrophilic surface, the increase of roughness will decrease the contact angle resulting in superhydrophilic surfaces. Starting from a hydrophobic surface, the increase of roughness will results in the increase of the contact angle.

The third model, the **Cassie Baxter-regime**, corresponds to the heterogeneous wetting regime (Figure 1.30) and refers to the fact that air bubbles are entrapped inside the grooves underneath the liquid. Without going into detail, the Cassie-Baxter equation

$$cos\theta_{CB}(x) = \ f_s(x)cos\theta - \left(1 - f_s(x)\right) \qquad \text{(Equation 42)}$$

implements the influence of topography via a factor f_s.

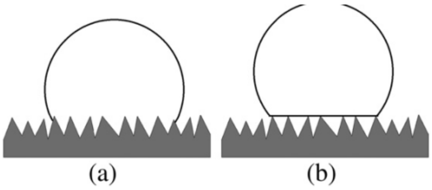

Figure 1.30 Illustration of the homogeneous (a) and heterogeneous (b) wetting regime [245].

The combination of geometrical morphology of the surface with a change in surface chemistry even introduced stimuli responsive, smart, interfacial materials that can be switched between superhydrophilicity and superhydrophobicity [82, 246]. Various phenomena, such as snow sticking, contamination or oxidation are expected to be inhibited on these surfaces which will bring great convenience is daily life as well as in many industrial processes [247].

6.1.2 Biomedical applications

Due to its excellent mechanical, physical and biological performance, the application of titanium (and its alloys) have been extended towards **tissue engineering**. Tissue engineering is a developing branch of science that combines the field of cell biology, molecular biology, bioengineering, material science and surgery in order to provide new functional tissue using living cells, biomatrices, and signaling molecules. Using this technology**, tissue loss or organ failure** in the living body can be treated by implantation of an engineered biological substitute, a 3D bio-degradable scaffold. This scaffold can either be functional at the time of implantation or has the potential to integrate and introduce the growth and multiplication of specific cells into a structure similar to tissue or the replaced organ [248, 249]. As mostly applied cells have the ability to differentiate[13] into multilineage cells such as adipocytes[14], chondrocytes[15] or osteoblasts[16] when cultured with specific growth factors, small biopsy specimens from relatively uninvolved sites can be obtained from the patient [250-253].

In the evolution of cement based bone implants towards cement-free implants, a certain type of implantation, called **osseointegration** have been introduced [254]. Osseointegration involves the direct contact between the living bone and the implant which aims an improved long term function of the implant. Osseointegration can be obtained with various types of metals including **titanium** [255] on which cells are able to attach and proliferate[17]. After the addition of an appropriate differentiation medium to the cell cultures, osteogenic[18] differentiation occurs [256] which makes TiO_2 an attractive material for **bone generation** as can be applied in orthopedic and dental surgery.
Considerable efforts has been expended in attempting to optimize the osseointegration of this metal [257] but the processes occurring at the implanted surface are extremely complex [258, 259] and remain poorly understood [260].

The success of osseointegration is influenced on the one hand on the interaction of the cells with the surface and on the other hand on the interaction of the implant with the formed bone.

---

[13] Cellular differentiation is the process by which a less specialized cell becomes a more specialized cell type. Differentiation dramatically changes the cell's size, shape, membrane potential, metabolic activity and responsiveness to signals.

[14] Fat cells

[15] Mature cells found in cartilage

[16] Bone forming cells

[17] An increase in the number of cells as a result of cell growth and cell division

[18] Composed of or originating from any tissue involved in the development, growth or repair of bone

The **interaction of the cells with the surface** occurs via cell extensions and cell membranes. The cell membranes are coated with bound proteins and receptor molecules. Molecules included in the initial attachment and spreading of the cells include extracellulare matrix (ECM) molecules such as collagen, thrombospondin, fibronectin, vitronectin and osteopontin and cell-surface receptors such as integrins. Various ECM **proteins** have been shown to mediate cell attachment to substrates. Fibronectin and vitronectin are thought to promote cell adhesion and reorganization of actin micro-filaments [261], thus influencing cytoskeletal networks, cell morphology and migration.

Protein **adsorption** is the first of a complex serie of events that regulates many phenomena at the nano –bio interface [262]. It is shown that the nanometric pore shape is the morphological parameter that influences this process.

Differentiation is associated with glycosaminoglycan (GAG) expression. GAGs[19] are long chains of disaccharides which form an important substance of the collagen rich vessels like bones. Results indicated that the synergetic effects of both mechanical stimulation through shear stress and the presence of ECM deposition onto the scaffold substrate profoundly enhanced osteoblastic differentiation [263]

It is clear that the success of a hard tissue implant not only depends on the initial attachment and subsequent proliferation of osteogenic cells, but also on their ability to form bone. Bone formation is a complex process and highly regulated by local factors such as cytokines and growth factors. Growth factors (usually proteins) are naturally occurring substances which are capable of stimulating cellular growth, proliferation and cellular differentiation. They can be incorporated in the bone implant and released gradually to allow bone formation.

Actually, surface **characteristics of the implant** such as surface chemistry, topography, wettabillity, charge, crystal structure, roughness, chemical potential, presence of impurities, and thickness of the TiO_2 layer, influence the strength and the speed of osseointegration. Surface properties affect processes such as protein adsorption, cell-surface interaction, and cell/tissue development at the interface between the biological environment and the biomaterial, all of which are relevant to the functionality of the implant [264]. Thus the cell adhesion and the bone formation is regulated by the interrelation between the surface properties (composition, surface energy, topography and roughness) [265]. The long term success, for example, of a dental implant depends on the rapid healing with safe integration into the jaw bone while geometry and surface topography are crucial for both short- and long term success.

---

[19] Examples of GAG are hyaluronic acid (important substance of proteoglycan in cartilage), heparine…

Surface topography influences spreading, proliferation, differentiation as well as protein synthesis. Based on the scale of the topography, implant surface roughness consists of macro, micro and nano-roughness. Micro-and nanotechnology has advanced the surface engineering in implant dentistry. The macro roughness directly relates to the implant geometry, with threaded screw (Figure 1.31) and macro porous surface treatments. It also enhances the mechanical interlocking between the macro features of the implant and the surrounding bone while microroughness (1-10 μm) maximizes the interlocking between mineralized[20] bone and implant surface. Nanoroughness (1-100 nm) plays a key role in the interactions between proteins and cells.

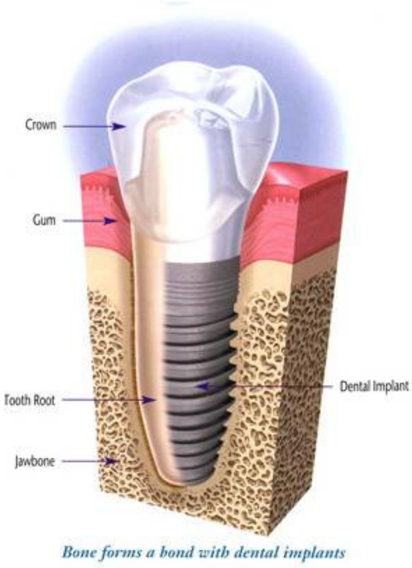

Figure 1.31 Illustration of a dental implant inserted in the jaw bone.

Another key factor for cell behavior is the **surface wettability** since it influences the degree of contact with the physiologic environment. At the nanoscale, a more textured surface topography increases the surface energy which in turn increases the wettability of the surface to blood, adhesion of cells to the surface, and facilitates binding of different biological molecules. These surfaces thus enhance the process of osseointegration by improving the wound healing following implant placement [266]. Nevertheless, there are contradictory conclusions about this property. Some studies indicate indeed that cells tend to attach better on hydrophilic surfaces which enhances the interaction between the implant surface and the biological environment (biomolecules like proteins) [267, 268]. Other reports, in contrast, argue that cells adhere better on intermediate hydrophobic surfaces [269-271]. These conflicting results are probably due to the use of different materials, different surface topographies and especially different surface chemistry applied to alter the wetting behavior [272].

---

[20] Mineralization refers to a process where an organism produces an inorganic substance, such as calcification and bone formation

Different cell lines

Various cells lines can be applied in tissue engineering: Osteoblast-like cells [273], chondrocytes (cartilage cells) [274], fibroblasts (connective tissue cells) [275], epithelial cells [276], etc. However, due to the lack of available donor cell sources for use in cellular therapy, the use of stem cells[21] are a natural choice for cell therapy, as they are pluripotent[22] from nature and obtain self-renewal capacity. Furthermore, these cells can be isolated from a variety of sources including embryos, umbilical cord blood, as well as from adult tissues [277]. The use of undifferentiated cells allows the creation of reserves of these cells which can be used to differentiate to a lineage of choice [278].

Literature overview

In this overview the focus mainly lies on the osteoblastic and stem cells as in this thesis, the ability of the nanostructures towards the differentiation into bone forming cells is studied.

The effect of nanoscale roughness on osteoblast response has been studied by several research groups [279-282], which mainly focused on the initial interaction between osteoblast and nanomodified polymeric substrates. It was indicated that nanoscale roughness can significantly affect cell adhesion[283], proliferation [284], and spreading [285]. Although similar results have been found for ceramics [286] and metallic [287] substrates, other studies report either a decrease in osteoblast profileration with an increase in nanoscale roughness [288], or no effect on nanoscale roughness on proliferation [289] in the absence of microscale surface roughness [290, 291]. Rosales-leal studied the effect of roughness, wettability and morphology of engineered titanium surface on osteoblast-like cell adhesion and concluded that for the same surface chemistry, cell growth was driven by topography features [292].

Relatively few studies have examined the effect of nanostructures on osteoblast differentiation [285, 286, 290, 293, 294]. Since cells have many structures at the nanoscale such as filipodia[23] and cytoskeleton and membrane proteins, which can interact with the surrounding environment, it is believed that their interaction with nanoscale features (even as small as 5 nm) influence the cell behavior by creating more natural cell growth and function [295, 296].

Nevertheless, more recent reports focused on the hierarchical combination of both micro- and nanoscale roughness to promote osseointegration on clinically relevant surfaces [290, 297-300]. Although some of these studies reported promising results of increased osteoblast proliferation and differentiation, it has been a challenge to create a tailored

---

[21] A progeny of cells that have the potential to differentiate into a variety of different lineages.

[22] Pluripotent cells are cells that can differentiate into all cell types of the adult organism, e.g. mesenchymal stem cells.

[23] Cytoplasmic projections which forms focal adhesions with the substrate.

hierarchical surface without altering underlying characteristics of the substrate. For this reason, it has been difficult to decouple the effect of nanoscale features from those of the other surface features, such as surface micro-roughness, surface chemistry, and/or surface energy. Additionally, the simultaneous increase in osteoblast proliferation and differentiation caused by nanoscale roughness remains controversial due to some contradictory results [288, 289, 299], which may have been influenced by differences in the type of cells and in the type of nanoscale surface modifications used in these experiments.

Various fabrication methods have been used such as photolithography, chemical vapor deposition, electron beam lithography etc [295] to develop different nanotopographies such as random, aligned, porous and core-shell nanofibers for various tissue engineering applications. Physical patterning techniques such as reactive ion etching, polymer molding etc. create **microgrooves** for designated cellular orientations [301, 302]. It has been shown that grooves of diverse dimensions may have a distinct effect on fibroblasts and endothelial cells [303], as patterned surfaces provide cues for cellular attachment, migration, orientation, and function.

Human dental pulp stem cells have been previously cultured on different scaffolds, from collagen [304], hydroxyapatite chips [305], fibrous titanium [304], to sintered titanium surfaces [306], although studies on TiO_2 **nano**structures are missing. Therefore, there is an urgent need to evaluate and understand the particular cell behavior of stem cells on nanostructures, which might eventually help to design a scaffold for enhanced tissue regeneration.

About the toxicity

When using TiO_2 nanoparticles as a film into the implant material, it must be considered that the nanoparticles can be released in the surrounding soft and hard tissues and eventually can reach distant organs (liver, spleen and lungs). Biodistribution, movement of nanomaterials through tissues and endocytosis[24] of nano-sized material, all have an impact on their potential toxicity. The toxicity of nanoparticles has been connected with several physicochemical properties such as the shape, the primary size and the specific surface area of the particles, their agglomeration state, surface potential and surface chemistry [95, 307].

---

[24] Endocytosis is a process by which cells absorb molecules (such as proteins) by engulfing them.

6.1.3 Dye sensitized solar cells

Dye-sensitized solar cells (DSSCs) have become a promising candidate in photovoltaics research after their invention by Grätzel who showed an overall solar to electrical power efficiency of 10% [154]. These cells consist of a photoelectrode, where the generation and collection of the charge carriers are realized, a redox electrolyte that transfers the charges between the two electrodes and a counter electrode, where the electrolyte ions are reduced back to complete the circuit. In Figure 1.32, the structure and function of the DSSC is presented.

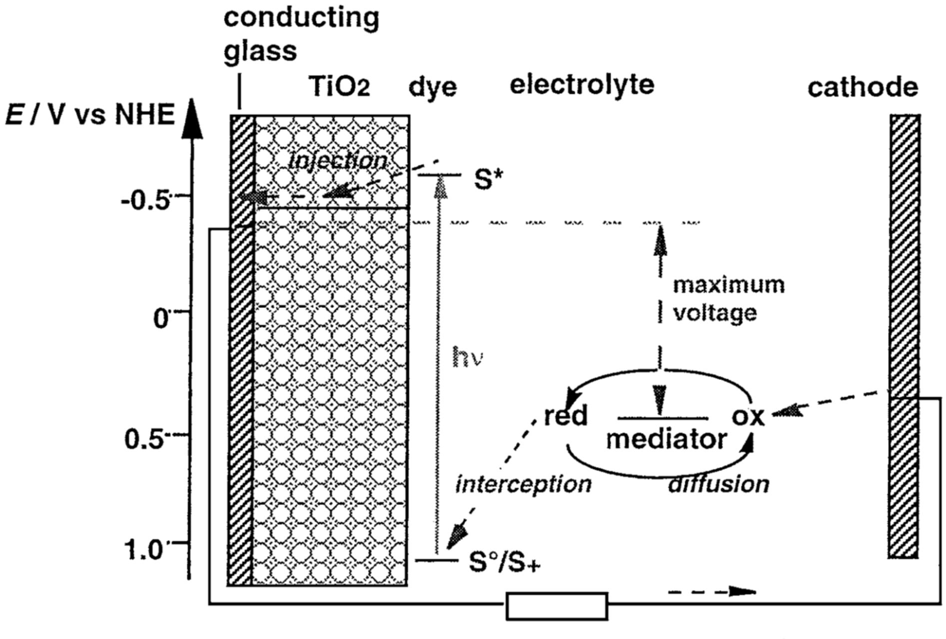

P. Bonhôte / EPFL-LPI

Figure 1.32 Schematic of structure and function of the dye-sensitised electrochemical photovoltaic cell. The nanoporous sensitised semiconductor photoanode receives electrons from the photoexcited dye which is thereby oxidised, and which is turn oxidises the mediator, a redox species dissolved in the electrolyte. The mediator is regenerated by reduction at the metallic cathode, while the electrons circulate in the external circuit [65].

The most extensively applied and successful material for the photoelectrode, is the high band gap semiconductor TiO_2, sensitized by a molecular dye (typically a Ruthenium(II) metallorganic complex). These DSSCs usually consist of a mesoporous anode formed by a sintered film of anatase TiO_2 that serves as the electron acceptor and a transport layer coated with a thin layer of sensitizer-dye molecules for light absorption and electron injection into the TiO_2 conduction band. A liquid electrolyte generally consists of an organic solvent such as acetonitrile and a redox couple I^-/I_3^- that serves as a redox agent to reduce the photo-excited dye molecules.

The key points to the observed high efficiency are efficient light harvesting, high injection yield of the electrons from the excited dye to the semiconductor and fast electron transport combined with low recombination [308]. These parameters depend largely on the surface properties, morphology and structure of TiO_2. In order to prepare an effective titania film, usually nanocrystalline layers consisted of interconnected colloidal particles, in the size range from 15 to 30 nm are deposited on a transparent conductive oxide (TCO) glass to give a thickness of the order of 5–15 μm [3]. These films possess a high surface area for efficient dye loading (the real surface is 1000 times greater than the geometric area) and accessible porosity (between 50% and 65%) that allows the liquid electrolyte to fill all pores of the film [4]. As described above, many techniques can be used to further improve the films structures by altering the particle size and morphology of TiO_2 [309, 310] developing new sensitizers [311], suppressing charge recombination [312] and improving interfacial energetic [313]. For example, vertically oriented TiO_2 nanotube arrays have higher charge collection efficiencies than a nanoparticle-based structure due to their faster transport and slower recombination of electrons [314]. Also for solar cell applications, the anatase structure of TiO_2 is preferred over the rutile structure, as anatase exhibits a higher electron mobility, lower dielectric constant, lower density, and lower deposition temperature [36].

References

[1] G. Pfaff, P. Reynders, Chemical Review 99 (1999) 1963.

[2] A. Salvador, M. Pascual-Marti, J. Adell, A. Requeni, J. March, Journal of pharmaceutical and biomedical analysis 22 (2000) 301.

[3] M.M. Viana, V.F. Soares, N.D.S. Mohallem, Ceramics International 36 (2010) 2047.

[4] J.H. Braun, A. Baidins, R.E. Marganski, Progress in organic coatings 20 (1992) 105.

[5] S. Yuan, W. Chen, S. Hu, Materials Science and engineering C 25 (2005) 479.

[6] A. Fujishima, K. Honda, Nature 37 (1972).

[7] A. Fujishima, T.N. Rao, D.A. Tryk, Journal of Photochemistry and Photobiology C: Photochemistry Reviews 1 (2000) 1.

[8] D.A. Tryk, A. Fujishima, K. Honda, Electrochimica Acta 45 (2000) 2363.

[9] M. Grätzel, Nature 414 (2001) 338.

[10] A. Hagfeldt, M. Graetzel, Chemical review 95 (1995) 49.

[11] L. Linsebigler, G. Lu, J.T. Yates, Chemical Review 95 (1995) 735.

[12] A. Millis, S.L. Hunte, Journal of Photochemistry and Photobiology A: Chemistry 108 (1997) 1.

[13] J.R. Smyth, D.L. Bish, Allen & Unwin (1988).

[14] H.Z. Zhang, J.F. Banfield, Journal of Physical Chemistry B 104 (2000) 3481.

[15] X.S. Ye, J. Sha, Z.K. Jiao, L.D. Zhang, NanoStructured Materials 8 (1997) 919.

[16] T. Mitsuhashi, O.J. Kleppa, journal of american ceramic society 62 (1979) 356.

[17] H. Zhang, J.F. Banfield, Journal of Materials chemistry 8 (1998) 2073.

[18] A.A. Gribb, J.F. Banfield, American mineralogist 82 (1997) 717.

[19] J. Yang, S. Mei, J.M.F. Ferreira, Journal of american ceramic society 83 (2000) 1361.

[20] E. Beyers, P. Cool, E.F. Vansant, Journal of physical Chemistry B 109 (2005) 10081.

[21] A.P. Alivisatos, Journal of Physical Chemistry 100 (1996) 13226.

[22] C. Burda, X. Chen, R. Narayanan, M. El-Sayed, Chemical Review 105 (2005) 1025.

[23] C.B. Murray, C.R. Kagan, Annual review of materials science 30 (2000) 545.

[24] Y. Yin, A.P. Alivisatos, Nature 437 (2005) 664.

[25] C. Kormann, D.W. Bahnemann, M.R. Hoffmann, Journal of Physical Chemistry 92 (1988) 5196.

[26] D.W. Bahnemann, Israel Journal of Chemistry 33 (1993) 115.

[27] L. Kavan, T. Stoto, M. Graetzel, D. Fitzmaurice, V. Shklover, Journal of Physical Chemistry 97 (1993) 9493.

[28] X. Chen, Y. Lou, S. Dayal, X. Qiu, R. Krolicki, C. Burda, C. Zhao, J. Becker, Journal of Nanoscience and Nanotechnology 5 (2005) 1408.

[29] C. Burda, Y. Lou, X. Chen, A.C.S. Samia, J. Stout, J.L. Gole, Nanoletters 3 (2003) 1049.

[30] X. Chen, C. Burda, Journal of Physical Chemistry B 108 (2004) 15446.

[31] X. Chen, A.C.S. Samia, Y. Lou, C. Burda, Journal of American chemical society 127 (2005) 4372.

[32] F. Pedraza, A. Vasquez, Journal of Physical Chemistry and solids 60 (1999) 445.

[33] A. Scolan, C. Sanchez, Chemistry Of Materials 10 (1998) 3217.

[34] J.P. Jolivet, C. Froidefond, A. Pottier, C. Chaneac, S. Cassaignon, E. Tronc, P. Euzen, Journal of material chemistry 14 (2004) 3181.

[35] S.J. Kim, S.D. Park, Y.H. Jeong, S. Park, Journal of the American Ceramic Society 82 (1999) 927.

[36] O. Carp, C.L. Huisman, A. Reller, Progress in solid state chemistry 32 (2004) 33.

[37] M. Kakihana, Journal of Sol-Gel science and technology 6 (1996) 7.

[38] M. Wu, G. Lin, D. Chen, G. Wang, D. He, S. Feng, R. Xu, Chemistry Of Materials 14 (2002) 1974.

[39] C.-C. Wang, J.Y. Ying, Chemical Materials 11 (1999) 3113.

[40] C.S. Kim, B.K. Moon, J.H. Park, S.M. Son, Journal of crystal growth 254 (2003) 405.

[41] S. Yin, Y. Fujishiro, J. Wu, M. Aki, T. Sato, Journal of materials processing technology 237 (2003) 45.

[42] K. Nagaveni, G. Sivalingam, M.S. Hegde, G. Madras, Applied Catalysis B: Environment 48 (2003) 83.

[43] S.S. Hong, M.S. Lee, G.D. Lee, K.-T. Lim, B.J. Ha, Materials Letters 57 (2003) 2975.

[44] S. Karuppuchamy, J.M. Jeong, Journal of oleo science 55 (2006) 263.

[45] S. Karuppuchamy, M. Iwasaki, H. Minoura, Applied Surface Science 253 (2006) 2924.

[46] A.C. Jones, P.R. Chalker, Journal of Physics D: Applied Physics 36 (2003) R80.

[47] K.K. Akurati, A. Vital, U.E. Klotz, B. Bommer, T. Graule, M. Winterer, Powder technology 165 (2006) 73.

[48] K.K. Akurati, A. Vital, G. Fortunato, R. Hany, F. Nueesch, T. Graule, Solid state sciences 9 (2007) 247.

[49] C.C. Chen, H.L. Bai, H.M. Chein, T.M. Chen, Aerosol science and technology 41 (2007) 1018.

[50] J.C. Yu, J.G. Yu, W.K. Ho, L.Z. Zhang, Chemical Communications (2001) 1942.

[51] A. Di Paola, G. Cufalo, M. Addamoa, M. Bellardita, R. Campostrini, M. Ischia, R. Ceccato, L. Palmisano, Colloids and Surfaces A: Physicochemical Engineering Aspects 317 (2008) 366.

[52] D.C. Hague, M.J. Mayo, Journal of the american Ceramic Society 77 (1994) 1957.

[53] D. Vorkapic, T. Matsoukas, Journal of the American Ceramic Society 81 (1998) 2815.

[54] J.L. Look, C.F. Zukoski, Journal of the American Ceramic Society 78 (1995) 21.

[55] J.L. Look, C.F. Zukoski, Journal of american ceramic society 75 (1992) 1587.

[56] T. Moritz, J. Reiss, K. Deisner, D. Su, A. Chemseddine, Journal of Physical Chemistry B 101 (1997) 8052.

[57] V. Venkatachalam, P. Wang, D. Wang, M. Palanichamy, V. Murugesan, Materials chemistry and physics 104 (2007) 454.

[58] Y.-F. Chen, C.-Y. Lee, M.-Y. Yeng, H.-T. Chiu, Journal of crystal growth 247 (2003) 363.

[59] R.A. Laudise, Chemical and engineering news 65 (1987) 30.

[60] E.D. Kolb, R.L. Barns, R.A. Laudise, Journal of crystal growth 50 (1980) 404.

[61] R. Roy, Journal of solid state chemistry 111 (1994) 11.

[62] M. Andersson, L. Osterlund, S. Ljungstrom, e. al., Journal of physical Chemistry B 106 (2002) 10674.

[63] S.Y. Chae, M.K. Park, S.K. Lee, Chemistry Of Materials 15 (2003) 3326.

[64] J. Yang, S. Mei, J.M.F. Ferreira, Journal of the European Ceramic Society 24 (2004) 335.

[65] M. Grätzel, Sol-gel Science and technology 22 (2001) 7.

[66] W.W. So, S.B. Park, K.J. Kim, S.J. Moon, Journal of Colloid and Interface Science 191 (1997) 398.

[67] C. Su, C.M. Tseng, L.F. Chen, B.H. You, M.C. Hsu, S.S. Chen, Thin solid films 498 (2006) 259.

[68] J. Yang, S. Mei, J.M.F. Ferreira, Materials science and engineering C 15 (2001) 183.

[69] W.S. Nam, G.Y. Han, Korean Journal of chemical engineering 20 (2003) 180.

[70] M.P. Finnegan, H.Z. Zhang, J.F. Banfield, Journal of Physical Chemistry C 111 (2007) 1962.

[71] D. Reyes-Coronado, G. Rodriguez-Gattorno, M.E. Espinosa-Pesquiera, C. Cab, R. De Cos, G. Oskam, Nanotechnology 19 (2008).

[72] K. Yanagisawa, Y. Yamamoto, Q. Feng, N. Yamasaki, Journal of Material research 13 (1998) 825.

[73] T. Sugimoto, Marcel-Dekker Inc (2000).

[74] R.E. Riman, edited by R. Pugh and L. Bergström (Marcel-Dekker, U.S.A. 1993) (1993).

[75] Inc software (1996-2002).

[76] A. Testino, I.R. Bellobono, V. Buscaglia, C. Canevali, M. D'Arienzo, S. Polizzi, R. Scotti, F. Morazzoni, Journal of american ceramic society 129 (2007) 3564.

[77] M. Kobayashi, K. Tomita, V. Petrykin, Journal of material science 43 (2008) 2158.

[78] J.H. Kim, B.H. Noh, G.D. Lee, S.S. Hong, Korean Journal of chemical engineering 22 (2005).

[79] J. Yang, S. Mei, J.M.F. Ferreira, Journal of the American Ceramic Society 84 (2001) 1696.

[80] A. Chemseddine, T. Moritz, European journal of inorganic chemistry (1999) 235.

[81] Q.H. Zhang, L. Gao, Langmuir 10 (2003) 967.

[82] X. Feng, J. Zhai, L. Jiang, Angewandte chemie international edition 44 (2005) 5115.

[83] Q. Huang, L. Gao, Chemistry Letters 32 (2003) 638.

[84] S. Yang, L. Gao, Chemistry Letters 34 (2005) 972.

[85] Y.X. Zhang, G.H. Li, Y.X. Jin, Y. Zhang, J. Zhang, L.D. Zhang, Chemical physics letters 365 (2002) 300.

[86] T. Kasuga, M. Hiramatsu, A. Hoson, T. Sekino, K. Niihara, Langmuir 14 (1998) 3160.

[87] J.I. Langford, A.J.C. Wilson, Journal of applied crystallography 11 (1978) 102.

[88] T. Lindgren, J.M. Mwabora, E. Avendano, J. Jonsson, A. Hoel, G. Granqvist, S.-E. Lindquist, Journal of Physical Chemistry B 107 (2003) 5709.

[89] V. Swamy, A. Kuznetsov, L.S. Dubrovinsky, Physical review B 71 (2005).

[90] N. Veronovski, P. Andreozzi, C. La Mesa, M. Sfiligoj-Smole, Surface and coating technology 204 (2010) 1445.

[91] D.J. Shaw, Butterworth-Heinemann Boston (1992).

[92] R.J. Hunter, Oxford Second Edition (2005).

[93] H. Van den Rul, Cursus (2007).

[94] D.J. Royer, New York, NY:McGraw-Hill, Inc. (1968).

[95] J. Jiang, G. Oberdörster, P. Biswas, Journal of nanoparticle research 11 (2009) 77.

[96] H.A. Barnes, IChemE, Rugby (1992).

[97] C.M. Sorenson, Handbook of surface and colloid chemistry (ed.K.S. Birdi) CRC Publishing, New York (1997).

[98] M.J. Garcia-salinas, F.J. de las Nieves, Progress in colloid and polymer science 110 (1998) 134.

[99] H.A. Barnes, University of Wales, Institute of non-Newtonian Fluid Mechanics (2000).

[100] A.P. Tinke, R. Govoreanu, K. Vanhoutte, American pharmaceutical review (2006).

[101] Malvern Instruments (Malvern, U.K.) MAN0317 (2004).

[102] Malvern Instruments (Malvern, U.K.) Technical note MRK654-01.

[103] Malvern Instruments (Malvern, U.K.) MAN0317 (2004).

[104] A. Aimable, P. Bowen, Processing and Application of Ceramics 4 (2010) 157.

[105] L.E. Oppenheimer, Journal of Colloid and Interface Science 92 (1983) 350.

[106] T. Detloff, T. Sobisch, D. Lerche, Powder technology (2007) 50.

[107] D. Lerche, Journal of Dispersion Science and Technology 23 (2002) 699.

[108] S. Fazio, J. Guzman, M.T. Colomer, Salomoni, M.T., R. Moreno, Journal of European Ceramic society 28 (2008) 2171.

[109] K. Suttiponparnit, J. Jiang, M. Sahu, S. Suvachittanont, T. Charinpanitkul, P. Biswas, Nanoscale research letters 6 (2011) 27.

[110] G. Baldi, M. Bitossi, A. Barzanti, US patent 20080317959 ((25th of december 2008)).

[111] M.H. Huang, Y. Wu, H. Feick, N. Tran, P. Yang, Advanced materials 13 (2001) 113.

[112] J.L. Deiss, P. Anizan, S.E. Hadigui, C. Wecker, Colloids and Surfaces A: Physochemical Engineering Aspects 106 (1996) 59.

[113] M. Iijima, M. Kobayakawa, M. Yamazaki, Y. Ohta, H. Kamiya, Journal of american ceramic society 131 (2009).

[114] B. Faure, J.S. Lindelov, M. Wahlberg, N. Adkins, P. Jackson, L. Bergström, Powder technology 203 (2010) 384.

[115] A. Hoshino, K. Fujioka, T. Oku, M. Suga, Y.F. Sasaki, T. Ohta, e. al, Nanoletters 4 (2004) 2163.

[116] T. Kotsokechagia, F. Cellesi, A. Thomas, M. Niederberger, N. Tirelli, Langmuir 24 (2008) 6988.

[117] J. Wang, J. Polleux, J. Lim, B. Dunn, Journal of American Ceramic Society 131 (2009) 1802.

[118] J.L. Widegren, L. Bergström, Journal of american ceramic society 85 (2002) 523.

[119] H.S. Bae, M.K. Lee, W.W. Kim, C.K. Rhee, Colloid and Surfaces A 220 (2003) 169.

[120] R. Advincula, W. Knoll, Wiley (2011).

[121] D. Mardare, G.I. Rusu, Materials Letters 56 (2002) 210.

[122] L. Zhao, Q. Jiang, J. Lian, Applied Surface Science 254 (2008) 4620.

[123] G. Hodes, Marcel-Dekker Inc (2002).

[124] H.-E. Cheng, Y.-R. Chen, W.-T. Wu, C.-M. Hsu, Materials Science and engineering B 176 (2011) 596.

[125] R.W. Schwartz, T. Schneller, R. Waser, Comptes Rendus Chimie 7 (2004) 433.

[126] H. Hirashima, H. Imai, M.Y. Miah, I.M. Bountseva, I.N. Beckman, V. Balek, Journal of non-crystalline solids 350 (2004) 266.

[127] N. Kitazawa, K. Sakaguchi, M. Aono, Y. Watanabe, , Journal of material science 38 (2003) 3069.

[128] J.-H. Yang, Y.-S. Han, J.-H. Choy, Thin solid films 495 (2006) 266.

[129] R. Waser, Wiley-VCH (2003).

[130] D.B. Hall, P. Underhill, J.M. Torkelson, Polymer engineering and science 38 (1998).

[131] A. Mihi, M. Ocana, H. Miguez, Advanced materials 18 (2006) 2244.

[132] C. Arcos, e. al., Physical Review E 77 (2008).

[133] M. Giuliani, W. Gonzalez-VInas, K.a. Poduska, A. Yethiraj, Journal of Physical Chemistry Letters 1 (2010) 1481.

[134] T.J. Rehg, G. Higgins, AlChE Journal 38 (2004) 489.

[135] A. Tok, F.Y.C. Boey, K.A. Khor, Proceedings of the 6th International Conference on Processing and Fabrication of Advanced Materials,Singapore, (1997).

[136] R. Moreno, American Ceramic Society Bulletin 71 (1992) 1521.

[137] R. Moreno, American Ceramic Society Bulletin 71 (1992) 1647.

[138] T. Chartier, E. Jorge, P. Bouch, Journal of European Ceramic society 11 (1993) 387.

[139] J.H. Feng, F. Dogan, Journal of american ceramic society 7 (2000) 1681.

[140] S.B. Reddy, P.P. Singh, N. Raghu, V. Kumar, Journal of Materials Science 5 (2002) 929.

[141] C. Euvananont, C. Junin, K. Inpor, P. Limthongkul, C. Thanachayanont, Ceramics International 34 (2008) 1067.

[142] B. Guo, Z.L. Liu, L. Hong, H. Jiang, J.Y. Lee, Thin solid films 479 (2005) 310.

[143] M.J. Carey, V.M. Burlakov, B.M. Henry, K.R. Kirov, G.R. Webster, H.E. Assender, G.A.D. Briggs, P.L. Burn, C.R.M. Grovenor, Organic Photovoltaics 5215 (2004).

[144] H.-E. Wang, Z. Chen, Y.H. Leung, C. Luan, C. Liu, Applied Physics Letters 96 (2010).

[145] C.-H. Wu, H. Li, H.H. Fong, V.A. Pozdin, L.A. Estroff, G.G. Malliaras, Organic Electronics 12 (2011) 1073.

[146] S. Mandal, R. Sharma, M. Monica Katiyar, Journal of chemical and Chemistry engineering 6 (2012) 625.

[147] T. Giornelli, A. Löfberg, E. Bordes-Richard, Applied Catalysis A: General 305 (2006) 197.

[148] J. Beusen, M.K. Van Bael, H. Van den Rul, J. D'Haen, J. Mullens, Journal of European Ceramic society 27 (2007) 4529.

[149] B. O’Regan, D.T. Schwartz, S.M. Zakeeruddin, M. Gratzel, Advanced materials 12 (2000) 1263.

[150] F. Yang, M. Shtein, S.R. Forrest, Nature Materials 4 (2005) 37.

[151] K. Rajeshwar, N.R. de Tacconi, C.R. Chenthamarakshan, Chemistry Of Materials 13 (2001) 2765.

[152] M. Adachi, Y. Murata, M. Harada, S. Yoshikawa, Chemistry Letters 29 (2000) 942.

[153] Y. Li, T. Sasaki, Y. Shimizu, N. Koshizaki, Journal of American chemical society 130 (2008) 14755.

[154] B. O' Regan, M. Graetzel, Nature 353 (1991) 737.

[155] T. Kasuga, M. Hiramatsu, A. Hoson, T. Sekino, K. Niihara, Advanced materials 11 (1999) 1307.

[156] B. Liu, E.S. Aydil, Journal of the American Chemical Society 131 (2009) 2985.

[157] D. Grosso, G.J.D. Soler-Illia, F. Babonneau, C. Sanchez, P.A. Albouy, A. Brunet-Bruneau, A.R. Balkenende, Advanced Materials 13 (2001) 1085.

[158] T. Kimura, Y. Yamauchi, N. Miyamoto, Chemical European Journal 16 (2010) 12069.

[159] S. Liang, M. Chen, Q. Xue, Z. Liu, Thin solid films 516 (2008) 3058.

[160] J.E. ten Elshof, S.U. Khan, O.F. Göbel, Journal of the European Ceramic Society 30 (2010) 1555.

[161] C. Goh, K.M. Coakley, M.D. McGehee, Nanoletters 5 (2005) 1545.
[162] A. Kumar, G.M. Whitesides, Applied Physical Letters 63 (1993).
[163] Y. Xia, G.M. Whitesides, Annual review of materials research 28 (1998) 153.
[164] Y. Masuda, W.-S. Seo, K. Koumoto, Solid state ionics 172 (2004) 283.
[165] J.A. Rogers, R.G. Nuzzo, Materials Today 6 (2005) 50.
[166] L. Malaquin, F. Carcenac, C. Vieu, M. Mauzac, Microelectronic engineering 61 (2002) 379.
[167] M.J. Hampton, S.S. Williams, Z. Zhou, J. Nunes, D.-H. Ko, J.L. Templeton, E.T. Samulski, J. DeSimone, Advanced Materials 20 (2008) 2667.
[168] G. Shi, N. Lu, L. Gao, H. Xu, B. Yang, Y. Li, Y. Wu, L. Chi, Langmuir 25 (2009) 9639.
[169] S. Leppävuori, J. Väänänen, M. Lothi, J. Remes, A. Uusimäki, Sensors and actuators A:Physical 42 (1994) 593.
[170] K.G. Sharp, G.S. Blackman, N.J. Glassmaker, A. Jagota, C.Y. Hui, Langmuir 20 (2004) 6430.
[171] P.M. Moran, F.F. Lange, Applied Physical Letters 74 (1999) 1332.
[172] S.H. Ahn, J.-H. Min, J. Kim, J. Moon, Journal of american ceramic society 91 (2008) 2143.
[173] J.N. Lee, C. Park, G.M. Whitesides, Analytical Chemistry 75 (2003) 6544.
[174] C. Marzolin, S.P. Smith, M. Prentiss, G.M. Whitesides, Advanced Materials 10 (1998) 571.
[175] O.F. Göbel, D.H.A. Blank, J.E. Ten Elshof, Applied materials &Interfaces 2 (2010) 536.
[176] W.S. Beh, Y. Xia, D.J. Qin, Journal of Material research 14 (1999) 3995.
[177] C.R. Martin, I.A. Aksay, Journal of materials research 107 (2003) 4261.
[178] O.F. Göbel, M. Nedelcu, U. Steiner, Advanced Functional Materials 17 (2007) 1131.
[179] S.U. Khan, O.F. Gobel, D.H.A. Blank, J.E. Elshof, ACS Applied Material Interfaces 1 (2009) 2250.
[180] J. Imasu, Y. Sakka, Journal of ceramic society of Japan 115 (2007) 697.
[181] O.F. Göbel, T.E. Branfield, T.M. Stawski, S.A. Veldhuis, D.H.A. Blank, J.E. Ten Elshof, Applied materials &Interfaces 2 (2010).
[182] P. Yang, T. Deng, D. Zhao, P. Feng, D. Pine, B.F. Chmelka, G.M. Whitesides, G.D. Stucky, Nature 282 (1998) 2244.
[183] S.U. Khan, J.E. ten Elshof, Science and technology of advanced materials 13 (2012).
[184] C.R. Martin, I.A. Aksay, Journal of electroceramics 12 (2004) 53.
[185] P.V. Kamat, Chemical Research 93 (1993) 267.
[186] M.R. Hoffmann, S.T. Martin, W. Choi, D.W. Bahnemann, Chemical Review 95 (1995).
[187] T. Ochiaia, A. Fujishimaa, Journal of Photochemistry and Photobiology C: Photochemistry Reviews 13 (2012) 247.
[188] A. Mills, C. O'Rouke, V. Kalousek, J. Rathousky, Journal of Hazardous Materials 211-212 (2012) 182.
[189] M. Kus, S. Ribbens, V. Meynen, P. Cool, Catalysts 3 (2013).
[190] M.N. Chong, B. Jin, C.W.K. Chow, C. Saint, Water Research 44 (2010) 2997.
[191] M.I. Litter, Applied Catalysis B 23 (1999) 89.
[192] F. Han, V.S.R. Kambala, M. Srinivasan, D. Rajarathnam, R. Naidu, Applied Catalysis A: General 359 (2009) 25.
[193] X. Chen, S.S. Mao, Chemical Review 107 (2007) 2891.
[194] K. Tanaka, M.F.V. Capule, T. Hisanaga, Chemical Physics Letters 187 (1991) 73.
[195] N.R.C.F. Machado, V.S. Santana, Catalysis today 107 (2005) 595.
[196] X. Deng, Y. Yue, Z. Gao, Applied Catalysis B: Environment 39 (2002) 135.
[197] S.S. Watson, e. al., Chemical Engineering Journal 95 (2003) 213.
[198] R.R. Yeredla, H. Xu, 1008 Nanotechnology (2008).
[199] N. Serpone, Reseacrh of chemical intermediates 30 (1994) 953.
[200] M. Vargová, G. Plesch, U.F. Vogt, M. Zahoran, M. Gorbár, K. Jesenák, Applied Surface Science 257 (2011) 4678.
[201] K. Venkata Subba Raoa, M. Subrahmanyamb, P. Boule, Applied Catalysis B: Environment 49 (2004).

[202] G. Mascolo, R. Comparelli, M.L. Curri, G. Lovecchio, A. Lopez, A. Agostiano, Journal of Hazardous Materials 142 (2007) 130.
[203] S. Bakardjieva, V. Stengl, L. Szatmary, J. Subrt, J. Lukac, N. Murafa, D. Niznansky, K. Cizek, J. Jrkovsky, N. Petrova, Journal of materials chemistry 16 (2006) 1709.
[204] R.R. Bacsa, J. Kiwi, Applied Catalysis B: Environmental 16 (1998) 19.
[205] K. De Witte, A.M. Busuioc, V. Meynen, M. Mertens, N. Bilba, G. Van Tendeloo, P. Cool, E.F. Vansant, Microporous and mesoporous materials 110 (2008) 100.
[206] M. Addamo, M. Bellardita, A. Di Paola, L. Palmisano, Chemical Communications (2006) 4943.
[207] M.L. Carreon, H.G. Carreon, J. Espino-Valencia, M.A. Carreon, Materials chemistry and physics 125 (2011) 474.
[208] M. Behpour, V. Atouf, Applied Surface Science 258 (2012) 6595.
[209] L. Jiang, G. Zhou, Materials Science in semiconductor processing 15 (2011) 108.
[210] R.G. Nair, S. Paul, S.K. Samdarshi, Solar Energy Materials & Solar Cells 95 (2011) 1901.
[211] A. Di Paola, M. Addamo, M. Bellardita, E. Cazzanelli, L. Palmisano, Thin solid films 515 (2007) 3527.
[212] Z. Zhang, C.-C. Wang, R. Zakaria, J. Ying, Journal of Physical Chemistry B 102 (1998) 10871.
[213] S. Hu, A. Wang, X. Li, H. Löwe, Journal of physics and chemistry of solids 71 (2010) 156.
[214] Y.-K. Lai, J.-Y. Huangc, H.-F. Zhanga, V.-P. Subramaniamb, Y.-X. Tangb, D.-G. Gongb, L. Sundarb, L. Suna, Z. Chenb, C.-J. Lina, Journal of Hazardous materials 184 (2010) 855.
[215] T. Kitamura, H. Kumazawa, Chemical engineering Communications 192 (2005) 795.
[216] L. Yang, Y. Wang, L. Zhao, Chinese Optics Letters 10 (2012).
[217] N. Arconada, A. Duran, S. Suarez, R. Portela, J.M. Coronado, B. Sanchez, Y. Castro, Applied Catalysis B: Environmental 86 (2009) 1.
[218] Z. Li, Y. Zhu, Q. Zhou, J. Ni, Z. Zhang, Applied surface Science (2011).
[219] Y. Zhang, J. Li, J. Wang, Chemistry Of Materials 18 (2006) 2917.
[220] D. Chen, Y. Gao, G. Wang, H. Zhang, W. Lu, J. Li, Journal of physical Chemistry C 111 (2007) 13163.
[221] Y. Hu, C. Yuan, Journal of crystal growth 274 (2005) 563.
[222] W.S. Kuo, P.H. Ho, Dyes and Pigments 71 (2006) 212.
[223] S. Zhang, B. Xie, F. Li, Key Engineering Materials 336-338 (2007) 1953.
[224] W.Y. Gan, K. Chiang, M. Brungs, R. Amal, H. Zhao, International Journal of Nanotechnology 4 (2007).
[225] Y. Chen, E. Stathatos, D.D. Dionysiou, surface & Coatings Technology 202 (2008) 1944.
[226] E.V. Skorb, L.I. Antonouskaya, N.A. Belyasova, D.G. Shchukin, H. Möhwald, D.V. Sviridov, Applied Catalysis B: Environmental 84 (2008) 94.
[227] X.M. Song, J.M. Wu, M. Yan, Thin Solid Films 517 (2009) 4341.
[228] A.G.G. Toh, R. Cai, D.L. Butler, Wear 266 (2009) 585.
[229] M. Uzunova-Bujnova, R. Todorovska, M. Milanova, R. Kralchevska, D. Todorovsky, Applied Surface Science 356 (2009) 830.
[230] M. Arin, P. Lommens, N. Avci, S.C. Hopkins, K. De Buysser, I.M. Arabatzis, I. Fasaki, D. Poelman, I. Van Driessche, Journal of the European Ceramic Society 31 (2011) 1067.
[231] S. Segota, L. Curkovic, D. Ljubas, V. Svetlicic, I.F. Houra, N. Tomasic, Ceramics International 37 (2011) 1153.
[232] M. Arin, P. Lommens, S.C. Hopkins, G. Pollefeyt, J. Van der Eycken, S. Ricart, X. Granados, B.A. Glowacki, I. Van Driessche, Nanotechnology 23 (2012).
[233] M.A. Nawi, S.M. Zain, Applied Surface Science 258 (2012) 6148.
[234] U. Diebold, Surface science reports 48 (2003) 53.
[235] T. Ohya, A. Nakayama, Y. Shibata, T. Ban, Y. Ohya, Y. Takahashi, Journal of Sol-Gel science and technology 26 (2003) 799.
[236] I. Truijen, M.K. Van Bael, H. Van den Rul, J. D'Haen, J. Mullens, Journal of Sol-Gel science and technology 41 (2007) 43.

[237] J. Yu, X. Zhao, Q. Zhao, G. Wang, Materials chemistry and physics 68 (2001) 253.

[238] A. Mills, S.K. Lee, Journal of Photochemistry and Photobiology A: Chemistry 152 (2002) 233.

[239] G. Yu, X.J. Zhao, Journal of Materials Science Letters 20 (2001) 671.

[240] R. Wang, K. Hashimoto, A. Fujishima, M. Chikuni, E. Kojima, A. Kitamura, e. al., Nature 388 (1997) 431.

[241] I. Woodward, W.C.E. Schofield, V. Roucoules, J.P.S. Badyal, Langmuir 19 (2003).

[242] B. Blossey, Nature Materials 2 (2003) 301.

[243] L. Feng, S. Li, Y. Li, H. Li, L. Zhang, J. Zhai, Y. Song, B. Liu, L. Jiang, D. Zhu, Advanced materials 14 (2002) 1857.

[244] X.F. Gao, L. Jiang, Nature 432 (2004) 36.

[245] Y.Y. Yan, N. Gao, W. Barthlott, Advances in Colloid and Interface science 169 (2011) 80.

[246] T. Sun, G. Wang, L. Feng, B. Liu, Y. Ma, L. Jiang, D. Zhu, Angewandte Chemie International Edition 43 (2004) 357.

[247] A. Nakajima, K. Hashimoto, T. Watanabe, Monatshefte für Chemie 132 (2001) 31.

[248] T. Holmes, Trends biotechnology 20 (2002) 16.

[249] V. Liu Tsang, S.N. Bhatia, Advanced drug delivery reviews 56 (2004) 1635.

[250] S.P. Bruder, B.S. Fox, Clinical orthopaedics 367 (1999) S68.

[251] S. Levenbergg, R. Langer, Current Topics in Developmental Biology 61 (2004) 113.

[252] D.J. Mooney, A.G. Mikos, Scientific American 280 (1999) 60.

[253] R.F. Service, Science 309 (2005) 683.

[254] P.I. Branemark, Journal of prosthetic dentistry 50 (1983) 399.

[255] T. Albrektsson, P.I. Branemark, H.-A. Hansson, J. Lindstrom, Acta Orthopaedica Scandinavica 52 (1981) 155.

[256] M. Maeda, M. Hirose, H. Ohgushi, T. Kirita, Journal of biochemistry (Tokyo) 141 (2007) 729.

[257] T. Albrektsson, P.I. Branemark, H.-A. Hansson, I. Lundström, Acta Orthopaedica Scandinavica 17 (1991) 132.

[258] L.L. Hench, H.A. Paschall, Journal of biomedical materials research 8 (1974) 49.

[259] P. Tengvall, I. Lundström, Clinical Materials 9 (1992) 115.

[260] B. Kasemo, Current opinion in solid state and materials science 3 (1998) 451.

[261] T. Kreis, R. Vale, Sambrook Tooze Publishers Oxford University Press (1993).

[262] P.E. Scopelliti, A. Borgonovo, M. Indrieri, L. Giorgetti, G. Bongiorno, A. Carbone, P. Milani, Plos one 5 (2010).

[263] M.P. Prabharakan, J. Venugopal, L. Ghasemi-Mobarakeh, D. Kai, G. Jin, S. Ramakrishna, Advanced polymer science 246 (2012) 21.

[264] B. Ratner, S. Porter, Interfacial phenomena and bioproducts Brash JLW, New York, Marcel Dekker (1996).

[265] R.W. Schwartz, B.D. Boyan, Journal of cell biology 56 (1994) 340.

[266] D.M. Dohan Ehrenfest, P.G. Coelho, B.S. Kang, Y.T. Sul, T. Albrektsson, Trends in biotechnology 28 (2010) 198.

[267] D.V. Kilpadi, J.E. Lemons, Journal of biomedical materials research 28 (1994) 1419.

[268] M. Textor, C. Sittig, V. Frauchiger, S. Tossati, D.M. Brunette, Titanium in medicine (2001) 171.

[269] N. Faucheux, R. Schweiss, K. Lutzow, C. Werner, T. Groth, Biomaterials 25 (2004) 2721.

[270] Y. Ikada, Biomaterials 15 (1994) 725.

[271] J. Lee, G. Khang, J.W. Lee, H.B. Lee, Journal of Colloid and Interface Science 205 (1998) 323.

[272] S. Bauer, J. Park, K. Von der Mark, P. Schmuki, Acta Biomaterials 4 (2008) 1576.

[273] B. Lowenberg, R. Chernecky, A. Shiga, J.E. Davies, Cells and Materials 1 (1991) 177.

[274] Z. Schwartz, J.Y. Martin, D.D. Dean, J. Simpson, D.L. Cochran, B.D. Boyan, Journal of biomedical materials research 30 (1996) 145.

[275] D.M. Brunette, Experimental Cell Research 164 (1986) 11.

[276] D.M. Brunette, Experimental Cell Research 167 (1986) 203.

[277] M. Mimeault, S.K. Batra, Stem cells 24 (2006) 2319.

[278] E. Dawson, G. Mapili, K. Erickson, S. Taqvi, K. Roy, Advanced drug delivery reviews 60 (2008) 215.

[279] A.M. Lipski, C.J. Pino, F.R. Haselton, I.W. Chen, V.P. Shastri, Biomaterials 29 (2008) 3836.

[280] A.S.G. Curtis, N. Gadegaard, M.J. Dalby, M.O. Riehle, C.D.W. Wilkinson, G. Aitchison, IEEE Trans Nanobioscience 3 (2004) 61.

[281] M.O. Riehle, M.J. Dalby, H. Johnstone, A. Macintosh, S. Affrossman, Materials science and engineering C:Biomimetic and supramolecular systems 23 (2003) 337.

[282] B.C. Ward, T.J. Webster, Materials science and engineering C:Biomimetic and supramolecular systems 27 (2007) 575.

[283] M.J.P. Biggs, R.G. Richards, N. Gadegaard, R.J. McMurray, S. Affrossman, C.D.W. Wilkinson, Journal of biomedical materials research 91A (2009).

[284] E. Palin, H.N. Liu, T.J. Webster, Nanotechnology 19 (2005) 1828.

[285] M.J. Dalby, D. McCloy, M. Robertson, C.D.W. Wilkinson, R.O.C. Oreffo, Biomaterials 27 (2006) 1306.

[286] T.J. Webster, C. Ergun, R.H. Doremus, R.W. Siegel, R. Bizios, Biomaterials 21 (2000) 1803.

[287] T.J. Webster, J.U. Ejiofor, Biomaterials 25 (2004) 4731.

[288] N.R. Washburn, K.M. Yamada, C.G. Simon, S.B. Kennedy, E.J. Amis, Biomaterials 25 (2004) 1215.

[289] K.Y. Cai, J. Bossert, K.D. Jandt, Colloids and surfaces B: Biointerfaces 29 (2006) 136.

[290] G. Zhao, O. Zinger, Z. Schwartz, M. Wieland, D. Landolt, B.D. Boyan, Clinical oral implants research 17 (2006) 258.

[291] O. Zinger, G. Zhao, Z. Schwartz, J. Simpson, M. Wieland, D. Landolt, Biomaterials 26 (2005) 1837.

[292] J.I. Rosales-Leal, M.A. Rodriguez-valverde, G. Mazzaglia, P.J. Ramon-Torregrosa, L. Diaz-Rodriguez, O. Garcia-Martinez, M. Vallecillo-Capilla, C. Ruiz, M.A. Cabrerizo-Vilchez, Colloids and surfaces A: Physochemical engineering aspects 365 (2010) 222.

[293] J. Guo, R.J. Padilla, W. Ambrose, I.J. De Kok, L.F. Cooper, Biomaterials 28 (2007) 5418.

[294] G. Mendonca, D.B.S. Mendonca, L.G.P. Simoes, A.L. Araujo, E.R. Leite, W.R. Duarte, e. al., Biomaterials 30 (2009) 4053.

[295] J.J. Norman, T.A. Desai, Annual Biomedical engineering 34 (2006) 89.

[296] A. Curtis, C. Wilkinson, Trends in biotechnology 19 (2001) 97.

[297] K. Kubo, N. Tsukimura, F. Iwasa, T. Ueno, L. Saruwatari, H. Aita, e. al., Biomaterials 30 (2009) 5319.

[298] G. Mendonca, D.B.S. Mendonca, F.J.L. Aragao, L.F. Cooper, Journal of biomedical materials research 94A (2010) 169.

[299] L. Zhao, S. Mei, P.K. Chu, Y. Zhang, Z. Wu, Biomaterials 31 (2010) 5072.

[300] V.C. Mendes, R. Moineddin, J.E. Davies, Biomaterials 28 (2007) 4748.

[301] C. Miller, H. Shanks, A. Witt, G. Rutkowski, S. Mallapragada, Biomaterials 22 (2001) 1263.

[302] C. Miller, S. Jeftnija, S. Mallapragada, Tissue engineering 8 (2002) 367.

[303] B. Chehroudi, T.R.L. Gould, D.M. Brunette, Journal of biomedical materials research 24 (1990) 1203.

[304] W. Zhang, X.F. Walboomers, T.H.v. Kuppevelt, W.F. Daamen, Z. Bian, J.A. Jansen, Biomaterials 27 (2006) 5658.

[305] A. Graziano, R. D'Aquino, M.G. Cusella- De Angelis, F. De Franscesco, A. Giordano, G. Laino, A. Piattelli, T. Traini, A. De Rosa, G. Papaccio, Journal of cellular physiology 214 (2007) 166.

[306] C. Mangano, A. De Rosa, V. Desiderio, R. D'Aquino, A. Piattelli, F. De Franscesco, V. Tirino, F. Mangano, G. Papaccio, Biomaterials 31 (2010) 3543.

[307] P. Baveye, M. Laba, Environmental Health Perspectives 116 (2008).

[308] S.M. Waita, B.O. Aduda, J.M. Mwabora, C.G. Granqvist, S.E. Lindquist, G.A. Niklasson, A. Hagfeldt, G. Boschloo, Journal of electroanalytical chemistry 605 (2007) 151.

[309] M. Adachi, Y. Murata, J. Takao, J. Jiu, M. Sakamoto, F. Wang, Journal of american ceramic society 126 (2004) 14943.
[310] N. Papageogiou, C. Barb, M. Grätzel, Journal of Physical Chemistry B 102 (1998) 4156.
[311] T. Horiuchi, H. Miura, S. Uchida, Chemical Communications (2003) 3036.
[312] A.V. Barzykin, M. Tachiya, Journal of Physical Chemistry B 108 8385.
[313] A. Kay, M. Grätzel, Chemistry Of Materials 14 (2002) 2930.
[314] G.K. Mor, K. Shankar, M. Paulose, O.K. Varghese, C.A. Grimes, Nano Letters 5 (1991).

PART I

Chapter 2: Synthesis of a stable, aqueous TiO_2 dispersion via a two step, low temperature hydrothermal method[1]

Abstract

In this first experimental chapter, the development of a low temperature method for the preparation of an aqueous TiO_2 dispersion is described. Via a two-step, hydrothermal synthesis method, using a maximum temperature of 130°C, a highly stable dispersion with a high solid load of TiO_2 nanoparticles is obtained. First the stability of the dispersion (against sedimentation and particle agglomeration) is extensively investigated by means of various analyses such as zeta potential analysis, viscosity measurements and interaction potential calculations. Then, the characteristics of the nanoparticles are studied by more conventional techniques such as Transmission Electron Microscopy and X-ray diffraction. In addition, the process parameters of the second hydrothermal treatment are studied in more detail in order to gain insight into the controlling parameters and reactions that are responsible for the successful dispersion and stabilization of the nanoparticles in the presented colloidal system.

---

[1] The work discussed in section 2.1 till 2.4 is published in Chemical Engineering Journal, volume 223 (2013). DOI: 10.1016/j.cej.2013.02.047

This chapter begins with the synthesis of very small crystalline TiO_2 nanoparticles, called as nanoseeds, as they are considered as the basic units for the further development of a stable dispersion of nanoparticles.

2.1 Synthesis of TiO_2 nanoseeds

The synthesis of TiO_2 nanoparticles with very small dimensions (< 10 nm) is based on a hydrothermal method published by Kartini [1], shown in Figure 2.1. As mentioned in chapter 1 (section 1.2.2), hydrothermal synthesis is an easy and controllable method for the synthesis of high crystalline metal oxides, at low temperatures. Since the growth of the anatase seeds is a function of the hydrothermal time, a hydrothermal treatment at 80°C for 4 h is applied to synthesize nanoseeds with dimensions < 5 nm [1].

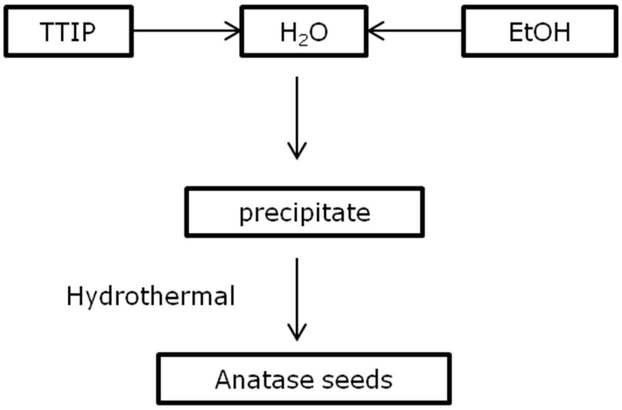

Figure 2.1 Flow diagram of the synthesis of anatase nanoseeds [1].

Experimental A mixture of 10 mL titanium(IV) tetraisopropoxide (TTIP, $[(CH_3)_2CHO]_4Ti$, Acros Organics, 98^+%) in 16.6 mL ethanol (EtOH, Acros Organics 99%) is added dropwise to a solution of 3.3 mL EtOH in 13.3 mL water (Mili Q water, Millipore, 18 MΩcm resistivity at 25°C). The obtained mixture is stirred for 2h at room temperature. The resulting suspension is transferred into a teflon-lined, non-stirred pressure vessel (Parr 4748, 120 mL) and heated in a furnace, preset at 80°C. To obtain a seed suspension of particles with dimensions smaller than 5 nm, a hydrothermal treatment with a duration of 4 h is applied [1]. After this hydrothermal step, the warm seed suspension is filtered (Pall Life Sciences Supor®100 filters, 0.1 µm pore sizes) and washed with water. The filter cake is dried for characterization. The particles obtained via this procedure are called *seeds*.

Size and shape of the *seeds* are analyzed by Transmission Electron Microscopy (TEM).
Figure 2.2 shows a bright field (left) and a dark field (right) image of the dried seeds. Based on the dark field TEM image, the primary crystallites have calculated dimensions of 6 nm ± 2 nm (120 particles, Ferets' diameter, by Image J), but are highly agglomerated. A diffuse SAED pattern (inset) is generated due to this high agglomeration and the small size of the crystallites. All except one diffraction ring in the SAED pattern can be ascribed to both anatase and brookite, as they overlap. Only the ring marked with an arrow can be attributed to the (1 2 1) peak, only characteristic to the brookite phase. In the XRD diffractogram (Figure 2.3), the peaks characteristic to both anatase and brookite confirm the simultaneous presence of these two phases. According to the JCPDS card No 29-130 for brookite, the peak corresponding to the hkl indices (1 2 1) contains 90% of the intensity of the main peak at 25° 2θ (1 2 0), indicating the brookite phase to be the minor phase.

In Raman (Figure 2.3) the characteristic anatase peaks at 145, 400, 517 and 627 cm^{-1} [2] are present where the peak at 627 cm^{-1} clearly shows a blue shift (compared to 639 cm^{-1}) due to the small particle size. Furthermore, the brookite impurity is confirmed by the small peaks around 236 and 356 cm^{-1} [3] compared to the anatase peaks. Yang et al. [4] reported a brookite impurity for powders obtained in a basic environment. Moreover, very small anatase or rutile are mostly accompanied by a brookite phase [5].
Using the Scherrer's equation applied on the XRD pattern of the seeds and using the (1 0 1) reflection of anatase at 25 °(2θ), the crystallite size is calculated to be 4 nm. This size is smaller than the size obtained from TEM due to the high agglomeration.

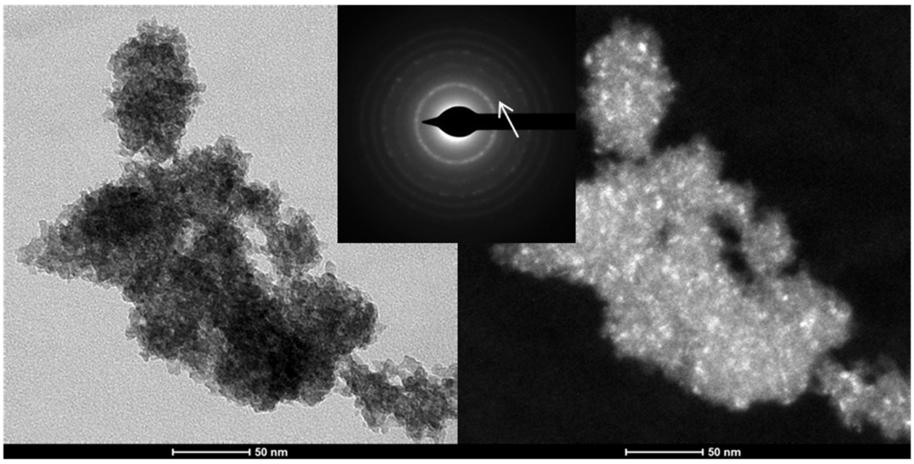

Figure 2.2 Bright field (left) and dark field (right) TEM images of the *seeds* after the first hydrothermal treatment of 4h at 80°C (Inset: SAED pattern)

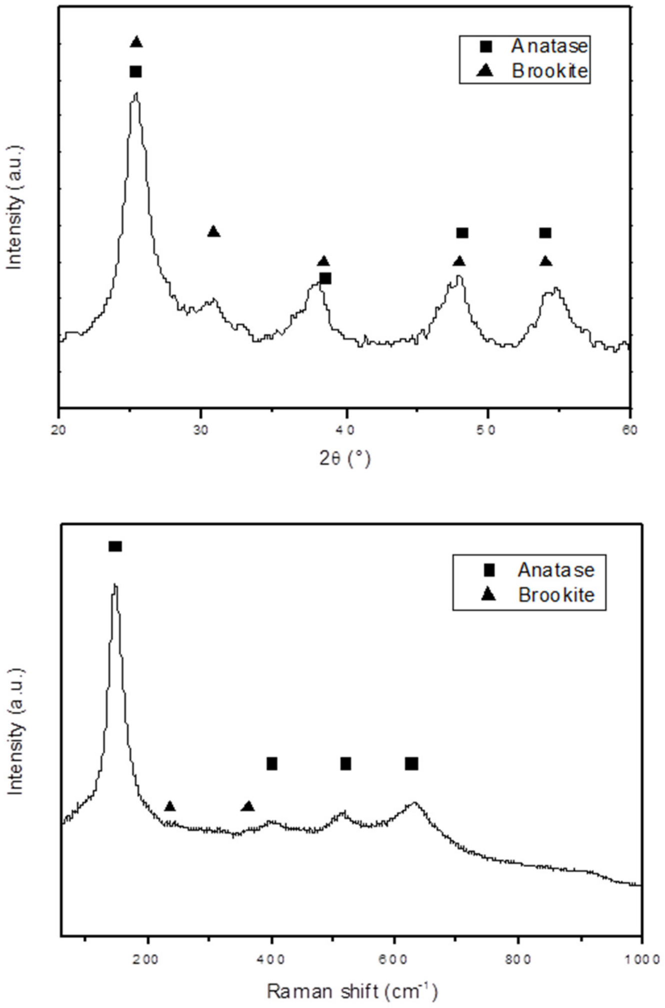

Figure 2.3 XRD pattern (top) and Raman spectrum (bottom) of the as-prepared *seeds*.

To quantify the amount of anatase and brookite in the seeds, quantitative XRD analysis is applied. The obtained fitting is shown in Figure 2.4 and results in a mixture of 10% anatase and 90% brookite. After substraction of the background, a different distribution is obtained: 50% anatase and 50% brookite. From this significant difference, it is concluded that the quantitative analysis is not reliable on the seeds, probably due to the high background which makes it difficult to correctly substract the background.

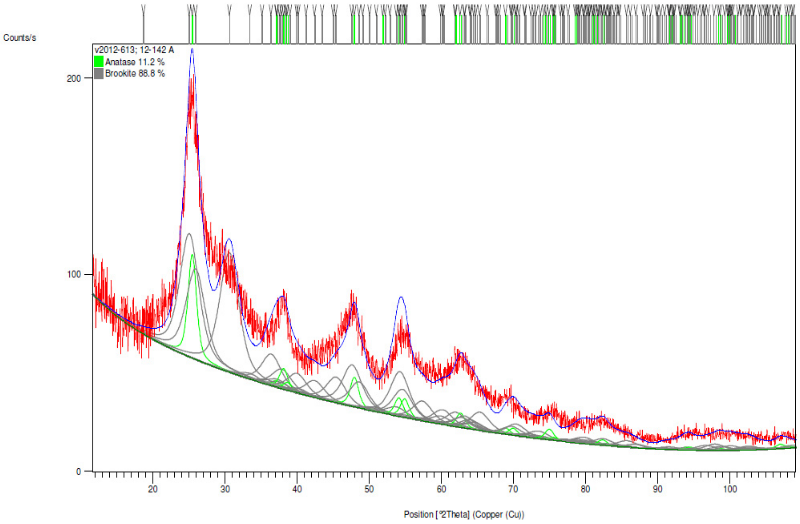

Figure 2.4 XRD pattern with fitted spectrum (blue line) for the quantitative analysis of the *seeds*.

The nanoseeds prepared by this method satisfy the aimed properties concerning phase (**anatase**) and particle size **(<10 nm**), especially with the view on its application in photocatalysis. However, the high agglomeration is more a problem when these seeds are aimed to use for deposition of homogeneous films wherefore they need to be dispersed in a solvent. Using the seed suspension, which is obtained directly after the hydrothermal treatment, is not an option as it quickly sedimentates, as shown in Figure 2.5.

Figure 2.5 Digital photograph of the seed suspension, after a few hours, obtained after hydrothermal treatment at 80°C for 4h.

The process of "dispersion" of particles in a medium entails overcoming the different binding forces (due to Brownian motion and the London dispersion interactions), by use of both physicochemical and mechanical means. Three fundamental processes influence the final dispersed state: wetting of the solid surface, dispersing the particles and stabilizing the dispersed particles in the suspension. Although **water** is chosen as ecofriendly dispersion medium, the following aspects need some attention:

1. Selection of type and concentration of the dispersing aids (i.e. wetting agent, de-agglomeration agent and stabilizing agent)
2. Selection of the type and duration of the mechanical dispersing treatment.

As deagglomeration agent, **tetraethylammonium hydroxide (TEAH)** is selected due to its proved success as peptizing agent for the deagglomeration of nanoparticles such as aluminum oxide [6], manganese oxide [7] and titanium dioxide [4, 8].

Nevertheless, sonication (bath of 200W, 10 min at a continuous pulse frequency of 60 Hz and horn of max 225W, 20 sec) of a suspension containing the seeds and an aqueous solution of TEAH, seemed not to be sufficient to deagglomerate and stabilize the nanoparticles in the aqueous medium, as is verified visually by sedimentation. As described in chapter 1 (section 1.2.2), particles can be deagglomerated by peptization, frequently combined with a hydrothermal treatment. This treatment is mostly intended to crystallize the amorphous powder to which the peptizing agent is added. In this work, a (second) **hydrothermal treatment** is chosen to efficiently provide the required energy to overcome the repulsion barrier between the highly agglomerated nanoparticles, as this seemed not to be possible by sonication alone.

2.2. Dispersing the nanoseeds via hydrothermal treatment

The pre-synthesized nanoseeds presented in section 2.1 are used as starting material to prepare a stable dispersion. Tetraethylammonium hydroxide, in this work considered as a surfactant based in the NIST definition (Chapter 1, section 1.3.1), is added to the filter dried (wet) cake.

The difference between the use of a filter dried(fresh, wet) cake or dried (aged) cake is discussed in section 2.6.

Experimental 7,6 g of the (freshly) prepared filter dried (wet) cake is transferred into a Teflon-lined autoclave and 8 ml water together with 0,3 ml of tetraethylammonium hydroxide (TEAH, $C_8H_{21}NO$, 20 wt% in water, Acros Organics) are added as well. This mixture is then hydrothermally treated for 18h in a preheated oven at 130°C. After cooling the autoclave, a stable dispersion is obtained. A flow chart of the total, two-step hydrothermal synthesis of the stable TiO_2 dispersion is shown in Figure 2.6.

The temperature and time selection of the second hydrothermal treatment in current work is based on the preparation of colloids reported earlier by Späth [8] and Barbé [9]. In their work, a basic reagent is used to peptize the precipitate, formed by hydrolysis of titanium tetraisopropoxide, followed by a hydrothermal treatment at 130°C for 12 h. For our synthesis, using the crystalline seeds instead of the hydrolyzed product, this duration didn't result in a stable dispersion and therefore is raised till 18h. Via the method described in Figure 2.6, a macroscopically stable dispersion is obtained which means that no sedimentation is observed, even not after weeks or months of storage at room temperature.

Analysis of the dispersion by optical microscopy[2] shows (Figure 2.7a) the presence of some large agglomerates, which could be deagglomerated by a sonication treatment (horn, max 225 W, 20 s, continuous mode), as shown in Figure 2.7b. After a subsequent filtering step (filter of 1 µm), the dispersion looks very homogeneous and no large agglomerates are detected. Nevertheless, sonication is not beneficial for the (long term) stability of the dispersion, which is discussed in more detail in section 2.3.

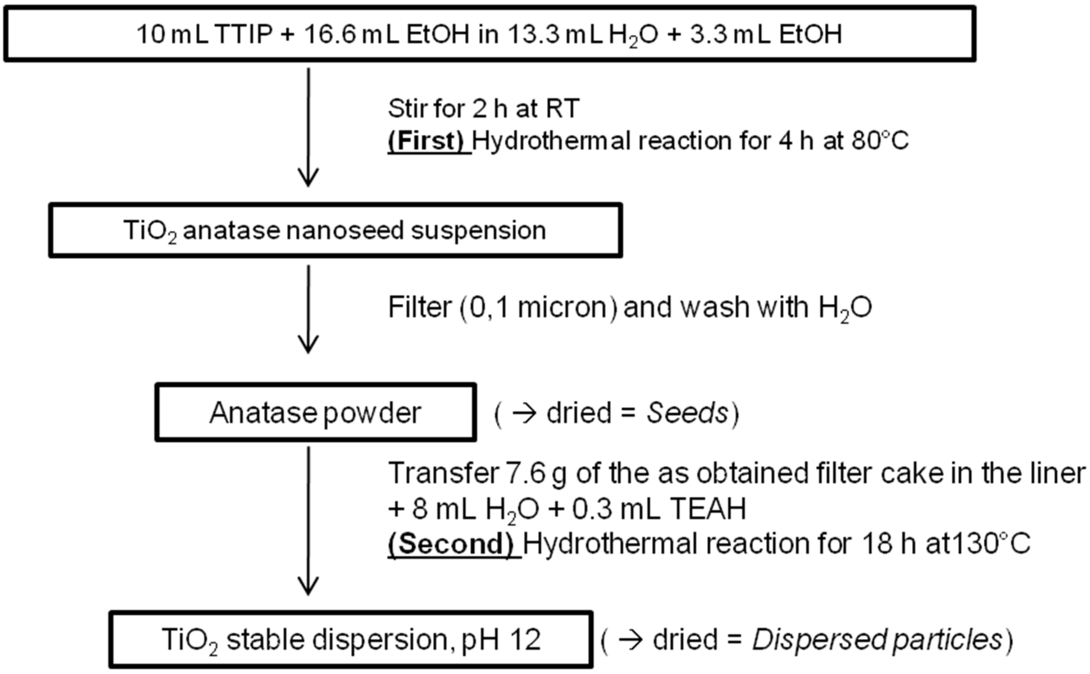

Figure 2.6 Flow chart of the two-step, hydrothermal synthesis route for a stable TiO_2 dispersion [10].

---

[2] The microscopy analysis is carried out at Umicore, with assistance of J. Gilleir.

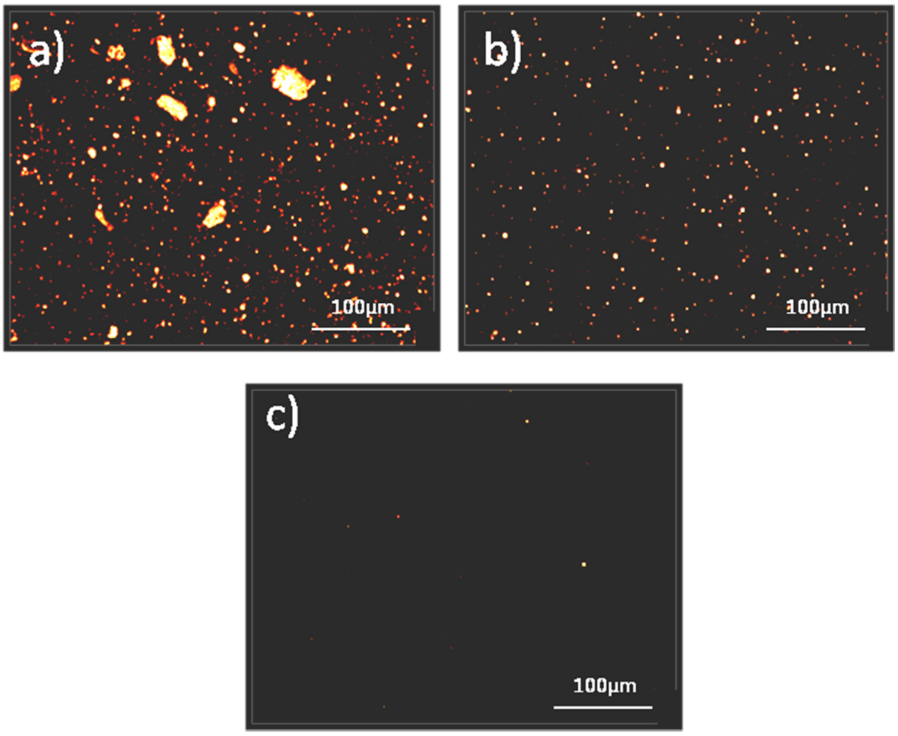

Figure 2.7 Optical micrographs of the dispersion before (a), after sonication (b) and after sonication and filtering (1μm) (c).

The **solid content** of the TiO_2 dispersion is determined by thermogravimetric analysis (Figure 2.8), which is 10 wt%. This is higher than the solid load reported by Baldi et al.[11], who prepared aqueous dispersions with a solid load limited to 6,7 wt% via heating titanium alkoxide in the presence of Triton-X as a surfactant. Other studies may report a higher solid load in their dispersions, mostly from commercial TiO_2 powders, but they lack information about the stability of the dispersions in function of time. Therefore, it may be concluded that, to the best of our knowledge, this is one of the highest solid load obtained for an aqueous TiO_2 dispersion starting from a pre-synthesized TiO_2.

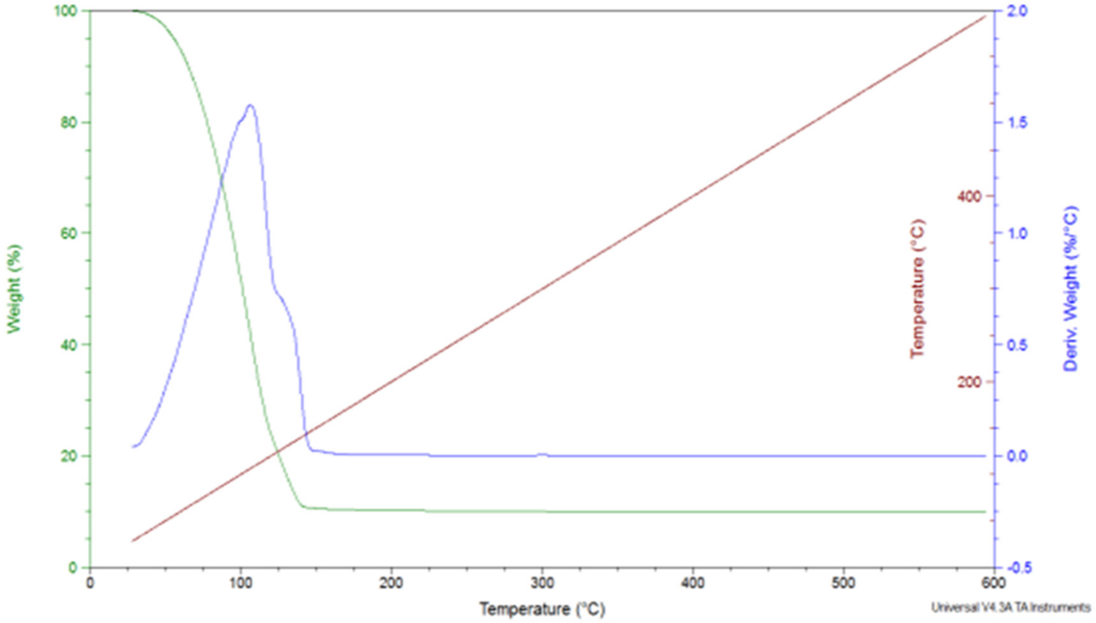

Figure 2.8 TGA- profile of the dispersion from room temperature till 600°C, at 5°C/min in dry air.

2.3 Study of the stability of the dispersion

To avoid any confusion, the term 'highly stable' in this thesis concerns the **absence of sedimentation in function of time**. One way to analyze the stability of a dispersion is by determination of the zeta potential. The zeta potential is measured by Laser Doppler Electrophoresis, as discussed in Chapter 1, section 1.3.2. The zeta potential of the freshly prepared dispersion is -51 mV at pH 12. This large negative value corresponds to the presence of highly negative surfaces and indicates the degree of repulsion between similarly charged particles in the dispersion. The high surface charge may induce a stronger and longer range electrostatic repulsion which can be related to low viscosity and long-term stability of the TiO_2 dispersion [12].To investigate the stability of the dispersion in function of time, the zeta potential is determined after two months of storage and showed a decreases till a value round -35 mV. This decrease can be related to the formation of agglomerates, but still no sedimentation is observed macroscopically. Since a high negative zeta potential isn't a direct proof of the stability of a dispersion against sedimentation, other techniques are applied to evaluate the stability of our dispersion:

- Macroscopic photos of the dispersion and dried dispersion
- Optical microscopy images of the dispersion
- Viscosity measurements in function of time
- Calculations of the sedimentation velocity
- Analysis of transmission in function of time in a centrifugal field

In order to study the stability of the dispersion against particle agglomeration (section 2.3.2, calculations of the interaction energy are carried out using the Hamaker software [13].

2.3.1 Stability against sedimentation

Several techniques, some result in only qualitative prove, are applied in order to study the stability of the dispersion against sedimentation in more detail.

Macroscopic photographs of the dispersion and the dried dispersion[3] The high stability of the dispersion is observed macroscopically based on the absence of visual sedimentation of particles after several months of storage at room temperature while standing. In Figure 2.9, a photograph of the dispersion after one month of storage is shown. Even after 2 months, no sedimentation front is observed and therefore the dispersion is considered as stable. The right picture in Figure 2.9 represents a photo of the dispersion dried at 60°C which indicate the homogeneity of the dispersion[4].

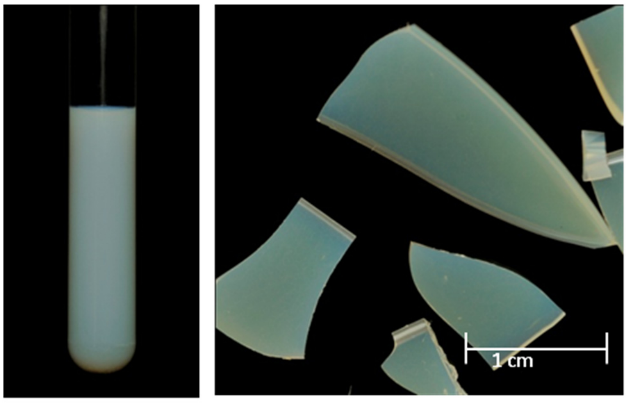

Figure 2.9 Digital photograph of the TiO_2 dispersion after one month of storage (left) and the dispersion dried at 60°C (right).

Optical microscope images of the dispersion As already mentioned in section 2.2, optical micrographs (Figure 2.7) indicate that the dispersion contains agglomerates which can be easily disintegrated by a short sonication treatment. Although sonication is frequently applied to break the agglomerates [14-16], it can also promote particle agglomeration (discussed in chapter 1, section 1.3.1) due to enhanced particle-particle interactions. Indeed, sedimentation is observed after some days, in the sonicated dispersion. To conclude, the dispersion is called stable based on the absence of flocculation in optical microscopy. Nevertheless, sonication only improves the temporarily dispersability of the dispersion but is only recommended when the dispersion is directly used afterwards, e.g. for film deposition.

---

[3] Photographs were taken at the UHasselt, by photographer Marc Withofs

[4] This kind of digital study is frequently used in industry to have a quick look on the homogeneity of their prepared dispersions.

Viscosity measurements in function of time[5] The stability of a system depends on different parameters including particle size, electrolyte concentration, crystal phase, solid load, viscosity, time, temperature, … , Although most reports concern about the study of the viscosity of TiO_2 dispersions in function of pH, solid concentration and particles size [17-19] to evaluate the aggregation behavior, in this study, it was selected to study the viscosity of the TiO_2 dispersion in function of time, since time has been chosen earlier as the dimension to express the stability of the dispersion.

Experimental The measurement of the viscosity is carried out with a double gapcylinder system (concentric cylinder) as measuring geometry. The displacement of the cylinder and the speed is measured. The change of shear stress needed to maintain the displacement constant, determines the viscosity. At a constant shear rate of 1.0 s^{-1}, the viscosity is continuously measured in function of time and plotted with each data point representing the average of a collection of 24 measurements.

At day 1, the viscosity of the dispersion at a shear rate of $1s^{-1}$ is 1.9 mPa.s, which is almost comparable[6] with water (0.89 mPa.s). After 17 days of continuous measurements, the viscosity has increased with a small amount (Figure 2.10), and no macroscopic sedimentation is observed. When sedimentation would occur, the resistance of the cylinder decreases due to the difference in concentration between the upper part and the bottom part in the dispersion in the cylinder, due to the settling of particles, which decreases the shear stress and the related viscosity [20].

Moreover, the small increase in viscosity during the measurement, can not be related to an increase in concentration (due to evaporation) since oil was applied on top of the dispersion to avoid evaporation during the long measurement.

---

[5] The viscosity measurements are carried out at VITO by Dr. Steven Mullens.

[6] The viscosity is expressed in a logarithmic scale.

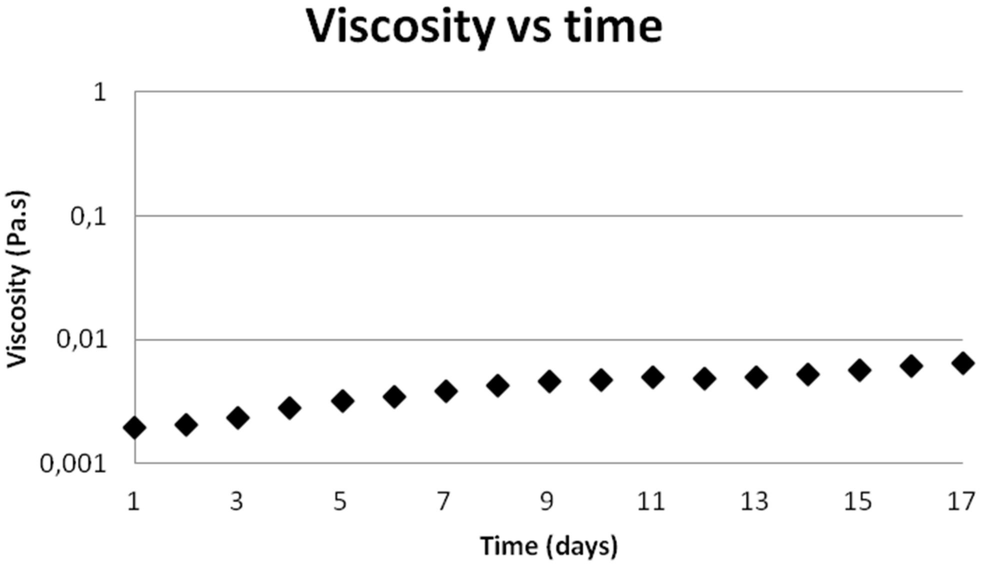

Figure 2.10 Viscosity versus time for the 10 wt% TiO_2 dispersion.

A more theoretical approach to study the stability of a dispersion is via **calculations of the sedimentation velocity.** The sedimentation rate (i.e., particles settling velocity) can be predicted by means of the Stokes equation (equation 18)

$$u_t = \frac{2}{9}\frac{(\rho_s - \rho_l)gr^2}{\eta}$$

Applying this equation on the TiO_2 dispersion, considering a monodispersed system of 9 nm particles[7], and using the viscosity at shear rate ~0, the sedimentation rate is calculated to be $2.09*10^{-14}$ m/s, which would corresponds to sedimentation of less than ~0.045 µm after 30 days. Using a particle size of 38 nm[8], a sedimentation velocity of $3.71 *10^{-13}$ m/s is calculated, corresponding to ~0.96 µm after 30 days. Based on these measurements and calculations, it can be concluded that the sedimentation velocity of the particles in de dispersion is very low, confirming the macroscopically stable dispersion against sedimentation. The addition of the concentration depending factor (equation 19), result in an exponential factor of ~5,2 for particles smaller than a micron. Applied on the TiO_2 dispersion with a solid load of 10wt% (~ 2,6 v%), this factor is ~ 0,87. which is almost equally to 1, and therefore will not strongly influence the sedimentation velocity predicted via the Stokes equation.

From these calculations, it is shown that it takes some time for a colloidal particle to settle for a reasonable distance through the medium under the influence of gravity alone. Therefore, the behavior of the nanoparticle in the dispersion under centrifugal field is studied in the following.

---

[7] Corresponds to the particle size (dv50) measured via a centrifugal method, as will be described in section 2.4

[8] Corresponds to the particle size (dv90) measured as will be described in section 2.4.

Analysis of transmission in function of time in a centrifugal field With the analytical centrifuge of the Lumisizer (principle explained in Chapter 1, section 1.3.2), transmission profiles of the dispersion in function of time are obtained. From the kinetics of the transmission profiles, the demixing behavior and/or dispersion stability is evaluated. In Figure 2.11, the transmission profiles in function of time are given: (1) represents the start position where the meniscus is at 108 mm and the bottom of the cell at 130 mm. In the start position, the transmission of the sample is 10%. This is high enough and no dilution of the sample is needed. After a few minutes, a peak around 111 mm appears whereas the transmission around this peak increases (2). This increase in transmission means that clearing is occurring. After a time, the transmission profiles move to the left in the direction of the meniscus (3). Here it seems that creaming occurs which means that particles/substances with a lower density than water have moved towards the meniscus. The only substances present in the dispersion with a density lower than water (d=1,00 g/cm^3), as will be demonstrated later, are ethanol (d= 0,79 g/cm^3) and isopropanol (d= 0,795 g/cm^3)[9]. After 30 minutes of measurement, the peak around 111 mm still increases and at the right side of the peak, sedimentation starts (4). In (5) sedimentation is unmistakably present: particles start to move towards the bottom of the cell. Even at the meniscus, sedimentation has started and the creaming effect has disappeared. The sedimentation is in full progress in (6) and the transmission profile at the end of the 2 hour measurement is shown in (7).

Based on the previous (more qualitative) analysis (digital photography, optical microscopy, viscosity measurements, …), it was concluded that the dispersion shows a high stability against sedimentation under gravitational field. Based on the results from the transmission study, it can be seen that demixing (more specific creaming) already occurs at the beginning of the measurement and that the sedimentation is in full progress after only 2 h of measurement. These results indicate a more medium to low stability of the dispersion under centrifugal field. The differences in the stability under gravitational and centrifugal field, may be explained by the occurrence of a phenomenon, i.e. creaming which does not occur (spontaneously) under gravitational field. Based on the assumption that the creaming is caused by the floatation of the alcohols (ethanol and isopropanol) and the alchohols provide a stabilizing effect (which is discussed further), the particles become less stabilized in the dispersion under centrifugal force and sedimentation is taken place. Furthermore, it may not be excluded that the presence of different forces in centrifugal field may overcome the repulsive forces which play a significant role in the dispersion of nanoparticles.

---

[9] The presence of these alcohols are proven in section 2.6. and are residues of the first hydrothermal reaction.

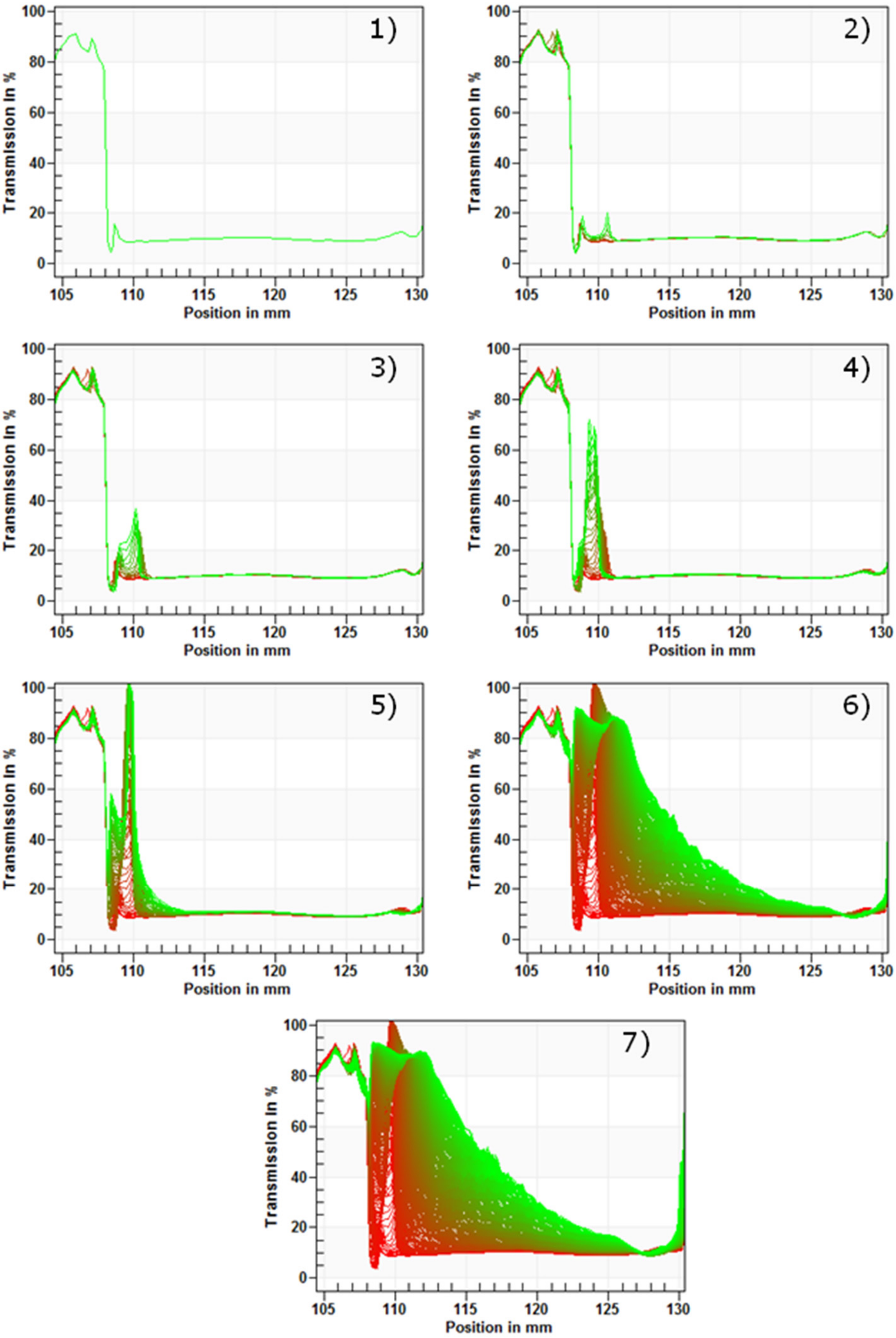

Figure 2.11 Transmission profiles of the dispersion in a centrifugal field in function of time (1-7) with the red and green curve indicating the time (sedimentation=red left, green right, creaming=green left, red right).

2.3.2 Stability against particle agglomeration

To understand which aspects control the stability of the nanoparticles in the system against particle agglomeration, theoretical calculations are performed using Hamaker 2.1 software [13, 21]. This software package calculates the interparticle interactions, applying the DLVO model with contributions for steric interactions and other interactions depending on the system[10]. Taking into account Van der Waals, electrostatic and steric contributions, the stability of the dispersion is evaluated. A more detailed discussion of this software, the use and the interpretation can be found in the appendix. The TEAH solution is considered as an electrolyte containing $N(C_2H_5)^+$ and OH^- ions in a concentration of 0.01 M, corresponding to the measured pH of 12. Interaction potential curves are determined for two different particle size, 9 nm and 38 nm, being dv50 and dv90 obtained via particle size distribution analysis (described in section 2.4). Although the particles of 38 nm are assumed to be agglomerates, they are treated as single particles in the software and considered to be spherical.

The required barrier (in the software) is defined as the interaction potential required to prevent agglomeration in the system. Via the software, for stability on a 12 h timescale, a barrier around 25 kT is predicted/calculated for a dispersion containing only particles of 9 nm, 38 nm and a mixture of 9 nm and 38 nm. Figure 2.12a shows the interaction potential between these titania–titania pairs without the contribution of possible steric interactions. For the dispersion of 9 nm particles and 9 and 38 nm, the maximum of the interaction potential lies far below the required barrier and so particle agglomeration is predicted at low distances. However, particles with only sizes of 38 nm, the tendency to agglomerate is tempered since the maximum of the interaction potential approaches the required barrier. In conclusion, the interaction potential curves indicate that the smallest particles are predicted to have a high tendency to agglomerate while the bigger sized particles, or agglomerates, will only agglomerate (or further grow) when their interaction potential is lower than the required barrier.

Since the TiO_2 nanoparticles are negatively charged (as confirmed by the high negative zeta potential), the interaction with the tetraethylammonium cations is assumed to be dominated by electrostatical forces. Although the alkylgroups in TEAH are only small, the interaction potentials are calculated taking into account possible steric interactions. As shown in Figure 2.12b, the derived steric barrier is too small to avoid particle-particle agglomeration and thus TEAH only provides the required electrostatic interactions for the stabilization of the small agglomerates.

---

[10] For example, mAgnetic interaction forces can be added for particles exhibiting this property.

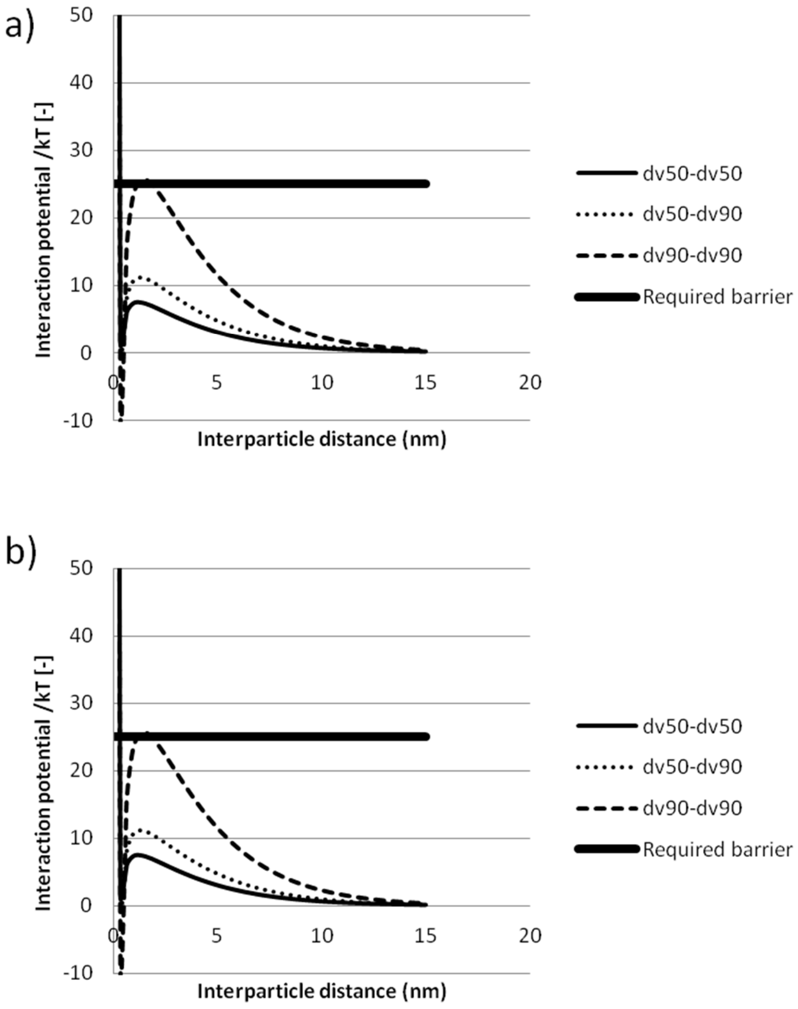

Figure 2.12 Interaction potential curves calculated using the Hamaker software for a variation of particle sizes (a) without the consideration of steric interactions and (b) with the consideration of steric interactions.

This predicted particle agglomeration in the system is observed in the optical microscopy image (Figure 2.7). As shown, a short sonication treatment of the dispersion destroys the formed agglomerates. However, sonication destroyed the long term stability of the dispersion against sedimentation. Based on the interaction potential curves, the occurrence of sedimentation, caused by an increased particle agglomeration, of the dispersion after sonication (section 2.3.1) can now be explained by the high energy of the sonication treatment (220 W) compared to the required barrier of 25 kT. For our system, only a sonication treatment with a energy lower as 7 kT is expected to not introduce enhanced particle agglomeration, if only electrostatic and van der Waals forces are playing.

To resume, although particle agglomeration occurs, it does not lead to sedimentation eventually (under gravitational force, as concluded in 2.3.1) and this is the most important issue for practical reasons. In Figure 2.13, the results and conclusions obtained in the study of the stability of the dispersion, under gravitational and centrifugal forces, are schematically overviewed.

	Under gravitational field g	Under centrifugal field 2300g
Dispersion , 10wt%	**Particle agglomeration** due to high interaction potential for small particles (Hamaker, optical microscopy) **No sedimentation** observed after 3 months (Digital photograph, viscosity, Stokes equation)	**Sedimentation** caused by creaming and particle agglomeration
Dispersion , 10wt%, **sonicated**	First **decreased particle agglomeration** followed by **sedimentation after time**, due to increased particle agglomeration introduced by high input energy (Optical microscopy)	

Figure 2.13 Schematic summary of the study of the stability of the dispersion.

2.4 Study of the dispersed particles

In this section, the particles in the dispersion, which is obtained after the second hydrothermal reaction, are studied. These particles are called *dispersed particles* to differentiate between the particles after the first hydrothermal treatment (*seeds*) and the particles after the second hydrothermal treatment.

As explained earlier (Chapter 1, section 1.3.2), for the analysis of the **particle size distribution** in the concentrated dispersion, techniques based on light scattering cannot be applied due to the need for high dilution. A high dilution can destabilize the system (due to change of pH and/or interactions) and this leads to results which do not reflect the concentrated state. Therefore CPS Disk centrifuge is applied to obtain a particle size distribution, via measurement of the sedimentation speed and using the Stokes equation, in a centrifugal field. Although a small dilution of the dispersion is still necessary for this analysis (20 times), this can be neglected compared to the dilutions needed for analysis based on light scattering (at least 100 times). The results, summarized in

Figure 2.**14** and

Table 2.**1**, show a bimodal size distribution indicating the presence of a large amount of particles between 5 and 10 nm and a smaller amount of larger particles between 10 and 60 nm, indicating some degree of agglomeration. According to the diameters based on volume,

50% of the volume of particles is smaller than 9 nm (dv50), 75% is smaller than 27 nm (dv75) 90% smaller than 38 nm (dv90) and 95% smaller than 42 nm (dv95), proving the dispersion of nanoparticles.

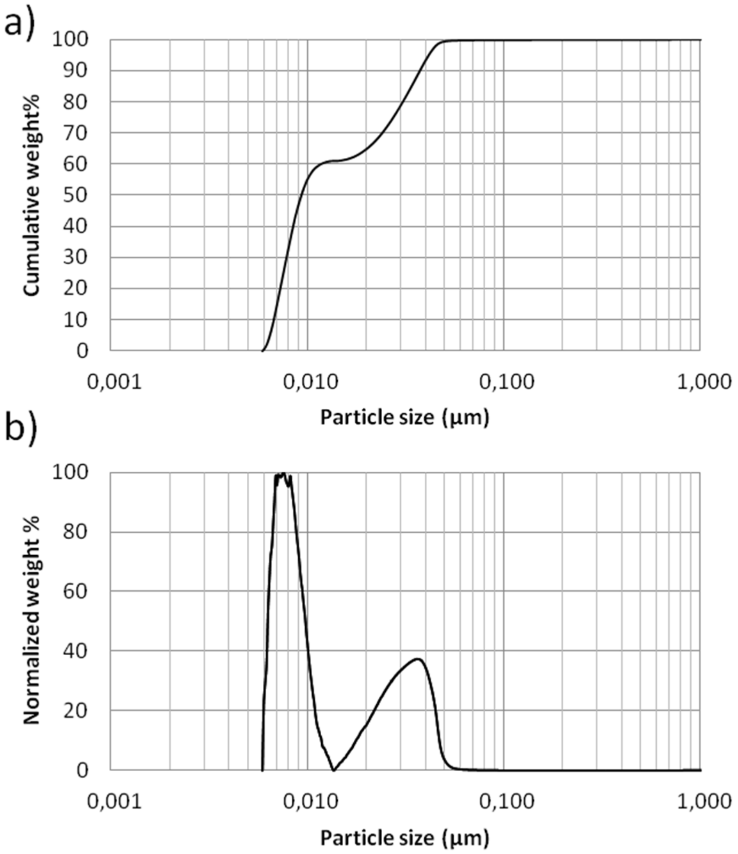

Figure 2.14 Particle size distribution in the TiO₂ dispersion (8 wt%) obtained via the CPS disc centrifuge, representing: (a) the cumulative weight distribution and (b) the normalized weight distribution.

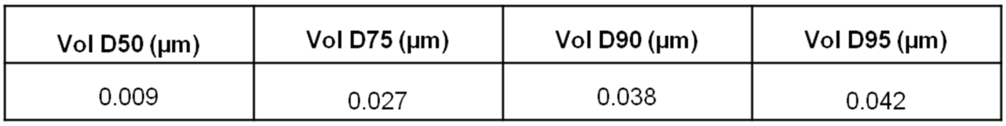

Vol D50 (µm)	Vol D75 (µm)	Vol D90 (µm)	Vol D95 (µm)
0.009	0.027	0.038	0.042

Table 2.1 Some important values describing the volumetric particle size distribution in the dispersion.

To confirm these results, the size distribution is calculated applying another technique. Via the transmission profiles obtained from the Lumisizer (as obtained in section 2.3.1), together with the Stokes' law and the law of Lambert Beer (explained in Chapter 1, section 1.3.2), the volume distribution of the dispersion can be determined The volume weighted distribution, given in Figure 2.15 shows a bimodal distribution like obtained with the CPS disc centrifuge (Figure 2.14). Analysis by the lumisizer is carried out on the undiluted dispersion (10 wt%) which result in different intensity and size range of the distribution compared to the distribution of the diluted dispersion (8wt%) obtained with CPS disc centrifuge. According to the Lumisizer results, less smaller particles (<10 nm) are present and more particles between 10 and 20 nm, which are small agglomerates. Comparing the dv95 from the CPS disc centrifuge (i.e. 42 nm) with the dv90 from the Lumisizer (i.e. 18 nm), given in Table 2.2, shows a difference which can be assigned to the formation of agglomerates caused by dilution, which was needed for the CPS analysis and not for the analysis by the lumisizer.

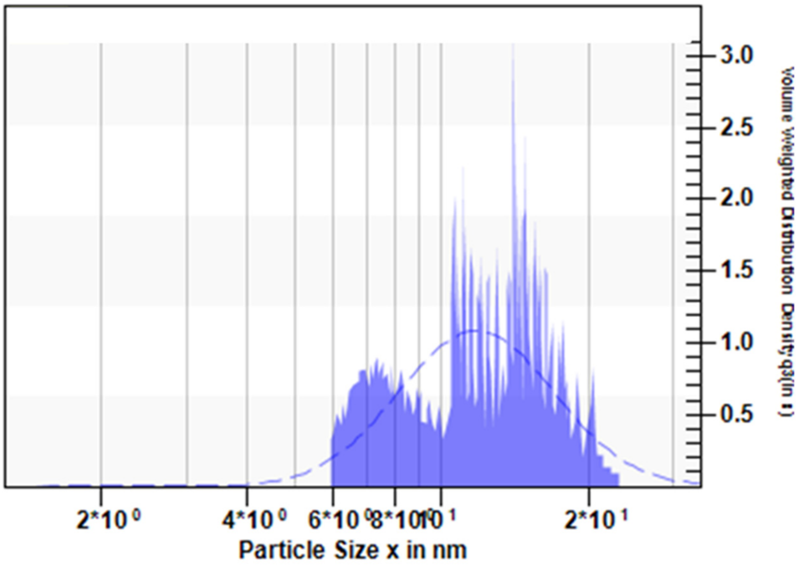

Figure 2.15 Volume weighted distribution of the 10wt% TiO_2 dispersion obtained via the Lumisizer.

Median	Std dev	≤ 10%	≤ 50%	≤ 90%
12 nm	4 nm	7 nm	12 nm	18 nm

Table 2.2 Values describing the particle size distribution obtained by the Lumisizer.

TEM analysis of the dispersed particles (= dispersion dried at 60°C)(Figure 2.16) confirms the **primary particle size** between 5 and 10 nm, as indicated in the particle size distribution (dv10). In contrast to the seeds, the shape of the dispersed particles is not fully spherical, but they appear as more elongated structures with a mean aspect ratio of 1.4 (mean value of the ratio of 10 calculated particles). The occurrence of more elongated particles is in agreement with Yang et al. [4], who showed more elongated TiO_2 structures when peptized with tetramethyl- or tetraethylammonium hydroxide. The evolution of the structures can be attributed to the different alkalinities of the peptizing agents where the OH^- groups, which replace the H_2O groups (as described in Chapter 1, section 1.2.2) cause condensation among the particles leading to the formation of structured particles [4].

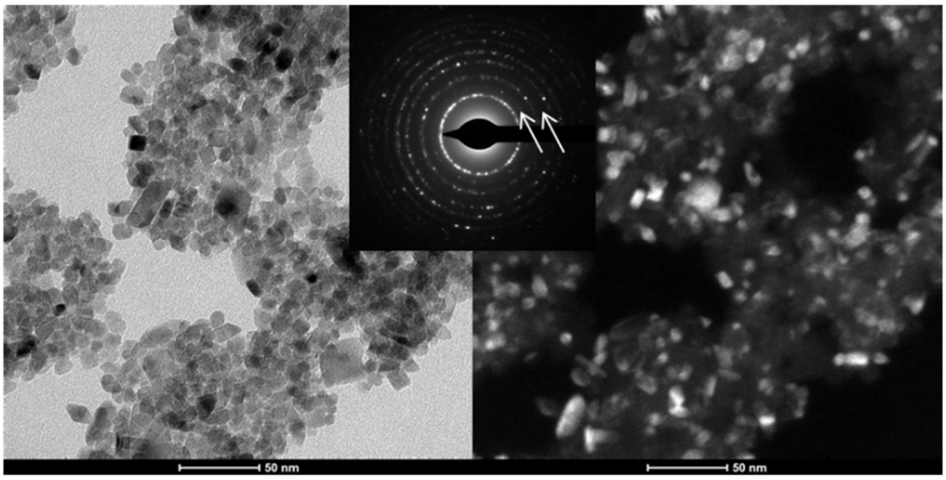

Figure 2.16 Bright field (left) and dark field (right) TEM image of the dispersed particles (inset: SAED pattern).

Furthermore, a decrease of agglomeration of the nanoparticles is observed after the second hydrothermal treatment (Figure 2.16) compared to the seeds (

Figure 2.**2**) after the first hydrothermal step. Moreover, the clear electron diffraction pattern, obtained for the *dispersed particles*, given in Figure 2.16 (inset), indicates the presence of a highly crystalline phase for the dispersed particles in contrast to the pre-synthesized *seeds* (inset

Figure 2.2). This diffraction pattern of the *dispersed particles* is indicative for both anatase and brookite. The marks (arrows) indicate the diffraction ring associated to brookite only. XRD analysis on the dispersed particles (Figure 2.17) confirms that the initial mixture of anatase and brookite is still present, as was before the second hydrothermal treatment (the *seeds*). The particle size of the crystallites calculated by applying Scherrer’s equation results in 8 nm sized particles, indicating only a very limited crystal growth during the second hydrothermal treatment. The Raman peaks at 141, 392, 510 and 630 cm^{-}1 in the Raman spectrum (Figure 2.17) demonstrate the presence of mainly anatase TiO_2 [2] accompanied with brookite [3, 22, 23].

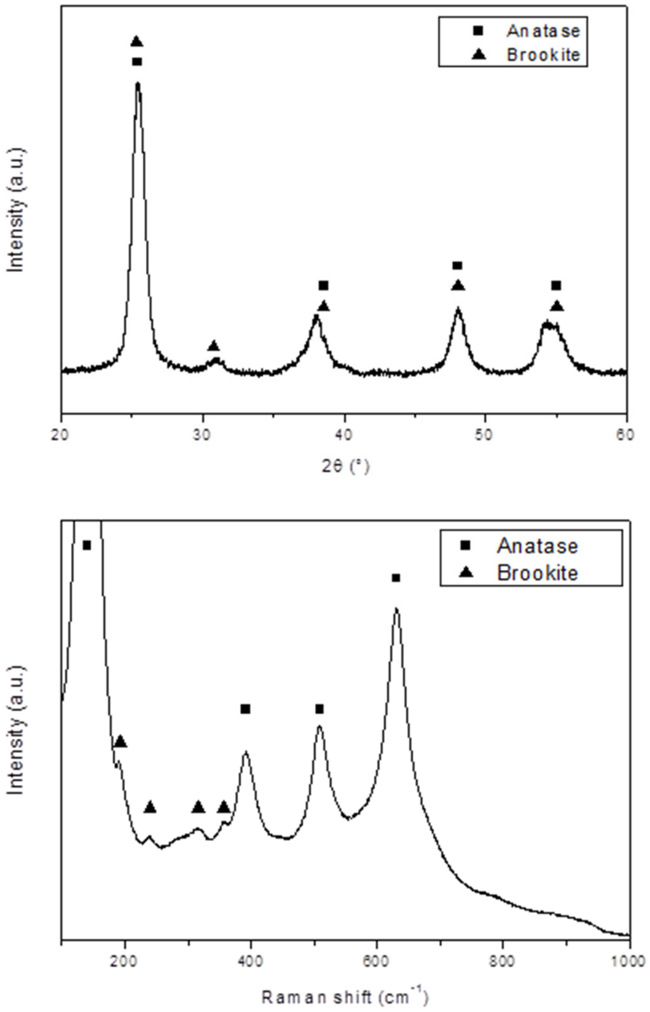

Figure 2.17 XRD spectrum of the dispersed particles (top) and Raman spectrum of the TiO_2 dispersion (bottom).

The high anatase crystallinity with an apparently more pronounced brookite impurity compared to the seeds (Figure 2.3), suggests an increase in crystallinity of the dispersed particles in comparison with the seeds before the second hydrothermal treatment. For that purpose, quantitative XRD analysis is carried out on the dispersed particles which shows the presence of 80% anatase and 20% brookite (Figure 2.18). Although this result can not be compared with the unreliable result from quantitative analysis of the *seeds*, the small increase of crystallite size of the *dispersed particles* compared to the *seeds*, confirms the improvement of crystallinity of the *seeds* during the second hydrothermal treatment, mainly into anatase.

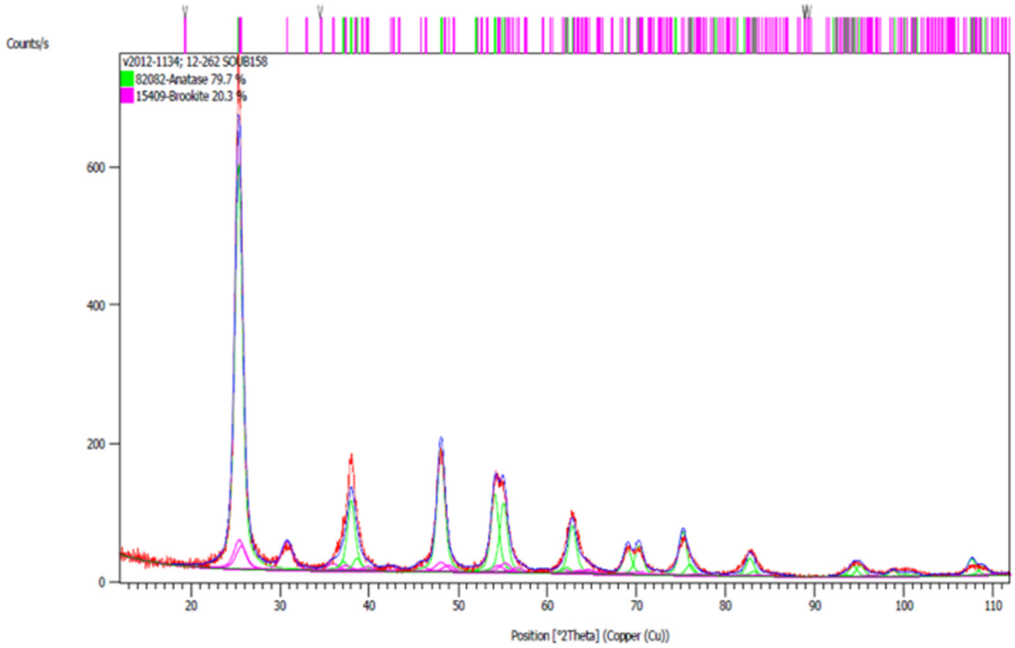

Figure 2.18 XRD pattern with fitted spectrum (blue line) for the quantitative analysis of the dispersed particles.

Since TEAH has the function of a structure and phase directing agent [7, 24], it is frequently used to direct or enhance the anatase content in powder synthesis. The influence of different peptizing agents on the crystal phases of hydrothermally synthesized titania powders was investigated by Yang et al. [4]. Dispersed rutile powders were obtained after peptization of titanium alkoxide species in an acid environment, whereas basic peptization promotes the formation of anatase powders. The mechanism, previously suggested by Jolivet and coworkers [25-27], is extensively explained by Yang (as described in section 1.2.2.). In the case of TEAH, the OH-groups replace the water groups in the amorphous TiO_2, leading to the formation of edge-sharing octahedral which are representative for the anatase phase.

The peptization effect of TEAH on TiO_2 results from the stabilization of the cationic group of $N(C_2H_5)^+$ with the polyanionic cores of titanium ($[TiO_X(OH)_Y]^{4-X-Y}$) in a basic medium. By means of this peptization mechanism characteristic for the synthesis of anatase nanocrystals, Yang et al. succeeded in breaking up the agglomerates of the precipitate derived from hydrolysis of titanium tetraisopropoxide of the anatase powder, which was formed in the subsequent hydrothermal treatment, into more dispersed particles in the powder. However in current work, we additionally demonstrate that a stable, highly loaded aqueous dispersion is obtained when TEAH is used in combination with already crystallized nano*seeds* and followed by a hydrothermal treatment. As the goal of this thesis is to deposited different nanostructured films with a high specific surface area, further study of the dispersed particles and the dispersion is expected to be meaningful.

2.5 Study of other properties (BET, Rheology)

In this section, the specific surface area of the dispersed particles is determined and compared to the seeds. Further, the rheological properties of the dispersion are described in more detail in order to understand the formation of the nanostructured films presented in chapter 3.

Analysis of specific surface area by N_2 sorption

Conventionally, N_2 sorption is applied on porous powders to gain information about the size, shape and distribution of the pores. In this work, the seeds and the dispersed particles are analyzed by N_2 sorption to gain, at first, information about the specific surface area as these powders are not porous.

Adsorption-desorption isotherms are recorded for the *seeds* and the *dispersed particles*. The recorded isotherms are shown in Figure 2.19. During the measurements, N_2 is adsorbed on the powder (in the spaces between the particles as the particles are not porous) with increasing pressure. The gas first fills the smallest interparticle pores (micropores), than the mesopores and at last the macropores. The hysteresis (steep increase of volume with small increase in pressure) indicates the moment that all pores are filled with gas. For the *seeds*, the hysteresis occurs at a relative pressure ~ 1, this means that the powder contains micropores, mesopores and macropores. The *dispersed particles* on the other hand, show a hysteresis at a lower relative pressure, indicating that this powder only contains micro- and mesopores (interparticle spaces). This differences in pores can be attributed to a difference in particle size distribution whereas the presence of micro-, meso and macro pores in the *seeds* indicate less uniform particles as compared to the powders containing the *dispersed particles*.

Based on the theory of Brunauer-Emmet-Teller (BET), the specific surface areas are determined at a relative pressure of 0.5. The BET of the *seeds* and the *dispersed particles* are 457 m^2/g and 132 m^2/g respectively. The high amount of interparticle spaces (mainly in the micro en meso order) in the *seeds* attribute to its high BET value.

For comparison, the adsorption-desorption isotherm of commercial P25 is shown in Figure 2.20. The shape of the isotherm of P25 is more comparable with the isotherm of the *seeds*. However, the BET of the *dispersed particles* is more than the double compared to the value of P25 which is 56 m^2/g. This increase is related to the smaller size of the dispersed particles compared to the P25 particles, and thus more interparticle spaces, indicating an increase of surface area of the *dispersed particles* compared to commercial P25.

Thus, besides the increase in particles size and crystallinity between the *seeds* and the *dispersed particles*, due to the second hydrothermal treatment, as demonstrated by TEM and XRD respectively (section 2.1 and 2.4), N_2 sorption analysis may indicate an **increase in uniformity** of the particles after the second hydrothermal treatment.

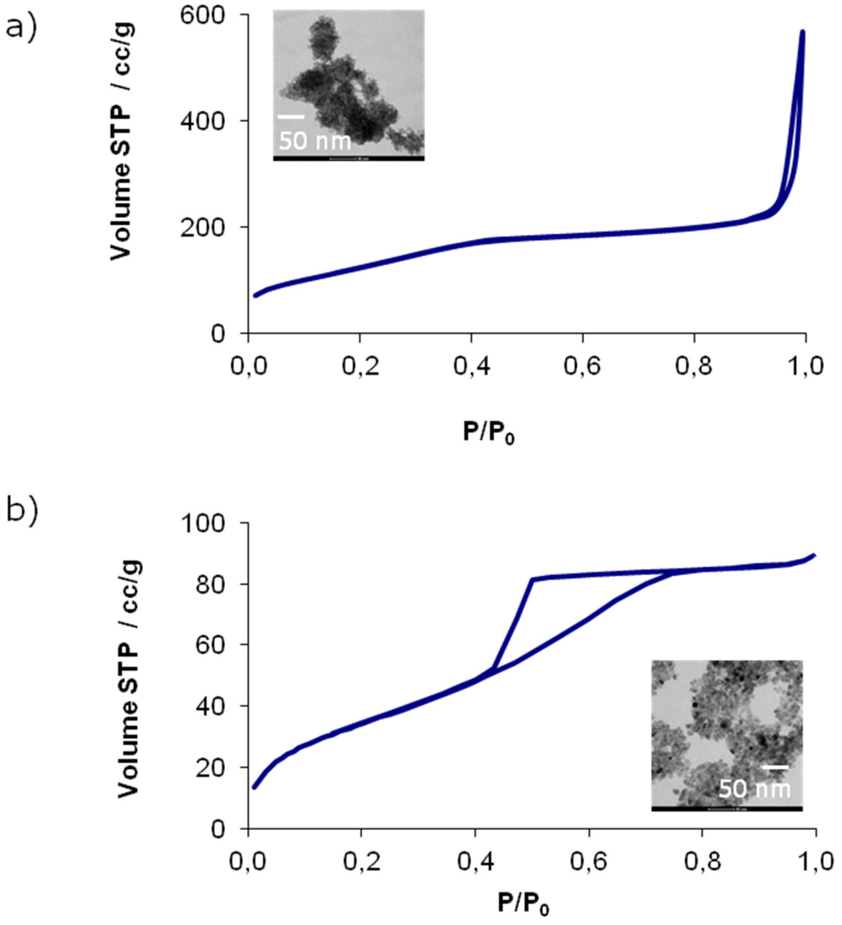

Figure 2.19 Nitrogen adsorption-desorption isotherms of the seed (a) and the dispersed particles (b). The TEM images of the powders are shown in inset.

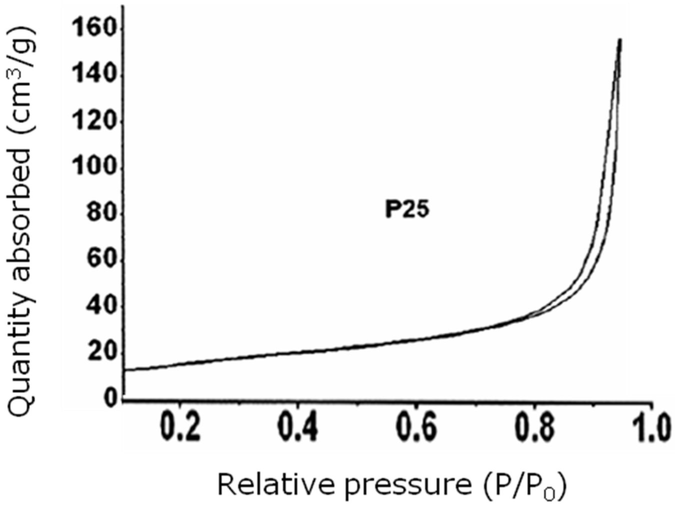

Figure 2.20 Nitrogen adsorption-desorption isotherm of commercial P25 [28].

Study of Rheology

As mentioned before, understanding the rheology of a liquid is very important for its applications as paint or coating. Therefore, the rheology of the TiO_2 dispersion is studied by following the viscosity in function of the shear rate. In section 2.3.1, the viscosity of the dispersion was measured at a constant shear, in function of time.

Figure 2.21, shows a non-Newtonian behavior, for the TiO_2 dispersion, at low shear rates, where the viscosity is decreases with increasing shear rate. This behavior is more known as **shear thinning** behavior. At higher shear rates, the viscosity is flattened which corresponds to a Newtonian behavior (viscosity is constant in function of shear rate).

As described in Chapter 1, section 1.3.1, the presence of electrical charges onto the particle influences the effective volume of particles, especially in concentrated dispersions, and determines the viscosity. In the absence of shear, the viscosity is 'high' due to the interactions between the nanoparticles, being mostly electrostatic. When shear is applied to the dispersion, the particles rearrange which decreases the viscosity. The shear thinning effect will be lower in dispersions with a lower solid load and is probably caused by the electric double layer interactions [29, 30]. From a certain shear rate, the particles align according to the flow direction and evolves to a situation where the particles form layers. From this point, the viscosity stays constant at increasing shear rate.

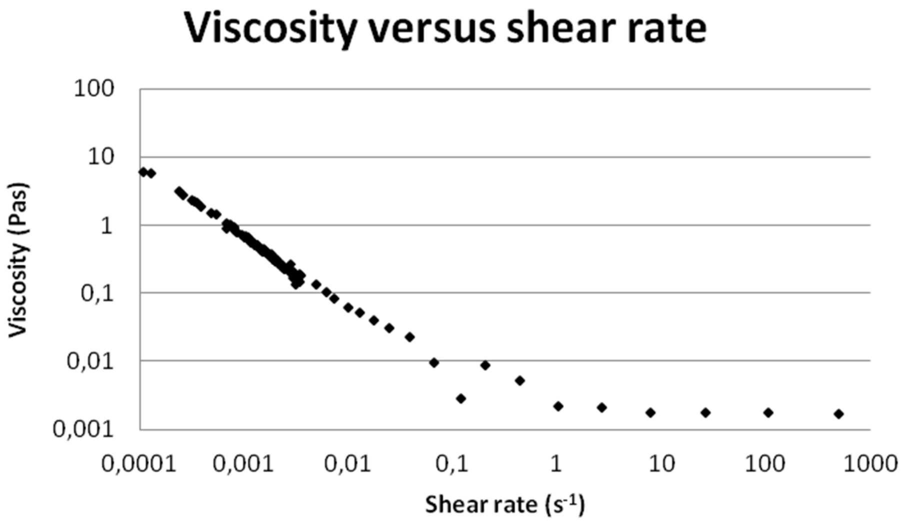

Figure 2.21 Viscosity of the TiO_2 dispersion in function of the shear rate.

Furthermore, macroscopic observations shows that the dispersion exhibit thixotropy, which is a shear thinning property. The dispersion becomes solid (gel like) after standing for several months (Figure 2.22a) but when shaking (=applying shear rate), the viscosity decreases and the dispersion become liquid again (Figure 2.22b).

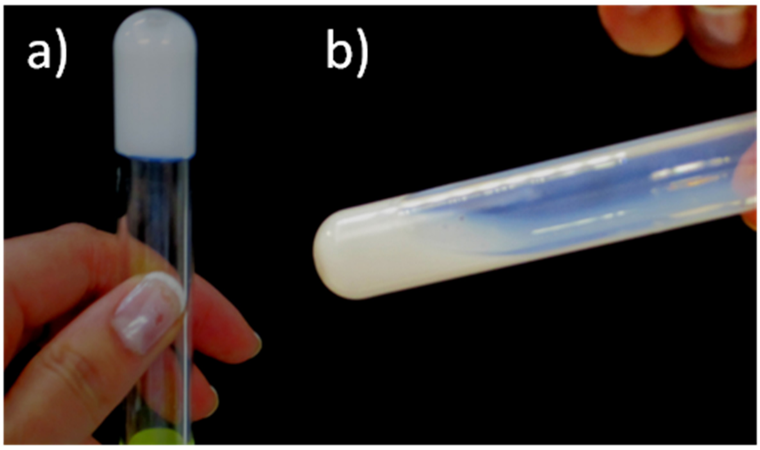

Figure 2.22 Digital photograph of the dispersion after months of standing (a) showing the thixotropic property (b).

2.6 Variation of parameters- study of mechanism[11]

Previous sections discussed the properties of the stable, aqueous TiO_2 dispersion, prepared via a two-step, low temperature hydrothermal method. It was observed that changing one of the parameters of the second hydrothermal treatment by an alternative condition didn't result in a stable dispersion, but in more a viscous, milky-like suspension which showed sedimentation after hours till days. In this section, it is discussed why only the combination of a filter dried (wet) cake, addition of TEAH as surfactant and pH directing agent and the specific hydrothermal conditions (temperature and duration) resulted in a successful stable dispersion. This study aims a more in depth study of the synthesis parameters in order to gain insight into the mechanisms behind the successful dispersion and stabilization. Each parameter of the process is studied and compared to an alternative condition to evaluate its importance in obtaining a stable dispersion.

Experimental A stable colloidal dispersion of TiO_2 nanoparticles (5-10 nm, 80% anatase) is prepared via a low temperature, two-step hydrothermal method, as described in previous sections. The simplified flow chart of the synthesis procedure is shown in Figure 2.23. Table 2.3 indicates the process parameters which are replaced in the synthesis method. Different analysis techniques are applied in order to study the mechanism of dispersion and stabilization during the second hydrothermal treatment.

---

[11] The content of this section is summarized in a manuscript in preparation entitled: "Hydrothermal dispersion and stabilization of an aqueous, colloidal titania dispersion: a mechanistic investigation".

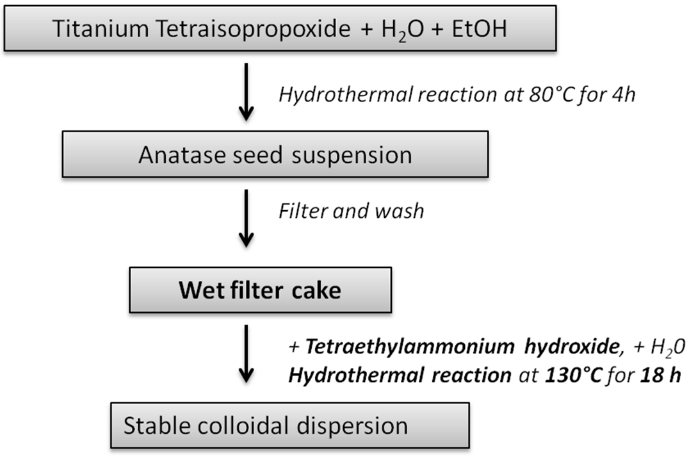

Figure 2.23 Flow chart of the synthesis of a stable colloidal TiO_2 dispersion.

Successful condition	Alternative condition
Filter dried (wet) cake	Dried cake
Hydrothermal reaction at 130°C	Reaction at 130°C under atmospheric pressure
Hydrothermal treatment at 130°C	Hydrothermal treatment at 100°C
TEAH as surfactant and pH regulator	No surfactant, NH_3 as pH regulator

Table 2.3 Overview of the process condition investigated by replacement.

First, it is observed that using a *filter dried (wet) cake* (= cake as obtained immediately after filtration) in the second hydrothermal treatment results in a successful dispersion of the particles while using a *dried cake* (obtained by drying the filter dried (wet) cake over night at 60°C) does not and sedimentation is observed. The differences between the two cakes are studied by TGA-MS analysis (Figure 2.24).

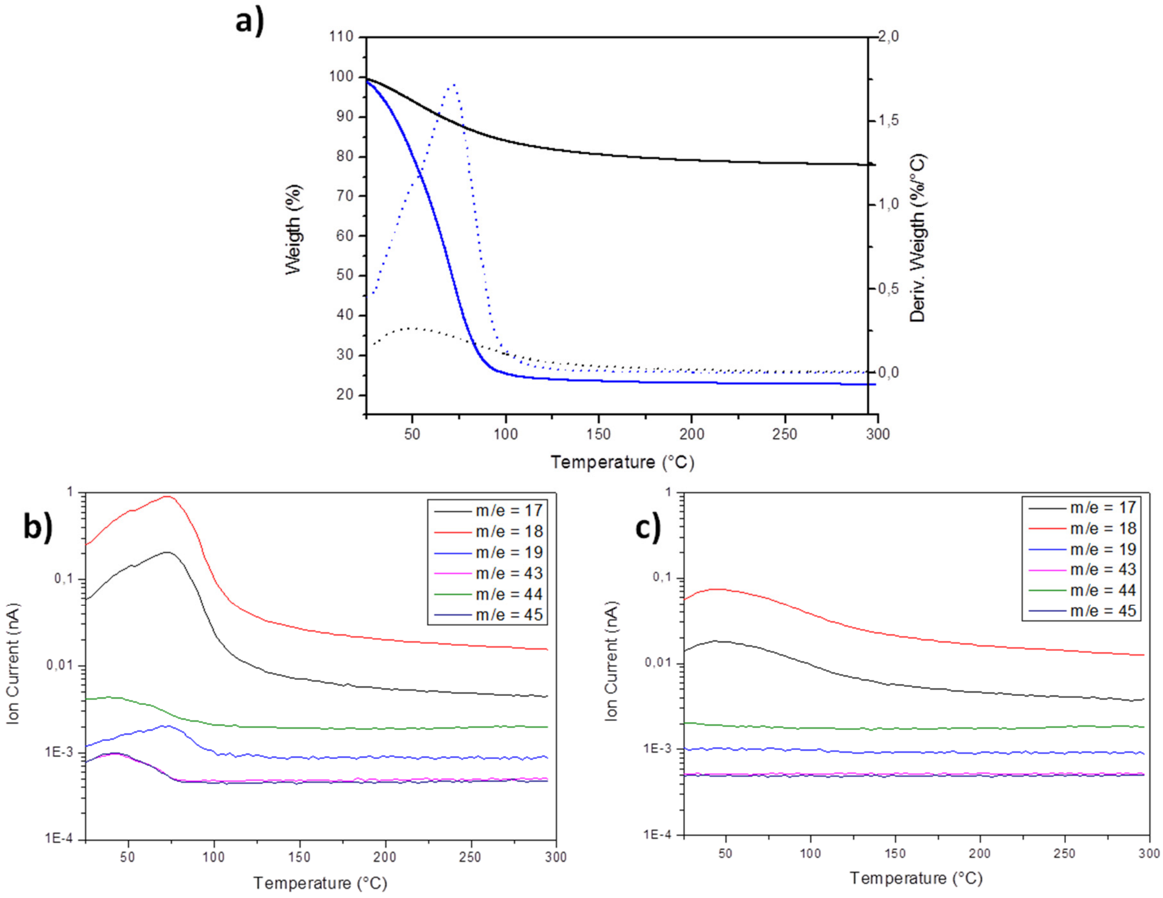

Figure 2.24 TGA-MS of the filter dried wet cake (blue curve in a) and mass spectrum in b)) and the dried cake (black curve in a) and mass spectrum in c)) obtained after the first hydrothermal treatment.

While for both *dried* and *filter dried (wet) cake* water is observed (m/e 17-18), the *filter dried (wet) cake* also contains residues of organics (m/e= 43-45). ^{1}H NMR analysis (Figure 2.25) of the TiO$_2$ dispersion, obtained using the filter dried (wet) cake in the second hydrothermal treatment, indicates the organics to be ethanol and isopropanol. These species are residues from the first hydrothermal synthesis step where ethanol is used in the medium to initiate the hydrolysis of titanium tetraisopropoxide. Residues of isopropanol found in the dispersion most likely remain on the particles surface after the first hydrothermal step due to incomplete hydrolysis [31]. Moreover the presence of fine structure in the 1D ^{1}H NMR spectrum and the lack of negative NOE's between the different resonances in the 2D NOESY spectrum (Figure 2.25c) indicate that it is likely that these organics are free in solution (not adsorbed onto the titania surface) [32]. The absence of organics in the *dried cake* can be explained by the removal of isopropanol on the nanoparticle surface by heating at 60°C due to further hydrolysis and condensation of the powder and evaporation of ethanol and isopropanol. Therefore, the unsuccessful dispersion when using the *filter dried (wet) cake* can be attributed the a higher degree of condensation, leading to a more difficult solubility/dispersibility during the second hydrothermal treatment [31]. Moreover, the difference in particle size of the *seeds* determined by TEM (6 nm) and the crystallite size obtained by XRD (4 nm), as discussed in section 2.1, may probably be caused by the unhydrolyzed groups at the boundary of the nanoparticles, leading to particles which are not fully crystallized yet.

Additionally, the presence of ethanol and a low amount of isopropanol in the dispersion can have a positive influence on the dispersibility since alcohols have the potential to decrease the surface tension in aqueous medium [33]. Furthermore, it was demonstrated that solvents with a high dielectric constant (such as ethanol) have a strong effect on the surface charge and zeta potential, thus the stability, of titania suspensions [34].

Based on the results obtained from the TGA-MS and NMR analysis and the literature, it can be concluded that the use of a *filter dried (wet) cake* in the second hydrothermal treatment resulted in a successful dispersion due to a combined effect. On the one hand, the lower degree of condensation in the filter dried (wet) cake facilitates the dispersibility while the presence of ethanol enhances the stability of the TiO_2 nanoparticles in the dispersion.

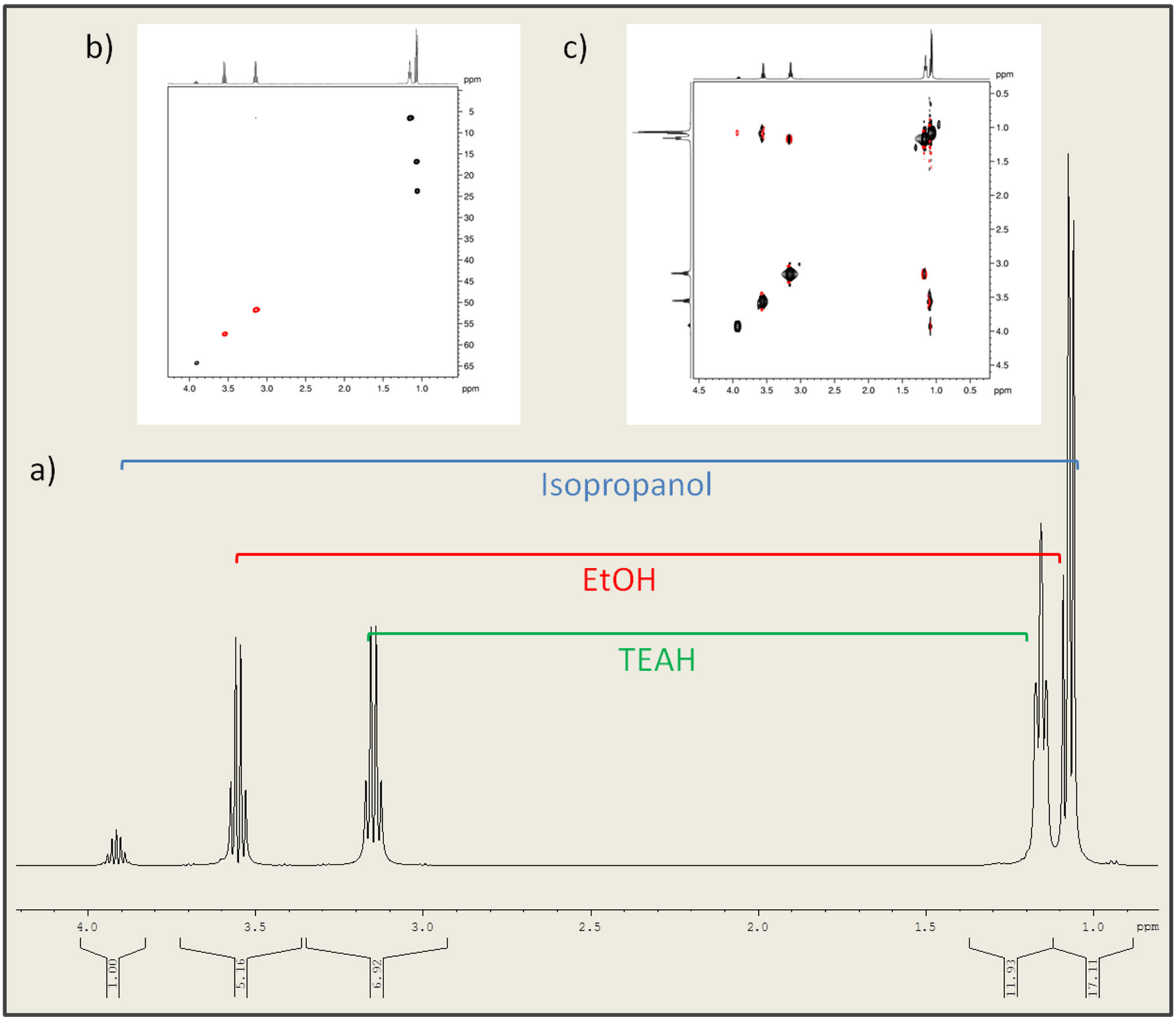

Figure 2.25 1D ^1H NMR spectrum of the TiO_2 dispersion (a) with the 2D spectra in inset (HSQC (b), and NOESY (c)).

When *replacing the hydrothermal treatment at 130°C by a reactionAT 130°C under atmospheric pressure*, a more viscous, unstable suspension is obtained, as presented in Figure 2.26. In contrast to atmospheric conditions, temperatures above the boiling point of the aqueous medium can be reached under hydrothermal conditions. To allow a good interaction of TEAH with the wet filter cake, the surface of the particles needs to be fully hydrolyzed. From the above results, it is known that the particles of the filter dried (wet) cake are not fully hydrolyzed but contain some isopropanol surface groups. Therefore, possibly, under atmospheric conditions, the isopropoxide groups are further hydrolyzed and condensed, leading to a limited amount of hydroxyl groups that can interact with the tetratethylammonium cations. Together with the more difficult dispersibility of the higher condensated powder, the insufficient stabilization due to the limited interaction between the hydroxyl groups and TEAH lead to an unstable dispersion which is macroscopically confirmed by sedimentation. While at atmospheric conditions the temperature of 130°C possibly has not even been reached due to the absence of additional pressure, the pressure present under hydrothermal conditions increases the boiling point of H_2O and seems to direct the reaction towards hydrolysis of the surface groups without too much condensation. Thus, the higher amount of hydroxylgroups, which are deprotonated in the basic medium, allows more interactions with the tetraethylammonium cations which result in a successful dispersion.

Nevertheless, applying a *hydrothermal temperature of 100°C,* these conditions seem to be insufficient to result in a stable dispersion, indicating the need for hydrothermal temperatures above the boiling point of the dispersion medium (mainly water) and the corresponding pressure. Furthermore, it was noticed that the hydrothermal duration also effects the stability, as a hydrothermal treatment for 14h (at 130°C) didn't result in a stable dispersion, indicating possible kinetic effects.

Figure 2.26 Photo of the suspension obtained after reaction under reflux (left) and the stable dispersion dispersion obtained under hydrothermal conditions (right).

The influence of TEAH in the dispersion and stabilization mechanism is studied *by replacing TEAH with NH_3* in the second hydrothermal reaction. TEAH is not only a stronger base, it is also known as a structure and phase directing agent (as discussed in section 2.4), especially for the anatase phase [7, 24, 35]. The second hydrothermal treatment in the presence of TEAH augmented the anatase crystallinity which was confirmed by quantitative analysis (section 2.4). The interaction of TEAH with the TiO_2 particles is studied with ^1H NMR. From two-dimensional Diffusion Ordered Spectroscopy (2D DOSY) NMR (Figure 2.27), it can be concluded that all observed species are small, free moving, molecules based on their high diffusion coefficients [32]. The presence of non adsorbed isopropanol also confirms the hypothesis that hydrolysis of the isopropanol groups occurs during the second hydrothermal treatment. Further, supposing a very small fraction of TEAH is adsorbed onto the particles, they can interchange with the excess of non adsorbed TEAH molecules on a very short time scale. Nevertheless, this interchange is not observed in NMR due to the absence of influence on the diffusion coefficient. As NMR analysis is not decisive, the interaction of TEAH with the nanoparticles is assumed to be electrostatic

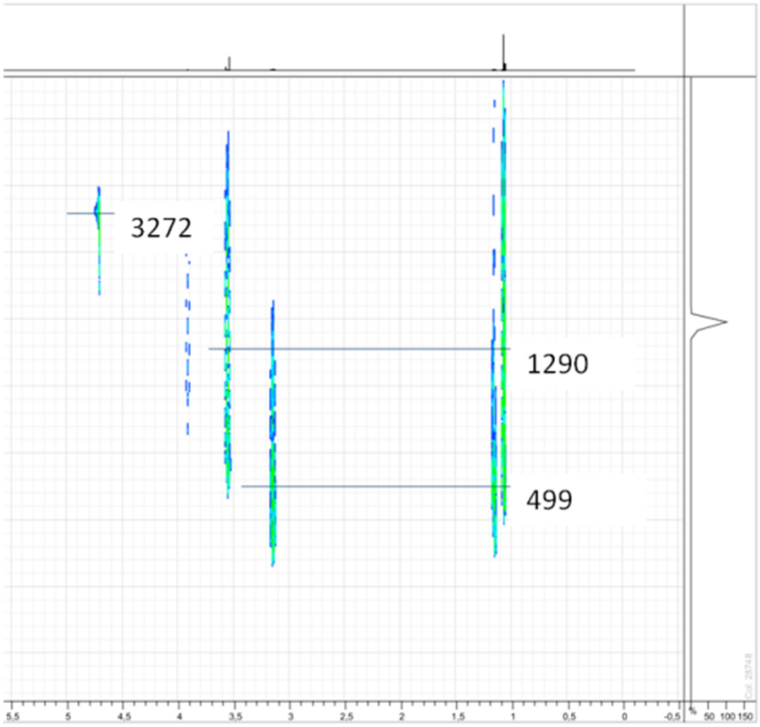

Figure 2.27 2D DOSY spectrum of the TiO_2 dispersion representing the diffusioncoefficients of water (3272 µm^2/s), ethanol (1290 µm^2/s) and tetraethylammoniumhydroxide (499 µm^2/s). (The diffusion coefficient of isopropanol is not indicated).

So far, the successful dispersion and stabilization of the nanoparticles by the combined use of a wet filter cake, tetraethylammonium hydroxide and the preset hydrothermal conditions can be assigned to complementary effects. . On the one hand, the improved dispersion can be attributed to the use of less condensated particles which have a higher dispersibility and more surface hydroxyl groups which reduced the particle agglomeration due to electrostatic repulsion (zeta potential of the dispersion is -51 mV, section 2.3) in the basic environment. The stabilization of the particles, on the other hand, is reinforced by electrostatic interactions of the negative TiO_2 with the positive tetraethylammonium cations and the high dielectric constant of ethanol in the dispersion medium.

It is known that TEAH, like other tetraalkylammonium hydroxides, decomposes into triethylamine and ethanol under thermal treatment, according to the mechanism shown in Figure 2.28 [36]. Chiesa et al used tetrapropylammonium hydroxide (TPAOH) as template for the synthesis of vanadium silicate nanoparticles dispersed onto mesoporous silica, and observed a loss of ligand upon acidification [37]. The loss of a ligand in the TPAOH template was demonstrated in Raman by a decrease in the CH_2/CH_3 ratio compared to the free template, suggesting a mixture of tripropylamine and TPAOH bound to the vanadium silicate nanoparticles. Taking this into account, in current work, it is investigated whether the hydrothermal conditions (130°C) in this work result in a decomposition of TEAH into an amine, which could be responsible for an additional hydrogen bonding causing an enhanced stabilizing effect of on the nanoparticles.

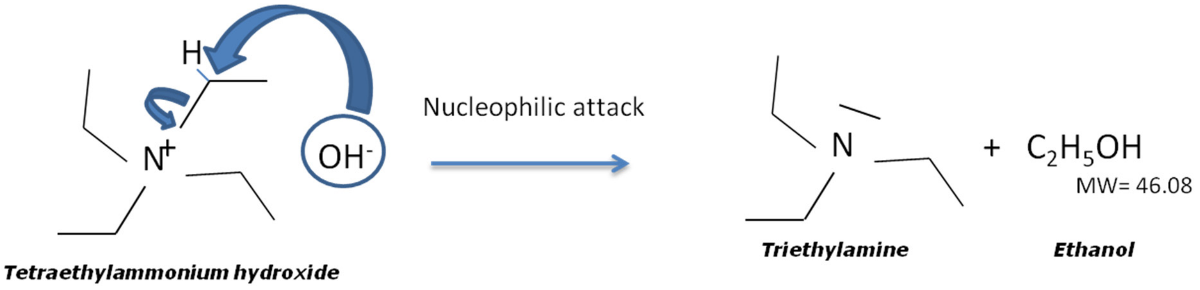

Figure 2.28 Decomposition of tetraethylammonium hydroxide into triethylamine and ethanol.

Thermogravimetric analysis (Figure 4) is applied on a TEAH solution and the TiO_2 dispersion to observe possible degradation products of TEAH.

At first sight, the TGA profile of TEAH and the TiO_2 dispersion show a comparable two step decomposition, only at different temperatures. The two step degradation in the TGA profile of the TEAH solution can be probably assigned to decomposition of TEAH, starting at a temperature around 200°C. Supposing decomposition of TEAH has occurred during the second hydrothermal synthesis, the lower weight degradation product triethylamine is expected to decompose at lower temperatures than the initial ammonium hydroxide. Nevertheless, the decomposition of TEAH under flow (TGA) is not comparable to the degradation under hydrothermal condities. Furthermore, when comparing to the thermogravimetric analysis of the dispersion, a large amount of solvent (ethanol, isopropanol and water) is evaporated in the temperature range in which the weight loss for the TEAH compound is expected. Based on these observation it can be concluded that TGA analysis is not usable.

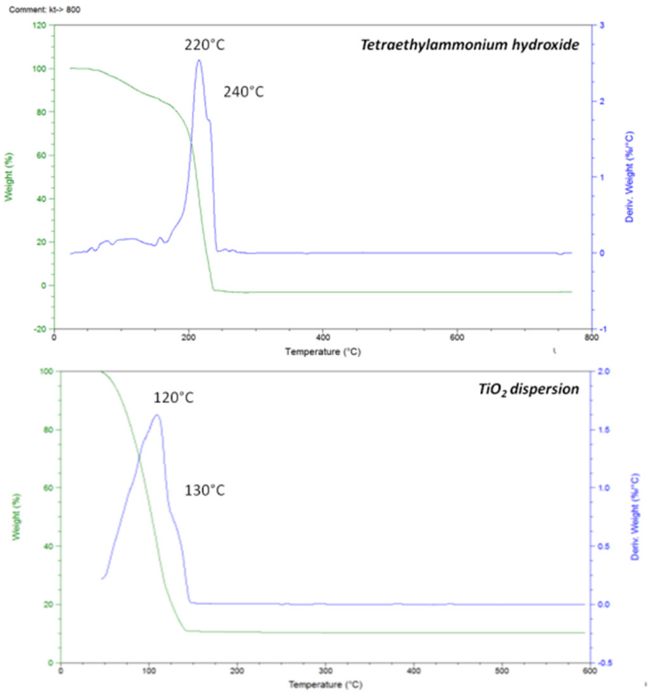

Figure 2.29 TGA profiles of tetraethylammonium hydroxide solution (20 wt%) and the TiO_2 dispersion (10 wt%).

Raman analysis (Figure 2.30) of the suspension before and after second hydrothermal treatment show a very small frequency shift (± 5 cm^{-1}) of the CH-stretching bands which indicate a small interaction of the ethyl ligands with the nanoparticles (via the N atom of the molecule). These results are in agreement with the hypothesis of the electrostatic interaction of TEAH with TiO_2 nanoparticles. The formation of triethylamine during the second hydrothermal treatment may be excluded based on the Raman analysis as the Raman shifts of the dispersion not approach the Raman shift of pure triethylamine. This is also confirmed via infrared by the absence of characteristic peaks of triethylamine in the dried dispersion (Figure 2.31), in the region between 1500 and 1000 cm^{-1} (a.o 1473, 1455, 1376, 1346, 1293, 1205, 1139, 1095 cm^{-1}, Figure 2.32). [38, 39]. The visible peaks in this region are assigned to the N-C stretching vibrations (1387 and 1177 cm^{-1}) and C-H bending vibrations (1487 cm^{-1}) of tetraethylammonium hydroxide.[40, 41].

Although the CH_2/CH_3 ratio show a decrease after the second hydrothermal treatment, it is not caused by to the formation of triethylamine (which show stretching bands at lower Raman shifts) but can probably be explained by the presence of ethanol and isopropanol in the dispersion due to the hydrolysis during the second hydrothermal treatment.

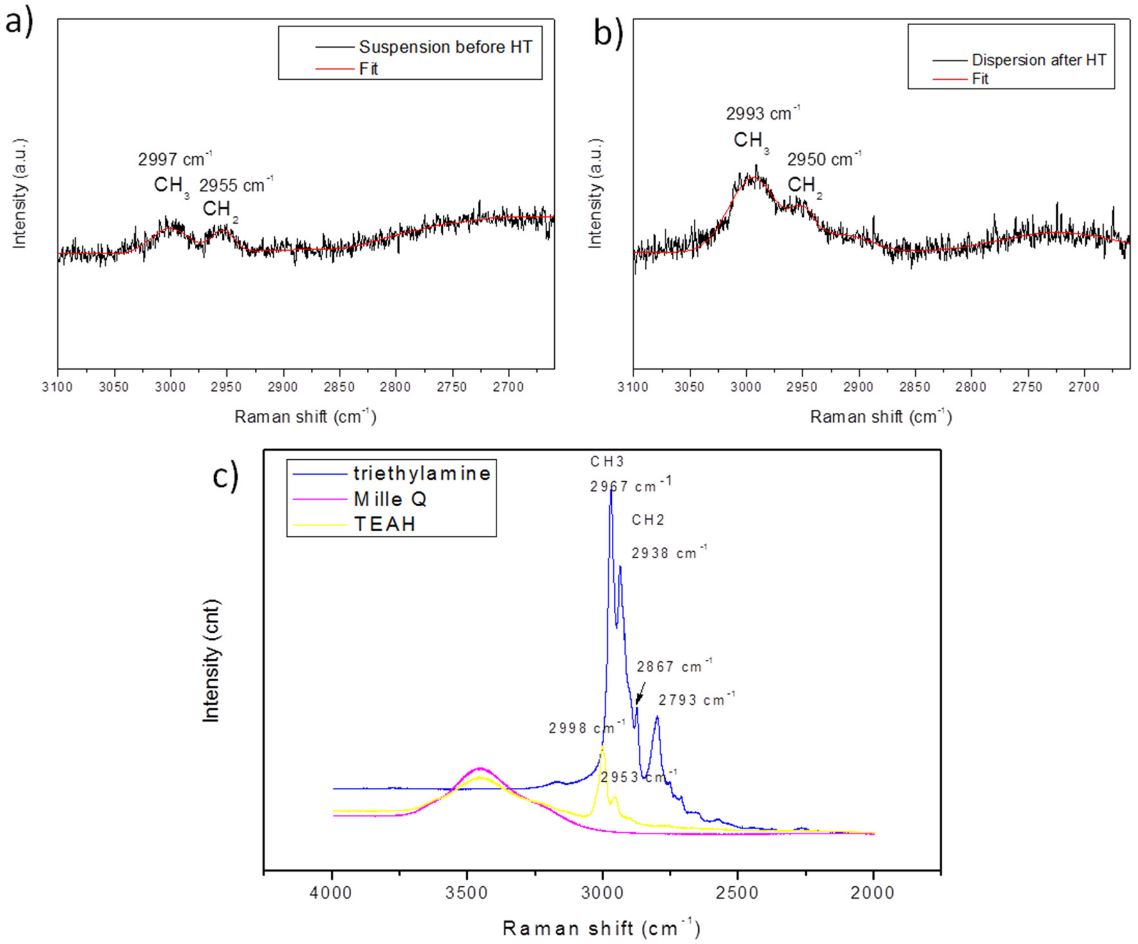

Figure 2.30 Raman spectra of the suspension before (a) and after (b) second hydrothermal treatment with the spectra of triethylamine, tetraethylammonium hydroxide and water for comparison(c).

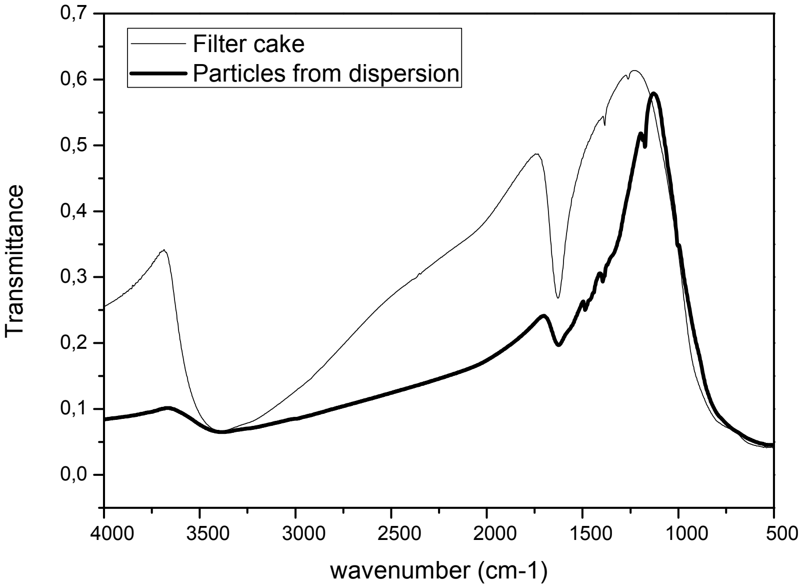

Figure 2.31 FTIR spectrum of the filter cake and the dried dispersion.

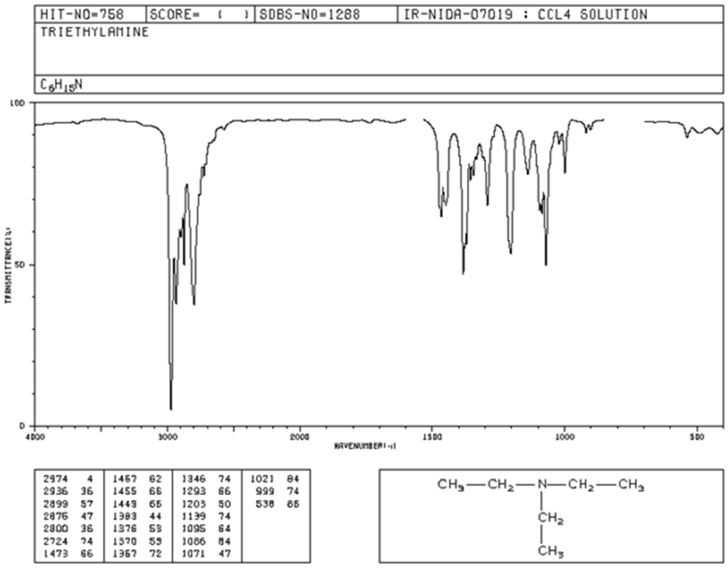
HIT-NO=758 | SCORE= ( ) | SDBS-NO=1288 | IR-NIDA-07019 : CCL4 SOLUTION

TRIETHYLAMINE

$C_6H_{15}N$

2974	4	1467	62	1346	74	1021	84
2936	36	1455	66	1293	66	999	74
2899	57	1449	65	1203	50	538	85
2876	47	1383	44	1139	74		
2800	36	1376	53	1095	64		
2724	74	1370	55	1086	84		
1473	66	1367	72	1071	47		

Figure 2.32 FTIR spectrum of triethylamine [41].

The hypothesis discussed above is resumed into a **flow chart**, given in Figure 2.33.

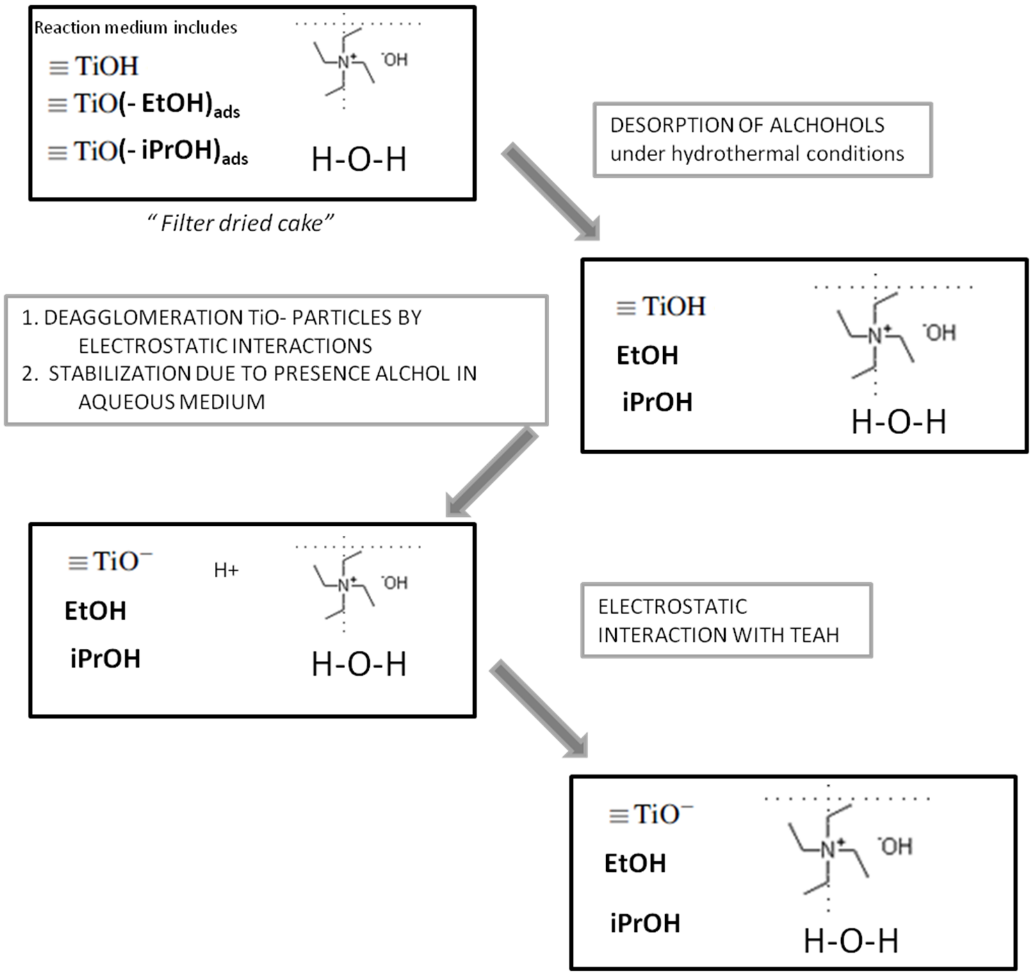

Figure 2.33 Flow chart of hypothetical stabilization mechanism of the crystallized TiO_2 nanoparticles via hydrothermal treatment with tetraethylammonium hydroxide.

2.7 Conclusion

In this chapter, the development of a stable aqueous TiO_2 dispersion starting from a pre-synthesized powder is discussed. The procedure exists of a first hydrothermal treatment for the preparation of anatase nanoseeds, followed by a second hydrothermal treatment of the freshly prepared powder in the presence of an aqueous solution of tetraethylammonium hydroxide. The dispersion obtained via this procedure shows a high stability (against sedimentation) and particles have dimensions between 5 and 10 nm, containing anatase and brookite in a 4:1 ratio. Both the stability against sedimentation and the stability against particle agglomeration has been evaluated and it was found that particle agglomeration occurs but has no pronounced influence on the dispersions' stability against sedimentation.

In addition, the parameters of the second hydrothermal treatment are studied in detail since they demonstrate to be crucial for the successful dispersion and stabilization of the particles during the hydrothermal treatment, compared to alternative conditions. Results show that only the combined use of a wet filter cake, TEAH as surfactant and pH regulator and hydrothermal conditions of 130°C and 18 h in the second hydrothermal synthesis step results in a stable dispersion of TiO_2 nanoparticles It is demonstrated that the filter dried (wet) cake still contains isopropanol and ethanol from the first hydrothermal reaction. The lower degree of condensation of the wet filter cake and the presence of ethanol in the dispersion medium after hydrothermal reaction are responsible for the enhanced dispersion and stabilization. Nevertheless, also TEAH was found to be crucial as the replacement with NH_3 as a base did not result in a stable dispersion. It is shown that no decomposition of tetraethylammonium hydroxide occurred during the hydrothermal treatment at 130°C, which confirms the role of TEAH in the stabilization of the nanoparticles. Moreover, the suggested electrostatic interaction of the surfactant with the TiO_2 surface is confirmed by spectroscopy.

In conclusion, it can be said that the obtained insights in this work may be used to expand the research towards the development of a general dispersion and stabilization method for other pre-synthesized TiO_2 nanopowders or even other metal oxide powders.

References

1. Kartini, I., Meredith, P., Diniz da Costa, J.C., and Lu, G.Q.M., A novel route to the synthesis of mesoporous titania with full anatase nanocrystalline. J. Sol-gel Sci. Technol., 2004. 31: p. 185-189.
2. Richard A. Nyquist, C.L.P., M. Anne Leugers, Handbook of infrared and Raman spectra of inorganic compounds and organic salts, 4-volume set, volume 2: infrared and raman spectral atlas of inorganic compounds and organic salts, Raman spectra.
3. Tompsett, G.A., Bowmaker, G.A., Cooney , R.P., Metson, J.B., Rodgers, K.A., and Seakins, J.M., The Raman spectrum of brookite, TiO_2 (Pbca, Z = 8). Journal of Raman Spectroscopy, 1995. 36: p. 57.
4. Yang, J., Mei, S., and Ferreira, J.M.F., Hydrothermal synthesis of nanosized titania powder: influence of peptization and peptizing agents on the crystalline phases and phase transitions. J. Amer. Ceram. Soc., 2000. 83(6): p. 1361-1368.
5. Zhang, Y.-H., Chan, C.K., Porter, J.F., and Guo, W., Micro-Raman Spectroscopy characterization of nanosized TiO_2 powders prepared by vapor hydrolysis. J. Mater. Res., 1998. 13(9): p. 2602-2609.
6. Yang, Y., Mei, S., and Ferreira, J.M.F., Hydrothermal synthesis of submicrometer a-alumina from seeded tetraethylammonium hydroxide-peptized aluminum hydroxide. J. Amer. Ceram. Soc., 2003. 86: p. 2055-2058.
7. Sharma, P.K. and Whittingham, M.S., The role of tetraethyl ammonium hydroxide on the phase determination and electrical properties of gamma-MnOOH synthesized by hydrothermal. Mater. Lett., 2001. 48: p. 319-323.
8. Späth, M., Sommeling, P.M., Van Roosmalen, A.M., Smit, H.J.P., Van der Burg, N.P.G., Mahieu, D.R., Bakker, N.J., and Kroon, J.M., Reproducible manufacturing of dye sensitized solar cells on a semi-automated baseline. Progress in photovoltaics: research and applications, 2003. 11: p. 207-220.
9. Barbé, C.J., Arendse, F., Comte, P., Jirousek, M., Lenzmann, F., Shklover, M., and Graetzel, M., Nanocrystalline Titanium Oxide Electrodes for Photovoltaic Applications. J. Amer. Ceram. Soc., 1997. 80(12): p. 3157-3171.
10. Souvereyns, B., Elen, K., De Dobbelaere, C., Kelchtermans, A., Peys, N., D'Haen, J., Mertens, M., Mullens, S., Van den Rul, H., Meynen, V., Cool, P., Hardy, A., and Van Bael, M.K., Hydrothermal synthesis of a concentrated and stable dispersion of TiO_2 nanoparticles. Chemical Engineering Journal, 2013. 223: p. 135-144.
11. Baldi, G., Bitossi, M., and Barzanti, A., Method For the Preparation of Aqueous Dispersions of TiO_2 in the Form of Nanoparticles, and Dispersions Obtainable With This Method. US patent 20080317959, (25th of december 2008).
12. Faure, B., Lindelov, J.S., Wahlberg, M., Adkins, N., Jackson, P., and Bergström, L., Spray drying of TiO2 nanoparticles into redispersible granules. Powders Technol., 2010. 203: p. 384-388.
13. Aschauer, U., Hamaker 2.1: A colloidal stability toolkit (version 2.1) [computer software]. Laboratoire de technologie des poudres, Ecole polytechnique fédérale de Lausanne, Switserland, Princeton University, USA, Retrieved May 2010: p. Available from http://hamaker.epfl.ch/.
14. Bihari, P., Vippola, M., Schultes, S., Praetner, M., Khandoga, A.G., Reichel, C.A., Coester, C., Tuomi, T., Rehberg, M., and Krombach, F., Optimized dispersion of nanoparticles for biological in vitro and in vivo studies. Particle and fibre toxicology, 2008. 5(14): p. 14-28.
15. Vicent, M., Sanchez, E., Santacruz, I., and Moreno, R., Dispersion of TiO_2 nanopowders to obtain homogeneous nanostructured granules by spray-drying. J. Eur. Cer. Soc., 2011. 31: p. 1413-1419.
16. Fazio, S., Guzman, J., Colomer, M.T., Salomoni, M.T., and Moreno, R., Colloidal stability of nanosized titania aqueous suspensions. J. Eur. Ceram. Soc., 2008. 28: p. 2171-2176.
17. Gustafsson, J., Nordenswan, E., and Rosenholm, J.B., Shear-induced aggregation of anatase dispersions investigated by oscillation and low shear rate viscometry. J. Colloid Interf. Sci., 2001. 242: p. 82-89.
18. Liddell, P.V. and Boger, D.V., Yield stress measurement with the vane, J. Non-Newtonian Fluid Mech. Journal of Non-Newtonian Fluid mechanism, 1996. 63.

19. Yang, H.-G., Li, C.-Z., Gu, H.-C., and Fang, T.-N., Rheological behavior of titanium dioxide suspensions. J. Colloid Interf. Sci., 2001. 236: p. 96-103.
20. Wolthers, W., Vandenende, D., Duits, M.H.G., and Mellema, J., The viscosity and sedimentation of aggregating colloidal dispersions in a Couette how. Journal of Rheology, 1996. 40(1): p. 55-67.
21. Aschauer, U., Burgos-Montes, O., Moreno, R., and Bowen, P., Hamaker 2: A Toolkit for the Calculation of Particle Interactions and Suspension Stability and its Application to Mullite Synthesis by Colloidal Methods. J. Dispersion Sci. Technol., 2010. 32(4): p. 470.
22. Hu, Y., Tsai, H.-L., and Huang, C.-L., Effect of brookite phase in the anatase-rutile transition in titania nanoparticles. J. Eur. Ceram. Soc., 2003. 23: p. 691-696.
23. Moret, M.P., Zallen, R., Vijay, D.P., and Desu, S.B., Brookite-rich titania films made by pulsed laser deposition. Thin solid films, 2000. 366: p. 8-10.
24. Yang, J., Mei, S., and Ferreira, J.M.F., Hydrothermal synthesis of TiO2 nanopowders from tetraalkylammonium hydroxide peptized sols. Mater. Sci. Engin. C, 2001. 15: p. 183-185.
25. Jolivet, J.P., Metal Oxide Chemistry and Synthesis: from solution to solid state. Wiley, 2000.
26. Jolivet, J.P., Cassaignon, S., Chanéac, C., Chiche, D., and Tronc, E., Design of oxide nanoparticles by aqueous chemistry. J. Sol-gel Sci. Technol., 2008. 46: p. 299-305.
27. Jolivet, J.P., Cassaignon, S., Chanéac, C., Chiche, D., Durupthy, O., and Portehault, D., Design of metal oxide nanoparticles: Control of size, shape, crystalline structure and functionalization by aqueous chemistry. Comptes Rendus chimie, 2010. 13: p. 40-51.
28. Raj, K.J.A. and Viswanathan, B., Effect of surface area, pore volume and particle size of P25 titania on the phase transformation of anatase to rutile. Indian Journal of Chemistry, 2009. 48A: p. 1378-1382.
29. Lewis, J.A., Colloidal processing of ceramics. J. Amer. Ceram. Soc., 2004. 83(10): p. 2341-2359.
30. Barnes, H.A., Rheology of emulsions- a review. Colloid and Surfaces A, 1994. 91(3): p. 89-95.
31. Hardy, A., D'Haen, J., Van Bael, M.K., and Mullens, J., An aqueous solution-gel citratoperoxo-Ti(IV) precursor: synthesis, gelation, thermo-oxidative decomposition and oxide crystallization. J. Sol-gel Sci. Technol., 2007. 44: p. 65-74.
32. Henz, Z. and Martins, J.C., A solution NMR toolbox for characterizing the surface chemistry of colloidal nanocrystals. Chem. Mat., 2013. 25(8): p. 1211-1221.
33. Meissner, H.P. and Michaels, A.S., Surface tensions of pure liquids and liquid mixtures. Industrial and Engineering Chemistry, 1949. 41(12): p. 2782-2787.
34. Yu, J.C., Jiang, Z.-T., Liu, H.-J., and Yu, J., Influence of solvatation interactions on the zeta potential of titania powders. J. Colloid Interf. Sci., 2003. 262: p. 97-100.
35. Lafjah, M., Mansour, R., Kadiri, M., Djafri, F., and Bengueddach, A., A new method for synthesis of BEA type boro-titanosilicate catalysts: dry cogel impregnation method. Bulletin of the Catalysis Society of India, 2007. 6: p. 34-41.
36. Arafat, A., Van Bekkum, H., Maschmeyer, T., and Janse, J.C., Effect of ageing on the decomposition of tetra-alkylammonium ions as studied by microwave heating. Studies in surface science and catalysis, 2001. 135.
37. Chiesa, M., Meynen, V., Van Doorslaer, S., Cool, P., and Vansant, E.F., Vanadium silicate-1 nanoparticles deposition onto the mesoporous walls of SBA-15. Mechanistic insight from a combined EPR and Raman study. Journal of American chemical society, 2006. 128: p. 8955-8963.
38. Farrokhi-rad, M. and Ghorbani, M., Stability of titania nano-particles in different alcohols. Ceramics International, 2012. 38: p. 3893-3900.
39. Pretsch, E., Bühlmann, P., and Badertscher, M., Structure determination of organic compounds-Tables of spectral data. Springer, 2009. 4th completely revised edition: p. 13, .
40. Silverstein, R.M., Bassler, G.C., and Morrill, T.C., Spectrometric identification of organic compounds. John Wiley & Sons, 1981. 4th edition(New York).
41. AIST:RIO-DB Spectral database for organic compounds, SDBS. sdbs.riodb.aist.go.jp.

Chapter 3: Deposition of nanostructures from the TiO_2 dispersion

Abstract

This chapter concerns the application of the concentrated, aqueous TiO_2 dispersion, presented in previous chapter, in combination with various deposition techniques such as spin coating, dip coating, tape casting, screen printing and soft lithography. Dependent on the applied deposition technique, different nanostructured TiO_2 films are obtained. Besides dense and porous layers, the formation of patterned films are studied, in order to increase the specific surface area of the substrate supported films. Furthermore, the importance of the process parameters are described, aiming at finding the optimal parameters for the different nanostructures and techniques. This research shows the versatility of types of films that can be prepared from one and the same dispersion. In a last section, the synthesis of TiO_2 nanorods via hydrothermal growth towards the anatase nanorods is discussed briefly.

3.1 Dense layers

The most applied deposition techniques in our research group as well as in literature for the preparation of homogeneous dense layers are spin coating and dip coating. In this work, both techniques are applied using the same TiO_2 dispersion and the results are shown and discussed below.

3.1.1 Spin coating

In our research group, a lot of experience is present for the deposition of molecular precursors via spin coating [1-7]. However, in this work, the dispersion used is a particulate precursor for which other spin conditions seem necessary, as the conventional spin conditions do not result in a macroscopic homogeneous film. The spin coat process steps applied in this work are shown in Figure 3.1. Before spin coating, the dispersion is dropped with a syringe with a filter of 0,2 µm. Si substrates are used which are cleaned before by SPM/APM [8].

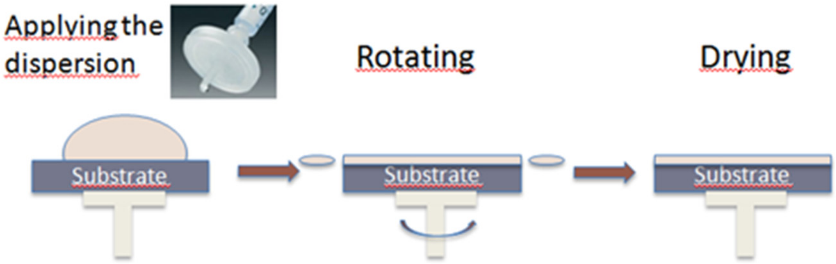

Figure 3.1 Process steps for the preparation of dense layers via spin coating.

First, different **spin velocities** are evaluated: 1000 rpm, 3000 rpm, 6000 rpm, with 3000 rpm the conventional, most applied velocity. The spin time and spin acceleration rate are 60 sec and 1000 rpm/sec, respectively. The dispensed volume (expressed in number of drops) consists of 6 drops. Only at a spin velocity of **1000 rpm**, deposition is observed by Scanning Electron Microsopy (SEM).

A thermal treatment temperature of 60°C and 300°C are chosen, based on the TGA profile of the TiO_2 dispersion (Figure 2.8). A temperature of 60°C is chosen to dry the wet film and 300°C is chosen to remove the surfactant TEAH from the film. The SEM results, given in Figure 3.2, show dense films when treated at 60°C. Increasing the thermal treatment time from 2 to 10 min for the treatment at 60°C, results in a decrease in film thickness to around 40 nm. Applying an additional thermal treatment at 300°C, further decreases the thickness and introduces porosity in the films, which should be avoided when desiring dense films.

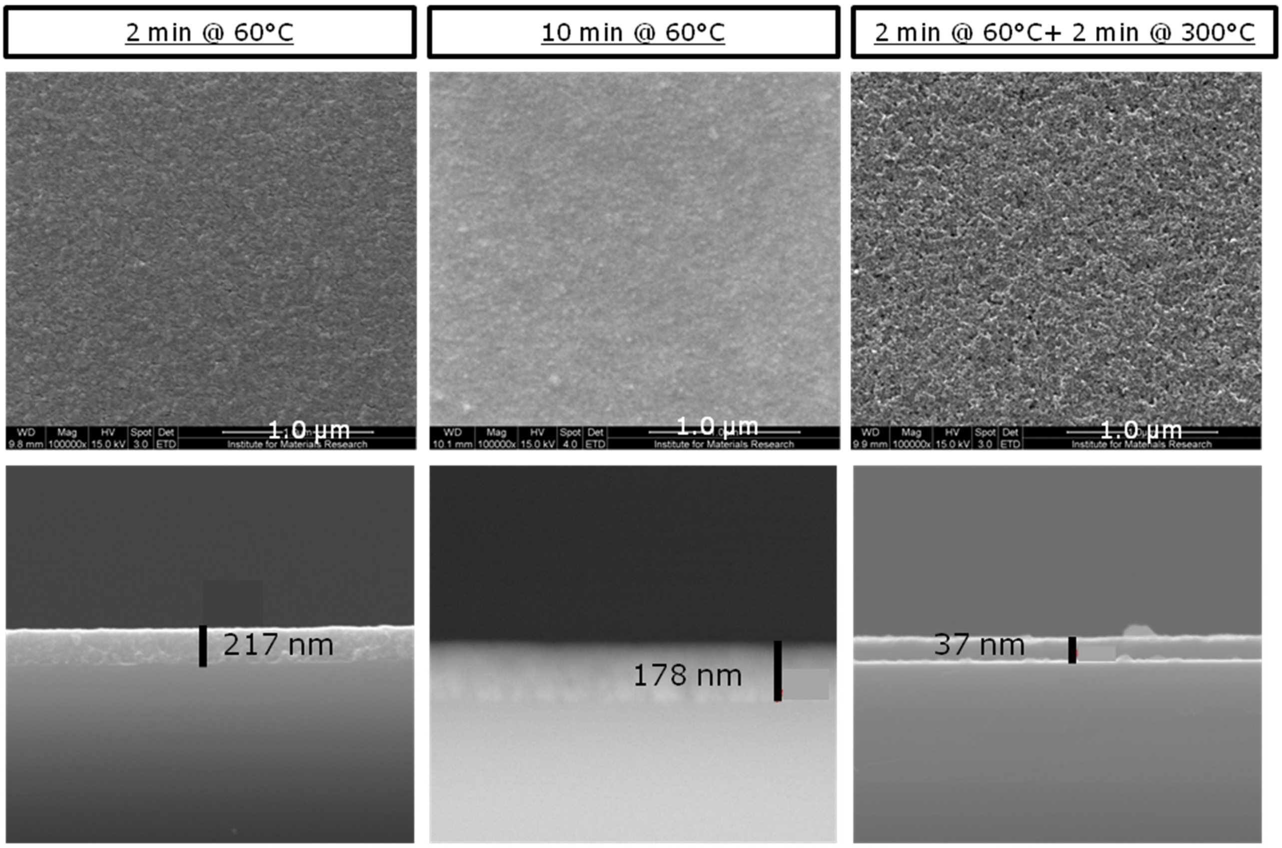

Figure 3.2 SEM images of the surface (top) and cross section (bottom) of different films deposited by spin coating at a spin velocity of 1000 rpm and thermally treated at different times and temperatures.

As we aim for layers around 100 nm, which is the required thickness of TiO_2 films in many applications, the influence of the **dispensed volume** (amount of drops) on the thickness of the films is studied. The films are prepared by spin coating 6 drops or 3 drops (=minimum amount of drops to cover the whole substrate) of the dispersion onto the cleaned Si substrates. The spin conditions are a velocity of 1000 rpm, spin acceleration rate of 1000 rpm/s and a spin time of 30 sec, followed by a thermal treatment of the wet film at 60°C for 2 minutes. Optical microscopy images of the surface of the films (Figure 3.3) already show a macroscopic difference. Both films show crack formation, with a more severe crack formation (mud cracks) for the film deposited from 3 drops of dispersion. Since a low thermal treatment temperature is used, it is more likely that these cracks are caused by the development of stress in the film as a result of a change in viscosity. As described in section 2.4 of chapter 1, during spin coating most of the suspension is flung off by centrifugal forces. The resultant thin film becomes more concentrated, due to solvent evaporation, leading to an increase in viscosity. Based on the difference in thickness of the final films (Figure 3.3), it can be said that the concentration of de *dispersed particles* in the wet film prepared from 3 drops is higher than the concentration of the *dispersed particles* in the wet film formed by 6 drops. This conclusion is based on the fact that the thickness of the final film is influenced by the solute concentration (Chapter 1, section 2.4). This demonstrates that the same amount of solvent is flung off and evaporated, whether 3 or 6 drops of dispersion are applied. Due to the lower concentration of particles in the wet film deposited from 6 drops, the viscosity of the wet film is lower than the viscosity of the wet film deposited by 3 drops. During the drying of the wet film, the viscosity increases further, leading to a rearrangement of the particles. This rearrangement causes stress between the particles in the film, which can explain the crack formation in the final film.

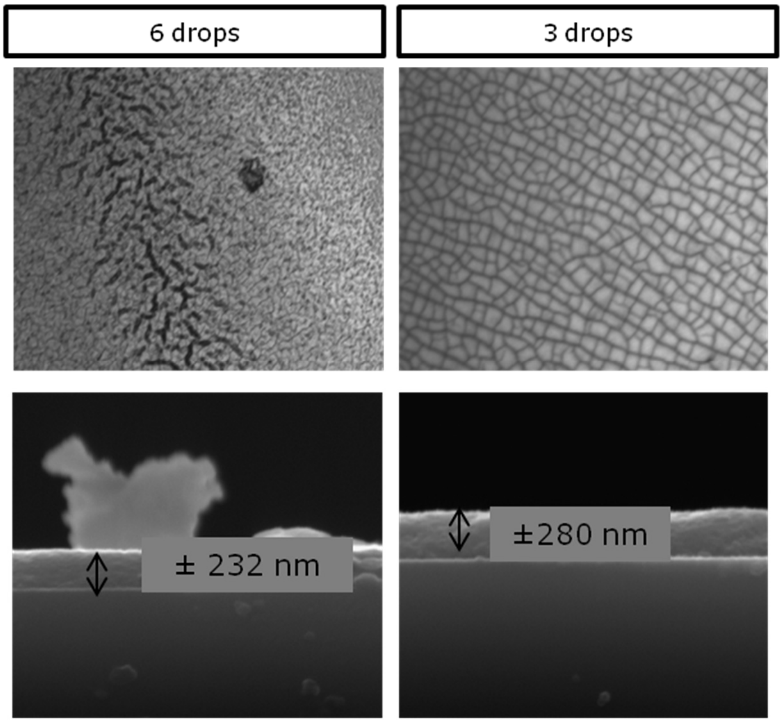

Figure 3.3 Optical microscopy images (top) and cross section SEM images (bottom) of the film prepared by spin coating a different dispensed volume.

Furthermore, the films prepared by spin coating show **edge effects** (Figure 3.4) which are caused by the accumulation of dispersion in the corners of the sample. Decreasing the amount of drops doesn’t reduce these effects (Figure 3.5). Although, the edge effects can be reduced by increasing the spin velocity (Figure 3.5), other coating **artifacts** are formed during the rotation process.

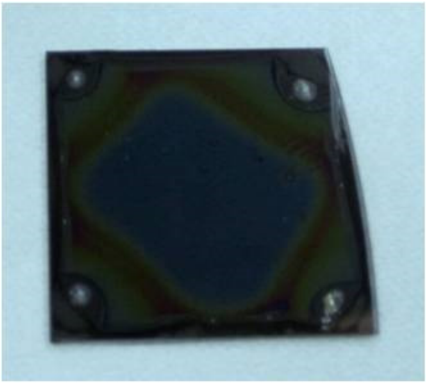

Figure 3.4 Photograph of the film by spin coating 6 drops of dispersion at 1000 rpm.

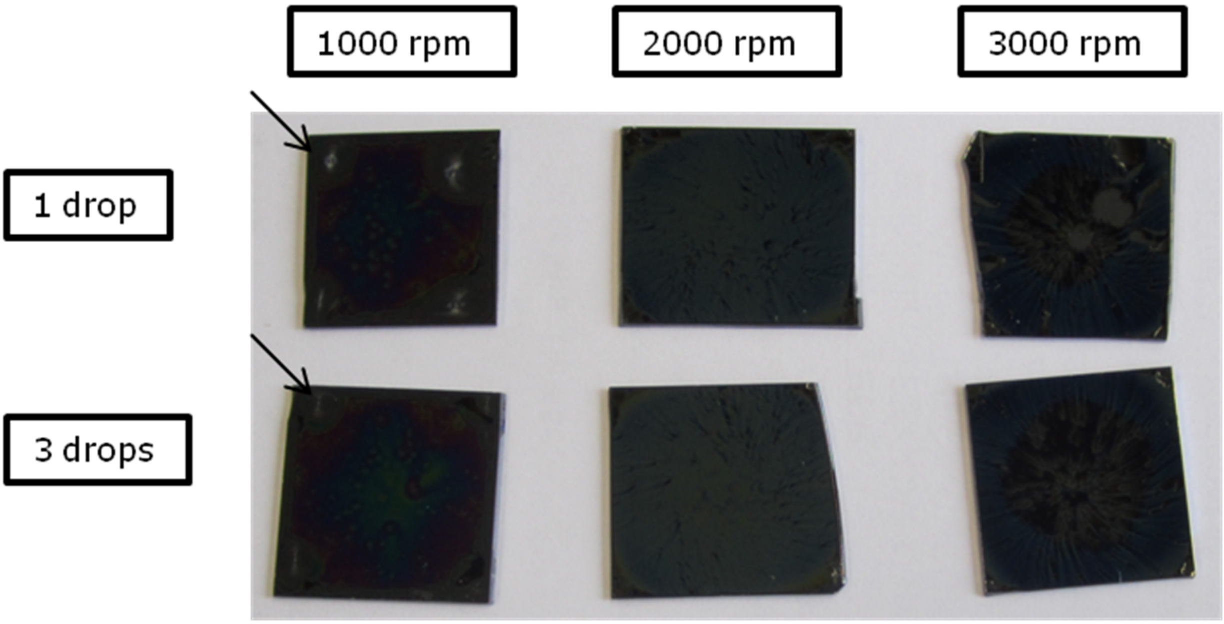

Figure 3.5 Photographs of films deposited by spin coating with 1 drop (top) or 3 drops (bottom) of dispersion at different spin speeds.

Usually, the formation of artifacts can be attributed to dust or a bad cleaning of the substrate. Nevertheless, in our work, the impact of these factors is minimized as a filter syringe is always used and the substrates are cleaned by an effective (SPM/APM) cleaning method. The observed artifacts are more known as **striations.** Striations are caused by evaporative convection, which is an instability phenomenon. Rehg and Higgins described this effect for a SiO_2 colloidal suspension in ethanol [9]. The driving force for this instability is assigned to surface tension gradients, known as the **Maragoni effect** [10]. This effect occurs in the beginning stage of the spin coating process and is mainly influenced by the spin acceleration rate. For ethanol-based systems, high spin acceleration rates are recommended to suppress the convective instability while for water-based systems, the formation of striations can be solved by decreasing the spin acceleration rate. As demonstrated in Chapter 2, section 2.6, our dispersion contains besides water, also a small amount of ethanol and isopropanol. When the dispersion is applied onto the substrate and the rotation starts, the present alcohols evaporate earlier which cause an enrichment of the water phase. The change in surface tension of the dispersion after evaporation of the alcohols may cause the instability effect. Another consequence of the solvent evaporation, is the increase of particle agglomeration. In section 2.3.1 of Chapter 2, it was demonstrated that the floatation of the alchohols, away from the rest of the dispersion, plays a role in stability of the particles, as particle agglomeration followed by sedimentation occurs. It is possible that this effect is also playing during rotation, meaning that the formed agglomerates may contribute to the formation of the striations.

Therefore, the **spin acceleration rate** is decreased till **500 rpm/s**, using a spin speed of 1000 rpm which apparently suppresses the formation of striations, as shown in Figure 3.6 (film 2).

The quality of a film can also be enhanced by increasing the **spin time**, as this condition influences the thickness of the film. The spin time in increased from 30 sec to **90 sec**, using a spin velocity of 1000 and 3000 rpm (film 2 and 4 in Figure 3.6). The film prepared at 1000 rpm still shows an improved macroscopic homogeneity (no difference in color) in the middle of the film. Increasing the spin velocity to 3000 rpm further increases the homogeneity and even minimizes the edge defects. Nevertheless, the higher spin velocity also has a negative effect on the formation of striations.

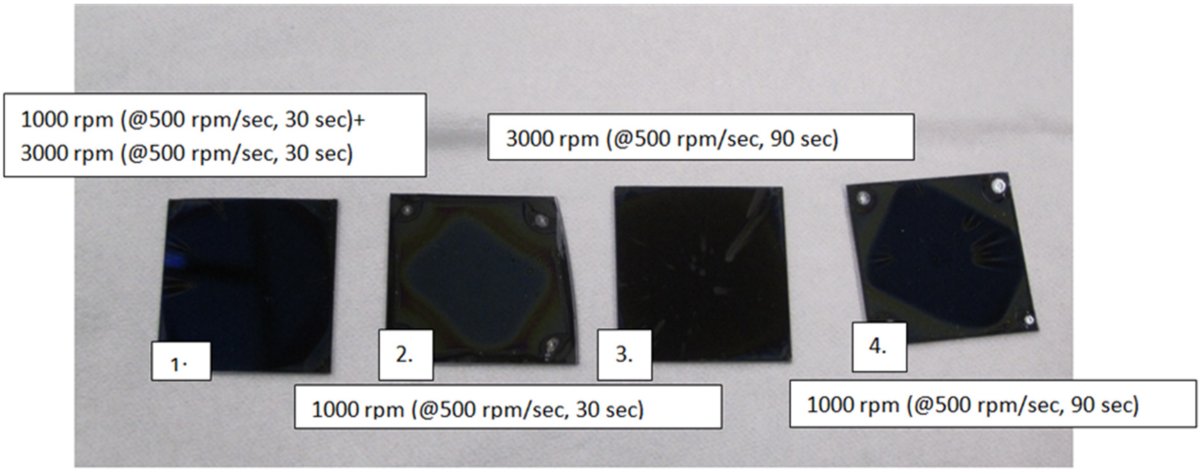

Figure 3.6 Images of films deposited by spin coating with 6 drops of dispersion at a spin acceleration rate of 500 rpm/s and different spin speeds.

From the results above, it can be concluded that using a spin velocity of 1000 rpm and a dispense volume 6 drops results in film with the **lowest crack formation**. Decreasing the spin acceleration rate from 1000 rpm/s to 500 rpm/s seems beneficial for the preparation of a macroscopic **defect free** (striations) film. Nevertheless, the use of a higher spin velocity of 3000 rpm and a prolonged spin time of 90 seconds, have a positive influence on the **homogeneity** of the film and the absence of **edge effects**. In order to combine these properties, a combined spin velocity setting is selected consisting of a first step at 1000 rpm, at 500 rpm/sec for 30 seconds, followed by a second step of 3000 rpm, at @500 rpm/sec for another 30 seconds. This combination of spin conditions results in a (macroscopically) homogeneous film with minimal edge effects and striations (Figure 3.6, film 1) and is considered here as the optimal spin conditions for the preparation of homogeneous films via spin coating the TiO_2 dispersions. The success of this spin coat set-up can be explained as follows: First the formation of striations, which occurs in the first seconds of the spin coat process, is suppressed by using a low spin velocity in the first step, combined with a low spin acceleration rate. After a few seconds, the spin velocity of 1000 rpm is reached, at which the rest of the solvent (in our case water) evaporates during rotation, increasing the viscosity of the wet film. In the next step, the spin velocity is further increased till 3000 rpm. The low spin rate allows a gradual increase of the viscosity which is stabilized during the rest of the spin time, being beneficial for the homogeneity of the film.

The **optimal experimental conditions** for the synthesis of a homogeneous, dense layer via spin coating are summarized in the following experimental frame.

> **Experimental** Si/SiO_2 substrates (with a native oxide layer of 1,2 nm) are cleaned via a SPM/APM procedure and stored in water [8]. Before dropping the dispersion onto the substrate, the wet substrates are dried by rotation at 3000 rpm (at 1000 rpm/sec, for 30 sec). 6 drops of the dispersion are applied onto the dried substrates by the use of a syringe filter of 0,2 µm. A homogeneous wet film is obtained by spin coating at a spin velocity combination of 1000 rpm (@500 rpm/sec, 30 s) + 3000 rpm (@500 rpm/sec, 30 sec). The wet film is dried at 80°C for 5 minutes, followed by a treatment at 200°C for another 5 minutes. A macroscopic image of the obtained film is shown in Figure 3.6, sample 1 and microscopic analysis of the film is given in Figure 3.7.

The thermal treatment conditions of the optimized films (= film prepared under optimal conditions as described in previous experimental) are different than applied in the beginning of this section. The reason for the decrease of the second treatment temperature is to reduce the porosity in the films, which was observed in the films treated at 300°C (Figure 3.7). The decrease in porosity of the film treated at 80°C and 200°C is not only the result of the difference in thermal treatment, but also the more optimized spin coat conditions attribute to a more dense and smooth layer (lower rms roughness).

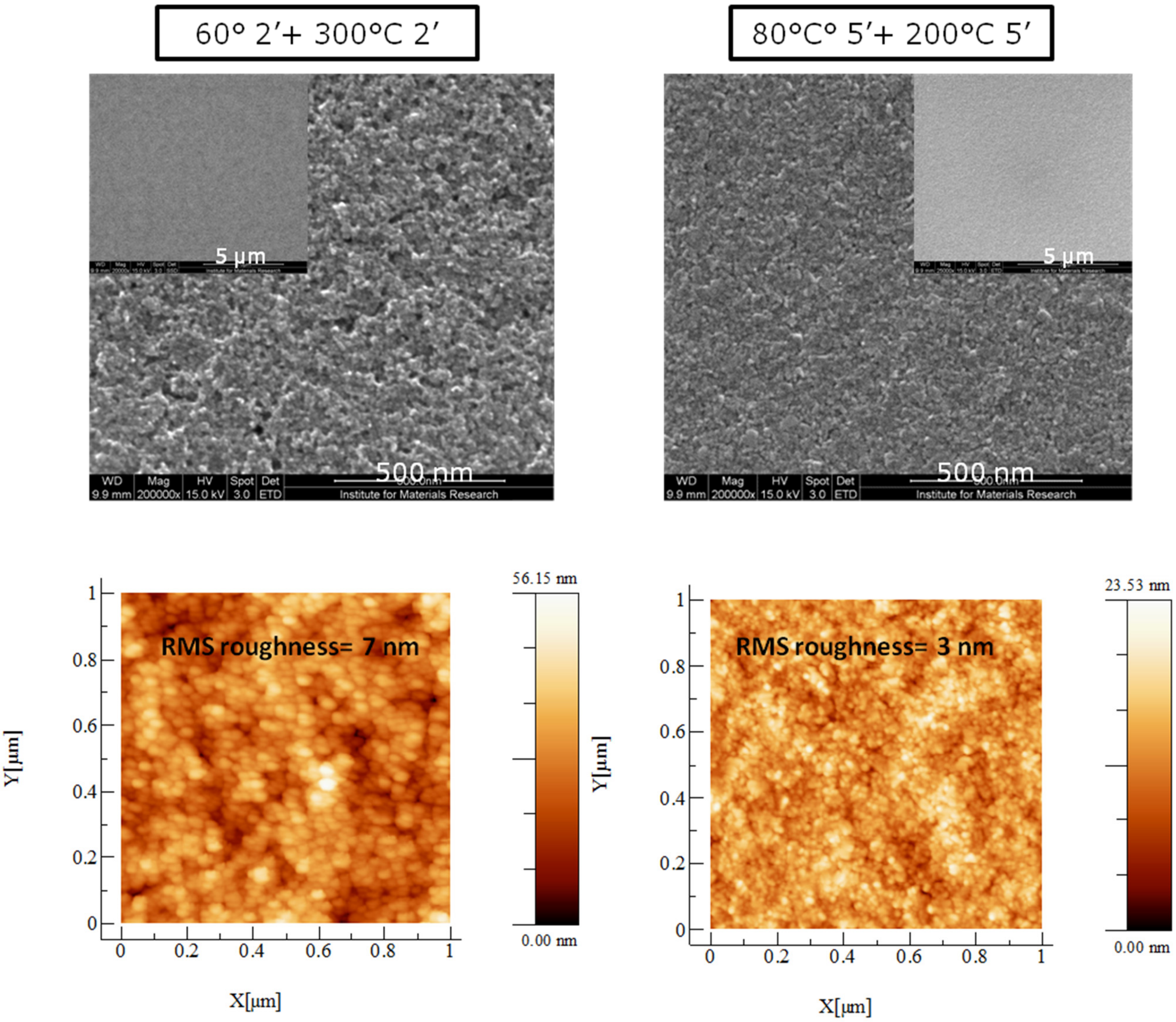

Figure 3.7 Surface analysis by SEM (top) and AFM (bottom) of (left) a film prepared by spin coating 6 drops at 1000 rpm (1000 rpm/s), thermally treated at 60°C 2′+300°C 2′ and (right) a film prepared by spin coating 6 drops at 1000 rpm (500 rpm/s)+3000 rpm (500 rpm/s), thermally treated at 80°C 5′ and 200°C 5′.

The mean thickness of a dense film prepared by optimal conditions is determined by cross section SEM (thickness determined at 3 different places at the sample), resulting in an average thickness of 95 nm, as shown in Figure 3.8.

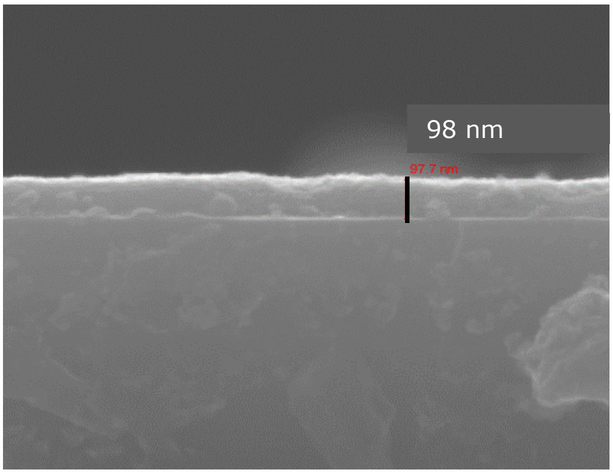

Figure 3.8 Cross-section of a dense film prepared under optimal settings.

The repeatability of the spin coating process (at the optimized conditions) in confirmed by SEM analysis of 3 different samples which are prepared using the same conditions and the same TiO_2 dispersion (Figure 3.9). The surface images of the three samples is comparable, as also the average thickness is.

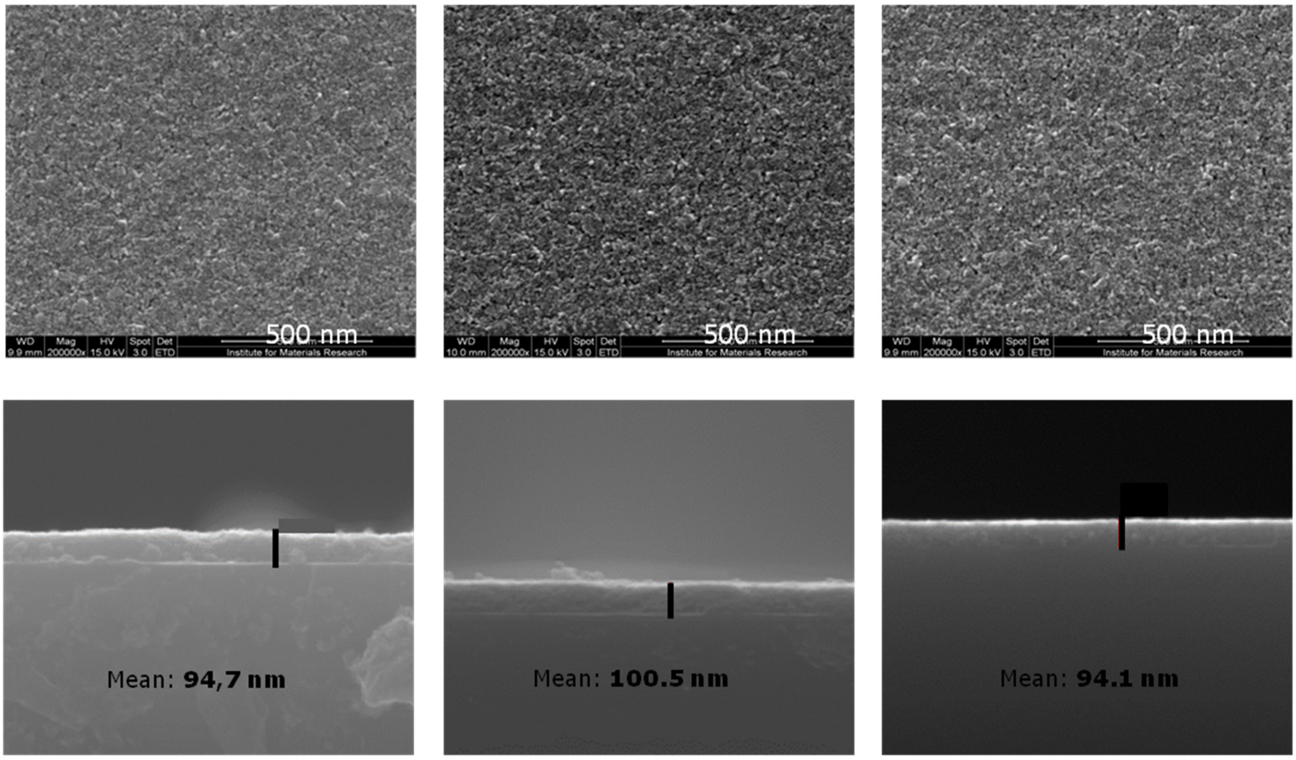

Figure 3.9 SEM of the films prepared under the same spin conditions using the same dispersion.

However, when using an aged dispersion (e.g. after a few days of standing) or a dispersion from another synthesis batch, large differences in thickness of the films are observed, although the rms roughness stays the same for all three samples. The most reasonable explanation is the difference in agglomeration between a fresh dispersion, and older (few weeks) one and another fresh dispersion, since the occurrence of particle agglomeration is demonstrated in chapter 2. Due to this repeatability issue, these films hinder the application where the thickness is important, but as we will see in Chapter 4, it not influences the performance in surface-related applications. From these results, we might question the reproducibility of the dispersion itself. However, in these experiments, the evaporation of the alcohols e.g. by using a syringe filter without cap during sample preparation, is not considered here. As discussed before, the early evaporation of solvent results in a higher start concentration or induces particle agglomeration which also influences the concentration of particles in the wet film and thus the film thickness.

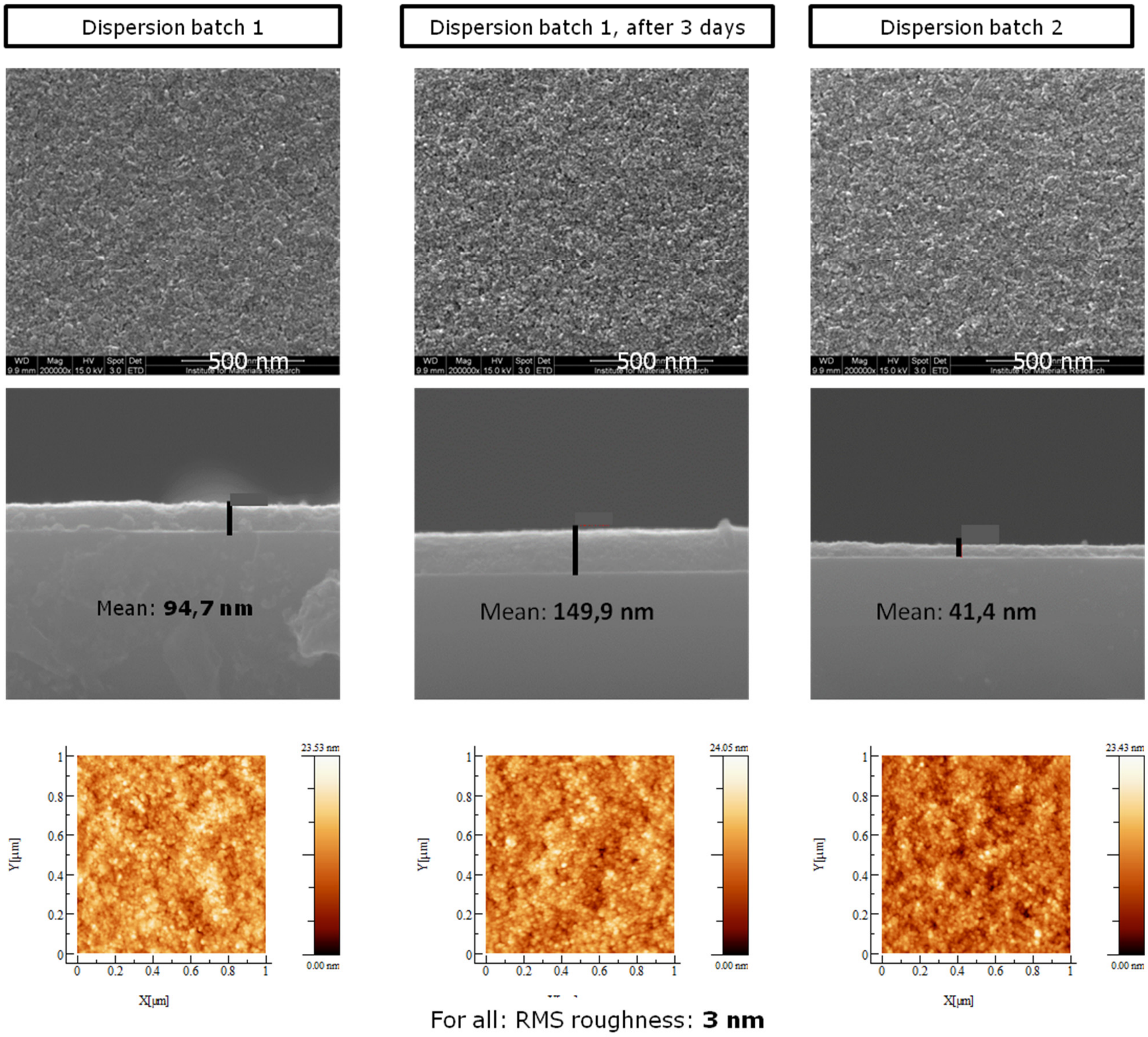

Figure 3.10 SEM images (top) and AFM analysis of films prepared via spin coating under the same spin conditions using a different batch of dispersion.

At last, it must me noted that when a diluted dispersion is used, no dense layers are obtained and the substrate is, only partially covered with agglomerates (Figure 3.11). As earlier mentioned, dilution of the dispersion enhances particle agglomeration which is clearly observed here via deposition.

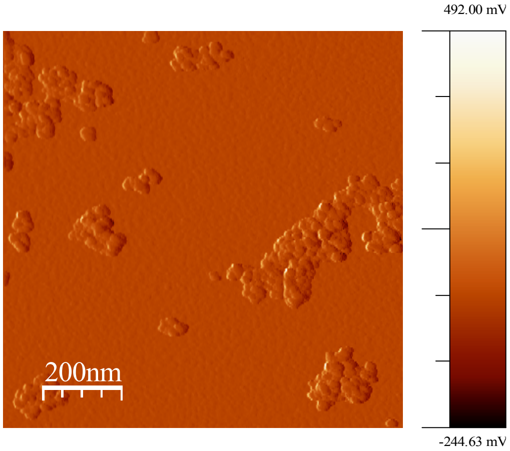

Figure 3.11 AFM image of a deposition using a diluted dispersion.

Now, what about the light absorption potential of the homogeneous, smooth TiO_2 layers?

In chapter 1, it is mentioned that TiO_2 only absorbs light in the UV region (absorption edge at 385 nm) which limits the use of TiO_2 under solar irradiation. Doping TiO_2, e.g with nitrogen [11], can extent the **absorption** response towards the visible light region, as shown in Figure 3.12. N-doped TiO_2 powder is synthesized mostly via de reaction (heating) of TiO_2 powder with a compound containing a nitrogen source, such as urea ($CO(NH_2)_2$) [11].

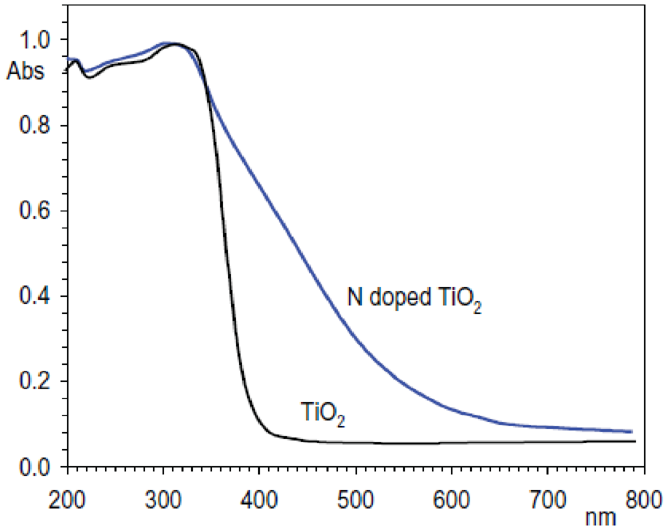

Figure 3.12 UV-VIS diffuse reflectance of TiO_2 and N-doped TiO_2 powders [11]

Since the N containing compound tetraethylammonium hydroxide is used in the synthesis of our dispersion, the spectral response in the UV-VIS region of the (undiluted) TiO_2 dispersion is analyzed first. A remarkable extension towards the visible light region (700-800 nm) is shown in Figure 3.13, although the non transparency and high concentration of the dispersion probably mislead this conclusion. As the concentrated dispersion is used for this analysis (filtered with 0.2 µm filter), the apparent absorbance is most likely caused by multiple scattering, which become more important at longer wavelengths. For low concentrated dispersions, the Rayleigh and Mie scattering theories can be applied. However, in higher concentrated samples, the interparticle spacing become less than the wavelength of the light. The interaction of the radiation fields of adjacent particles lowers the backscattering of the multiple scattering function and thus less light reaches the detector, showing an apparent high absorption Furthermore, the agglomerates in the dispersion also contribute to a larger absorbance as indicated by the white/blue color of the dispersion. Nevertheless, based on this analysis, no exclusion can be made about a possible N-doping effect.

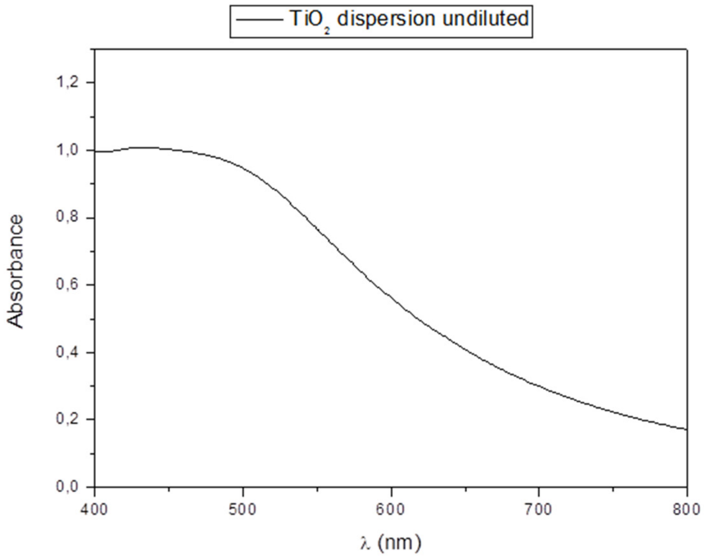

Figure 3.13 UV-VIS absorbance spectrum of the undiluted TiO_2 dispersion[1].

Since the film prepared from the TiO_2 dispersion on a glass substrate (3 drops at 1000 rpm) shows high transparency, this film is analyzed and compared to a dense film prepared by an aqueous Ti-citratoperoxoprecursor [12]. In Table 3.1, the differences of the films prepared from the TiO_2 dispersion and the citratoperoxo Ti-precursor are listed.

	TiO_2 film from dispersion	TiO_2 film from precursor [12]
Particle size	5-10 nm	20-30 nm
Film thickness	± 100 nm	180 nm
Crystal phase	Anatase and brookite	Anatase and rutile

Table 3.1 Overview of the differences in particle size, film thickness and crystal phase of the dense layers prepared from the dispersion and from the citratoperoxo Ti- precursor.

Looking to the transmission spectra of the both films, a small blue shift is observed. The repetition of waves are called interference waves which are caused by light interference [13]. Also a large difference in diffraction index between the film (±2.5) and the substrate (±1.5) causes these waves, which are therefore typical for thin films. For the film prepared from the citrate-peroxoprecursor, the interference is higher since the refractive index is possibly increased by a higher annealing temperature and a larger crystallite size [14].

The estimated band gap for the TiO_2 films from the dispersion and from the citrato-peroxoprecursor are 3.31 eV (374 nm) and 3.37 eV (365 nm), respectively. Although a blue shift refers to a quantum size effect, it can not be confirmed here for the analyzed films due to

---

[1] Measured at UHasselt by Huguette Pexten

differences in a.o. film thickness, crystallite size and phase content [15]. Moreover, the film containing larger particles show a higher blue shift which is contradictory with the expectation that smaller crystallite sizes give a larger band gap due to quantum size effects.

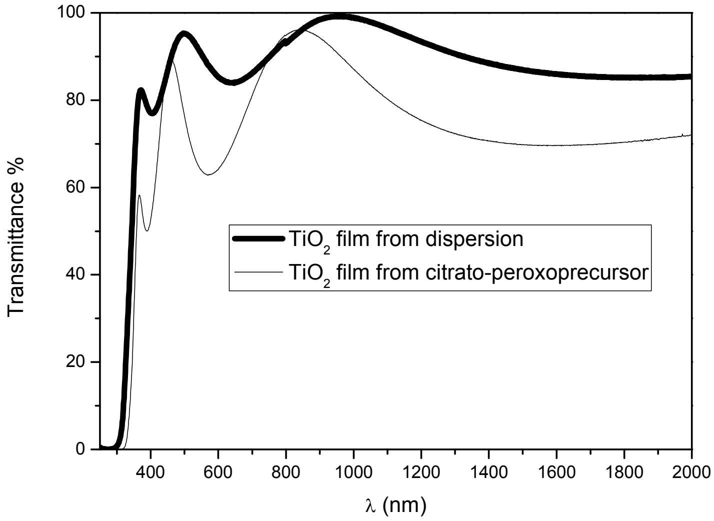

Figure 3.14 Transmission spectrum of two different TiO$_2$ dense films.

In this section, optimal conditions are found for the synthesis of homogeneous, dense films via spin coating using the TiO$_2$ dispersion. It was demonstrated that the agglomeration in the dispersion not influences the surface properties of the film. Nevertheless, the difference in degree of agglomeration (due to evaporation) in the dispensed volume certainly determines the thickness of the films which may be important for some applications.

3.1.2 Dip coating

Another frequently used technique for the preparation of smooth and dense layers is dip coating, shown in Figure 3.15. This section is intended to show the potentials of the use of the dispersion in combination with dip coating, without going into detail into the mechanisms and theoretical background of the process.

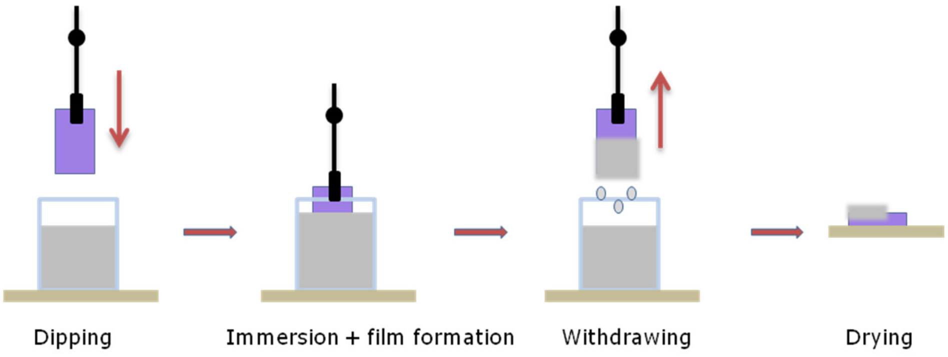

Figure 3.15 Process steps for the preparation of dense layers by dip coating.

Experimental A SPM/APM cleaned Si substrate is immersed in a filtered (0,2 µm) dispersion with a dipping velocity of 1 mm/min (dipping and withdrawal speed) and a immersion time of 30 sec. The wet film is thermally treated at 60°C for 2 minutes, followed by a treatment at 300°C for another 2 minutes.

As observed in Figure 3.16, the film prepared by dip coating contains some dense covered parts (inset Figure 3.16) but in general the film is not fully continuous and more rough as those prepared by spin coating. The evaporation of solvent (at room temperature), the subsequent particle agglomeration, the thermal treatment at 300°C, all may contribute to the formation of defects in the film and a higher rms roughness.

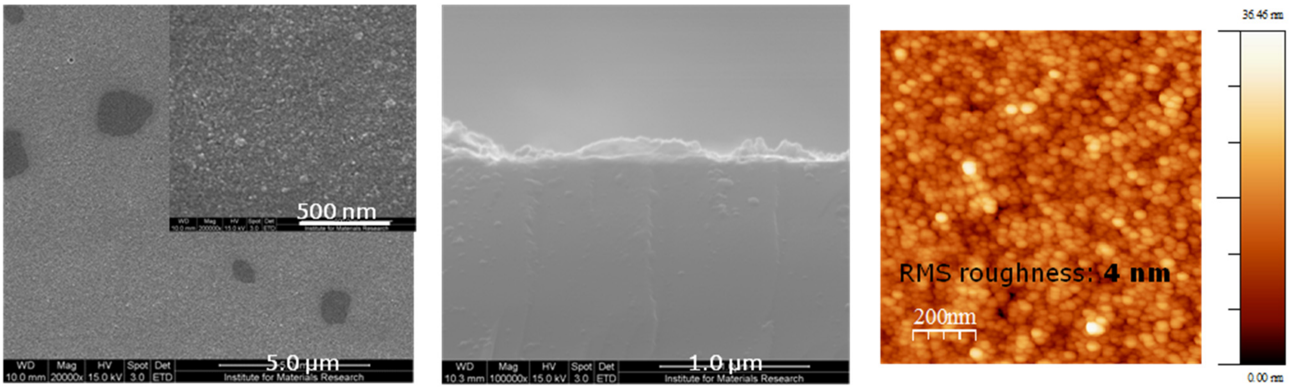

Figure 3.16 SEM and AFM analysis of a deposited film via dip coating at 1 mm/min and thermally treated at 60°C 2’ and 300°C 2’.

When the films are only thermally treated at 60°C (Figure 3.17), the coverage is not improved, even not at a higher treatment time.

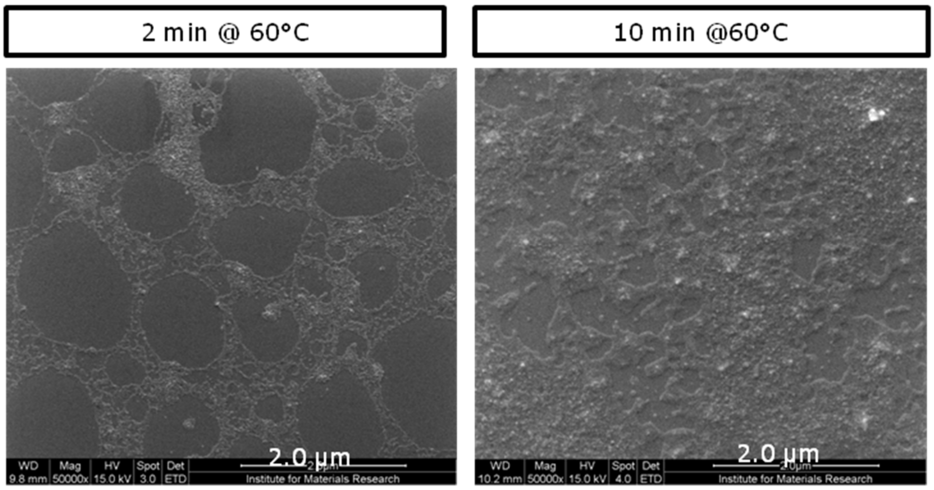

2 min @ 60°C

10 min @60°C

Figure 3.17 SEM images of the surface of TiO_2 films deposited by dip coating (1mm/min), at thermally treated at 60°C for 2 or 10 minutes.

From the above results, it is clear that other factors influence the coverage of the substrate. It is possible that the same effects, which introduces striations in the film during spin coating, are playing during the withdrawal, which occurs very slow (1 mm/min). The evaporation of solvent (alcohols or water) during the withdrawal, changes the surface energy of the wet coating and induce concentration gradients.

To minimize the possible effect of evaporation and concentration gradient during withdrawal of the substrate, the dipping velocity is increased to 10 mm/min (both dipping as withdrawal). Compared to the deposition at a lower dipping speed, the coverage is enhanced and a very thin layer with an average of 30 nm obtained (Figure 3.18).

Another reason for the improved coverage could be found in the decreased viscosity of the coated film during withdrawal. The characteristic shear rate of a typical dip coating process is 10^1-10^2 s^{-1} [16], at which the viscosity of the TiO_2 dispersion and the particle-particle interactions are low, as shown in section 2.5 of Chapter 2, leading to an enhanced coverage of the substrate. In this work, only very small substrates (1 cm x 2 cm) can be applied for dip coating due to the low volume of dispersion (±20 ml) that is yielded from one synthesis. Therefore, spin coating is preferred for the deposition of homogeneous films.

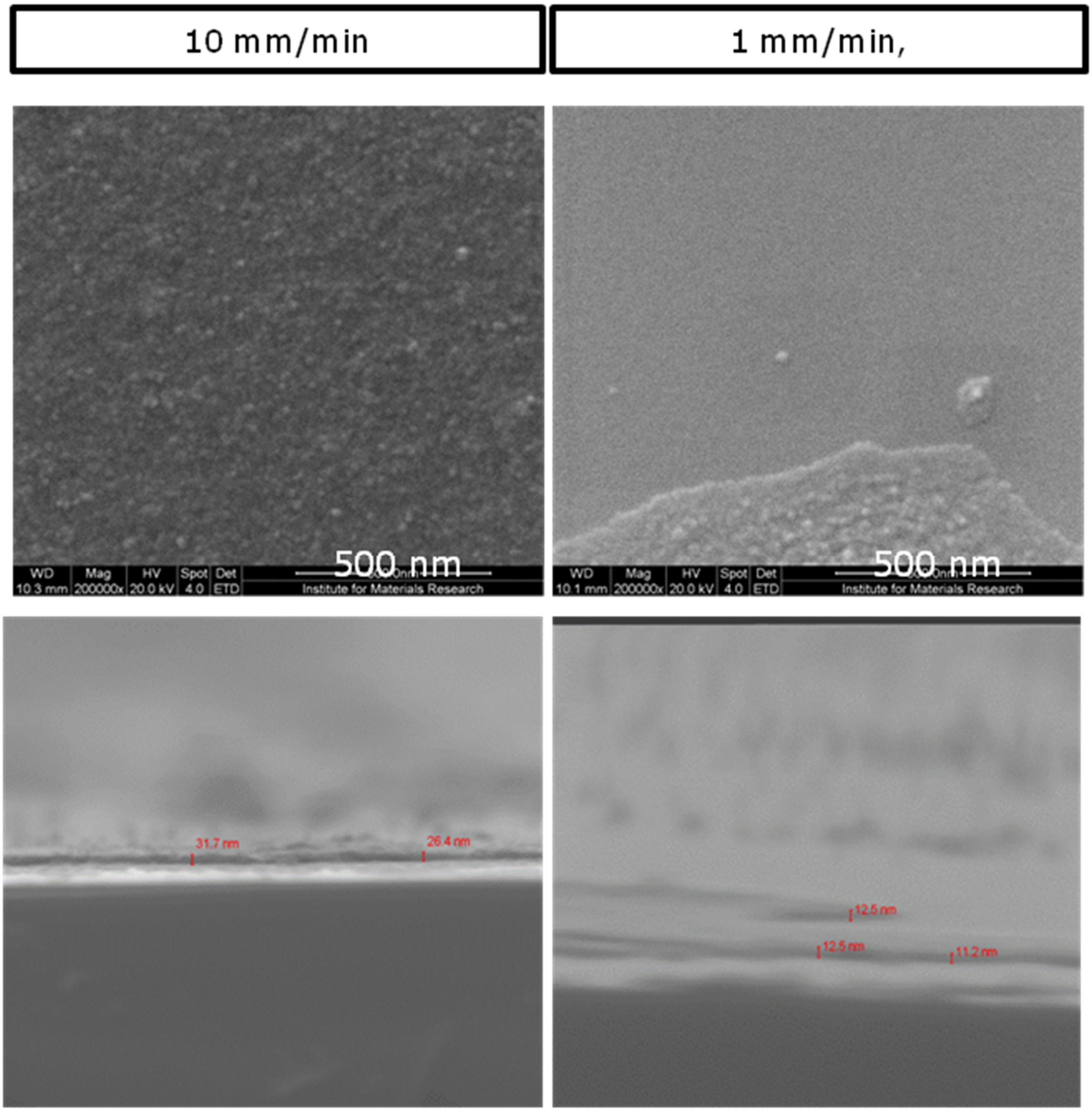

Figure 3.18 SEM images of films deposited by dip coating at a different velocity, thermally treated at 60°C for 10 min.

3.2 Porous layers by tape casting

In order to prepare thick (meso)porous layers, tape casting is applied as deposition technique and represented in Figure 3.19. A critical step in the preparation of uniform layers by tape casting, is the preparation of a stable, well dispersed slurry [17]. The stable TiO_2 dispersion of this thesis is therefore an ideal candidate, although the viscosity of the dispersion is quite low. To increase the viscosity, the additive hydroxypropylcellulose (HPC) is selected as thickener and pore forming agent, based on the results of Beusen et al. [18], different concentrations of HPC-dispersion mixtures are prepared. As in this section, the potential use of the dispersion and selected additive(s) is tested, tape casting is carried out by hand, although the automatic equipment is available in our lab.

Experimental A 5wt%, 10 wt% and 20 wt% solution of HPC (MW~100 000 g/mol) and TiO_2 dispersion (fresh) is prepared by first dissolving 0,5 g, 1 g and 2 g HPC in 4ml of water, respectively. Then this mixture is added drop wise to 4 ml of TiO_2 dispersion (10 wt%, filtered with 0.2 µm syringe filter) while stirring. This suspension is stirred for another 24 h before using it for deposition. Then 4 drops of the HPC-TiO_2 suspension are applied on a cleaned glass substrate and smeared (at ± 1 cm/s) with another glass substrate, using the thickness of scotch tape (60 µm) as guidance (thickness definer). The cleaning of the substrates consist of a more soft cleaning consisting of the next three steps: 5 min ultrasonic immersion in isopropanol, 5 minutes ultrasonic immersion in water followed by a UV-O_3 treatment at 50°C for 20 minutes. Before UV treatment, the substrates are dried under a nitrogen flow. After tape casting, the films are dried at room temperature for 3 days followed by a thermal treatment of 5 minutes at 150°C, 5 minutes at 300°C and 5 minutes at 450°C.

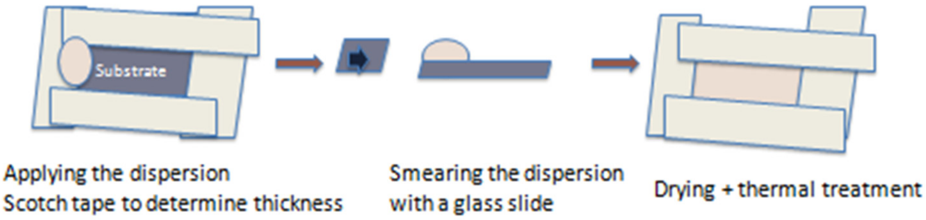

Figure 3.19 Representation of the (manual) tape casting procedure.

Thermogravimetric analysis of a HPC-TiO_2 suspension shows that all organics are burned out at 450°C (Figure 3.20). A gradual increase in thermal treatment is applied to reduce possible breaking of the used glass substrates by thermal shock.

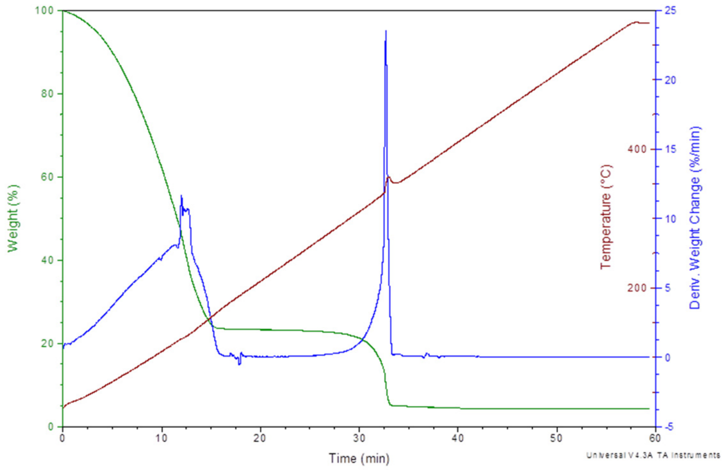

Figure 3.20 TGA profile of the 20 wt% HPC-TiO_2 suspension from room temperature till 600°C, at 5°C/min in dry air.

The films obtained from tape casting the 5 wt%, 10 wt% and 20 wt% HPC-TiO_2 suspension are shown in Figure 3.21. For all concentrations of HPC, a porous film is obtained. The pores are not homogeneously distributed and not equally sized (50-100 nm, 100-500 nm, > 500 nm). A cross-SEM image of a film prepared from a 20 wt% HPC-TiO_2 suspension shows that the pores are present throughout the whole layer and the layer has a thickness of ± 6 μm (Figure 3.22). Depending on the aimed application, the thickness and pore size determines the usability of these layers. For example in dye-sensitized solar cells, the aimed thickness of the porous layers is 10 μm, with interconnected pores, preferably mesopores.

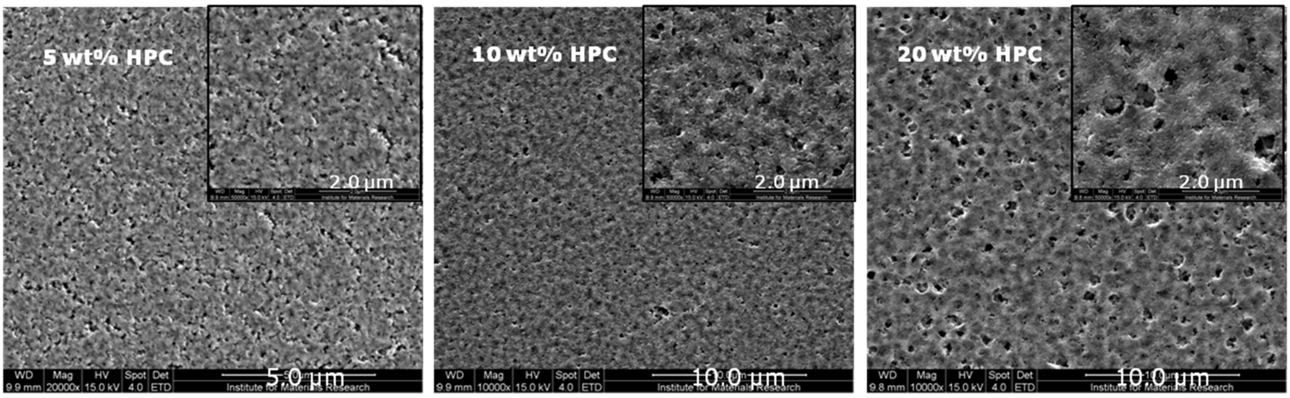

Figure 3.21 SEM analysis of the porous films prepared by tape casting different concentrations of HPC-TiO_2 suspension.

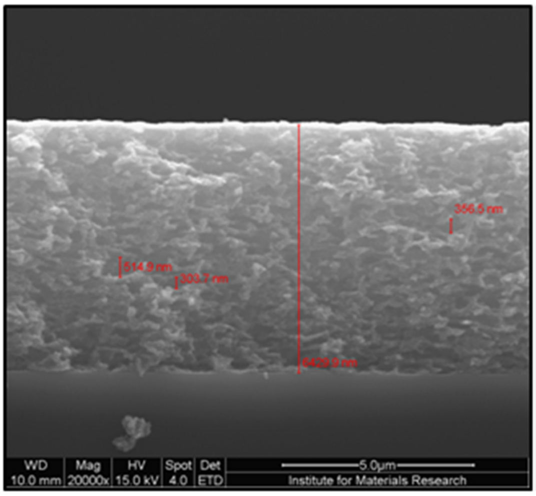

Figure 3.22 Cross-SEM of a porous layers prepared by tape casting a 20 wt% HPC-TiO_2 suspension.

For a more quantitative study of the pore sizes and pore volume, gas adsorption analysis is applied. The principle is the same as for the N_2 sorption analysis on powders, only another gas, Krypton at 87K, is used because of the lower material available as films, compared to powders. The porous layer obtained from a 10 wt% HPC-TiO_2 suspension, with a thickness of 600 nm measured by DEKTAK, is analyzed by Kr sorption.

The adsorption isotherm of this sample, given in Figure 3.23, shows the absence of capillary condensation, i.e. small increase in relative pressure causes a large increase in volume (as shown in Figure 2.19. in section 5 of chapter 2). A more flat adsorption branch is observed which is attributed to the broad pores size distribution and high fraction of pores larger than 14 nm[2]. Only the smaller pores are filled during the measurement while the very large pores are not filled yet.

---

[2] At a relative pressure of 0.73, the volume of Kr correspond to a pore size of 14 nm.

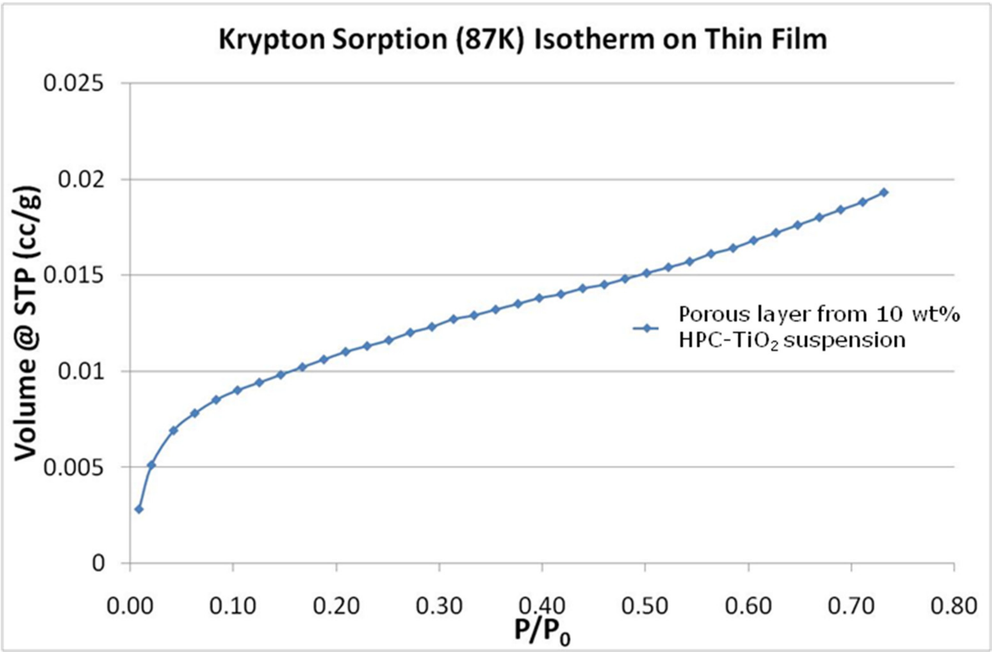

Figure 3.23 Krypton adsorption isotherm on a porous film prepared by tape casting a 10 wt% HPC-TiO_2 suspension.

At a relative pressure of 0.73, the pore volume of pores smaller than 14 nm is 2.77 x 10^{-5} cc/g. The calculated specific surface area of the porous layer (pores larger than 14 nm not included) is then calculated to be 67.6 m^2/g , which is equal to 285 m^2/cm^3. The calculations are given in the appendix. It is clear that only the pores formed by the nanoparticles are measured and not the pores formed by HPC since these molecules form larger pores than 50 nm. As in literature, the specific surface area of TiO_2 films is mainly determined by N_2 sorption [19, 20], no comparison with our results can be made so far.

To verify if the thermal treatment at 450°C (temperature needed to fully remove HPC) influenced the anatase crystallinity, Raman Spectroscopy is applied on porous layers prepared on glass and silicon. Even at a prolonged treatment at 450°C for 60 minutes, no other peaks than characteristic for anatase are observed (Figure 3.24). Rutile has characteristic peaks at a Raman shift of 446 and 611 cm^{-1} [21], which clearly lack in the spectra.

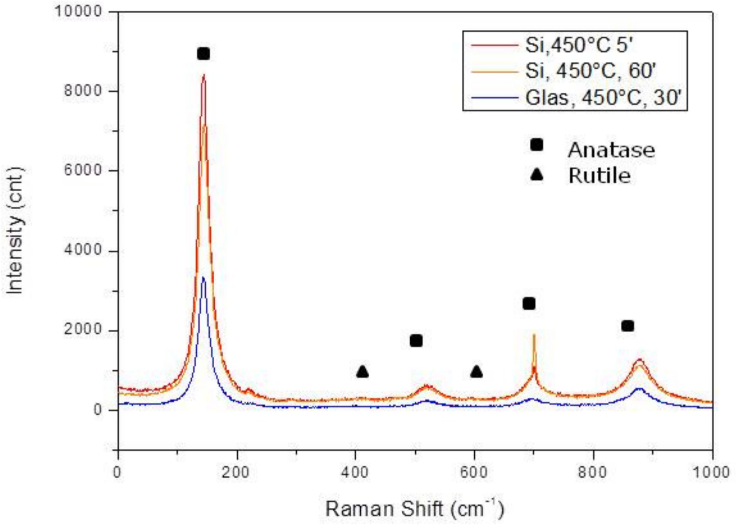

Figure 3.24 Raman spectra of porous layers prepared from a 10 wt% HPC-TiO_2 suspension**.**

The SEM image of a porous film treated at 450°C for 30 minutes is shown in Figure 3.25 (left). No densifications seems to occur at a prolonged thermal treatment at 450°C. Nevertheless, when treated at a higher temperature for a longer time, at 600°C for 60 minutes, a small increase in particle size occurs (Figure 3.25 right), indicating crystal growth at temperatures around 600°C.

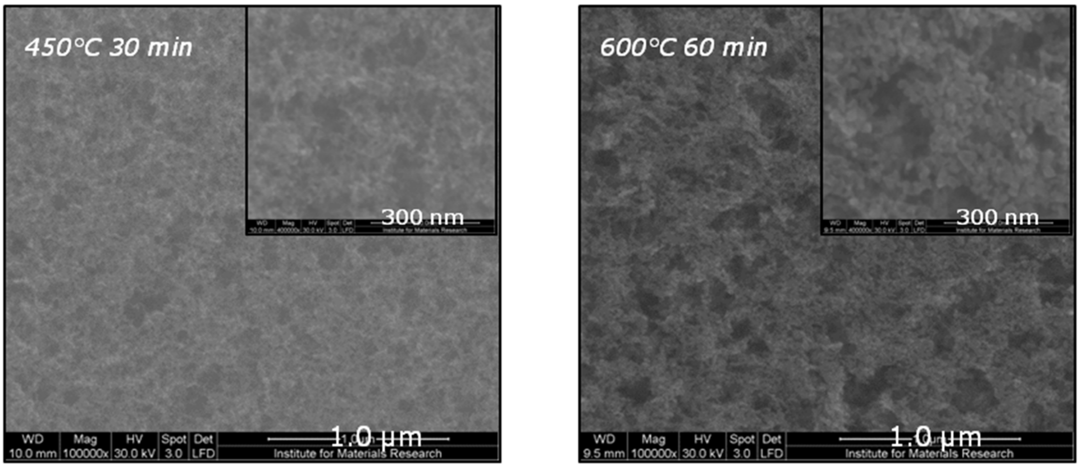

Figure 3.25 SEM images of porous films treated at different temperatures and time.

It may be clear that HPC as a pore forming agent, in this work, gives randomly distributed, large pores. Other pore forming agents are tested o.a. Pluronic P123 and PEG 400 in order to introduce smaller pores. The best results, concerning homogeneous and crack-free films, are obtained when using PEG 400, shown in Figure 3.26.

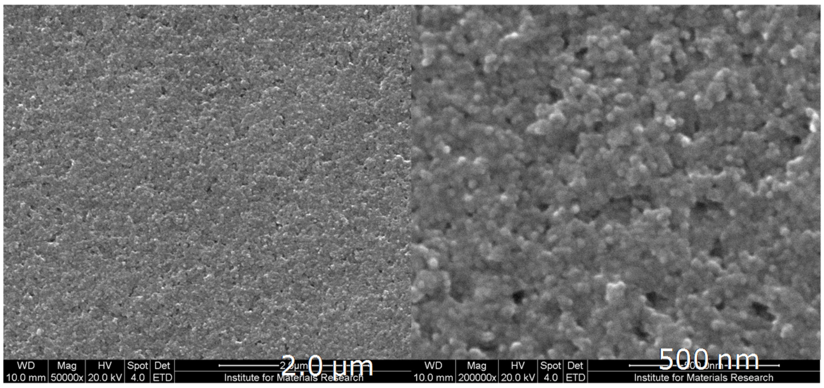

Figure 3.26 SEM image of the porous layer prepared by tape casting a PEG400-TiO_2 suspension.

This section demonstrates the use of the dispersion as a basis for the deposition of porous, thick layers by tape casting. It was shown that large pores (> 50 nm) are formed using HPC as additive while the pores between the particles are more in the range of tens of nanometers. In view of applications, the pore size and the thickness of the films need more optimization.

3.3 Dense and porous layers by screen printing[3]

In this section, preliminary experiments are presented using the TiO_2 dispersion (of Chapter 2) as an ink for the deposition of **dense** layers[4] via the screen printing technique, illustrated in Figure 3.27. This technique makes use of a screen mesh, which is placed above the substrate, and a squeegee. A solution or ink is deposited in front of the squeegee which makes contact with the mesh. As the squeegee moves along its stroke, the tension in the mesh pulls the mesh out of the ink and the ink is drawn out of the mesh by the adhesive force. Printing occurs when the surface energy forces overcome the cohesive forces in the liquid.

---

[3] Cooperation with IMO- printing Group of Dr. Ir. W. Deferme

[4] In DSSCs, dense TiO2 layers are deposited underneath the porous TiO2 layers in order to prevent leakage of the electrolyte (Peng et al. (2004) Coordination Chemistry Reviews 248: 1479-1489.

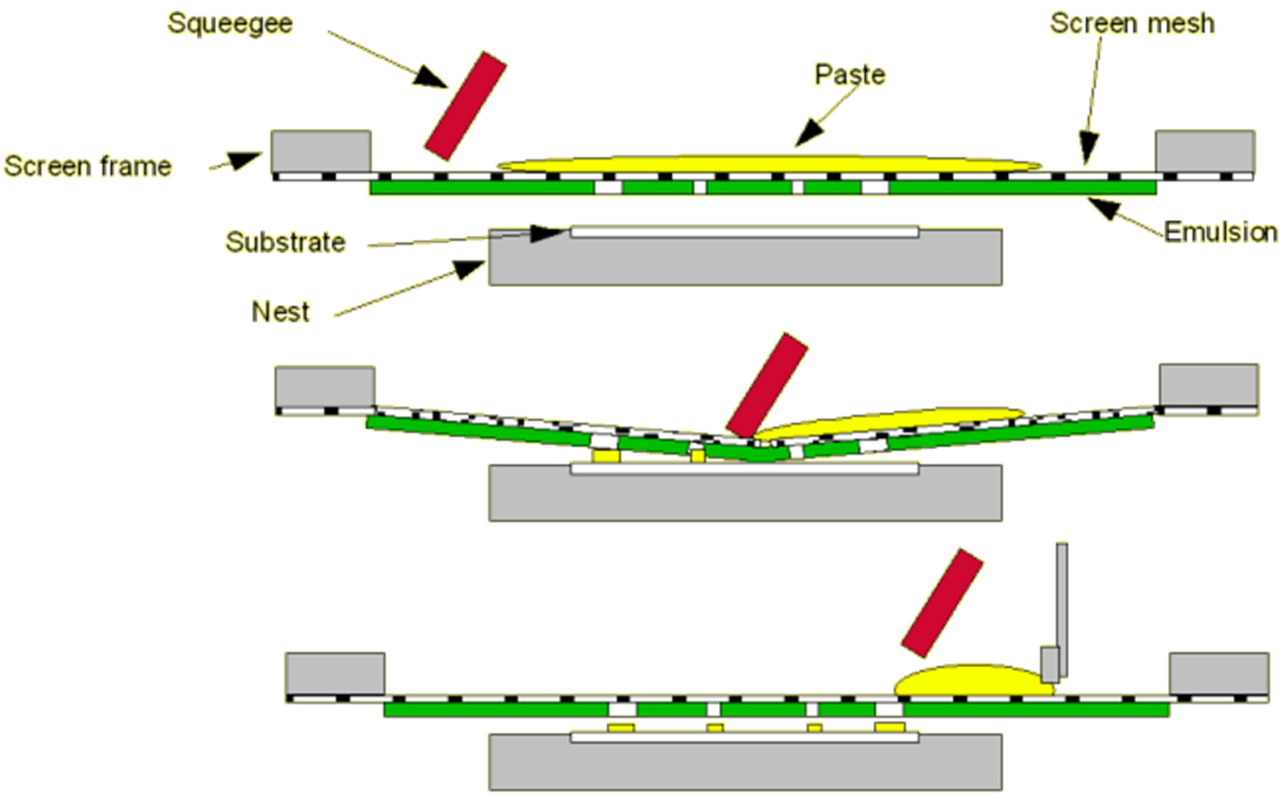

Figure 3.27 The basic screen print process [22].

The screen printing process is sometimes more considered as an art rather than a scientific manner of producing films due to the large amount of parameters influencing the process such as [23]:

- Ink (viscosity, rheology, particle size and distribution, homogeneity, adhesion, stability, …)
- Substrate (cleanliness, surfaces roughness, …)
- Screen (mesh count, mesh opening, mesh thickness, emulsion thickness, screen tension…)
- squeegee (hardness, parallelism, size and shape of edge…)
- Printing machine (precision, parameter control, repeatability…)
- Printing process (speed, direction, set up…)

As the experience within imo-imomec more concerns the screen printing of polymeric solutions, the parameter and machine settings of the screen printing process using the aqueous dispersion required extra attention and optimization. For example, the printing speed becomes more important when using low viscous solutions such as the aqueous TiO_2 dispersion. Furthermore, the thickness (viscosity) of the suspension influences the flow of the dispersion in the mesh and subsequent deposition. When the thickness is too low, the deposited structure will be toothed, while irregular coatings will be the result of highly viscous suspensions, as illustrated in Figure 3.28

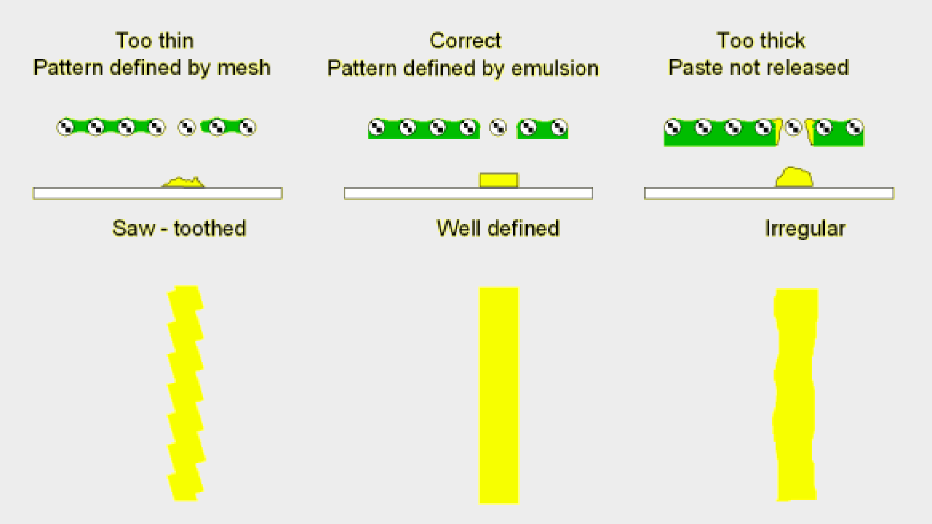

Figure 3.28 Effects of emulsion thickness on print definition [22].

Using the TiO_2 dispersion as such and a screen of 180/31[5], dense films are obtained but they are not homogeneous as observed via optical microscopy (Figure 3.29). This inhomogeneity may be caused by the low viscosity of the dispersion (1,9 mPa.s) which is beyond the lowest printable viscosity value of the screen printer (10 mPa.s). Therefore, the viscosity of the dispersion is increased by the addition of glycerine, in two different concentrations. A higher print velocity could be applied using these suspensions compared to the low viscous pure TiO_2 dispersion. The screen printed layers from the glycerine-TiO_2 suspensions are shown in Figure 3.29. More homogeneous layers are obtained with 16,6 v% TiO_2 in glycerine, while a higher concentration of TiO_2 in the glycerine solution doesn't result in a layer, as only large condensed shapes are observed. The TiO_2 nanoparticles in the dispersion are electrostatically stabilized by tetraethylammonium cations (as concluded in chapter section 2.6). Increasing the concentration of TiO_2 in the TiO_2/glycerine suspension, and thus an increase of tetraethylammonium cations, could induce particle agglomeration due to the disturbance of the electrostatic stabilization by competition with the hydroxyl groups of glycerine, which are deprotonated in the basic environment of the initial TiO_2 dispersion.

Although no homogeneous, dense films are obtained, these experiments indicate that the choice of the additive in the case of using the TiO_2 dispersion as an ink, requires a more sophisticated approach, taking into account the species that stabilize the nanoparticles in our dispersion.

---

[5] 180 treads/ inch and a tread thickness of 31 µm

Pure TiO_2 dispersion, z 180/31, v 704 mm/s (300°C)

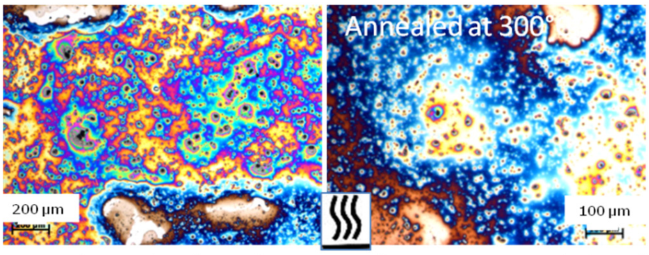

16,6 v% TiO_2 in **glycerine**, z 180/31, v 604 mm/s (300°C)

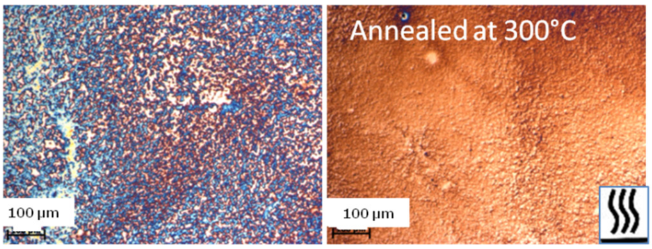

33 v% TiO_2 in **glycerine**, z 180/31, v 604 mm/s (300°C)

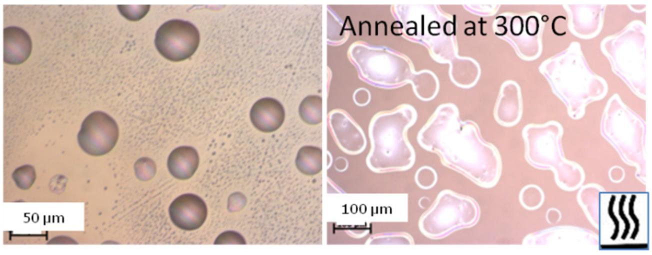

Figure 3.29 Optical microscopy images of screen printed and thermally treated films from the pure dispersion and the dispersion mixed with different concentrations of glycerine.

In order to use screen printing for the deposition of **porous** layers, the viscosity needs to be adapted by additives that have the ability to form pores. As the addition of HPC and PEG, discussed in previous section, resulted in homogeneous porous films, the same approach is applied here with screen printing as deposition technique. The obtained films are analyzed by optical microscopy and SEM, given in Figure 3.30. From the SEM analysis, it is observed that the film from the HPC/TiO_2 suspension results in a more homogeneous (and porous) layer in comparison with the film from the PEG/TiO_2 suspension.

During screen printing of the above suspensions, it was observed that the some material remained in the meshes of the screen. Referring to Figure 3.28, this would mean that the viscosity of the suspension is too high and therefore results in more irregular layers.

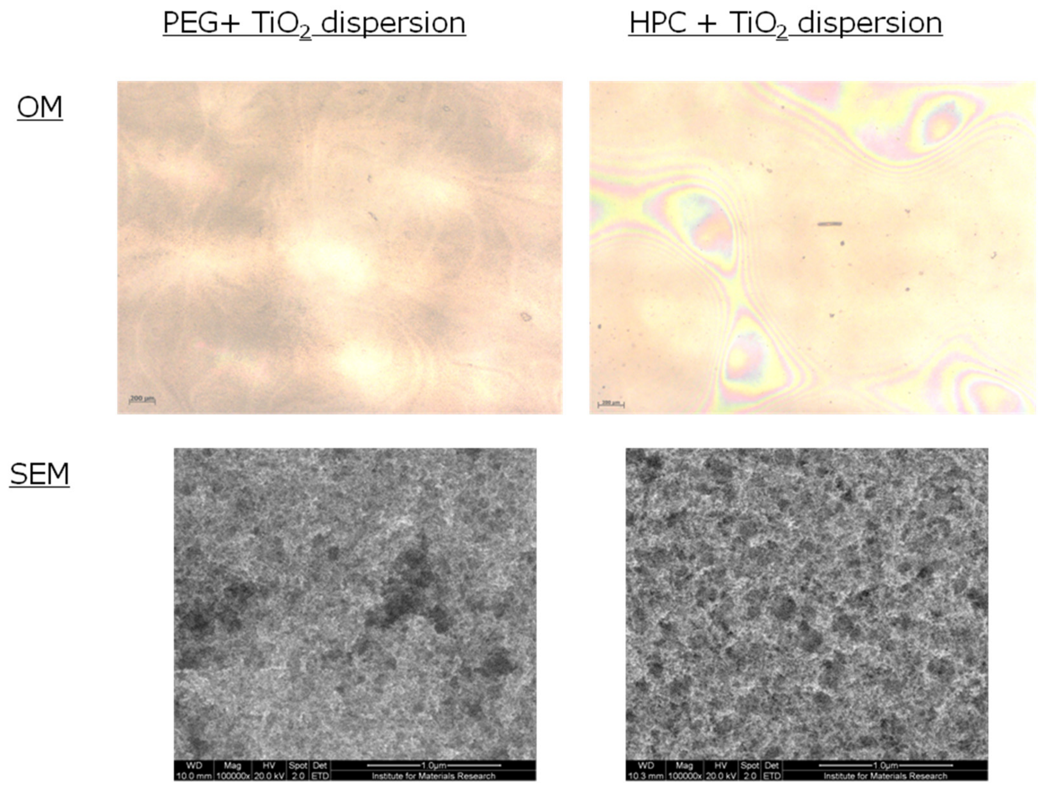

Figure 3.30 Optical microscopy images of screen printed films from PEG/TiO$_2$ and HPC/TiO$_2$ suspensions.

From these preliminary results, it is clear that a more systematic study concerning the viscosity and the used additives is needed for the preparation of both dense and porous layers via screen printing, as the rheological characteristics of the aqueous suspension greatly influence the quality of the print [24]. Nevertheless, these experiments can be considered as a first step towards the implementation of an aqueous dispersion in combination with screen printing.

3.4 Patterned layers

The aim of the preparation of patterned TiO$_2$ films is the increase of specific surface area compared to a flat film, as is illustrated in Figure 3.31, gaining surface by the height and the sequence of the patterns.

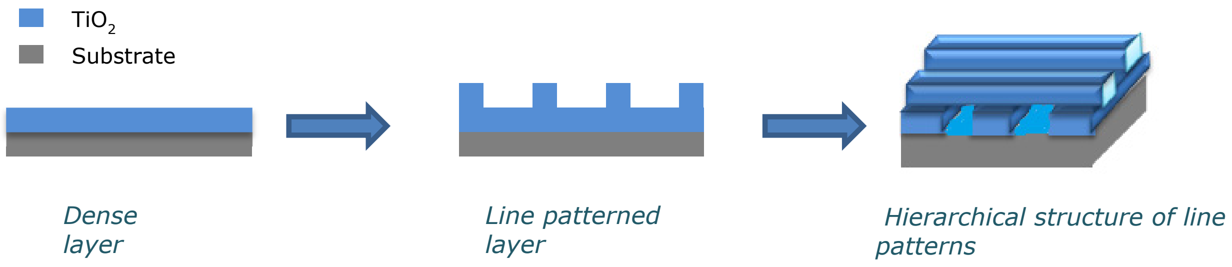

Figure 3.31 Schematic representation of the change in surface area by patterning.

Although most reports concern the use of structured Si masters prepared by expensive photolithographic techniques, in this work, we study the use of easy available and cheap commercial optical discs (CDs), which consist of line patterns in the submicron-to nanoscale, as a master for the synthesis of TiO_2 nanopatterns.

Further, the expansion toward the use of CDs (width of patterns ±750 nm) [25] to DVDs (width of patterns ± 350 nm) and even blu-rays (width of patterns ± 200 nm) (illustrated in Figure 3.35), is motivated by the expected increase of specific surface area by decreasing the dimensions of the patterns. Via the calculation of the area enhancement factor (AEF), the increase in surface area using these masters is estimated. The area enhancement factor is defined as the area of the patterned layer divided by the area of the dense layer. In Figure 3.32, the AEF is plotted in function of the width of the pattern, with a constant average thickness of 50 nm. An average thickness of 50 nm derives from the possible shrinkage (> 50%) of the final oxide pattern compared to the original master [26]. The graph demonstrates an increase of only 5% by patterning but increase of 50% of surface area when decreasing the width from 1 µm to 100 nm. The deposition of a second patterned layer[6] further increases the AEF, taken into account the loss of surface of the first layer due to the overlap with the second layer in the hierarchical structure, as illustrated in Figure 3.31. According to the calculations, a hierarchical structure of lines with a width of 100 nm and a height of 50 nm is estimated to double the specific surface area.

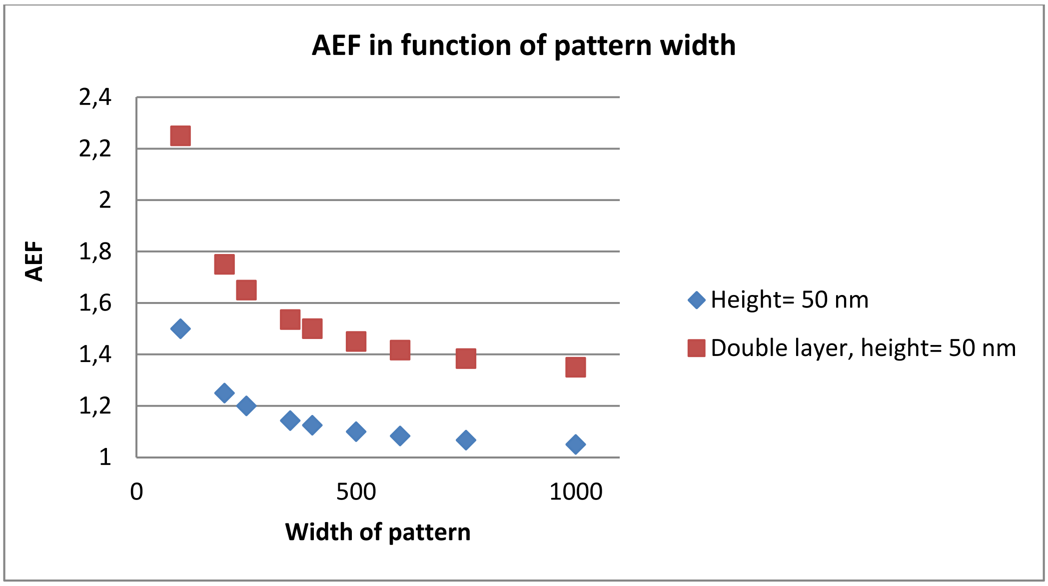

Figure 3.32 Graph of the expected increase of surface area (expressed as AEF) in function of the pattern width and an average height of 50 nm, for a one layer and two layered patterned film.

For a patterned film consisting of a pattern with a width of 750 nm (using the CD master) or 350 nm (using the DVD master), the AEF is calculated in function of thickness, for one layer and two layers (Figure 3.33). For the one layered films, the increase of surface area by increasing the height is the highest for a width of 350 nm, compared to 750 nm. Also for the double layered films, with a width of 350 nm, a steep increase (of 50%) is estimated when increasing the height from 50 till 120 nm.

---

[6] For the calculations, the second layer is considered as illustrated in figure 3.27, on top of the first layer.

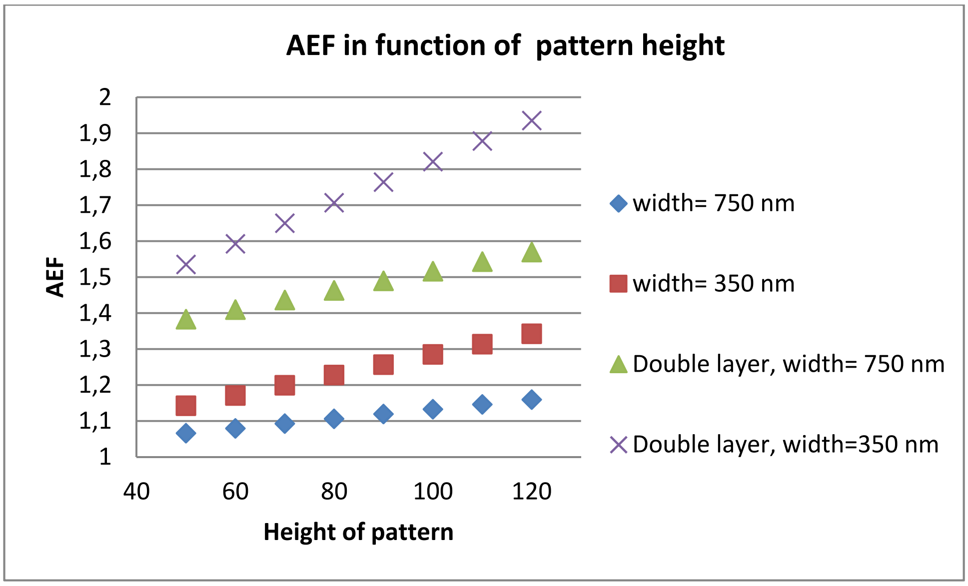

Figure 3.33 Graph of the expected increase of surface area (expressed as AEF) in function of the pattern height and a width of 750 nm or 350 nm, for a one layer and two layered patterned film.

Based on these calculations, the synthesis of patterned TiO_2 layers to increase the surface area of the films look promising. In this work, the soft lithographic technique, micromoulding (also called replica moulding) is applied to prepare the patterned films. The general principle of this technique is to emboss a structured stamp into a wet precursor layer in order to transfer the pattern and obtain a structured film, after drying, of the aimed material with or without post-patterning treatment.

As a precursor 'ink', the stable, aqueous TiO_2 dispersion (presented in chapter 2) is used from which a homogenous wet film is prepared by spin coating. As previously mentioned, the chosen masters are commercial optical discs for storage of digital data (CD, DVD, blu-ray) from which their pattern is transferred into PDMS for the preparation of a stamp. In the following, each step/parameter in the applied patterning process is described in more detail, concerning the choice and optimization of the process parameters. The general steps are represented in Figure 3.34.

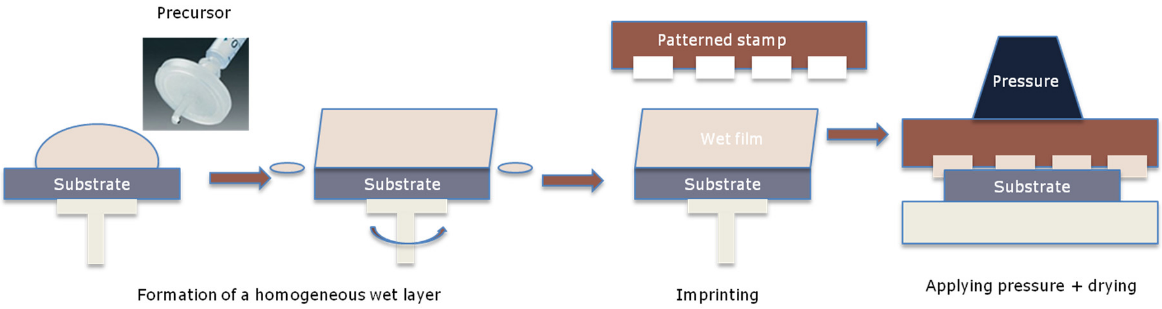

Figure 3.34 Process steps for the preparation of a patterned TiO_2 film by micromoulding.

a) Selection of a suitable patterned master

The optical discs selected for this work, are a commercial example of materials manufactured by the replica moulding technique where a nickel master is imprinted into a polycarbonate layer [27]. As the optical discs consist of many patterned and non patterned layers, as overviewed in Figure 3.35 (first column), only the polycarbonate layer of the optical discs is used as a master. The surfaces of the polycarbonate layer are analyzed by SEM, as presented in Figure 3.35 (second column).

b) Preparation of the PDMS stamp

The elastomer polydimethylsiloxane (PDMS) is used in this work to transfer the patterns of the selected master (disc) into a PDMS mold.

Experimental PDMS stamps are prepared by using the Sylgard 184 silicone elastomer kit (as received by Dow Corning) [28]. The base agent (prepolymer) and the curing agent are mixed in a 10:1 weight ratio followed by extraction of air bubbles under vacuum. The liquid is then casted against relief polycarbonate layers of the CD (CD-R 700 MB), DVD DVD +R, 4.7GB) and Blu- ray (Blu-ray disc rewritable, 25 GB, single layer). The PDMS on the relief structured masters is cured for 45 minutes at 80°C, peeled off the masters and cut to a size larger compared to the size of the substrates to be patterned. The PDMS stamps derived from the CD, DVD and Blue ray are called 'CD stamp', 'DVD stamp' and 'B-ray stamp' respectively. The PDMS stamps are used repeatedly for all sample preparations after cleaning with diluted HNO_3 (5%) and water and dried.

Curing the prepolymer with the curing agent results in a highly cross-linked three-dimensional structure which is obtained via the hydrosilylation reaction between vinyl ($SiCH=CH_2$) groups and hydrosilane (SiH) groups [29]. Another advantage than discussed in chapter 1, section 1.5.1, of using PDMS as a stamp is its high durability which implies a repeated use of the stamp for more than 50 times over a period of months without noticeable degradation in performance [30]. The different patterned stamps are analyzed by Atomic Force Microscopy (AFM) and shown in Figure 3.35 (third column).

Comparing the dimensions of the lines in the polycarbonate layer and in the PDMS stamp, it can be concluded that the pattern transfer has occurred with success. The small difference in dimensions may be attributed to the AFM measurement itself. Note that the interdistance of the master should be the inverse of the width of the stamp and vice versa. An AFM image of the B-ray stamp is missing since no pattern is observed on the surface of this stamp. Nevertheless, a pattern is obtained (as will be show later) using this stamp. The absence of pattern observed in the B-r ay stamp may therefore be explained by the low height of the pattern (only 10 nm in the master) combined with the elastomeric material of the PDMS stamp compared to the tip of the AFM.

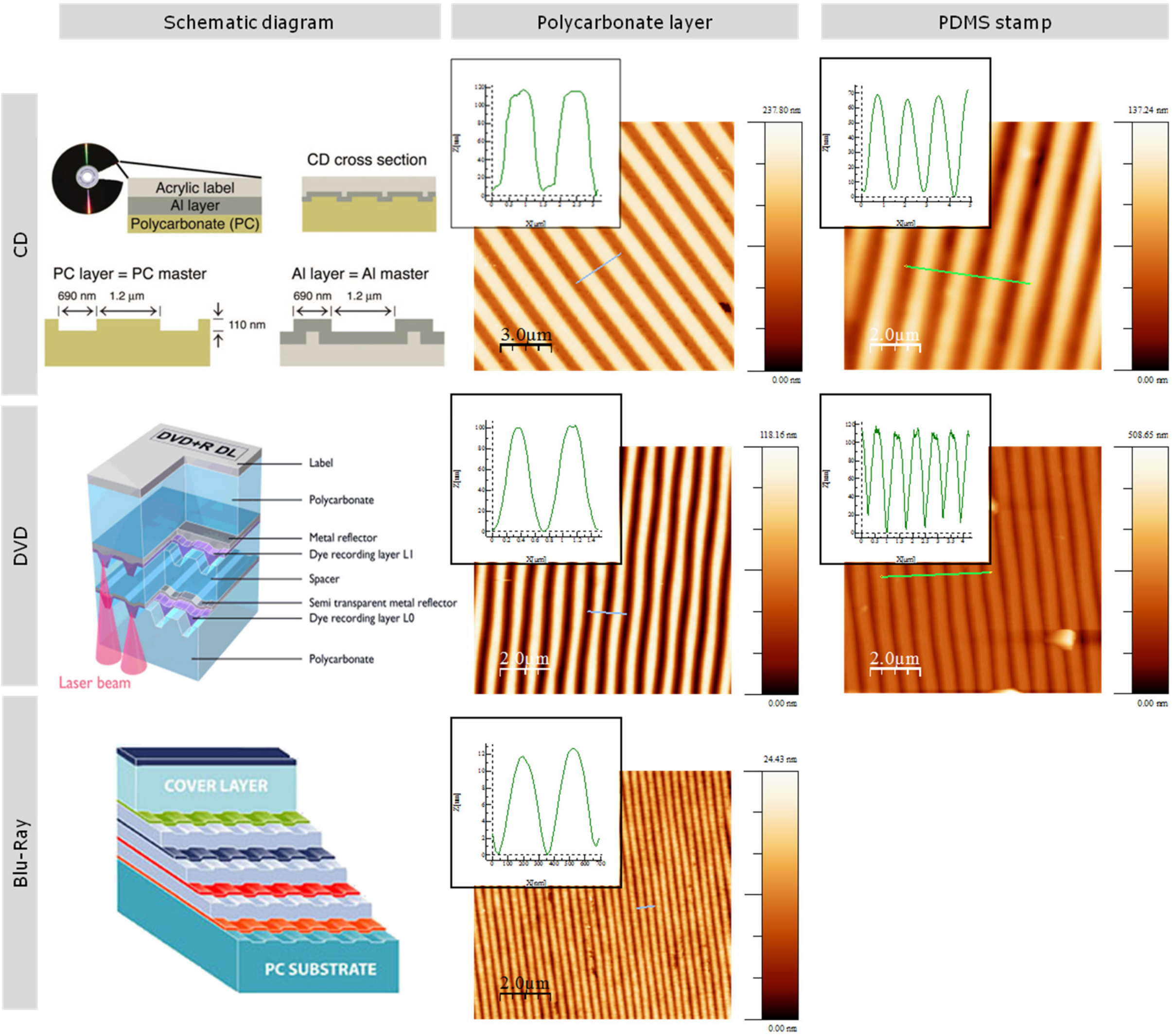

Figure 3.35 Schematic diagram [31-33], AFM of the polycarbonate layer and AFM of the PDMS stamp prepared from the polycarbonate layer of a CD, DVD and B-ray.

c) *Choice of precursor 'ink'*

As the 10 wt% TiO_2 dispersion, presented in chapter 2, shows wide application possibilities for the deposition of dense and porous layers (section 3.1, 3.2 and 3.3), it is also used for the preparation of patterns by micromoulding in this section. Another advantage of using a crystalline dispersion in micromoulding is a lower expected loss of material since no post-patterning treatment is necessary to form the desired phase.

d) Embossing, drying and curing

The first, actual step in the imprinting process is embossing the stamp into a wet film of dispersed TiO_2 particles. For the preparation of the wet film by spin coating, the spin coating conditions for the preparation of a dense layer (1000 rpm, 6 drops) could not be transferred, as no pattern is observed. Therefore, an experimental study for the optimal spin coat conditions for the preparation of wet film of dispersed TiO_2 particles for patterning is given here.

Experimental Glass substrates (2,5*2,5 cm) are cleaned via ultrasonic treatment in IPA (5 min ultrasonic) and water (5 min ultrasonic), followed by UV-O_3 treatment (50°C, 20 min). The TiO_2 dispersion is used undiluted but filtered using a syringe filter of 0,2 µm. Various amount of drops (1-6) and various spin velocities (250, 300, 350, 500 rpm for 30 s) are tested for the deposition of a homogeneous wet film of dispersed TiO_2 particles. The CD stamp is embossed into the wet film and a pressure is applied using a weight of 2 kg. A heat treatment of 80°C for 15 minutes is applied with the stamp on the substrate. After removal of the stamp, the patterns are treated at 200°C for 5 minutes. The resulted films are analyzed by macroscopic view and by optical microscopy (magnification of 50 times).

The reason for the need of lower spin velocities for the patterning compared to the velocities for the preparation of a smooth film, is that lower velocities lead to a thicker wet film in which the stamp can be pressed. Decreasing the spin speed below 1000 rpm, resulted in a good pattern transfer due to the excess of dispersion, as verified via edge effects on the dried layer prepared by spin coating at 500 rpm (Figure 3.36a).

The best pattern transfer is obtained using 3 drops and a spin coat velocity of 350 rpm. The success of the pattern transfer is first macroscopically confirmed by the observation of a rainbow effect, which is visible when tilting the substrate against the light, as shown in Figure 3.36b. The rain bow effect derives from difference in scattering of light by the nanopatterns. Via optical microscopy (Figure 3.36c), the pattern is clearly visible which confirms the successful pattern transfer.

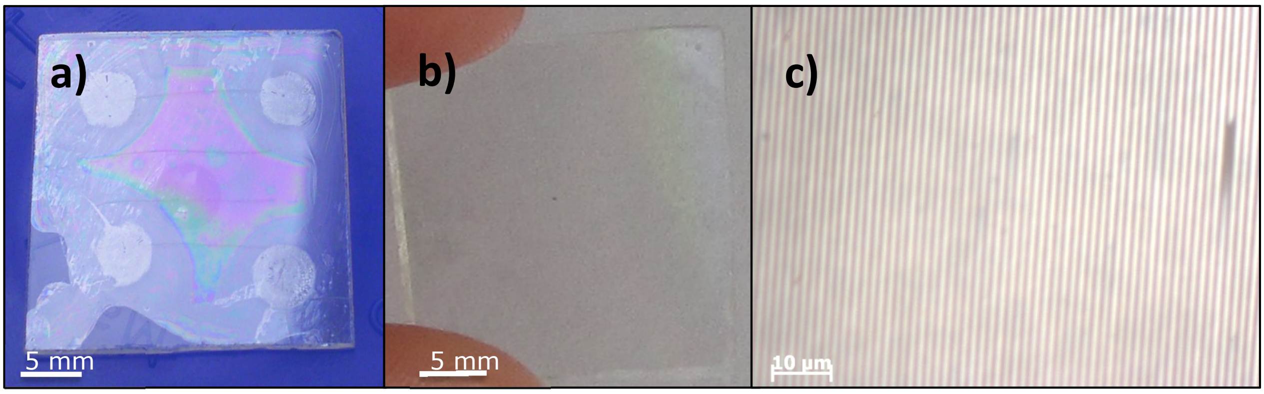

Figure 3.36 Photo of a dried film obtained at a spin velocity of 500 rpm and a photo (b) and optical micrograph (c) of a patterned film at a spin velocity of 350 rpm and photo.

The temperature and time used to dry and form the pattern when the stamp is embossed, is set on 80°C for 15 min. Due to the aqueous solvent for the dispersion, a temperature of 80°C is sufficient to allow slow drying of the dispersion and formation of the pattern. A drying time of minimum 15 minutes is applied in order to improve the packing efficiency of the particles. Lower temperatures require a treatment of at least 30 minutes to dry the pattern and a higher temperature would dry the pattern too fast which could lead to defects in the pattern.

The choice for glass substrates arises on the one hand from the low cost and on the other hand from the aim to use the patterned films for photocatalytic experiments (as shown in chapter 4), for which transparent, non absorbing substrates are preferred.

Both cleaning methods (SPM/APM cleaning as the cleaning in IPA, H_2O, followed by the UV-ozon treatment) are applied for patterning formation. However, when using the UV-O_3 cleaning, the absence of a scum layer can be clearly distinguished (Figure 3.37).

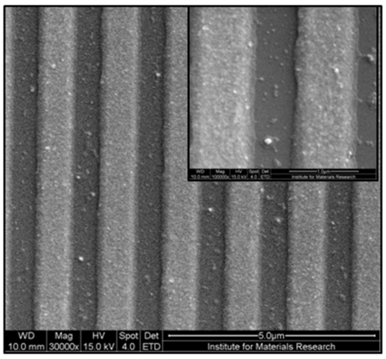

Figure 3.37 SEM image of a patterned TiO_2 layer from a CD stamp on Si cleaned by IPA/H_2O and UV-O_3.

When pressing the stamp into the wet film, the excess of liquid has to be removed from underneath the protruding parts where the residual (scum) layer forms. It is excepted that the higher the pressure, the thinner the residual layer will be. Göbel et al. [34] reported the absence of a scum layer at a pressure as low as 0,2 bar. The applied pressure in this work, which corresponds with a weight of 2 kg on a sample area of 6,25 cm^2, is 0,3 bar. As the applied pressure is constant for all sample preparations, the cause of the absence of a scum layer is assigned to another factor, namely the surface energy of the substrate.

At a pressure of 0,3 bar, it can be assumed that the protruding parts of the stamp are in contact with the substrate. Not only the interactions between the stamp and the substrate but also between the substrate and the dispersion and the stamp and dispersion will influence the dewetting. As earlier discussed (Chapter 1, section 1.5.1), the dewetting is related to the differences in interfacial tensions between the before mentioned interactions [35]. Therefore, as only a scum layer is formed on SPM/APM cleaned substrates, the surface energy and the water contact angles on the two types of cleaned surfaces are determined. The results of the water contact angle measurements, shown in Table 3.2, show no difference in contact angle between glass and silicon substrates, which was already assumed. Nevertheless, a small difference in the contact angles on the differently cleaned substrates can be noticed. The SPM/APM cleaning is a very effective cleaning procedure and results in superhydrophilic surfaces, which is ideal to deposit defect free films. The IPA/H_2O/UV-O_3 cleaning shows a little difference in contact angles which is the result of this less effective cleaning. Although there is a (slight) variation in water contact angle between the cleaned substrates, the effect on the surface free energy is minimal as they show an almost negligible difference. Therefore, based on these results, the absence of a scum layer when the UV-O_3 cleaning is used, can not be explained based on the surface free energy of the cleaned substrates.

Substrate	CA (H_20)	SFE (N/m)
Glas UV-O_3	<4	0.0669
Glas SPM/APM	0	0.06650
Si UV-O_3	<4	0.06681
Si SPM/APM	**0**	**0.06711**

Table 3.2 Water contact angles of the UV-O_3 and SPM/APM cleaned glass and silicon substrates.

In the following, the TiO_2 line patterns prepared from a **CD stamp, DVD stamp and B-ray stamp** are studied.

Experimental Glass substrates (2,5*2,5 cm) are cleaned via ultrasonic treatment in IPA and water, followed by UV-O_3 treatment (50°C, 20 min). The TiO_2 dispersion is used undiluted but filtered using a syringe filter of 0,2 µm, like for the previous deposition techniques. A wet dispersion film is prepared by spin coating 3 drops at 350 rpm (30 s). The PDMS CD stamps, DVD stamps and B-ray stamps are used for imprinting into the wet film and a pressure is applied by a weight of 2 kg. A heat treatment of 80°C for 15 minutes is carried out with the stamp on. After removal of the stamp, the pattern is further treated at 200°C for 5 minutes. The resulted line patterned films are analyzed by SEM and AFM.

The SEM and AFM analysis of the lines prepared by using the CD stamp, the DVD stamp and the B-ray stamp are presented in Figure 3.38, Figure 3.39 and Figure 3.40, respectively. The dimensions of the as-prepared TiO_2 features are listed in Table 3.3. The width of the lines and the interdistance (between the lines) is determined via the SEM images and the height is determined using topographical profiles from AFM (width at half height). From the B-ray stamp, patterns are observed although the presence of patterns in the PDMS stamp could not be visualized by AFM.

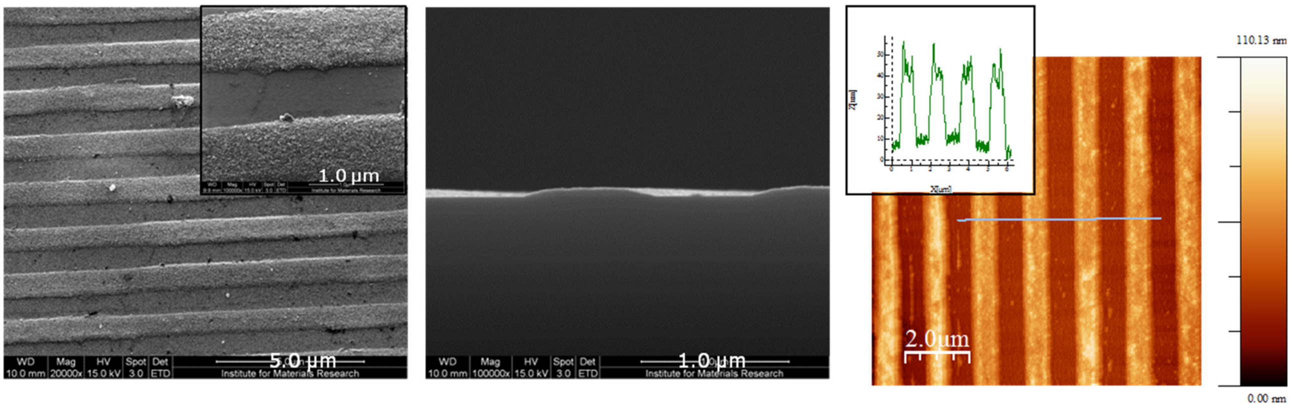

Figure 3.38 SEM and AFM analysis of a line pattern prepared using a CD stamp.

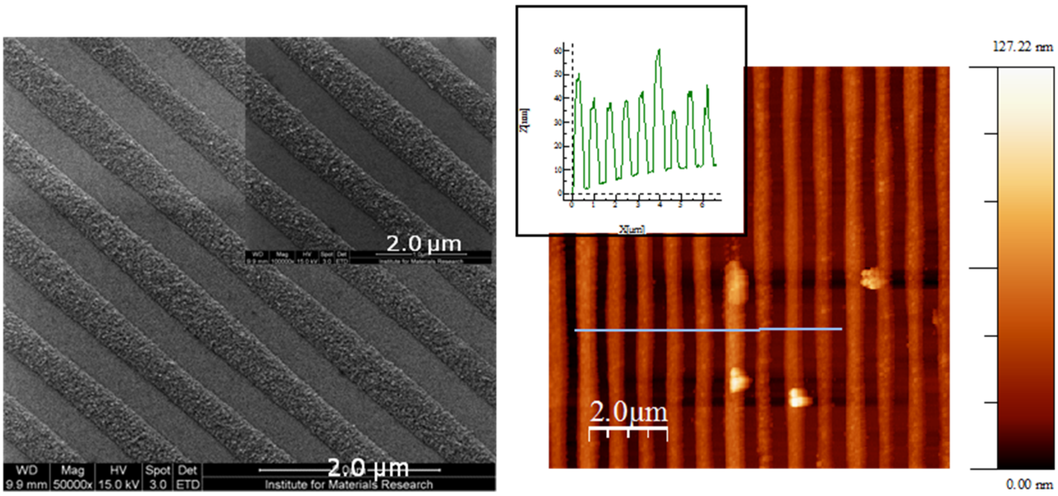

Figure 3.39 SEM and AFM analysis of a line pattern prepared using a DVD stamp

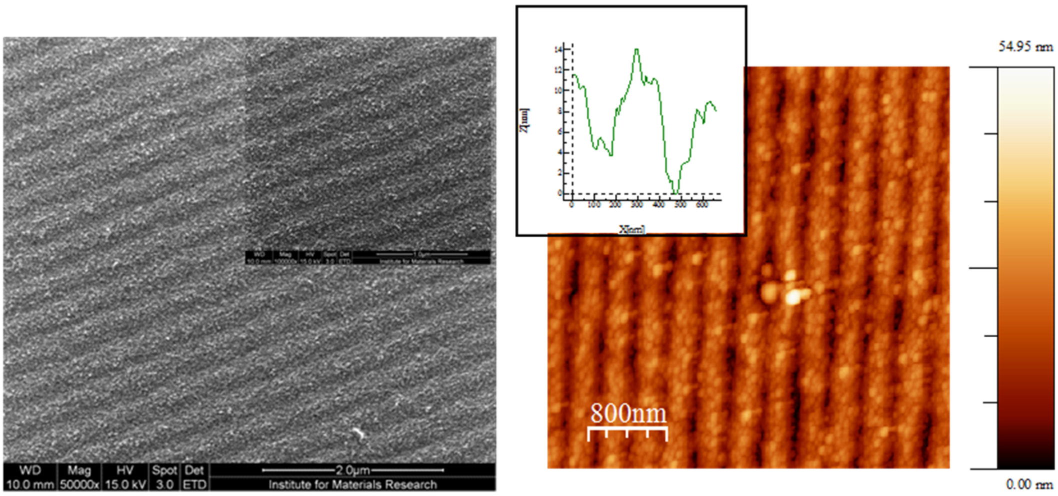

Figure 3.40 SEM and AFM analysis of a line pattern prepared using a blu-ray stamp

Line pattern from	Width	Interdistance	Height
CD	930 nm	710 nm	50 nm
DVD	450 nm	360 nm	30 nm
Blue-ray	300 nm	60 nm	10 nm

Table 3.3 Dimensions of the features of the TiO_2 line patterns prepared from the CD, DVD or blu-ray stamp.

The width and the interdistance of the TiO_2 patterns, prepared from the CD and DVD stamp and determined by SEM, correspond well to the dimensions of the polycarbonate layer. As intended by using the DVD as a stamp, the width of the patterns is halved compared to the CD stamp, which results in a double amount of patterns per surface. The amount of patterns can even be increased more when using the B-ray stamp. Remarkable, is the decrease of the height of the TiO_2 patterns till more than 50% compared to the height of the masters, excepted for the pattern derived from the B-ray stamp. Although no precursor based solution is used, a quite large shrinkage of the pattern derived from the TiO_2 dispersion is observed. The possible factors that can influence the height of the patterns are:

- *The solid content of the used dispersion* which is 10 wt% (corresponding to ~2,5 vol%). The calculated volume of a hypothetical cuboid in the cave of a line structure, consisting of the dimensions of the polycarbonate layer from the CD (i.e. 900 nm *0,12 µm (height) * 1µm) is $108 * 10^6$ nm^3. Supposing this cuboid is filled with TiO_2 dispersion and assuming a decrease in volume – in one dimension- of more than 97% (solid load of 2,5 vol%), the cuboid will only be filled till a height of 0,003 µm. Thus, the height of the pattern when using a 2,5 vol% dispersion is expected to be only 3 nm. However, the concentration of the particles in the dispersion layer is increased after spin coating (as discussed in chapter 1, section 1.4), leading to an larger height than calculated.

Comparing the volume of a cuboid from the cave of the CD master with dimensions 900 nm* 1 µm*120 nm and the volume of a cuboid from the TiO_2 pattern with dimensions of 930 nm*1 µm*50nm, a volume loss of ± 55% is calculated.

In the case of a DVD as master, a cuboid from the cave of the DVD master with dimensions 500 nm*1 µm*100 nm compared to a cuboid from the TiO_2 film with dimensions of 450 nm*1 µm*30 nm, result in a volume loss of ±70%. These lower volume losses (compared to 97%) confirms the increased concentration of particles in the dispersion layer after spin coating. By increasing the starting concentration, the height of the patterns could be increased more as the solid loading of ceramic liquids has a significant effect on the aspect ratio of the ceramic features [36, 37]. Although, in this research, the increase of the concentration of TiO_2 in the dispersion is not studied, it is expected that the addition of more TiO_2 nanoparticles to the dispersion would not only affect the dispersions stability, it also would increase the viscosity. An increase in viscosity of the dispersion would change its behavior during embossing of the stamp and would have an effect on the formation of a scum layer. Nevertheless, when using colloidal suspensions in micromoulding, solid loadings as high as 40 vol% are preferred [38, 39].

- The *interaction between the dispersion/particles and the stamp* which affects the adhesion of particles to the stamp during the removal. This implies that a part of the formed pattern sticks to the PDMS stamp after removal. This effect will be discussed later in this section.

- A*dhesion between particles* which can be too low and thus leads to a loss of dried particles from the nanostructures, resulting in a lower height than expected.

- *Deformation of the patterns in the stamp* by the applied pressure would not only decrease the height of the stamp, but also influence the other dimensions which showed less difference compared to the dimensions of the stamp. Although deformation of the stamp (illustrated in fig.1.23) would reflect in a change of shape in the patterns, which is not observed here, it is observed in the TiO_2 patterns prepared from the DVD stamp that the interdistance and the width has increased and decreased with ± 50 nm respectively, compared to the dimensions of the PDMS stamp. This indicates a very small collapse of the features in the DVD stamp by the weight of 2 kg, resulting in a small decrease of height of the pattern.

- The *hydrophobicity* of the PDMS stamp (WCA = 106°), can influence the wetting and thus the filling of the pattern by the aqueous dispersion. If this effect is playing, the other dimensions of the pattern would also be influenced, which is not observed in current work.

- The decrease in height can also be caused by the trapping of air bubbles in the cavities of the patterns. Air bubbles are trapped when the gravitational force is smaller than the capillary force [40].

In the following, only patterns from the CD stamp and the DVD stamp are prepared since the height of the pattern prepared by the B-ray stamp is too low for aiming at an increase in surface area.

Till now, the coverage of the samples is not yet discussed. From optical microscopy[7], it is observed that some areas on the substrate have not been patterned. These defects can be attributed to the manual action of applying a pressure by putting a weight onto the stamp, represented in Figure 3.41 (left). Manually applying the weight onto the stamp, which is impressed into the wet film, requires a very precise handling to avoid shifting or even slipping of the stamp over the substrate due to the wet film, which decreases the accuracy of the pattern transfer. To solve this issue, **a semi-automated system** is developed (in-house)(Figure 3.41, right) which applies the pressure equally by a micrometer[8]. It was observed that this process enhances the pattern transfer to the substrate.

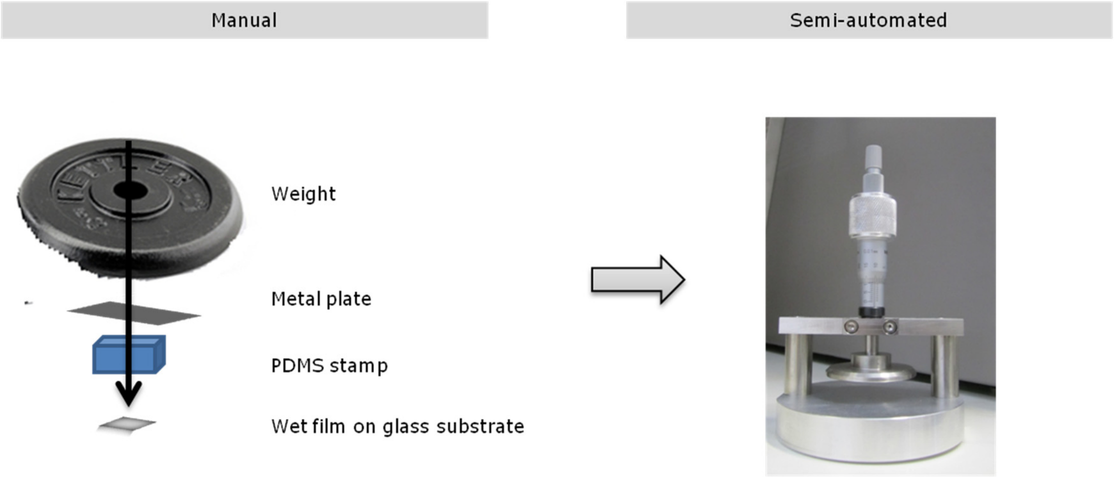

Figure 3.41 Schematic overview of impressing the stamp in a wet film by putting a weight (left) and a photo of the home-made more automated system to apply pressure on the stamp.

As the increase of specific surface area by patterning is aimed, the absence of TiO_2 between the lines (no scum layer) is not compensated by the low height of the patterns. Actually, the surface area of the line patterned layers (from both CD as DVD stamps) has decreased compared to

---

[7] The patterns prepared from the DVD stamp cannot be analyzed by OM since the used light approaches the dimensions of the pattern.

[8] The micrometer can apply a pressure corresponding to a weight of maximum 4 kg

dense layers. To meet our goal, the absence of a scum layer is not beneficial and so a dense layer is provided between the patterns.

Experimental A dense layer is deposited as described earlier on SPM/APM cleaned glass substrates, by spin coating 6 drops of the dispersion (filter of 0.2 µm) using spin conditions of 1000 rpm (at 500 rpm/sec, 30 sec), followed by 3000 rpm (at 500 rpm/sec, 30 sec). The wet films are dried for 5 minutes at 80°C , followed by a heat treatment at 200°C for another 5 minutes. The line patterns (indicated with the symbol '//') are deposited on top of the dense layer, by spin coating 6 drops of the TiO_2 dispersion (filter of 0,2 µm), using a spin speed of 350 rpm for 30 sec. The PDMS stamp is then pressed into the wet film and pressure is applied by the micrometer (semi-automated system). A thermal treatment at 80°C for 15 minutes is followed after which the stamp is carefully removed after cooling down.

SEM, Figure 3.42, confirms the presence of TiO_2 between the line patterns. For a line patterned film from a CD stamp (on top of a dense layer) with dimensions 750*50 nm, the AEF is calculated to be 1.06. For a line patterned layer on top of a dense layer prepared using a DVD stamp, this factor increases only 2%, for lines of 350*30 nm. A higher increase is expected since the horizontal dimensions are half between a CD and a DVD stamp. However, the height is a very limiting factor in the increase of the surface area. To compensate for the height, another patterned layer is applied, which would result in a higher AEF, as shown in Figure 3.33.

Experimental Two different morphologies are prepared by micromoulding, the so called line patterns (indicated with the symbol '//') and square patterns (two layered pattern, indicated with the symbol "#"). All patterned layers are deposited onto a dense layers, prepared as described in previous 'experimental' box. For the line patterns, a wet film is prepared by spin coating 6 drops of the TiO_2 dispersion on top of the dense layer using a spin velocity of 350 rpm for 30 sec. The PDMS stamp is then pressed into the wet film and pressure is applied by a micrometer. A thermal treatment at 80°C for 15 minutes is followed. The stamp is carefully removed after cooling down and a UV-Ozone treatment is applied (50°C for 20 minutes).

Square patterns are prepared starting from the line pattern as described above (after UV-O_3 treatment). A second line pattern is deposited by applying the PDMS stamp into the wet film (prepared as above) in a direction perpendicular to the direction of the lines of the first layer. The subsequent steps are the same as for the line pattern, inclusive the post UV-ozone treatment.

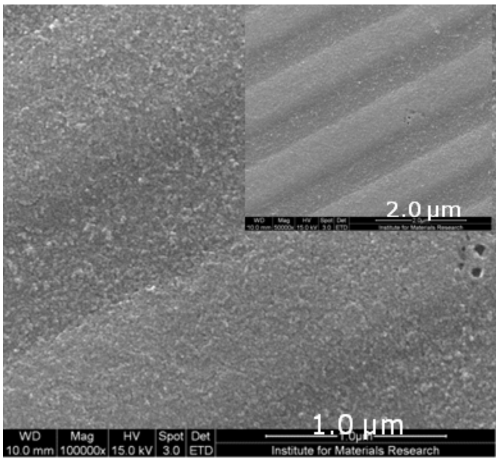

Figure 3.42 SEM images of a pattern prepared from a CD stamp on top of a dense layer.

It was shown from water contact angle measurements (Figure 3.43) that the TiO_2 line pattern from a CD stamp has a water contact angle (WCA) of 106°, which is hydrophobic and thus limits the deposition of an additional layer. However, after UV-ozone treatment (20 minutes at 50°C), the WCA decreased to zero indicating a superhydrophilic surface. Comparing these results with the WCA of a patterned stamp, which is 120°, the hydrophobic property of the TiO_2 line pattern may be assigned to 'residues' of the stamp onto the TiO_2 patterns. It is excluded that the high WCA of the line pattern is associated with topographical effects (see Chapter 4) since the vertical dimensions of the pattern are not distinctive enough.

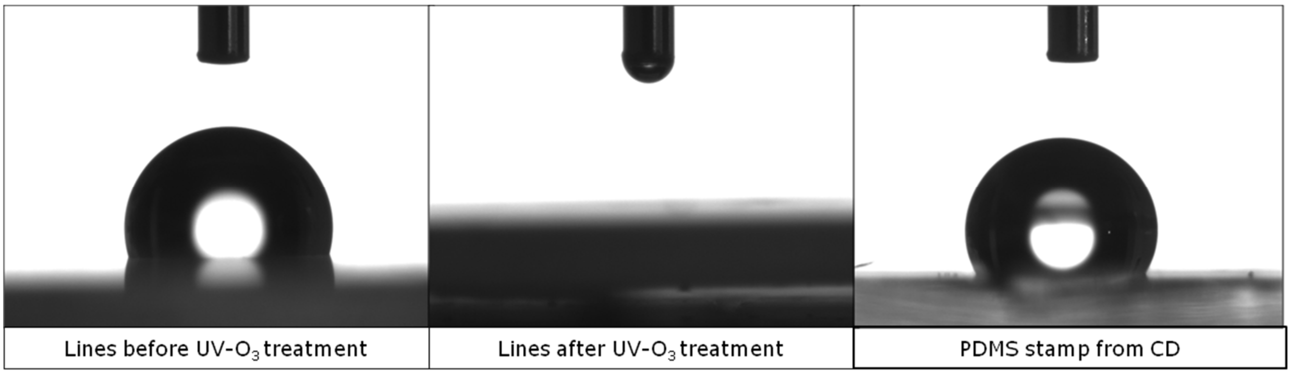

Figure 3.43 Photographs of a water droplet on a TiO_2 lined pattern before UV-ozone treatment (left), and after (middle) and on the patterned side of a PDMS stamp of a CD.

On the hydrophilic line patterns, an additional patterned film is deposited by the same conditions as before, except the direction of the stamp, which is pressed into the wet film with the lined pattern orthogonal on the direction of the lines of the first layer. By this way, square patterned films are obtained, as shown in Figure 3.44 and Figure 3.45.

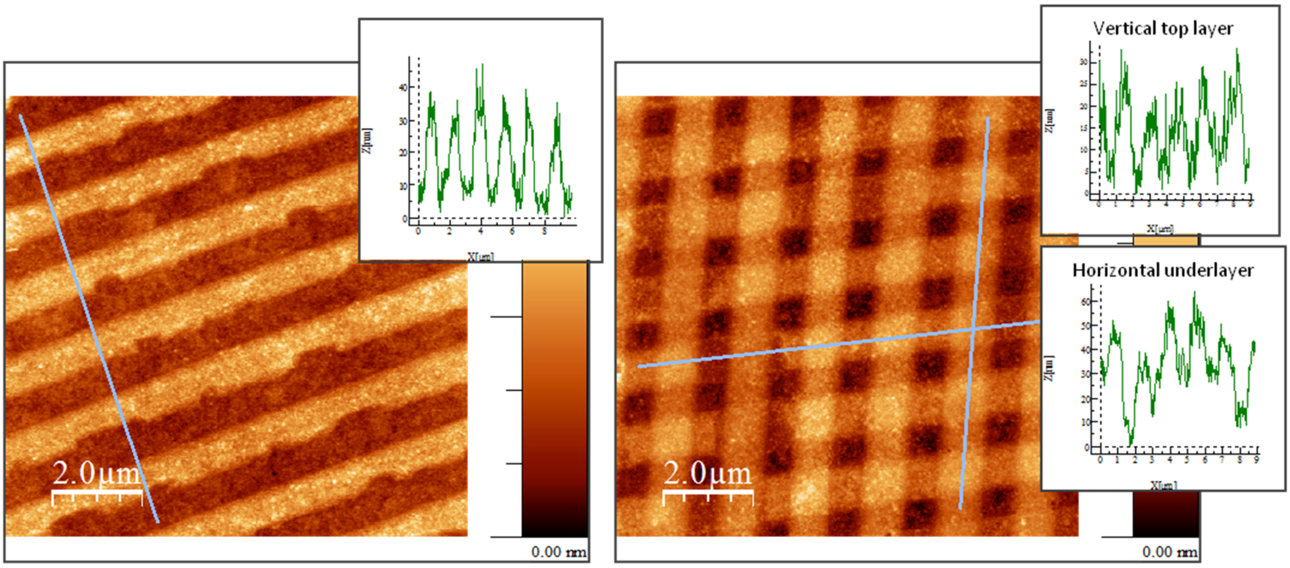

Figure 3.44 AFM images of the line (left) and square (right) patterned films derived using the CD stamp, with the surface profiles in the inset.

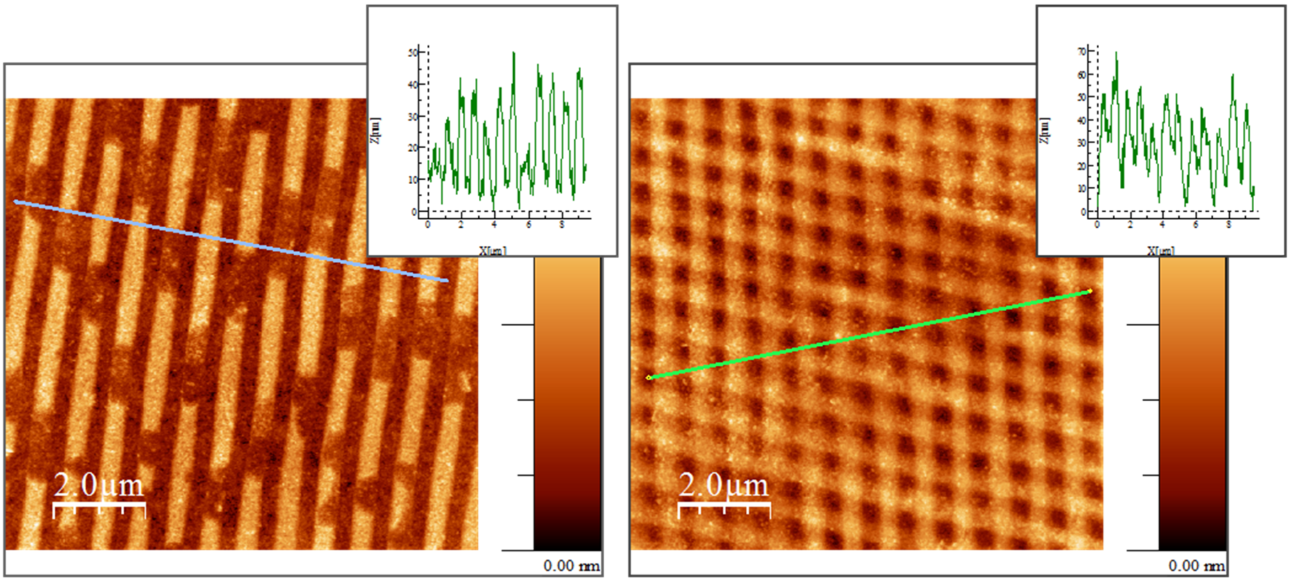

Figure 3.45 AFM images of the lines (left) and squares (right) patterned films derived using the DVD stamp, with the surface profiles in the inset.

Looking at the surface profiles of the square patterned film (Figure 3.45 right), the height of the overlapping areas has not increased by a factor 2. Therefore, it is concluded that the second layer merely fills the spaces between the lines of the first layer. The AEF calculated for the square patterns in given in Table 3.4. The deposition of two patterned layers, from both the DVD as the CD stamp, is estimated to increase the surface area with 30%.

Pattern	AEF (non floating)	AEF (floating)
Line pattern (750*50 nm)	1,06	/
Line pattern (350*30 nm)	1,08	/
Square pattern (750*50 nm)	1,35	1,38
Square pattern (350*30 nm)	1,37	1,42

Table 3.4 Area enhancement factor of one layered and two layered patterned films.

Furthermore, it is can be noticed that the amount of defects (bad coverage, incomplete lines) is higher in the lines derived from the DVD stamp than in the lines derived from the CD stamp. A possible reason for this could be a different surface tension and thus capillary interaction for stamps with smaller dimensions. A SEM image of the DVD stamp after patterning, shown in Figure 3.46(left) confirms the adhesion of nanoparticles in the caves of the pattern. This could explain the defects in the obtained pattern. Some particles are sticking onto the top of the structure of the stamp, which explains the defects in the TiO_2 layer between the patterns Figure 3.46 (right). Another cause for the defects could be the difference in TiO_2 concentration for each drop (inhomogeneity due to evaporation, also discussed in section 3.1). At a higher solid load, the particle packing density is high enough to replicate the lines of the stamp, while a lower solid load leads to a lower packing density, which leads to fracture, missing parts and a loss of fidelity of the micromoulding process [40].

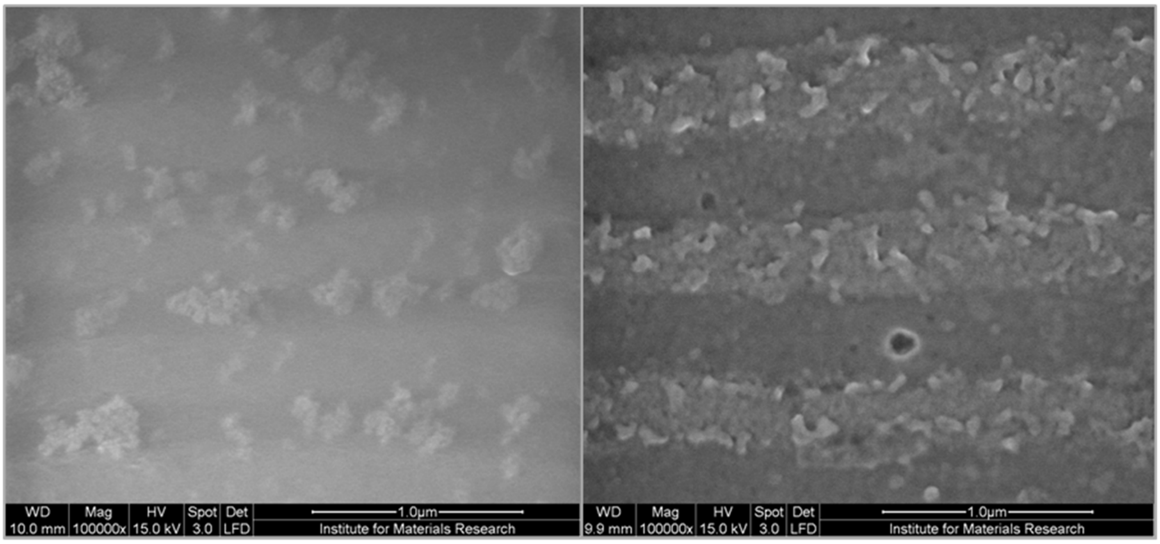

Figure 3.46 SEM images of the surface of a line patterned TiO_2 film (right) prepared from a PDMS DVD stamp (left)[9].

Here, we not only show that it is possible to pattern in two directions, but also in more directions, as presented in Figure 3.47. Four layered patterns could be obtained (Figure 3.47c and d) which indicate the possibility towards a further increase of surface area. Nevertheless, one must also take into account that the amount of defects will increase by stacking and the fidelity of the

---

[9] The images of the stamp and the TiO_2 pattern are not complementary.

nanostructure will be lowered. Göbel et al. [41] reported multiple stacking by micromoulding, demonstrating multiple depositions of up to 5 relief patterned functional oxide thin films

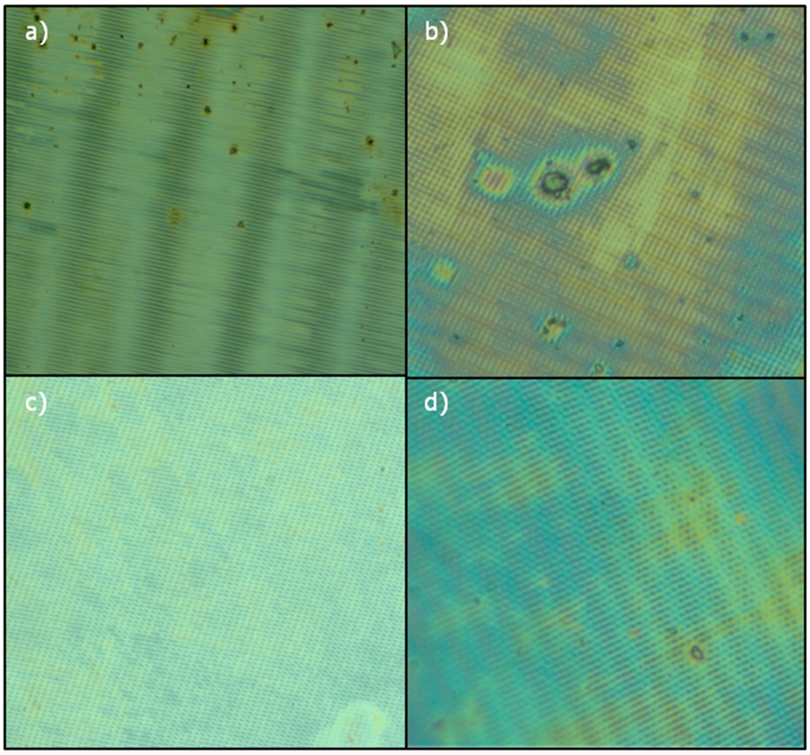

Figure 3.47 Optical micrograph images (magnification of 50x) of patterns prepared by changing the direction of the line patterned CD stamp in a) 3 times 0°, b) 1x 0°, 1x 90°, 1x 0°, 1x 90°, c) 1x 0°, 1x 90°, 1x 45°) and d) 1x 0°, 1x 90°, 1x 135°, 1x 45°, with 0°, 90°, 45° and 135° meaning horizontal, vertical, "/" and "\" respectively.

As the next section handles the deposition of nanorods, using a precursor different than the TiO_2 dispersion, a concluding summary of the previous sections is first given below.

3.4 Conclusion (deposition from the TiO_2 dispersion)

In this chapter, it is demonstrated that the concentrated aqueous TiO_2 dispersion can be used in combination with different deposition techniques. While spin coating results in smooth and homogeneous layers, porous layers are obtained using the dispersion (with appropriate additive) for deposition by tape casting. Applying dipcoating and screen printing on the dispersion, doesn't result in homogeneous films and further research is necessary.

Via the soft lithographic technique, micromoulding, line patterns are deposited, using optical discs as master for the PDMS stamp preparation. Morphologies with different dimensions and surface areas are aimed in view of their application in surface reaction based systems. To the best of our knowledge, this study is the first in reporting the use of the same precursor (TiO_2 dispersion) in combination with various deposition techniques. Nevertheless, each of the above deposition techniques show their drawbacks when combined with the aqueous TiO_2 dispersion and further research is needed to optimize the presented films. In conclusion, it can be said that the TiO_2 is a suitable 'ink' for the deposition of different nanostructured films, each with its characteristic thickness, porosity and nanomorphology. Moreover, the ability to use the same dispersion for different nanostructured films offers high potential for the study concerning the influence of topography on its performance in a specific application.

3.5 Synthesis of TiO_2 nanorod arrays

TiO_2 nanoparticles with sizes of 10–20 nm have been typically used to construct a mesoporous photoelectrode used in DSSCs. However, **slow electron transport** through the particulate TiO_2 film with a large grain boundary has the potential to increase the **recombination** probability between injected electrons and electron acceptors in redox species [42, 43], as the grain boundaries contain sites at which electron-hole recombination can occur. Furthermore, the infiltration of large molecular weight solid polymer electrolytes or hole transporting materials is only efficient in a TiO_2 films with an ordered nanoporous structure. Therefore, well-defined mesoporous TiO_2 films containing an ordered structure of nanorods, nanowires, nanotubes and nanosheets arrays have attracted much attention recently [44, 45].

In nanoparticle based DSSCs, the charge collection efficiency is determined by both the rate of electron recombination and the transport of the electrons through the film. Transport and recombination are interdependent which means that they cannot be changed independently. On the other hand, in nanorods, the electron transport occurs via extended states in the conduction band leading to the independency of recombination and transport. Thus, nanorods provide a direct path for the charges towards the electrode with less grain boundaries. Besides reducing the recombination, they also ensure an increased interface area for the adsorption of the dye and the electrolyte, improving the efficiency in solid-state DSSCs [46].

One the most applied, low temperature, water based method for the preparation of nanorods is via **hydrothermal growth**, which allow the deposition on different substrates [47]. Further, the deposition of a seed layer prior to the hydrothermal growth not only influences the microstructure [48], but it also enhances the efficiency in solar cells by providing a dense blocking layer in the photovoltaic devices [49].

In this work, the synthesis of **anatase nanorod arrays via** hydrothermal growth is envisioned since they are one of the most promising nanostructures to a higher efficiency. The applied method is similar to the method reported by Liu [50]and the several steps are given in Figure 3.48.

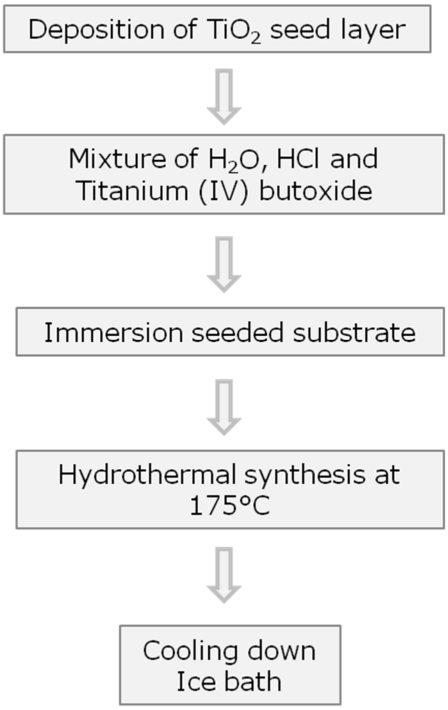

Figure 3.48 Schematic representation of the synthesis of nanorod arrays.

The first step is the synthesis of a **TiO_2 seed layer**. Earlier work within our research group [51], demonstrated the growth of rutile TiO_2 nanorods via a similar method (as in Figure 3.48), starting from a seed layer deposited using the aqueous citrato-peroxo Ti-precursor (earlier used in section 3.1.1) [12]. In current work, the influence of the seed layer is studied via the use of two types of precursor: a homogeneous precursor (the citrato-peroxo Ti precursor) and a particulate precursor (the TiO_2 dispersion described in chapter 2). As the TiO_2 dispersion contains a high anatase crystallinity, obtained via a low temperature method, it is aimed to study its influence on the crystal phase of the nanorods, grown on the seed layer prepared from the dispersion.

Experimental A dense TiO_2 layer from the dispersion is deposited onto a SPM/APM cleaned Si substrate by spin coating (1000 rpm), followed by a heat treatment at 80°C and 200°C. In order to enhance the adherence of the film to the substrate and to densify the film, a post thermal treatment at 300°C for 30 min is applied. The growth medium is prepared in the Teflon-liner, by dissolving 10 ml hydrochloric acid (HCl, 37 wt%, sigma Aldrich) into 10 ml of distilled water. After stirring for 10 minutes, 0.34 ml titanium butoxide ($Ti(O(CH_2)_3CH_3)_4$, 98%, sigma aldrich) is added in small droplets to the mixture. The substrate with the seeded layer ($1{,}25*1{,}25\ cm^2$) is placed against the side of the Teflon-liner, with the coated layer facing down. The hydrothermal synthesis is carried out at **175°C for 3 h** in a preheated laboratory furnace. After cooling down the autoclave to room temperature in an water-ice bath, the substrates are taken out and rinsed extensively with deionized water and dried at room temperature under a N_2 gas flow.

Unfortunately, the seed layer from the dispersion was dissolved in the growth medium solution during hydrothermal treatment an no nanorods could observed. The reason for the dissolution is not clear and not studied further, although the most possible explanation is the acid growth medium which dissolves the titania layer. Nevertheless, using the TiO_2 dense layer prepared from the citrate-peroxo Ti-precursor, the synthesis of nanorods has been observed [51].

In the following, the influence of the **concentration** of the citrato-peroxo Ti-precursor on the morphology and density of the nanorod array is studied. It must be noted that in current work, only one layer of the precursor is deposited, compared to the 10 layered seed layer in preceding work [51].

Experimental TiO_2 dense layers are deposited on SPM/APM cleaned substrates using the aqueous citrato-peroxo Ti-precursor with different concentrations (0.1, 0.2, 0.4, 0.6 M) by spin coating (3000 rpm), followed by a heat treatment at 180°C 2′, 300°C 2′ and 600°C 3′. The films are crystallized by a post thermal treatment at 650°C for 1 h. The further steps concerning the preparation of the growth medium, immersion of the seeded layer and the hydrothermal growth are the same as described above.

A blank silicon substrate is used for the growth of nanorods to show the importance of a a seed layer. As can be seen in Figure 3.49a, no rod film is formed but only a few very large rods are present. Comparing the rods grown on the seed layer prepared from different concentrations of Ti-precursor (Figure 3.49b,c and d), arrays of quite dense and high aspect ratio nanorods arrays are formed with a diameter between **130 and 190 nm**, and a length of **1.8 µm** for a precursor concentration of 0.6M (Figure 3.49d). In Figure 3.50, the mean diameter of the nanorods is plotted in function of the concentration of the Ti-precursor used for the seed layers. These results demonstrate that the concentration of the precursor used for the seed layer has a small influence of the diameter of the nanorods grown on these seed layers. Previous work, where lead titanate films were prepared from a precursor consisting the same citratrato-peroxo Ti-precursor, demonstrated that smaller grains were obtained with decreasing precursor concentration [2]. This relation explains the small increase in diameter of the nanorods.

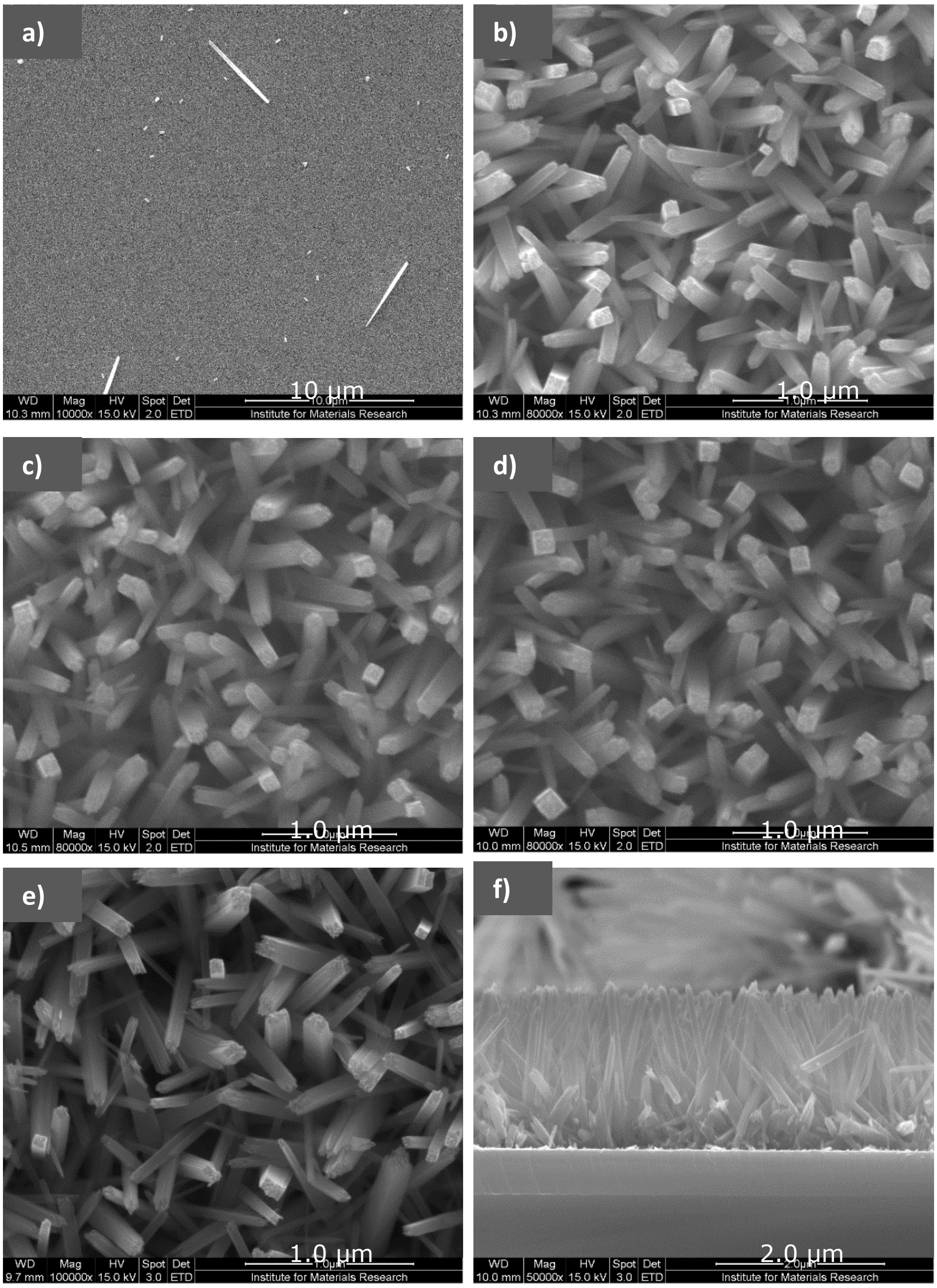

Figure 3.49 SEM images of nanorods grown on a bare silicon substrate (a), a seed layer from the Ti-precursor with concentration of 0.1M (b), 0.2 M (c), 0.4M (d) and 0.6 M (e) and cross SEM image (d) of the nanorod array corresponding to rods of (e).

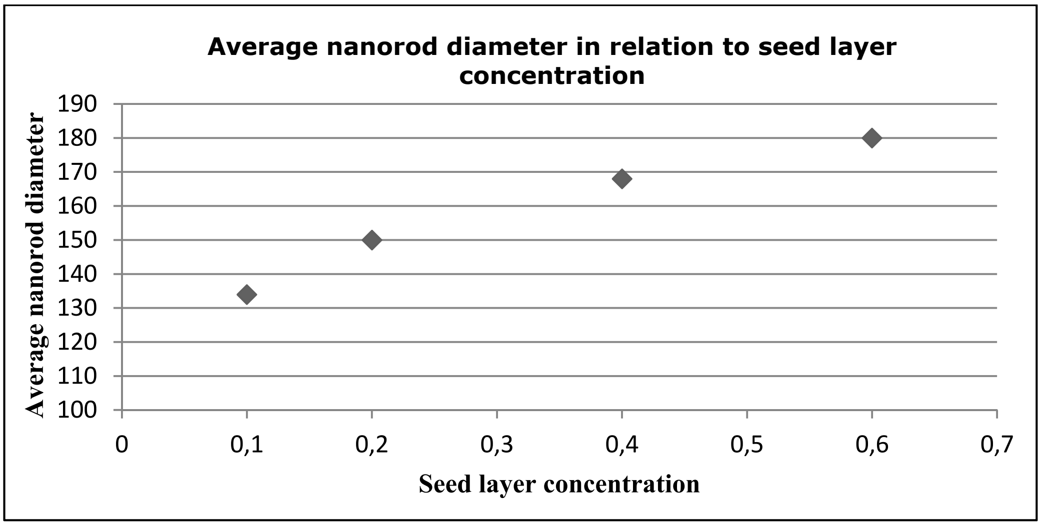

Figure 3.50 The average nanorod diameter in function of the precursor concentration for the deposition of the seed layer.

Raman spectroscopy of the nanorod arrays, given in Figure 3.51, shows that the nanorods consist mostly of rutile (237 cm^{-1}, 444 cm^{-1} and 607 cm^{-1} [21]), although a very small characteristic peak (145 cm^{-1}) of anatase is present. This additional small anatase peak is probably attributed to the anatase fraction present in the seed layer, which is detected by Raman through the nanorods. Due to a small difference in density in the nanorod arrays prepared from diffent seed layers, the intensity of this peak is different for the different used concentrations of precursor.

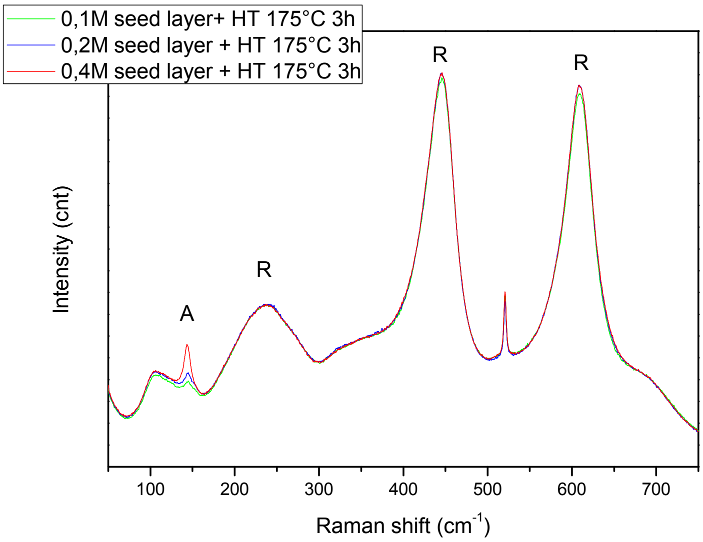

Figure 3.51 Raman spectra of the nanorods grown on a TiO_2 seed layer prepared from a Ti-precursor with different concentrations (A=anatase, R= rutile).

In previous study, rutile nanorods with a diameter of 80 nm and a length of 2 μm were obtained, deposited on a seed layer of 180 nm from a 0.5 M citratoperoxo-precursor, using hydrothermal conditions of 150°C for 6h [51]. In current work, it is demonstrated that even een seed layer as thin as 18 nm (1 layer of precursor deposited [12]) result in an array of nanorods with a comparable length.

Nevertheless, the use of a lower **hydrothermal temperature** (then 175°C) is preferable and therefore, the temperature is decreased till 140°C. Furthermore, the influence of the **hydrothermal time** on the nanorod dimensions and crystal phase is studied, using a seed layer prepared from the 0,4 M Ti-precursor. The following hydrothermal conditions are applied: 3h @175°C, 2h @175°C and 3h@140°C.

Comparing dimensions of the nanorods grown at 140°C (length of 275 nm) and 175°C for 3h (length of 1.6 μm) indicate a decrease in diameter and length of the rods with decreasing temperature. Further, the alignment of the rods also deteriorates with decreasing temperature. In previous study [51], it was concluded that the hydrothermal reaction time influences the nanorod length, while in this study, the **influence of the temperature on the nanorod length** is demonstrated.

Decreasing the time (comparing 175°C 3h and 175°C 2h) also decreases the nanorod dimensions (nanorod length from 1.6 μm to 800 nm), but still maintaining an aspect ratio of 10.

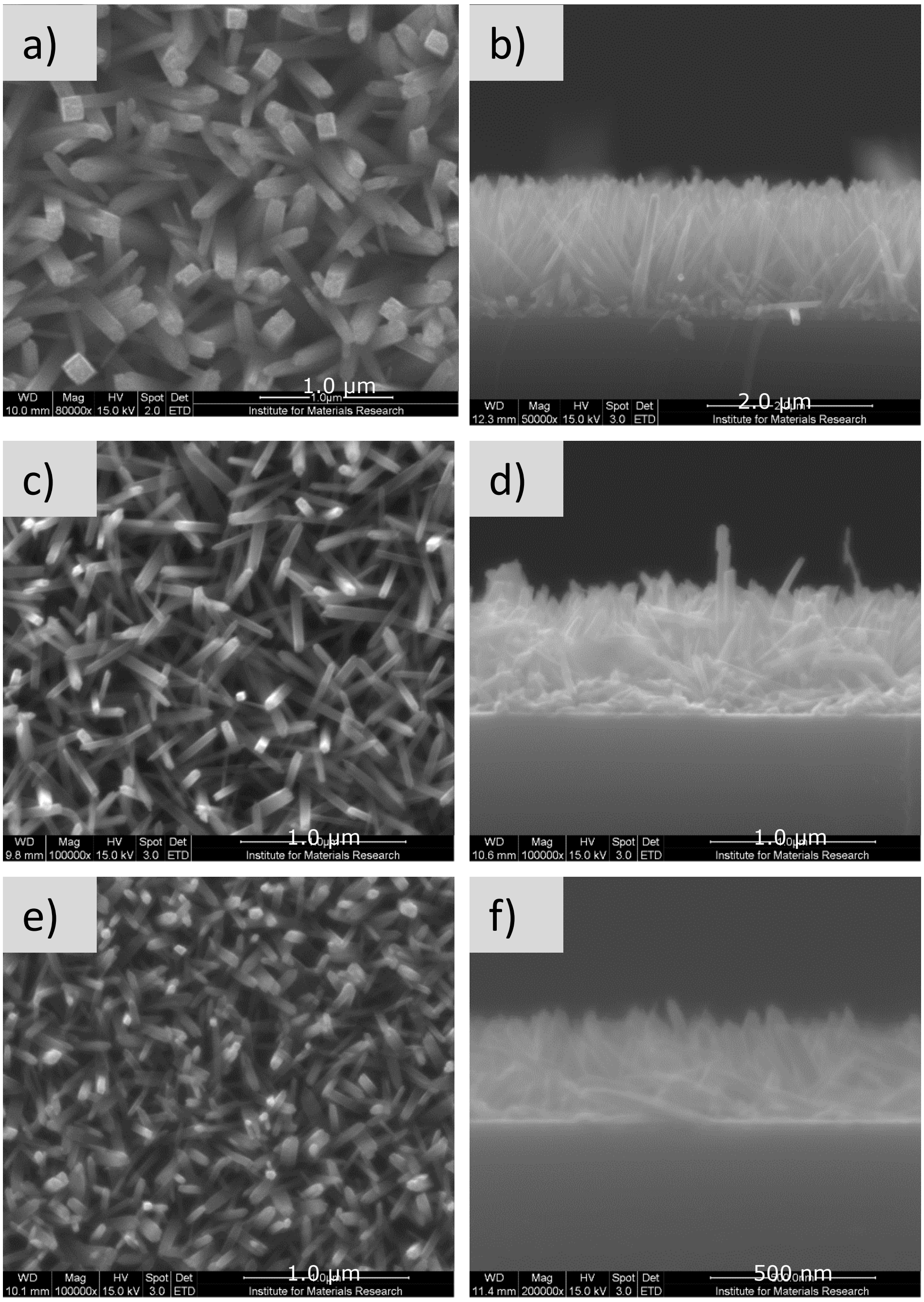

Figure 3.52 SEM images (top view and cross section) of the nanorods grown for 3h at 175°C (a and b), 2h at 175°C (c and d) and 3h at 140°C (e and f).

Comparing the crystal phase of the prepared nanorods, Raman spectra (Figure 3.53) show more distinctive rutile peaks for the growth at 175°C, while for the growth at 140°C the rutile peaks are very broad and low in intensity compared to the broadening of the anatase peak, confirming the smaller nanorods obtained at this temperature. The change in the intensity of the anatase peak compared to the rutile peaks for the nanorods, between the rods prepared at 175°C and 140°C, can not be directed with certainty to an increase of anatase in the nanorods themselves.

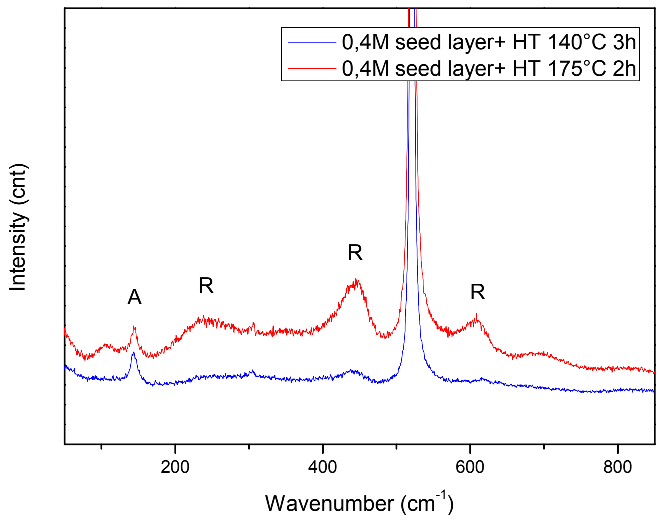

Figure 3.53 Raman spectra of the nanorod arrays grown at 140°C for 3h and at 175°C for 2h.

Furthermore, **the selective growth** of nanorods is studied by the growth on a **patterned seed layer**. Since the seed layer from the TiO₂ dispersion didn't result in a nanorod array, a patterned TiO₂ film is prepared from the citrato-peroxo Ti-precursor. Nevertheless, the patterned films from this precursor, previously studied [52], contains a scum layer between the lines.

Experimental A patterned seed layers is prepared by embossing a CD stamp into a wet precursor film which was deposited by spin coating the 0.4 M Ti precursor [52]. The preparation of the growth medium, immersion of the seeded layer and the hydrothermal growth are the same as described above.

A nicely dense and aligned nanorod array is obtained when grown on a patterned seed layer (Figure 3.54). The nanorods have diameters between 50 and 250 nm and have a very high aspect ratio due to its length of 4 µm (AR between 16 and 80). Thus, both the polydispersity as the aspect ratio of the rods seem to be increased when grown on a patterned seed layer compared to the rods grown on a dense layer. However, the selective growth of the nanorods can not be demonstrated based on the cross-section SEM image, as the thickness of the patterned layer (<100 nm) is very small in comparison with the thickness of the nanorod array.

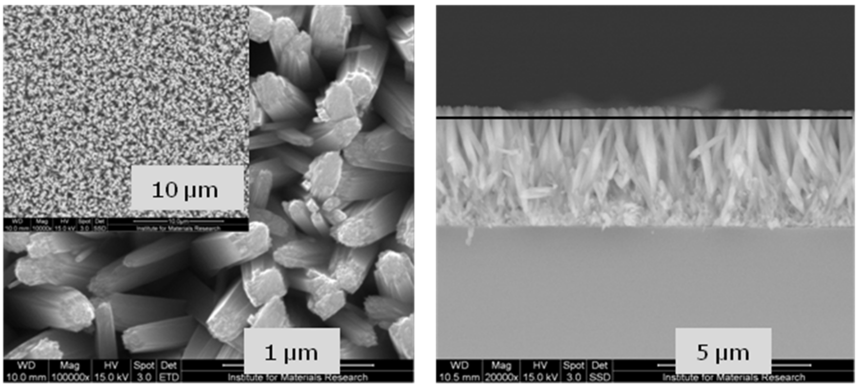

Figure 3.54 SEM top and cross section images of a nanorod array grown on a patterned TiO_2 seed layer.

3.6 Conclusion (TiO_2 nanorods)

Towards the synthesis of anatase TiO_2 nanorods, hydrothermal growth is applied onto a TiO_2 seed layer containing anatase and rutile. It is demonstrated that nanorods can be grown on a seed layer as thin as 18 nm. Furthermore, the influence of the concentration of the precursor used for the seed layer deposition is studied. The results show quite dense array of nanorods with a length of 1.8 µm and a diameter varying from 130 to 190 nm and demonstrate the increase of diameter with increasing the precursor concentration. Decreasing the hydrothermal time from 3 to 2 h decreases the rod length till the half. Decreasing the temperature from 175°C to 140°C reduces the nanorod length from 1.8 µm to 275 nm, confirming the need for a longer treatment when a lower temperature is applied. Although the crystal phase of the seed layer and the nanorods itself could not be distinguished by Raman analysis, a change in anatase intensity compared to the rutile peaks is observed for the nanorods prepared at 140°C, indicating a possible, first step towards nanorods with a higher anatase content. Nevertheless, further research including the use of more (advanced) analysis is necessary

References

1. Truijen, I., Van Bael, M.K., Van den Rul, H., D'Haen, J., and Mullens, J., Synthesis of thin dense titania films via aqueous solution-gel method. J. Sol-gel Sci. Technol., 2007. 41: p. 43-48.
2. De Dobbelaere, C., Hardy, A., D'Haen, J., Van den Rul, H., Van Bael, M.K., and Mullens, J., Morphology of water-based chemical solution deposition (CSD) lead titanate films on different substrates: Toward island formation. J. Eur. Cer. Soc., 2009. 29: p. 1703-1711.
3. De Dobbelaere, C., Mullens, J., Hardy, A., and Van Bael, M.K., Thermal decomposition and spectroscopic investigation of a new aqueous glycolato(-peroxo)Ti(IV) solution-gel precursor. Thermochimica acta, 2011. 520: p. 121-133.
4. Peys, N., Ling, Y., Dewulf, D., Gielis, S., De Dobbelaere, C., Cuypers, D., Adriaensens, P., Van Doorslaer, S., De Gendt, S., Hardy, A., and Van Bael, M.K., V6O13 films by control of the oxidation state from aqueous precursor to crystalline phase. Dalton Transactions, 2013. 42(4): p. 959-968.
5. Riskin, A., De Dobbelaere, C., Elen, K., D'Haen, J., Van den Rul, H., Mullens, J., Hardy, A., and Van Bael, M.K., Deposition of functionalized gold nanoparticles onto modified silicon substrates. Physica status solidi A, 2010(1-8).
6. Stanulis, A., Hardy, A., De Dobbelaere, C., D'Haen, J., Van Bael, M., and Kareiva, A., SnO2 thin films from an aqueous citrato peroxo Sn(IV) precursor. J. Sol-gel Sci. Technol., 2012. 62(1): p. 57-64.
7. Dewulf, D., Peys, N., Van Elshocht, S., Rampelberg, G., Detavernier, C., De Gendt, S., Hardy, A., and MK, V.B., Interfacial reactions of Gd- and Nb-oxide based high-k layers deposited by aqueous chemical solution deposition. Microelectronic engineering, 2011. 88: p. 1338-1341.
8. Van Bael, M.K., Nelis, D., Hardy, A., Mondelaers, D., Van Werde, K., D'Haen, J., Vanhoyland, G., Van den Rul, H., Mullens, J., Van Poucke, L.C., Frederix, F., and Wouters, D.J., Aqueous chemical solution deposition of ferroelectric thin films. Integrated Ferroelectrics, 2002. 45: p. 113-122.
9. Rehg, T.J. and Higgins, G., Spin coating of colloidal suspensions. AlChE Journal, 2004. 38(4): p. 489-501.
10. Rehg, T.J. and Higgins, B.G., Evaporative Convection in spin coating. AlChE Journal, 1992. 38(4): p. 489.
11. Vu, A.T., Nguyen, Q.T., Bui, T.H.L., Tran, M.C., Dang, T.P., and Tran, T.K.H., Synthesis and characterization of TiO2 photocatalyst doped by transition metal ions (Fe3+, Cr 3+ and V5+). Advance in natural sciences: nanoscience and nanotechnology, 2010. 1.
12. Truijen, I., Studie van de invloed van syntheseparameters op de microstructuur van TiO_2 lagen voor fotovoltaïsche toepassingen. Doctoraatsproefschrift, 2007.
13. Negishi, N. and Takeuchi, K., Preparation of photocatalytic TiO transparent thin film by 2 thermal decomposition of Ti-alkoxide with alpha-terpineol as a solvent. Thin solid films, 2001. 392: p. 249.
14. Sarode, M.T., Shelke, P.N., Gunjal, S.D., Khollam, Y.B., Takwale, M.G., Adkar, S.R., Kale, B.B., Mohite, K.C., and Koinkar, P., Effect of annealing temperature on optical properties of titanium dioxide thin films prepared by sol-gel method. International Journal of Modern Physics: Conference series, 2012. 6: p. 13-18.
15. Yu, J.C., Yu, J.G., and Zhao, J.C., Enhanced photocatalytic activity of mesoporous and ordinary TiO2 thin films by surfuric acid treatment. Applied Catalysis B: Environmental, 2002. 36(1): p. 31-43.
16. Barnes, H.A., A handbook of elementary rheology. University of Wales, Institute of non-Newtonian Fluid Mechanics, 2000.
17. Roosen, A., Basic requirements for tape casting of ceramic powders. In Ceramic Transactions,Vol. 1, Ceramic Powder Science II, ed. G. L. Messing, E. R. Fuller and H. Hausner. The American Ceramic Society, 1988. Westerville, OH: p. 675–692.
18. Beusen, J., Van Bael, M.K., Van den Rul, H., D'Haen, J., and Mullens, J., Preparation of a nanoporous nanocrystalline TiO_2 layer by deposition of hydrothermally synthesized nanoparticles. J. Eur. Ceram. Soc., 2007. 27: p. 4529-4535.
19. Chen, Y.J., Stathatos, E., and Dionysiou, D.D., Microstructure characterization and photocatalytic activity of mesoporous TiO2 films with ultrafine anatase nanocrystallites. Surf. Coat. Technol., 2008. 202(10): p. 1944-1950.

20. Arconada, N., Duran, A., Suarez, S., Portela, R., Coronado, J.M., Sanchez, B., and Castro, Y., Synthesis and photocatalytic properties of dense and porous TiO_2-anatase thin films prepared by sol-gel. Applied Catalysis B: Environmental, 2009. 86: p. 1-7.
21. Mazza, T., Barborini, E., Piseri, P., Milani, P., Cattaneo, D., Bassi, A.L., Bottani, C.E., and Ducati, C., Raman spectroscopy characterization of TiO(2) rutile nanocrystals. Physical Review B, 2007. 75(4).
22. www.gwent.org.
23. Boukennous, Y., Benyahia, B., Charif, M.R., and Chikouche, A., Antireflection coating of TiO2 study and deposition by creen printing method. Journal de physique III, 1995. 5: p. 1297-1305.
24. Reed, J.S., Principles of ceramics processing. John Wiley & Sons, 1995.
25. Meenakshi, V., Babayan, Y., and Odom, T.W., Benchtop nanoscale patterning using soft lithography. Journal of chemical education, 2007. 84: p. 1795-1798.
26. ten Elshof, J.E., Khan, S.U., and Göbel, O.F., Micrometer and nanometer-scale parallel patterning of ceramic and organic-inorganic hybrid materials. J. Eur. Cer. Soc., 2010. 30: p. 1555-1577.
27. Haverkorn van Rijsewijk, H.C., Legierse, P.E.J., and Thomas, G.E., Manufacture of laservision discs by a photopolymerization mechanism. Philips Technical Review, 1982. 40: p. 198-309.
28. Xia, Y. and Whitesides, G.M., Soft Lithography. Annual review of materials research, 1998. 28: p. 153-184.
29. Clarson, S.J. and Semlyen, J.A., Siloxane Polymers. Englewood Cliffs, 1993. NJ:Prentice Hall.
30. Lopez, G.P., Biebuyck, H.A., Harter, R., Kumar, A., and Whitesides, G.M., Fabrication and imaging of two dimensional patterns of proteins adsorbed on self- assembled monolayers by scanning electron microscopy. Journal of american chemical society, 1993. 115(23): p. 10774-10781.
31. Meenakshi, V., Babayan, Y., and Odom, T.W., Benchtop Nanoscale Patterning Using Soft Lithography. Journal of chemical education, 2007. 84(11): p. 1795-1798.
32. The hardware autority: Sony DRU. www.cdrinfo.com/sections/reviews, 2004.
33. Tech media network: Tom's Hardware, the authority on tech. Best of media group, 1999-2013.
34. Göbel, O.F., Blank, D.H.A., and Ten Elshof, J.E., Thin films of conductive ZnO patterned by micromoulding resulting in nearly isolated features. Applied materials &Interfaces, 2010. 2(2): p. 536-543.
35. Marzolin, C., Smith, S.P., Prentiss, M., and Whitesides, G.M., Fabrication of glass microstructures by micro-moulding of sol-gel precursors. Adv. Mater., 1998. 10: p. 571-574.
36. Göbel, O.F., Nedelcu, M., and Steiner, U., Soft Lithography of Ceramic Patterns. Advanced Functional Materials, 2007. 17: p. 1131-1136.
37. Khan, S.U., Gobel, O.F., Blank, D.H.A., and Elshof, J.E., Patterning Lead Zirconate Titanate Nanostructures at Sub-200-nm Resolution by Soft Confocal Imprint Lithography and Nanotransfer Molding. ACS Applied Material Interfaces, 2009. 1(10): p. 2250-2255.
38. Ahn, S.H., Min, J.-H., Kim, J., and Moon, J., Process mechanism of vacuum-assisted microfluid lithography with ceramic colloidal suspensions. J. Amer. Ceram. Soc., 2008. 91(7): p. 2143-2149.
39. Macak, J.M., Tsuchiya, H., Ghicov, A., Yasuda, K., Hahn, R., Bauer, S., and Schmuki, P., TiO2 nanotubes: self-organized electrochemical formation, properties and applications. Current opinion in solid state and materials science, 2007. 11: p. 3-18.
40. Chen, B., Lu, K., and Ramsburg, K., ZnO submicrometer rod arrays by soft lithographic micromoulding with high solid loading nanoparticle suspension. J. Amer. Ceram. Soc., 2013. 96(1): p. 73-79.
41. Göbel, O.F., Branfield, T.E., Stawski, T.M., Veldhuis, S.A., Blank, D.H.A., and Ten Elshof, J.E., Stacks of functional oxide thin films patterned by micromoulding. Applied materials &Interfaces, 2010. 2(11).
42. Zhu, G., Pan, L., Xu, T., Zhao, Q., Lu, B., and Sun, Z., Microwave assisted CdSe quantum dot deposition on TiO2 films for dye-sensitized solar cells. Nanoscale, 2011. 3: p. 2188.
43. Dewalque, J., Cloots, R., Mathis, F., Dubreuil, O., Krins, N., and Henrist, C., TiO2 multilayer thick films (up to 4 µm) with ordered mesoporosity: influence of template on the film mesostructure and use as high efficiency photoelectrode in DSSCs, . J. Mater. Chem., 2011. 21: p. 7356.
44. Varghese, O.K., Paulose, M., and Grimes, C.A., Long vertically aligned titania nanotubes on transparent conducting oxide for highly efficient solar cells. Nature Nanotechnology, 2009. 4(592).

45. Yu, J., Fan, J., and Lv, K., Anatase TiO2 nanosheets with exposed (001) facets: improved photoelectric conversion efficiency in dye-sensitized solar cells. Nanoscale, 2010. 2: p. 2144.
46. Snaith, H.J. and Schmidt-Mende, L., Advances in liquid-electrolyte and solid-State dye-sensitized solar cells. Advance Materials, 2007. 19: p. 3187.
47. Roberson, L.B., Poggi, M.A., Kowalik, J., Smestad, G.P., Bottomley, L.A., and Tolbert, L.M., Correlation of morphology and device performance in inorganic-organic TiO2-polythiophene hybrid solid-state solar cells. Coordination Chemistry Reviews, 2004. 248: p. 1491.
48. Guo, M., Diao, P., Wang, X., and Cai, S., The effect of hydrothermal growth temperature on preparation and photoelectrochemical performance of ZnO nanorod array films. Journal of solid state chemistry, 2005. 178: p. 3210.
49. Peng, B., Jungmann, G., Jäger, C., Haarer, D., Schmidt, H.-W., and Thelakkat, M., Systematic investigation of the role of compact TiO2 layer in solid state dye-sensitized TiO2 solar cells. Coordination Chemistry Reviews, 2004. 248: p. 1479-1489.
50. Liu, B. and Aydil, E.S., Growth of oriented single-crystalline rutile TiO_2 nanorods on transparent conducting substrates for dye-sensitized solar cells. Journal of the American Chemical Society, 2009. 131: p. 2985-3990.
51. Baeten, L., Nanorod metal oxide based electrodes and their application in hybrid photovoltaics. Doctoraatsproefschrift, 2012.
52. De Dobbelaere, C., Lagetemperatuursdepositie en structuurvorming als nieuwe uitdaging voor waterige oplossing-gel route: een case studie met PbTiO3. Doctoraatsproefschrift, 2011.

PART II

Chapter 4: TiO_2 nanostructures in photocatalysis

Abstract

The photocatalytic performances of the different nanostructured TiO_2 films (lines and squares), prepared in previous chapter via micromoulding the aqueous TiO_2 dispersion, using the CD and DVD as mould, are studied in this chapter, and compared with the smooth TiO_2 layer. For that purpose, the photobleaching and photomineralization of the dye Rhodamine 6G under UV illumination in the presence of the different TiO_2 morphologies is analyzed and evaluated in comparison with the activity of the dense TiO_2 films. This preliminary study[1] is aimed at the investigation of the role of morphology/topography on the efficiency of the heterogeneous photocatalyst, as all films are prepared from the same TiO_2 dispersion. Furthermore, the first step in the study of the application of patterned layers as self-cleaning coatings is presented.

---

[1] This study is carried out within the scope of a common research project with the University of Antwerp, financially supported by FWO (project number G.0237.09).

The photocatalytic activity of titania films are affected by the structural characteristics of crystalline structure, surface morphology, specific surface area and porosity, etc [1, 2], which depends heavily on thin film fabrication techniques. Different chemical deposition techniques are applied: dip coating [2, 3], electrochemical anodization [4], pulsed laser deposition [5], spraying [6], glancing angle deposition [7], microcontact printing [8], spin coating [9], ink-jet printing [10] to prepare different morphologies such as dense/thin layers [2, 6, 11] mesoporous layers [8, 12], patterned structures [13], columned layers [4, 7] etc. The thicknesses of the films vary from 100 nm for the dense layers till 10 µm for the porous films. In addition, the industrial demands encourage the development of water based precursors especially for water treatment applications.

Although a lot of research has been done on the influence of the properties of TiO_2 (particle size, crystal phase) on the photocatalytic activity, less is known about the morphological influence of the film on the photocatalytic activity. Therefore, a comparative study on the photocatalytic degradation of (various) dyes by titania films with various nanostructures is desirable [14]. As the nanostructured films in this thesis are all prepared from the same TiO_2 dispersion, the influence of surface chemistry is minimized which is beneficial to study only the effect of surface topography.

4.1 Photocatalytic degradation on nanostructured films

In this work, the photocatalytic activity[2] of the TiO_2 films is tested via preliminary experiments. For this purpose, the photodegradation of the cationic dye Rhodamine 6G (Rh6G) in aqueous medium, is evaluated as a model.

An experimental procedure is followed, based on an international standard, the BS ISO 10678: 2010 norm [15]. Some differences between our set up and the norm are, listed in Table 4.1: (a) the use of Rhodamine 6G is instead of methylene blue, as methylene blue have shown in previous experiments some photo-activity without the presence of TiO_2, and (b) a higher concentration of the dye compared to the norm as a minimum concentration is required to be detected in TOC.

	ISO norm	**Present work**
Concentration dye	$1*10^{-6}$ M Methylene Blue	$2*10^{-5}$ M Rhodamine 6G
Geometrical surface	100-1500 mm^2	1250 mm^2
Amount of dye solution	35 ml (50 ml for 1000 mm^2)	70 ml

---

[2] This work was done in cooperation with the group Adsorption and Catalysis of UA (M. Kus, V. Meynen, P.Cool)

Table 4.1 Overview of some measuring conditions prescribed in the ISO norm compared to the conditions applied in present work.

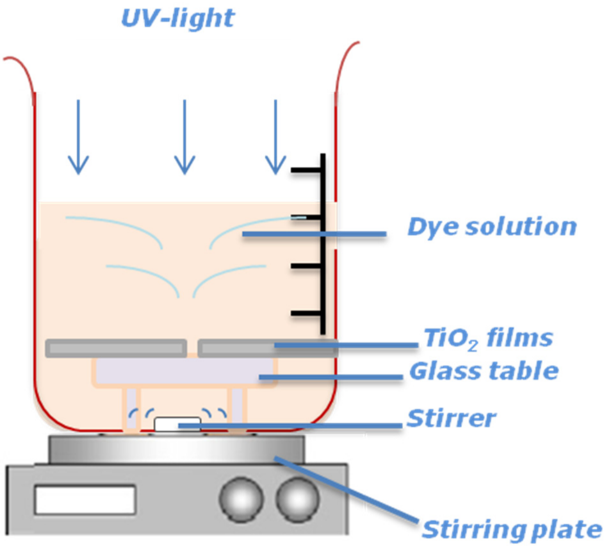

Figure 4.1 Schematic representation of the experimental set up for photocatalytic experiments on films applied in this work.

As illustrated in Figure 4.1, the catalyst (film) is brought in the solution, on top of a small porous glass table at the bottom of the beaker, with the TiO_2 surface pointed upwards. To provide a homogeneous material flux and a uniform contact between dye solution and TiO_2 surface, the dye solution is stirred by means of a stirring plate and a stirrer which is located underneath the glass table.

First the **adsorption-desorption** equilibrium between the surface of the catalyst and the dye is determined, without UV irradiation, in order to define the time interval needed in the photocatalytic experiments. By measuring the absorbance of the dye solution, in time intervals (e.g. each 10 minutes) with UV-Vis, the equilibrium is reached when the absorbance approaches a constant value.

Then the dye solution with catalyst, is placed under an UV lamp by which the titania surface is activated and the dye is degraded. The photocatalytic efficiency is studied by parallel UV-Vis and TOC measurements, which lack in most reported studies.

An overall photocatalytic reaction can mainly be divided into 5 steps, represented in Figure 4.2:

1. Mass transfer of the organic contaminant(s) (e.g. A) in the bulk solution to the TiO_2 surface.
2. Adsorption of the organic contaminant(s) onto the photon activated TiO_2 surface (i.e. surface activation by photon energy occurs simultaneously in this step).
3. Photocatalysis reaction for the adsorbed phase on the TiO_2 surface (e.g. A/B).
4. Desorption of the intermediate(s) (e.g. B) from the TiO_2 surface.

5. Mass transfer of the intermediate(s) (e.g. B) from the interface region to the bulk fluid.

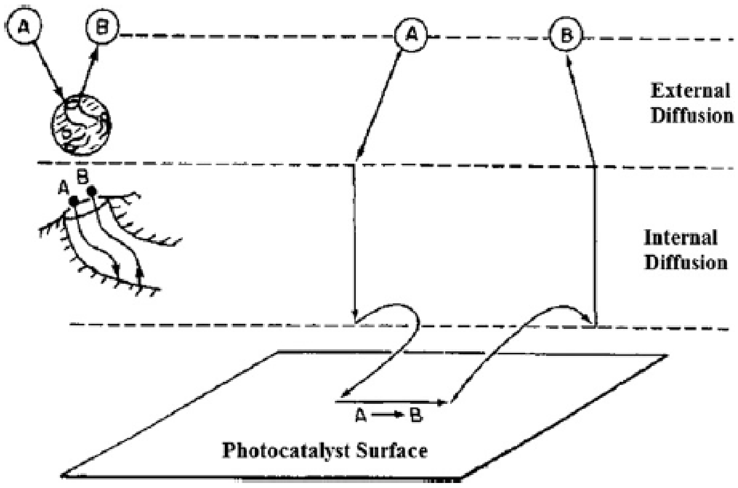

Figure 4.2 General steps in heterogeneous catalytic reaction [16].

The different TiO_2 films studied in this chapter are: the smooth layers, the line and square patterned films from the CD stamp and the line and square patterned films from the DVD stamp.

Experimental[3] The dense layers are prepared on a SPM/APM glass substrate by spin coating the TiO_2 dispersion at a spin velocity combination of 1000 rpm (@500 rpm/sec, 30 s) + 3000 rpm (@500 rpm/sec, 30 sec), followed by a heat treatment at 80°C 2′, 200°C 5′ and 450°C 1h. The line patterns (indicated with the symbol '//') are deposited on top of the dense layer, by spin coating 6 drops of the TiO_2 dispersion (filter of 0,2 μm), using a spin speed of 350 rpm for 30 sec. The PDMS stamp (from CD or DVD) is then pressed into the wet film and pressure is applied by the micrometer (semi-automated system). A thermal treatment at 80°C for 15 minutes is followed after which the stamp is carefully removed after cooling down. A further treatment with UV-O_3 (50°C for 20 minutes) and at 450°C for 1h is applied. Square patterns (indicated as '#') are prepared starting from the line patterns as described above (after UV-O_3 treatment). applying the PDMS stamp (from CD or DVD) into the wet film (prepared as above) in a direction perpendicular to the direction of the lines of the first layer. The post treatment is the same as for the line patterns.

The photocatalytic degradation is studied in 70 ml of a 2.10^{-5}M Rhodamine 6G solution, (each time a few ml) under UV irradiation (emitted by a 100 Watt Hg-lamp) at 526 nm. The surface area of the catalyst is 1250 mm^2 (2 substrates of 25* 25 mm^2) and the photodegradation is analyzed (by measurement of the absorption of the dye via UV-Vis

---

[3] The experimental parameters of the samples are not described in detail there the results obtained from the photocatalytic experiments are not used to compare with other results reported in this thesis.

spectroscopy at 526 nm, each 10 minutes, during 120 minutes). The photomineralization is studied in parallel via microvolume (μV) TOC, a destructive method which only requires a very small volume of the solution (±650 μL) for each measurement.

Three batches of samples are prepared with the same procedure and used for the evaluation of the photocatalytic degradation of Rhodamine 6G under UV irradiation. A blank glass substrate is measured as a reference.

The measured absorbances of Rhodamine 6G at the wavelength of 526 nm are converted into concentrations via the law of Lambert-Beer (equation 37, Chapter 1). The extinction coefficient is determined by a calibration curve. The catalytic activity is calculated by following formula:

$$\%cat = \frac{C_i - C_f}{C_i}.100$$

With C_i the initial concentration and C_f the final concentration of the dye.

The μV-TOC analysis consists of two separate measurements in which (1) the total amount of carbon is measured and (2) the total amount of inorganic carbon (IC) is determined. The total amount of organic carbon is then calculated by following equation:

$$TOC = TC - IC$$

The decrease of Rhodamine 6G in function of time, analyzed with UV-Vis and TOC, on the **first batch** of samples, is represented in Figure 4.3 and Figure 4.4, respectively and summarized in Table 4.2. The adsorption-desorption is indicated by the negative time scale.

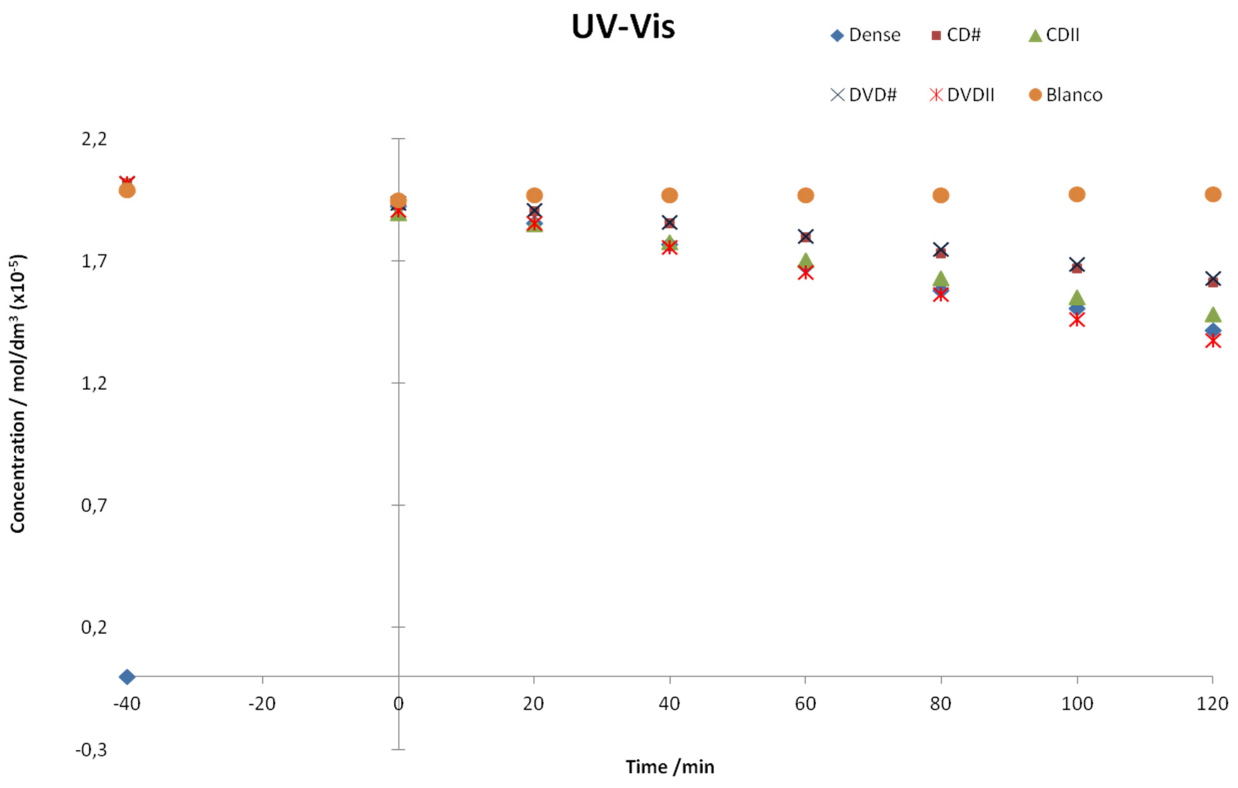

Figure 4.3 Changes of Rhodamine 6G concentration with time, measured by UV-Vis, during photocatalytic reaction by dense layers and patterned layers (from CD and DVD stamps) of batch 1.

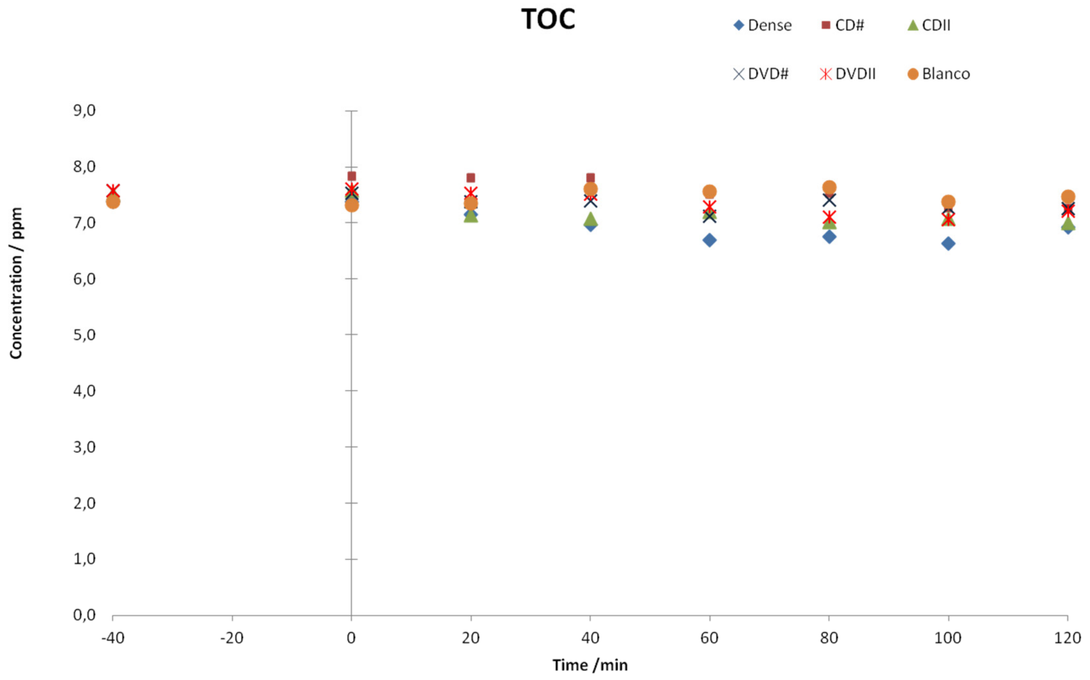

Figure 4.4 Changes of Rhodamine 6G concentration with time, measured by µTOC, during photocatalytic reaction by dense layers and patterned layers (from CD and DVD stamps) of batch 1.

	UV-Vis			***TOC***
	% adsorbed Rh6G	% degraded Rh6G (at 60 min)	% degraded Rh6G (at 120 min)	% degraded Rh6G (at 120 min)
Dense layers	4.7	12.9	23.6	6.2
Lines from CD	5.7	10.2	21.8	7.7
Lines from DVD	5.4	13.3	27.8	5.3
Squares from CD	4.5	6.8	16.3	7.4
Squares from DVD	3.9	7.2	16.0	3.7

Table 4.2 Table of the catalytic activity measured by UV-Vis and TOC of the different films of batch 1.

Concerning the samples of batch 1, UV-Vis analysis shows the highest degradation for the lines prepared from the DVD stamp while the lowest degradation is observed for the squares prepared from the DVD stamp. The % degradation (at 120 min) decreases as follow: DVD// > Dense layers > CD// >CD # >DVD # while the expected sequence, based on the calculated area enhancement factor (AEF, Chapter 3 section 3.4), would be DVD # > CD# > DVD // >CD // > dense layers, if only the specific surface area influences the photocatalytic activity.

The degradation profile obtained by TOC (Figure 4.4), shows a different trend whereas the lines and the squares from the CD stamp show the highest degradation of Rh6G into CO_2, followed by the dense layers. The lowest degradation into CO_2 is observed for the squares from the DVD stamp.

A possible explanation for this unexpected trend is a **limited diffusion** of the dye and/or the intermediates in the areas between the lines and the squares (cavities), which influences the refreshment of the liquid (mass transfer of the initial molecules and intermediates, Figure 4.2) at the structured surface and can cause the occurrence of dead volume within the cavities

- On the one hand, this diffusion effect would become more significant at decreasing pattern dimensions and when comparing lines with squares.
- On the other hand, when refreshment of the liquid in the cavities of the lines or squares is hindered, only the top of the nanostructures would be active, showing a higher activity for the patterns from the DVD stamp than from the CD stamp.

The repeatability[4] is studied by reusing the same samples of batch 1, after washing away the residues of previous experiment, in a new catalytic experiment under the same conditions. The new catalytic activities are listed in Table 4.3.

	% Degraded Rh6G (UV-Vis) of batch 1	
		After cleaning
Dense Layer	23.6	11.8
Lines from CD	21.8	13.5
Lines from DVD	27.8	20.5
Squares from CD	16.3	11.8
Squares from DVD	16.0	11.7

Table 4.3 Catalytic activities of the remeasurement of the samples of batch 1 after cleaning with water with the first results of batch 1 in grey for comparison.

After remeasurement, all the catalytic activities have decreased but still the same trend is observed. Possible reasons for this decrease are (i) a decrease of TiO_2 surface (e.g. by dispersion of the film in the dye solution of the previous catalytic experiment) or (ii) due to the adsorption of residues of the dye (or intermediates) of the previous experiment, limiting the available active sites for the dye.

Photocatalytic experiments on the samples of **batch 2 and 3** are carried out using the same experimental conditions as described before and summarized in Table 4.4.

	Batch 1		Batch 2		Batch 3	
	UV-Vis	*TOC*	*UV-Vis*	*TOC*	*UV-Vis*	*TOC*
Dense layer	23.6	6.2	/	/	23.5	6.5
Lines from CD	21.8	7.7	23.9	10.1	/	/
Lines from DVD	27.8	5.3	16.9	8.9	25.6	5.5
Squares from CD	16.3	7.4	18.9	3.0	/	/
Squares from DVD	16.0	3.7	15.3	1.3	26.9	9.5

Table 4.4 Table of the catalytic activities measured by UV-Vis and TOC of the different films of batch 2 and 3, with the results from batch 1 in grey for comparison.

The UV-Vis results, in Table 4.4, demonstrate reproducible results for the dense layer while for the other samples, each batch shows different activities and a different trend. Furthermore, it is noticed that only for batch 3, the DVD patterns show quite high degradation percentages (in comparison with the results of the previous batches). The difference in preparation of the samples exist in the fact that for batch 3, an unused PDMS stamp is used, while for the other batches, the stamps are reused after cleaning them ultrasonically with nitric acid and water. The high activities for the sample in batch 3 could indicate that the DVD stamps are more sensitive for reuse, as they can contain still some residues from the previous deposition due to the same limited diffusion of liquids.

---

[4] The absolute difference between two independent measurements carried out within a short time period, for the same sample in the same laboratory by the same operator using the same experimental and analytical measuring device.

Also the results from the TOC measurements of batch 2 and 3 show a different trend compared to batch 1 (Table 4.4). While for the dense layers, similar results are obtained, the results from the other samples totally contradicts the above hypothesis

Aiming to evaluate the influence of the topography on photocatalysis, the above results not only demonstrate a variation in results between different batches, but also only a small, almost negligible difference in activity between the dense and the patterned layers.

When the photocatalytic activity of the dense layer is expressed by the rate constant k, which is determined from the linear relation between the logarithm of relative concentration of rhodamine 6G ($\ln(C/C_0)$) and irradiation time, a value of $19*10^{-4}$ min^{-1} is obtained for an illumination time of 120 min. This result is higher compared to the rate constant of a commercial TiO_2 film (Saint-Gobain bioclean© glass[5], as reference), which is $5*10^{-4}$ min^{-1} for an illumination time of 300 min [10], indicating the deposited TiO_2 (from the TiO_2 dispersion) to be photocatalytic active.

Concerning the patterned samples, an increase of photocatalytic activity with decreasing feature size of TiO_2 square patterns, from 400 µm to 100 µm was demonstrated by Chen et al.[13]. Our preliminary results only show that the photocatalysis on nanostructured films is much more complicated and further research is necessary, taken the following factors into account:

- Due to the lack of reproducibility between the results of different batches, an **improvement of the samples** towards sample handling and complete pattern formation may be needed. Further, the influence of topography may be increased by an increase of aspect ratio of the patterned films.
- The phenomenon of **limited diffusion** in nanocavities of nanostructured films, as mentioned earlier, which result in low degradation compared to the dense layer
- the scattering and/or absorption of the irradiated UV light by the protruding parts of the nanopatterns, which could lead to a loss of the incoming light. This is known as **shadow effect** and is expected to be the highest for the square patterns.

Conclusion

In this chapter, the photocatalytic degradation of Rhodamine 6G in the presence of the nanostructured films discussed in chapter 3 (lined and square patterned films) is followed, in order to study the effect of topography on their photocatalytic performance, with a dense layer as reference. Results confirm the photocatalytic activity of the synthesized TiO_2, as for the

---

[5] Saint-Gobain glass is photocatalytically active commercial glass, available in UK Ltd, Eggborough, UK.

dense layer a degradation of 25% is obtained after 120 minutes of UV illumination, based on UV-Vis analysis. For the patterned films, comparable degradation efficiencies are obtained. Nevertheless, TOC measurements give no information as different trend are obtained for each batch of samples. These preliminary results only indicate the need for further research. On the one hand, the samples require some improvement mostly concerning the pattern formation, as different results are obtained between samples of a different batch. On the other hand, other processes such as diffusion and light absorption, seem to play a role as comparable efficiencies are obtained with the dense, unpatterned layer. Nevertheless, these kinds of nanostructured films are not yet studied elsewhere, which make them attractive systems for further research.

4.2 TiO_2 nanostructured films for self-cleaning applications[6]

The leaves of the lotus flower show a phenomenon which protect itself against contamination or pollution even when the lotus is surrounded by muddy water. This repellence against water has been explained by the surface roughness as its surface is structured at different hierarchical levels. The hierarchical structure, which can consist of two or more layers of different sizes, minimizes the wetting of the surface, due to the air that is enclosed in the cavities of the structure. This mechanism is described by the Cassie-Baxter regime (Chapter 1 section 1.6.1.2) en illustrated in figure 1.30. Besides the surface roughness, also the arrangement/alignment of the surface structures such as in tubule-like and platelet like structures, influences the wettability.

In order to investigate the hydrophobic properties of the patterned structures (without scum layer) described in this work in Chapter 3, water contact angle (WCA) measurements are applied. In Figure 3.43, it was already shown that the TiO_2 line patterns from the CD are hydrophobic but after post treatment with UV-Ozon (to remove possible 'residues' of the stamp), the patterns showed superhydrophilic behavior (WCA=0). As we started from a hydrophilic dense layers, the patterning increased the hydrophilicity, as described by the Wenzel equation (Chapter 1, equation 41), considering the aspect ratio of the nanostructures as too low to enclose air drops.

To enhance the hydrophobic properties of nanostructures, modification with modified surface free energy materials such as fluoroalkylsilanes, is frequently applied [17]. In this thesis, perfluorodecyltriethoxysilane and perfluorohexyltrichlorosilane are used as hydrophobing agents to increase the WCA of the TiO_2 lines and squares from the CD stamp.

Experimental The CD lines and squares, as well before UV-O_3 treatment as after, are chemically treated with hydrophobing agents. The CD lines and squares before UV-O_3 treatment are immersed overnight in a beaker with 0.4 g (= 0.288 ml)

---

[6] These experiments are carried out in cooperation with Sirris (Dr. H. Van den Rul)

perfluorodecyltriethoxysilane in 38.2 ml hexane +1 ml H_2O/Hac pH 3, followed by drying at 100°C for 1h. For the lines and squares after UV-O_3 treatment two different hydrophobing agents are applied: perfluorodecyltriethoxysilane and perfluorohexyltrichlorosilane. 2 v% hydrophobing agent is added to a mixture of ethanol/ water (95/5 v%). After 5 minutes of condensation, the samples are immersed 1-2 minutes in the solution. Then the samples are rinsed with ethanol and dried at 110°C for 5-10 minutes. To enhance the hydrolysis/condensation, the ethanolic solution is acidified with acetic acid to a pH of 4,5-5,5 (referred in Table 4.5 as acid catalyst). Cleaned (uncoated) glass substrate (IPA/H_2O and UV-O_3) are used for comparison.

Morphology	**Hydrophobing agent**	WCA before	WCA after
CD Lines (before UV-O_3 treatment)	perfluorodecyltriethoxysilane	106°	115°
CD Squares (before UV-O_3 treatment)	perfluorodecyltriethoxysilane	106°	116°
CD lines (after UV-O_3 treatment)	perfluorodecyltriethoxysilane	23°	78° (±8)
CD lines (after UV-O_3 treatment)	perfluorohexyltrichlorosilane	0°	106° (±6)
CD Squares (after UV-O_3 treatment)	perfluorodecyltriethoxysilane	0°	52° (±2)
CD Squares (after UV-O_3 treatment)	perfluorohexyltrichlorosilane	0°	105° (±2)
CD lines (after UV-O_3 treatment)	Perfluorodecyltriethoxysilane + acid catalyst	13°	78° (±9)
CD lines (after UV-O_3 treatment)	Perfluorohexyltrichlorosilane + acid catalyst	10°	109°
CD Squares (after UV-O_3 treatment)	Perfluorodecyltriethoxysilane + acid catalyst	20°	82° (±4)
CD Squares (after UV-O_3 treatment)	Perfluorohexyltrichlorosilane + acid catalyst	0°	95° (±12)
Cleaned glass substrate	Perfluorodecyltriethoxysilane + acid catalyst	28°	114° (±1)
Cleaned glass substrate	Perfluorohexyltrichlorosilane + acid catalyst	18°	108°

Table 4.5 Table of the obtained water contact angles before and after hydrophobizing the different TiO_2 nanopatters, with cleaned glass substrates as reference.

The results are summarized in Table 4.5. The patterns which are not UV-O_3 treated only shows a very small, almost negligible increase of WCA after modification. The modification with silane occurs via a reaction between silane and the oxide, thus surface groups such as TEAH or the PDMS residues may hinder this reaction. Therefore, UV-O_3 treated patterns are applied for hydrophobising. Besides perfluorodecyltriethoxysilane as agent, also perfluorohexyltrichlorosilane is used to exclude the influence of agentia (e.g due to size or volume of the molecule).

The results show that using the perfluorohexyltrichlorosilane agent, the WCA increases more than when perfluorodecyltriethoxysilane is used, and result in hydrophobic surfaces (WCA> 90°). To enhance the hydrolysis/condensation of the silane with TiO_2, an acid catalyst (acetic acid) is added to the ethanolic solution. For both the treatments with perfluorodecyltriethoxysilane or perfluorohexyltrichlorosilane, no distinctive increase of WCA is observed when the acid catalyst is used. This would mean that the reaction of silane with the oxide can take place without the use of an acid catalyst, although the acid catalyst show a little improvement.

The highest WCA found after hydrophobising the patterned samples with the silanes is 109°C, for the modification with perfluorohexyltrichlorosilane, in the presence of the acid catalyst The mostly observed WCA of a fluoro-treated surface is 120°C which can be further increased by patterning. However, comparing this result with the WCA measured after hydrophobising a (flat, blank) glass substrate (i.e.114°) indicates that the structuring of the patterned samples in this work is not distinctive enough to effect the water contact angle towards superhydrophobicity. This is probably caused by the limited (small) aspect ratio and thus the limited roughness of TiO_2 nanopatterns does not optimally enclose the air which influences the wetting behavior towards (super)hydrophobicity. Nevertheless, we believe that patterns with a higher aspect ratio will show more potential as hydrophobic surfaces, as they will show a higher roughness.

Conclusion

In this section, the potential of the lined and square patterned structures, described in chapter 3, towards (super)hydrophobic coatings is evaluated. As the nanostructures as such obtain superhydrophilic properties, modification with fluorosilanes is applied, which show a small increase of the water contact angle. Nevertheless, the water contact angle of the nanostructures after modification is comparable to the water contact angle of a modified blank substrate. This indicates that the topography of the nanostructures is not distinctive enough to influence the contact angle in such a way that the nanostructures become superhydrophobic. Finally, it is suggested that an increase of aspect ratio of the patterns could show a higher potential towards hydrophobic surfaces, as the cavities will be higher for air bubble entrapment although modification would possibly be needed anyhow.

References

1. Hoffmann, M.R., Martin, S.T., Choi, W., and Bahnemann, D.W., Environmental applications of semiconductor photocatalysis. Chemical Review, 1995. 95(69-96).
2. Di Paola, A., Addamo, M., Bellardita, M., Cazzanelli, E., and Palmisano, L., Preparation of photocatalytic brookite thin films. Thin solid films, 2007. 515: p. 3527-3529.
3. Arconada, N., Duran, A., Suarez, S., Portela, R., Coronado, J.M., Sanchez, B., and Castro, Y., Synthesis and photocatalytic properties of dense and porous TiO_2-anatase thin films prepared by sol-gel. Applied Catalysis B: Environmental, 2009. 86: p. 1-7.
4. Lai, Y.-K., Huangc, J.-Y., Zhanga, H.-F., Subramaniamb, V.-P., Tangb, Y.-X., Gongb, D.-G., Sundarb, L., Suna, L., Chenb, Z., and Lina, C.-J., Nitrogen-doped TiO2 nanotube array films with enhanced photocatalytic activity under various light sources. Journal of Hazardous materials, 2010. 184: p. 855-863.
5. Zhao, L., Jiang, Q., and Lian, J., Visible-light photocatalytic activity of nitrogen-doped TiO_2 thin film prepared by pulsed laser deposition. Applied Surface Science, 2008. 254: p. 4620-4625.
6. Skorb, E.V., Antonouskaya, L.I., Belyasova, N.A., Shchukin, D.G., Möhwald, H., and Sviridov, D.V., Antibacterial activity of thin-film photocatalysis based on metal-modified TiO_2 and TiO_2:In_2O_3 nanocomposite. Applied Catalysis B: Environmental, 2008. 84: p. 94-99.
7. Li, Z., Zhu, Y., Zhou, Q., Ni, J., and Zhang, Z., Photocatalytic properties of TiO2 thin films obtained by glancing angle deposition. Applied surface Science, 2011.
8. Chen, Y.J., Stathatos, E., and Dionysiou, D.D., Microstructure characterization and photocatalytic activity of mesoporous TiO2 films with ultrafine anatase nanocrystallites. Surf. Coat. Technol., 2008. 202(10): p. 1944-1950.
9. Yu, H.-F. and Wang, C.-W., Photocatalysis and characterization of the gel-derived TiO_2 and P-TiO_2 tranparent thin films. Thin solid films, 2011. 519: p. 6453-6458.
10. Arin, M., Lommens, P., Hopkins, S.C., Pollefeyt, G., Van der Eycken, J., Ricart, S., Granados, X., Glowacki, B.A., and Van Driessche, I., Deposition of photacatalytically active TiO_2 films by inkjet printing of TiO_2 nanoparticle suspensions obtained from microwave-assisted hydrothermal synthesis. Nanotechnology, 2012. 23.
11. Gan, W.Y., Chiang, K., Brungs, M., Amal, R., and Zhao, H., Dense TiO_2 thin film: photoelectrochemical and photocatalytic properties. International Journal of Nanotechnology, 2007. 4(5).
12. Arin, M., Lommens, P., Avci, N., Hopkins, S.C., De Buysser, K., Arabatzis, I.M., Fasaki, I., Poelman, D., and Van Driessche, I., Inkjet printing of photocatalytically active TiO_2 thin films from water based precursor solutions. J. Eur. Cer. Soc., 2011. 31(6): p. 1067-1074.
13. Chen, D., Gao, Y., Wang, G., Zhang, H., Lu, W., and Li, J., Surface Tailoring for controlled photoelectrochemical properties: effect of patterned TiO_2 microarrays. Journal of physical Chemistry C, 2007. 111: p. 13163-13169.
14. Song, X.M., Wu, J.M., and Yan, M., Photocatalytic degradation of selected dyes by titania thin films with various nanostructures. Thin Solid Films, 2009. 517(15): p. 4341-4347.
15. BSISO10678:2010, Fine ceramics (advanced ceramics, advanced technical ceramics)- Determination of photocatalytic activity of surfaces in an aqueous medium by degradation of methylene blue. BSI Standards publication, 2010.
16. Fogler, H.S., Elements of Chemical Reaction Engineering: Chapter 10: Catalysis and Catalytic Reactors. Prentice-Hall PTR Inc, 1999: p. 581-685.
17. Nakajima, A., Fujishima, A., Hashimoto, K., and Watanabe, T., Preparation of Transparent Superhydrophobic Boehmite and Silica Films by Sublimation of Aluminum Acetylacetonate. Advance Materials, 1999. 11(16): p. 1365.

Chapter 5: TiO_2 nanostructures in biomedical applications

Abstract

In this chapter[1], the influence of the different nanotopographies (prepared in chapter 3) on the cell growth is studied, in view of the application of TiO_2 as implant material. Hereto, human dental pulp stem cells (hDPSCs), isolated from dental pulp tissue, are seeded onto various titanium nanostructures (as scaffold) and incubated with osteogenic medium. The effect of nanotopography on the cell morphology, cell guidance and osteoblastic differentiation potential is studied. Furthermore, the cellular uptake of TiO_2 nanoparticles, prepared in this thesis, is studied to investigate their potential as a trace molecules for clinical diagnosis.

---

[1] This work is accomplished in cooperation with prof.dr. I. Lambrichts (Uhasselt, Department Morphology).

5.1 Study of the growth of human cells on TiO_2 nanostructured films

TiO_2 has shown a complete osseointegration on different titanium surfaces [1, 2]. On the one hand, it has the ability to serve as a scaffold on which bone cells can attach, migrate, grow and divide, a phenomenon defined as **osteoconductivity** [3, 4]. It is said that bone healing response is "conducted" through the graft site. On the other hand, it also has the potential to be **osteoinductive,** meaning that it has the ability to stimulate primitive "stem cells" or immature bone cells to grow and mature, forming healthy bone tissue.

In the last decade, stem cell nanotechnology has gained huge momentum and it is currently being applied for the treatment, repair and regeneration of cells and tissues.

As mentioned before (Chapter 1, section 1.6.2), the interaction between implant surface and tissue can be influenced by o.a. geometry, roughness and topography. Several investigators have revealed that nanoscale topography also influences cell adhesion and osteoblastic differentiation [5, 6]. The different topographies of nanostructured films presented in current thesis (dense layers, line structured films, porous films) are studied as a potential implant material for the growth of human dental pulp stem cells (hDPSCs). They are prepared from the same TiO_2 dispersion aiming at studying the effect of surface topography on the cell growth. Further, the possible osteoinductivity and osteoconductivity of the TiO_2 nanostructures is studied using hDPSCs. As current study is only preliminary, the results are not discussed in detail, as also the background of this more specialized research subject is missing in our research group.

In order to study the osteoinductivity and osteoconductivity, first the stem cells need to get attached to the TiO_2 surface, grow on it and divide. Then the cells are stimulated to differentiate into bone forming cells (osteoblasts) which can then be further evolve/differentiate/develop into bone tissue.

The first indication of cell morphology, proliferation or growth, can be visualized using Scanning Electron Microscopy, which allows simultaneous analysis of topography and morphology, providing information on cell size, anchorage and spreading. As SEM analysis requires a vacuum in order to detect the scattered or emitted electrons, the biological samples must be freeze dried first and, if non-conducting, coated with gold or carbon. Detailed analysis of morphology and content of the cells is carried out by Transmission Electron Microscopy.

5.1.1 Dens TiO_2 films

The study of the growth of cells onto TiO_2 dense films has already been started in previous work by I. Truijen (PhD 2007, [7]). The films were prepared from the aqueous citrato-peroxo Ti-precursor (obtained by sol-gel). In order to continue this work, two kinds of dense layers are studied in current work: layers prepared from the aqueous citrato-peroxo Ti-precursor and layers prepared from the aqueous TiO_2 dispersion (Chapter 2). The differences between the use of dense layers prepared from the solution gel precursor or the dispersion are listed in section 3.1.1.

Furthermore, in current study, human dental pulp cells are used as they can be easily isolated and cultured, while preceding work studied the growth of mesenchymal stem cells (from connective tissue).

5.1.1.1 Dense films from Ti-precursor- proceeding work started by I. Truijen

Experimental A dens TiO_2 layer is deposited on glass substrates by spin coating 10 layers of a 0.4 M Ti-citratoperoxoprecursor [8, 9]. The films are treated thermally on the hot plates of 180°C 2', 300°C 2' and 450°C 2' and calcined at 600°C for 30 minutes (10°C/min).

Human dental pulp stem cells (hDPSC) are retained from dental pulp tissue and cultured in alpha-MEM[2] supplemented with 10% fetal calf serum (control medium). Cells are grown on thermanox[3] coverslips (as control) and on the TiO_2 dense layers at a density of 10 000 cells/cm² on 1 cm² samples.

After 10 days, cells are fixed in 2% glutaraldehyde in 0.05 M sodium cacodylate buffer. Afterwards, cells are washed twice for 5 minutes with 0.05 sodium cacodylate buffer (pH= 7.3) and 0.15 M saccharose at 4°C. Postfixation is achieved by treating the samples with 2% osmiumtetroxide in 0.05 M sodium cacodylate buffer for 1 hour at 4°C. Dehydration of the samples is performed by exposing the samples to ascending concentrations of aceton. The dehydrated samples are impregnated overnight in a 1:1 mixture of aceton and araldite epoxy resin at room temperature. Next, the samples are embedded in araldite epoxy resin at 60°C. After application of the pop-off method, the embedded samples are cut in slices of 40-60 nm using a Leica EM UC6 microtome. Slices are transferred to 50 mesh copper grids coated with 0.7% formvar and stained with 0.5% uranyl acetate and a stabilized solution of lead citrate. TEM analysis is performed with a Philips EM208 S electron microscope with a Morada Soft Imaging System camera to acquire high resolution images of the evaluated samples. The images are processed digitally with iTEM-FEI software. Topographical images are performed with SEM.

TEM analysis shows the cells on the TiO_2 surfaces after *10 days of incubation* (Figure 5.1 a en b) where attachment of the cells to the TiO_2 is observed. Compared to control cells, the morphology of the attached cells is different. Control cells (Figure 5.1 c and d) are spindle shaped with cell organelles only around the nuclei. Also, the extracellular matrix surrounding the hDPSC is empty. Cells grown on the TiO_2 surface show a lot of actin (stress) fibers and

---

[2] Minimum Essential Medium, widely used medium for cell culture
[3] Flexible, transparent plastic coverslips

contain vesicles which are distributed in the whole cell (not only in the peri-nuclear area). The vesicles (Figure 5.1a) contain glycosaminoglycans and other extracellular matrix molecules which mediate the cell attachment [10], as described in section 1.6.2.

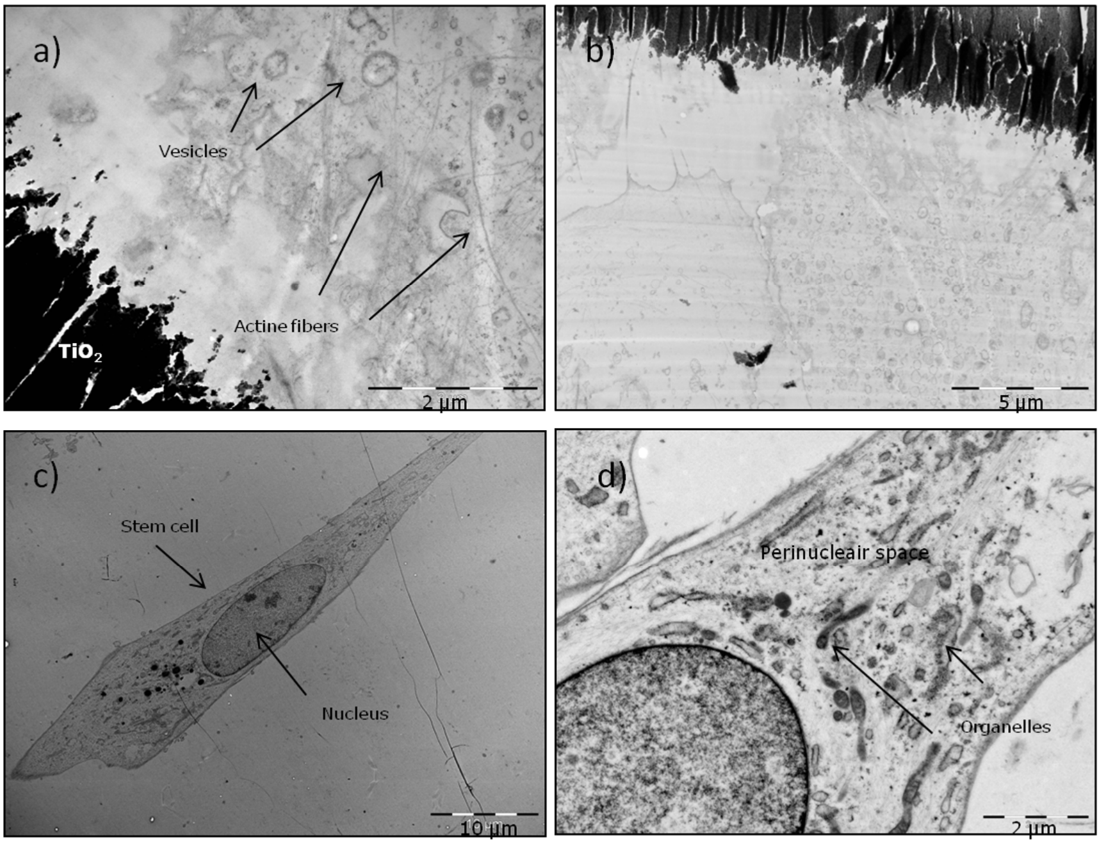

Figure 5.1 TEM images of embedded cells grown on TiO_2 dense layer from the Ti-precursor (a and b) and on thermanox (c and d) for 10 days.

At a incubation time of 10 days, only the osteoconditivity of the dense TiO_2 layers is observed. Therefore, different *incubation times (4 days, 2 weeks and 3 weeks*) are applied in order to detect some signs of possible differentiation. SEM and TEM analysis are presented in Figure 5.2 and Figure 5.3.

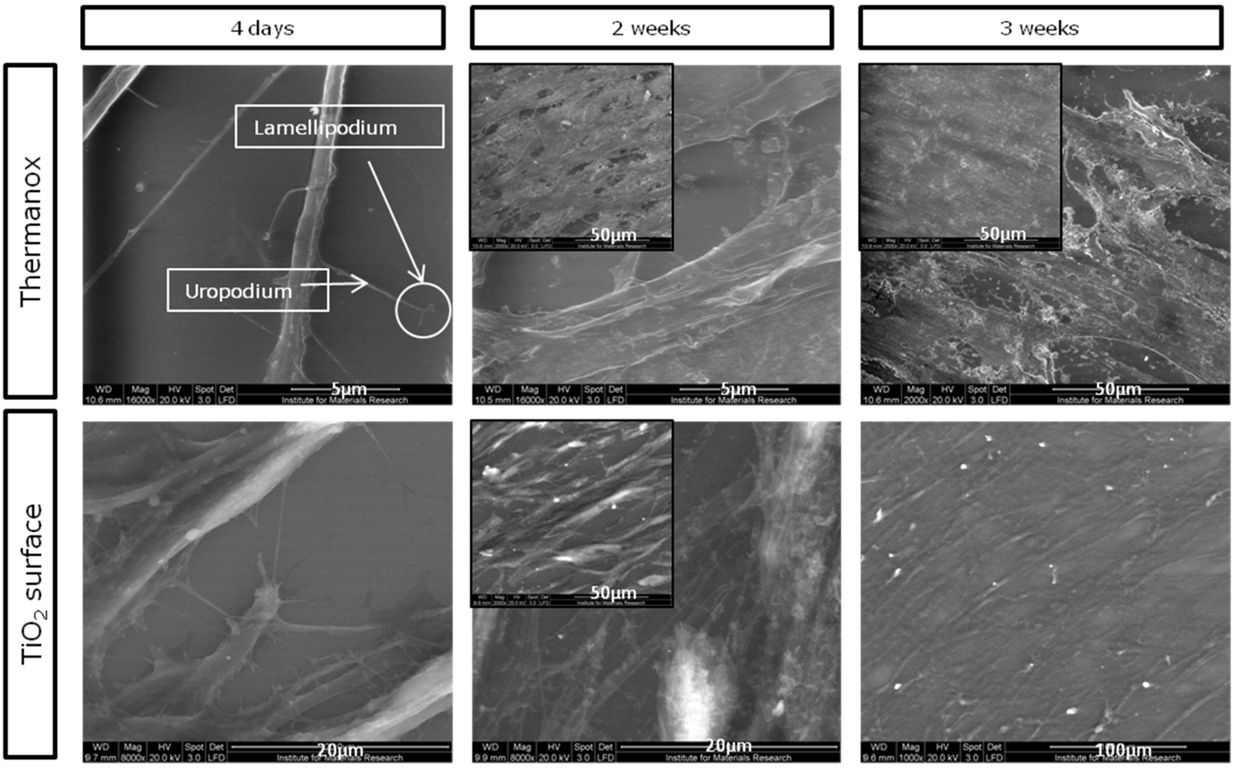

Figure 5.2 SEM analysis of cells grown on thermanox and TiO_2 dense layers from the Ti-precursor for different incubation times.

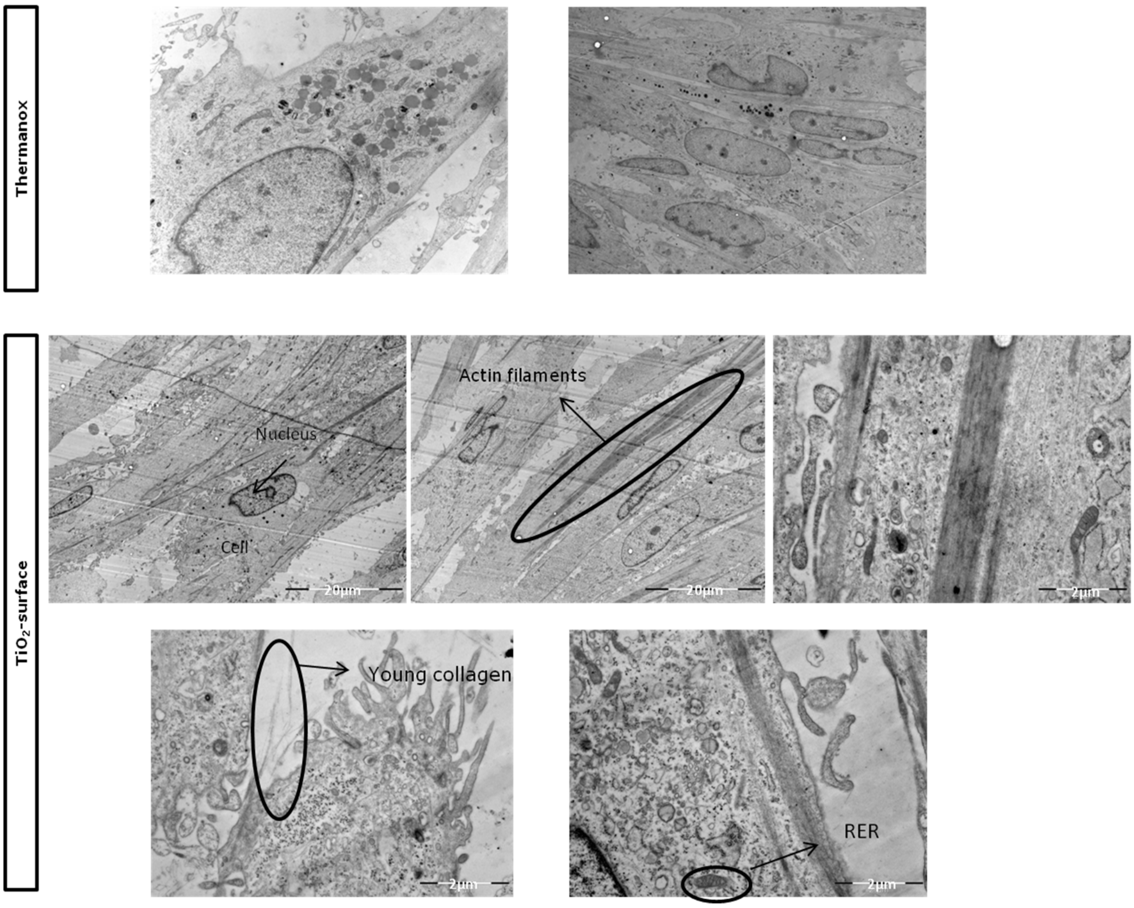

Figure 5.3 TEM analysis of cells grown on thermanox and TiO_2 dense layers from the Ti-precursor after an incubation time of 3 weeks.

The cells grown on thermanox have dimensions of 15-20 µm and are nicely spread on the surface. The surface is almost fully covered with the exception of some open areas. Cytoplasmic extenstions, which make contact between the cells, are observed. The long arms are called uropodia and the 'hands' that are in direct contact with the cells are defined as lamellipodia. The density of the cell coverage has increased by extending the incubation till 2 weeks (Figure 5.2). Incubating the cells for another week, didn't result is a further raise of the coverage density.

The cells grown on the TiO_2 dense layers have a more shaped and organized morphology than the cells grown on thermanox. The **cytoplasmic extensions** are also observed here, which show an augmentation in connections and extentions with increasing incubation time.

For both substrates, no collagen is observed in the SEM images but due to their size (40-50 nm), it is more likely to detect them via TEM.

Via TEM analysis (Figure 5.3), electron dense lines, assigned to **filaments**, are observed in the cells grown on the TiO_2-surfaces. These filaments are most likely actin filaments as actin plays a role in the cell division, shaping the cell and allows the cell to move (osteoconductivity). An indication for cellular growth is given by the presence of a Rough Endoplasmatic Reticulum (RER), where **proteins** are synthesized. Further, young **collagen** is also detected in the extracellular space which can be a premature indication of the differentiation into osteoblasts (osteoinductivity).

In contrast, the cells grown on thermanox are more broad and plane and show different organelles. Collagen is not observed in these samples which confirms the absence of a osteoinductive effect of the plastic on the cells.

In conclusion, the cells grown on the TiO_2-surfaces, prepared from the Ti-precursor, seem to produce fibers which are an indication that the cell is changing. A further increase in incubation time (> 3 weeks) s needed to detect and confirm the signs for osteoinductivity. However, this was not further investigated within this thesis.

5.1.1.2 Dense films from TiO_2 dispersion

Experimental The dense layers are deposited onto glass substrates, which are cleaned by IPA/H_2O/UV-O_3, by spin coating 3 drops at 1000 rpm (30 sec) and heat treated at 80°C for 5 minutes (chapter 3 Figure 3.5). The hDPSCs are incubated in the presence of a control medium (CM) on the dense films and the samples are fixated for SEM analysis at the different incubation times of 3 days, 7 days and 3 weeks. To study osteodifferentiation, the cells are incubated for 7 days and 3 weeks on the dense layers in the presence of osteogenic differentiation medium (ODM) [11], and the presence of calcium is evaluated by EDX analysis.

SEM analysis of hDPCs cultured on thermanox show a dense coverage of the cells after 3 weeks (Figure 5.4). The absence of differentiation is confirmed by the low Ca signal (present in bone tissue) in the EDX spectrum. On TiO_2 dense layers, the cell coverage is already very high after 7 days of cell growth (Figure 5.5) but after 3 weeks, still no differentiation has occurred.

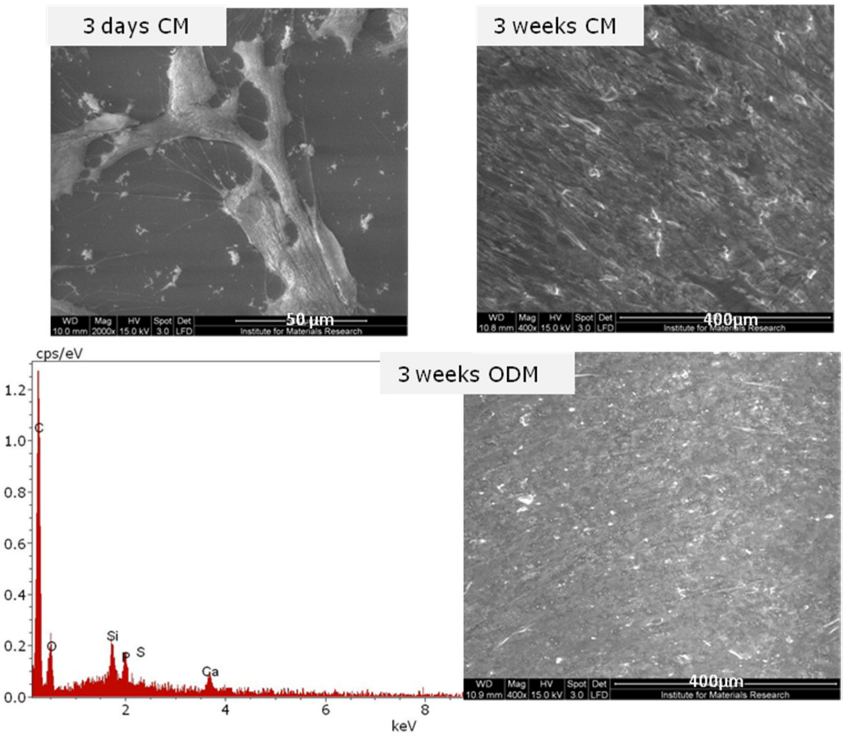

Figure 5.4 SEM analysis hDPSCs cultured on Thermanox in control medium (CM) for 3 days and 3 weeks and in osteogenic differentiation medium (ODM) for 3 weeks, with corresponding EDX spectrum.

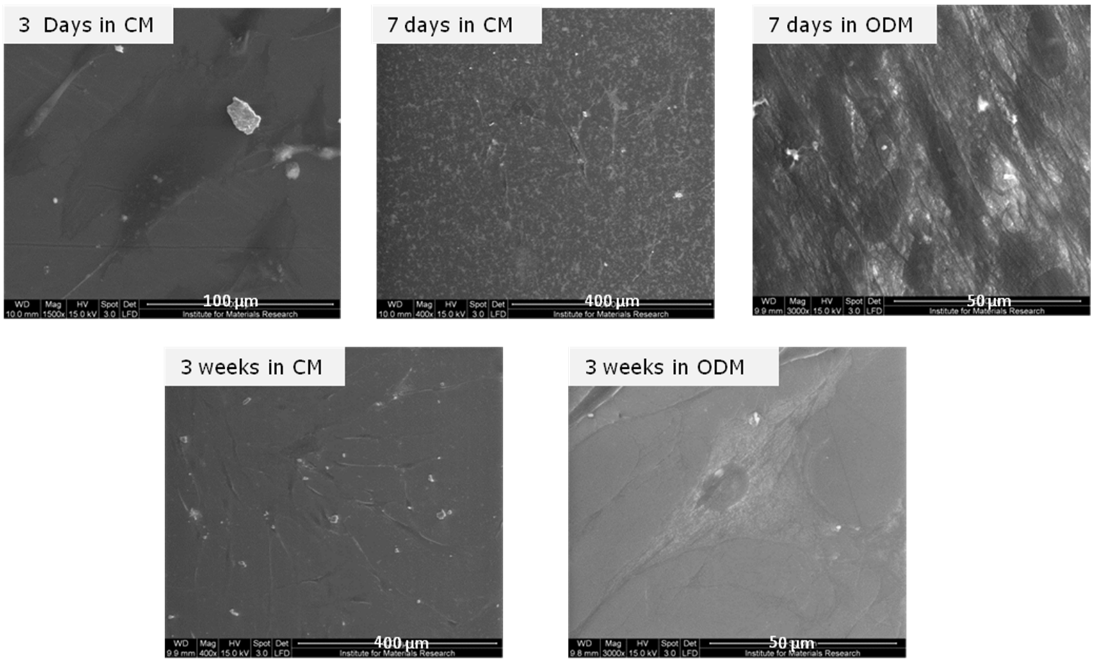

Figure 5.5 SEM analysis hDPSCs cultured on TiO_2 dense layers from the dispersion for 3 days, 7 day and 3 weeks in control medium (CM) and for 7 days and three weeks in osteogenic differentiation medium (ODM).

For the cell growth on the dense layers, it can be concluded that the growth is high for both types of dense layers (from solution gel precursor and from TiO_2 dispersion). Cells grown on TiO_2 produces fibers and collagen which is absent when the cells are grown on thermanox. The presence of the fibers and the collagen indicate that the cell is changing. Nevertheless, even after an incubation time of 3 weeks, the possible differentiation of the stem cells into osteoblasts could not be detected yet.

5.1.2 Patterned TiO_2 films[4]

It is known that cells respond to the micro-topography of a surface [12], indicated as ‘contact guidance’ and involves alterations in cell shape, orientation and polarity. Contact guidance has been observed in a number of different substrate systems with a wide range of topographies [13], with dimensions as small as 130 nm [14]. Human corneal epithelial cells even showed alignment along patterns of 70 nm, demonstrating an increased alignment with increasing groove depth [15].

In current preliminary experiments, the line patterned films (without scum layer) derived from the CD stamp are used. The surface chemistry of all patterns are considered as the same as all patterns are prepared from the same TiO_2 dispersion and treated equally.

Experimental The line patterns are deposited onto cleaned glass substrates (Figure 3.38) by spin coating 3 drops at 350 rpm and pressing a CD patterned PDMS stamp into

---

[4] A part of the work in this section has been processed into an manuscript (Letter) entitled “The effect of TiO_2 nano-patterns prepared by soft lithography on the oriented growth of human dental pulp stem cells “, submitted to Materials Letters.

the wet film. Pressure is applied by a weight of 2 kg (manual printing) and the pattern is formed by drying at 80°C for 15 minutes. A post treatment by UV-O_3 is applied at 50°C for 20 minutes. Cell culture and sample preparation is carried out as described in section 5.1.1.1 Same incubation times as for the growth on dense TiO_2 layers from the dispersion are applied for comparison. EDX spectra are recorded to study the presence of Ca which indicates bone formation (osteodifferentiation).

After an incubation time of 3 days, shown in Figure 5.6, no guidance effect is observed for the line patterned films. After 7 days of incubation, the surface is fully covered with randomly oriented cells. Furthermore, after an incubation of 3 weeks in special differentiation medium, the amount of Ca has not increased, as indicated in EDX. It is concluded that no differentiation into bone cells has occurred, although some premature collagen is observed in TEM (Figure 5.8).

The **absence of a guidance effect** in our preliminary study can probably assigned to the **dimensions of the lines**. The grooves in this work have dimensions of ±900 nm (width) and ±40 nm (height). Other work showed contact guidance effects on cell growth and migration on microgrooves with widths ranging from 2-12 µm. Even microgrooves between 1 and 10 µm showed the capacity to induce cell guidance and cell morphology change [16, 17] with a higher degree of cell guidance observed on smaller grooves (2 and 4 µm) [18].

Furthermore, the dimensions of the used cells may influence the cellular response, as a stronger effect was observed using grooves with sizes comparable to the dimensions of the cell [19]. Distinctive cell orientation was observed on grooves wider than the cell [20], while others showed a more effective guidance when the grooves are smaller than the cell size [21]., even on grooves as narrow as 260 nm *[14].* In current work, the **dimensions of the cell** are 10-15 µm which are quite large compared to the dimensions of the grooves*.* As proteins mediate the interaction between the biomaterial and the cells and regulates the final cell behavior through complex signaling pathways, the absence of guidance in our experiments could be ascribed to the reason that the nanogrooves are too small to accommodate cell focal contacts where the proteins can attach. Besides the surface nanostructure, also the nanometric pore shape influences the adsorption of proteins [22], indicating the **height (depth) of the grooves** as an additional factor influencing the contact with the cell. In general, deep grooves are more effective than shallow ones in guiding cell orientation [19]. It is reported that the extent of orientation increases with groove depth from hundreds of nanometers up to approximately 25 µm [20, 23-25]. However, the effects of the depth on the cell orientation are complex as the cell–substrate contact and adherence occurs primarily on the ridges [26].

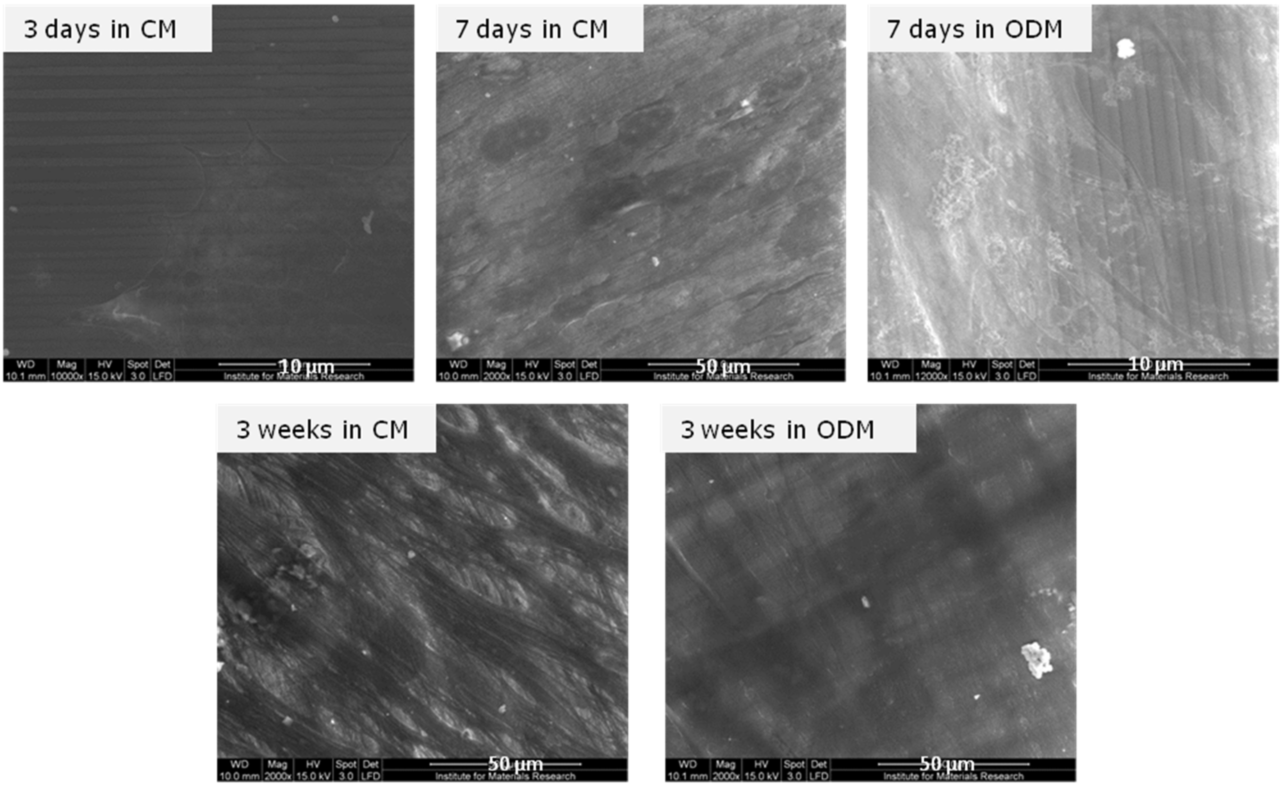

Figure 5.6 SEM analysis of the stem cells cultured in control medium (CM) and osteogenic differentiation medium (ODM) on line patterned TiO_2 film for different culture times.

Nevertheless, it is difficult to compare the aforementioned studies with our results as they use specific cell lines and grooves with different surface chemistry. Whether the absence of guidance can be assigned to the width of the nanogrooves or the height, or both, could not be unraveled yet. It can only be concluded that the cell-substrate interaction is far too complex to simply be explained by one or even a few factors such as chemistry and topography and further research is necessary.

5.1.3 Porous TiO_2 films

For comparison, the porous layers prepared by tape casting (Chapter 3, section 3.2, Figure 3.21, 10wt% HPC) are used as substrates for cell growth. The porous layers induce a fast cell growth and full coverage already after 7 days (Figure 5.7). White crystals (Ca or Ti?) seem to have formed in a early stage (7 days) and at 3 weeks of incubation, twice more Ca is detected compared to the dense layers. The potential of these porous films towards osteodifferentiation is confirmed by the presence of collagen, observed in TEM (Figure 5.8).

Furthermore, a large amount of titanium is detected by EDX which could indicate a lower coverage of the cells or the uptake of titanium in the cells. Whether the high Ti signal in EDX derives from NPs inside the cell or attached to the cell membrane cannot be discriminated based on the TEM analysis, which is a method to confirm the internalization of TiO_2 particles by the cells [27]. Nonetheless, both the attachment of NPs to cellular membranes and their internalization can interfere with cell function and are relevant in the assessment of possible NPs' cytotoxic effects, as discussed in next section.

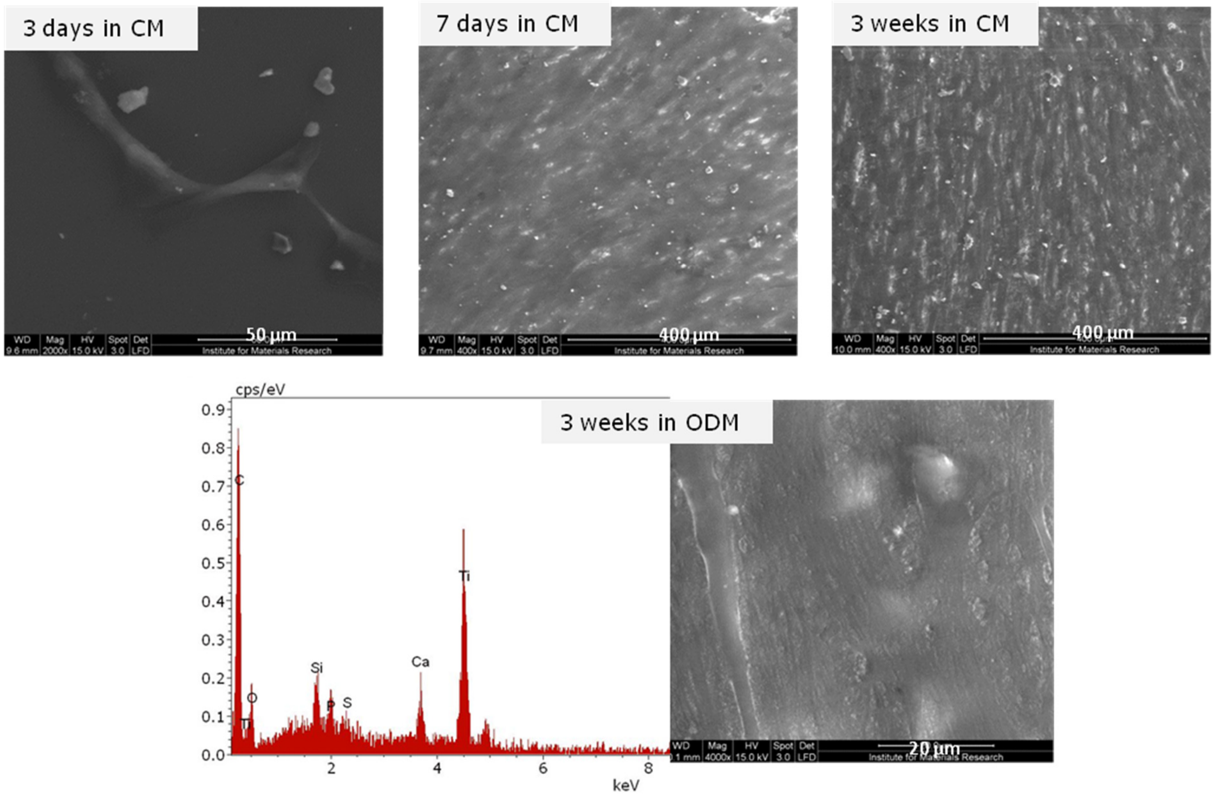

Figure 5.7 SEM analysis of the stem cells cultured (in CM and ODM) on the porous TiO_2 films for different culture times and EDX spectrum for osteodifferentiation analysis.

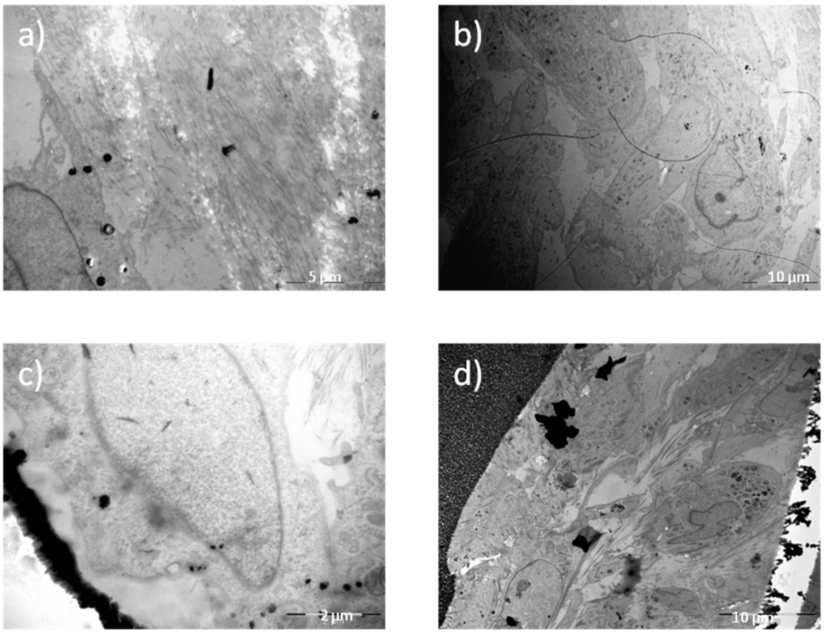

Figure 5.8 TEM of the hDPSCs after incubation of 3 weeks in ODM on dense layers (a), lines (b), squares (c) and porous films (d).

5.2 Study of TiO_2 uptake in the cell

Due to the size of the **nanoparticles**, which is comparable to natural carriers and other biomolecules, they are able to cross physiological barriers and access different tissues followed by an efficient cellular uptake and intracellular internalization [28]. Therefore, nanoparticles can be applied as fluorescent markers [29] e.g. via magnetic resonance imaging (MRI) techniques [30] to detect the migration and homing of transplanted cells and even cancer cells or for other **clinical diagnosis** [28, 31]. For these applications, the uptake of the nanoparticles is encouraged and it was shown that nanoparticles with sizes up to 500 nm could be endocytosed[5] by eukaryotic cells with a decrease in efficiency of cell incorporation with increasing particle size [32, 33], showing the highest incorporation particles of 100-200 nm. As the cell membrane is mostly negatively charged, the **uptake** of the particles can be enhanced by functionalizing the particles with ligands [34]. As the linking chemistry relies on peptide (amide)bond formation between carboxylic acids and amines, the most interesting ligands are those which contain amine or carboxyl groups so that these groups are present at the outer surface when functionalized. Not only from biological point of view, altering the effective surface charge by functionalization could also prevent the electrostatically stabilized particles form particle agglomeration. This is especially important under physiological conditions where the electrolyte concentration is high, decreasing the electrostatic repulsion between the particles.

Although **iron nanoparticles** (35 nm) are commonly used for labeling stem cells, they show a few disadvantages such as a low intracellular labeling efficiency, non corresponding cell count and no ability for a distinction between the living cells and the death cells. Furthermore, to avoid the rapid dilution of the labeling agent by cell division, the cells need to be labeled with a larger number of nanoparticles with a smaller size. The cellular uptake of iron nanoparticles can be facilitated by cationic compounds such as poly-L-Lysine (PLL) due to their interaction with the negatively charged cell surface and subsequent endosomal uptake [35], as illustrated in Figure 5.9. Nevertheless, high intracellular concentration of iron nanoparticles have shown to affect the actin cytoskeleton, which resulted on diminished cell proliferation [36].

---

[5] Endocytosis is a process by which cells absorb molecules (such as proteins) by engulfing them.

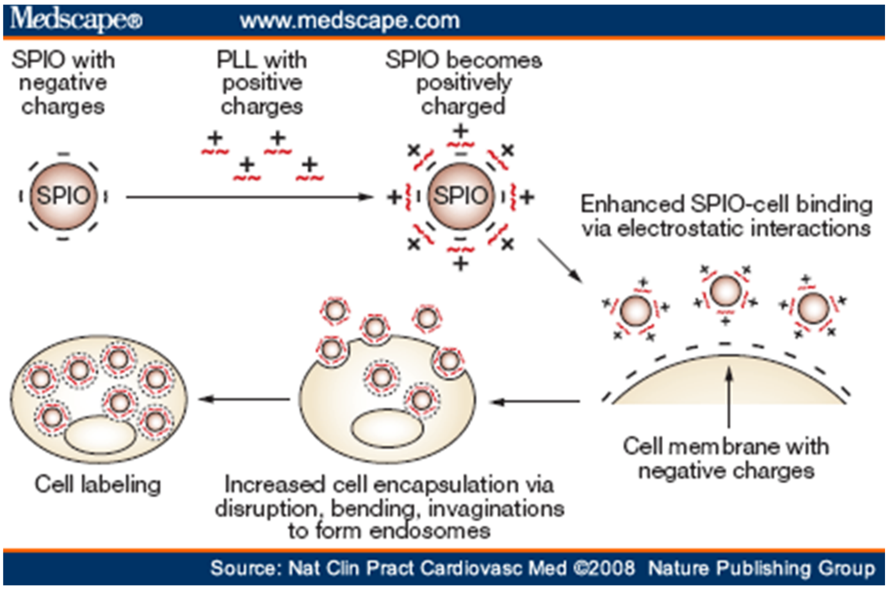

Source: Nat Clin Pract Cardiovasc Med ©2008 Nature Publishing Group

Figure 5.9 Representation of the interaction between the superparamagnetic iron oxide nanoparticles (SPIO) and the cell membrane [37].

Therefore, the possible replacement of the iron nanoparticles by the very small **TiO_2 nanoparticles** (5-10 nm) as trace molecules is investigated in current work. The driving force for the replacement of iron oxide by TiO_2 is the small particles size of the TiO_2 nanoparticles which could increase the number of particles uptaken by the cell, compared to the iron particles. In view of the application of TiO_2 nanoparticles in imaging techniques, they can be labeled with optical fluorescent agents [38] or other elements like gadolinium [39].

In this preliminary study, the uptake of the TiO_2 nanoparticles into the human dental pulp stem cells is studied. As both the nanoparticles (zeta potential of -51 mV, Chapter1 section 2.3.1) in our dispersion and the membrane are negatively charged, PLL is added in different concentrations to the TiO_2 dispersion. The dispersion itself is used as a low degree of particle agglomeration enhances the uptake. Different concentrations of the TiO_2 nanoparticles (actually of the dispersion) are incubated with the cells. For comparison, the cells are also labeled (incubated) with iron nanoparticles. The uptake of the TiO_2 nanoparticles is evaluated via the measurement of the viability of the stem cells. As nanoparticles can affect the cellular activity, they are able to induce cell death. Toxicity of the iron oxide and titanium dioxide to the hDPSCs is analyzed using the MTT essay. This essay is based on the reduction of the yellow tetrazolium salt (MTT ;3-(4,5-Dimethylthiazol-2-yl)-2,5-diphenyltetrazolium bromide) to the purple formazan. This conversion only occurs in the mitochondria of metabolic active and thus viable cells. The amount of formazan, as measured by the absorbance between 500-600 nm, is proportional to the quantity of viable cells and thus inversely proportional to the toxicity of TiO_2 particles.

Experimental First the cells are seeded in a 96-well tray for 24 h. Different concentrations of the TiO_2 dispersion (0.1, 5 and 25 µg/ml) are prepared with α-MEM (without FCS[6]) as dispersion medium and mixed with different concentrations of PLL (0, 0.75 and 1.5 µg/ml). The mixing takes 1 h to ensure the binding of PLL with the particles. A 20% DMSO solution is used as a negative control. For comparison, iron particles are also dispersed with different PLL concentrations. Then, the medium of the cells are removed and 100 µL of the different particle-PLL dispersions are added to the cells in the wells (well plate).The cells are incubated with the nanoparticle dispersions and the DMSO solution for 48 h at 37°C.

An MTT assay is carried out to evaluate the toxicity of the TiO_2 to the cells. 100 µl of a 0,5 mg/ml MTT solution in α-MEM is added to the cells, after removing the incubation medium (particle-PLL dispersions), followed by another incubation for 4 h at 37°C. After incubation, the supernatans (MTT solution) is removed from the wells and 175 µL of a 14% glycine solution in DMSO is added to dissolve the formed purple formazan crystals. The concentration of the purple solution is determined by measuring the absorbance at a wavelength of 540-550 nm.

The results of the MTT survival assay are presented in Figure 5.10 with the different nanoparticle dispersions in the x-axis and the obtained viability (%) in the y-axis. The control sample (0 µg/ml nanoparticles and 0 µg/ml PLL) is defined as 100% viability. DMSO, not shown in the figure, is used as a positive control of cell death and it resulted in 1% viability due to its high toxicity.

The assay demonstrates that without the addition of PLL, TiO_2 (in any concentration up to 25 µg/ml) has no influence on the cell viability. This can mean two things: either the cells did not interact with the nanoparticles due to the unfavorable electrostatic interactions or either the cells did interact with the nanoparticles but the nanoparticles are not toxic for the cells. Looking back to the results in section 5.1.3 concerning the Ti signal, it can be concluded, based on the MTT assay, that if the cells are able to uptake the TiO_2 nanoparticles from the porous layer (section 5.1.3), no cell death is induced, at least till a concentration of 25 µg/ml, since the toxicity is dose-dependent [27].

Nevertheless, the addition of PLL clearly affects the viability with increasing concentration of TiO_2 and PLL. In contrast, iron oxide shows no influence on the cell viability, in any concentration of PLL. The data suggest that high TiO_2 concentrations (5 µg/ml and 25 µg/ml) might reduce the viability of the cells because they are incorporated into the cell cytoplasm. This is in sharp contrast with the Fe particles which are known to be endocytosed by the cells and do not affect cell survival. The Fe nanoparticles even seem to increase the viability as they

---

[6] Fetal calf serum, which can interfere with the labeling

affect the cell metabolism [40]. At very low concentrations of TiOx (0,1 µg/ml) a similar effect seem to occur.

From these preliminary experiments, it can be concluded that a further optimization of the PLL concentration, more specifically in combination with a concentration of 5µg/ml of TiO_2, as the concentration only causes a reduction of 20% of cell viability, might be interesting for further research. Furthermore, TEM analysis are needed to confirm the incorporation of TiO_2 nanoparticles into the cell cytoplasm.

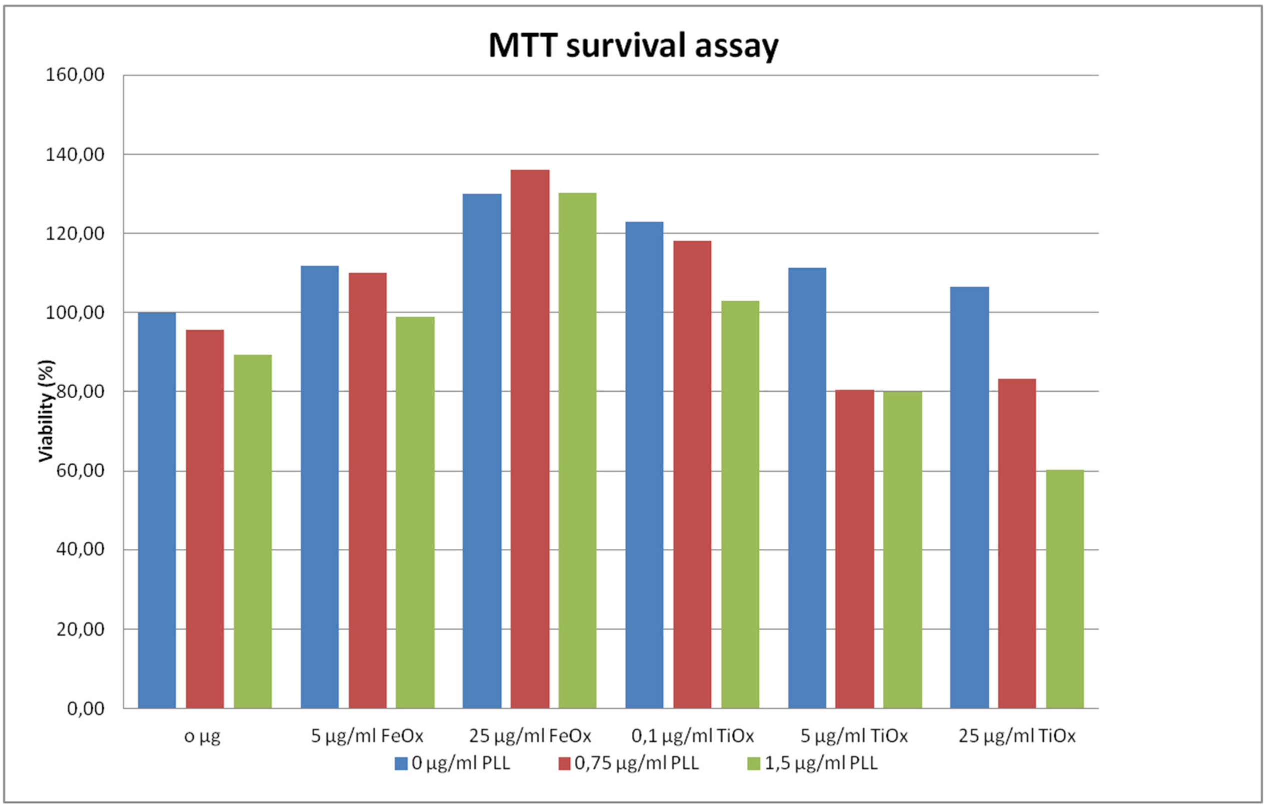

Figure 5.10 Effect of the Fe_3O_4 and TiO_2 nanoparticles on the hDPSCs after 48h of incubation.

5.3 Conclusion

In this chapter, human dental pulp stem cells are cultured on different nanostructured TiO_2 films such as dense films, line patterned films and porous films. The effect of nanotopography on the cell morphology, cell guidance and osteoblastic differentiation potential is evaluated. As shown in microscopy, the morphology of the hDPSCs is influenced by the TiO_2 surfaces, leading to more shaped cells, compared to the cells grown on plastic. Unfortunately no guidance effect is observed when applying the patterned nanostructures as growth layer. This lack of guidance may be attributed to the size difference between de cells (10-15 µm) and the nanopatterns, where also the height of the nanopatterns is suggested to be a determining factor, as it may influence the protein attachment. In the evaluation of osteodifferentiation, only the growth of cells on the porous layers induced an increase of Ca, detected by EDX, which indicate the potential of these layers toward bone formation (osteoinductivity). For the observed Ti- signal, it was concluded based on the viability test, that if the cells are able to uptake the TiO_2 nanoparticles from the porous layer, no cell death is induced.

As the viability test aimed the study of the uptake of TiO_2 in the cells, towards to replacement of iron nanoparticles in clinical diagnosis, PLL is added to the dispersion of nanoparticles to enhance the interaction of the particles with the cells. The results show a decrease in viability at increasing TiO_2 and PLL concentration. As these preliminary results indicate the uptake of the nanoparticles, the optimization of the TiO_2 and PLL concentrations show an interesting prospective towards further research.

References

1. Mangano, C., De Rosa, A., Desiderio, V., D'Aquino, R., Piattelli, A., De Franscesco, F., Tirino, V., Mangano, F., and Papaccio, G., The osteoblastic differentiation of dental pulp stem cells and bone formation of different titanium surface textures. Biomaterials, 2010. 31: p. 3543-3551.
2. Graziano, A., D'Aquino, R., Cusella- De Angelis, M.G., De Franscesco, F., Giordano, A., Laino, G., Piattelli, A., Traini, T., De Rosa, A., and Papaccio, G., Scaffold's surface geometry significantly affects human stem cell bone tissue engineering. Journal of cellular physiology, 2007. 214(1): p. 166-172.
3. Yamamoto, D., Kawai, I., Kuroda, K., Ichino, R., Okido, M., and Seki, A., Osteoconductivity of anodized titanium with controlled micron-level surface roughness. Materials Transactions, 2011. 52(8): p. 1650-1654.
4. Yamamoto, D., Kawai, I., Kuroda, K., Ichino, R., Okido, M., and Seki, A., Osteoconductivity and hydrophilicity of TiO2 coatings on Ti substrates prepared by different oxidizing processes. Bioinorganic chemistry and applications, 2012.
5. Dalby, M.J., Andar, A., Nag, A., Affrossman, S., Tare, R., McFarlane, S., and Oreffo, R.O.C., Genomic expression of mesenchymal stem cells to altered nanoscale topographies. Journal of Royal Society, 2008. 5: p. 1055-1065.
6. Webster, T.J., Siegel, R.W., and Bizios, R., Osteoblast adhesion on nanophase ceramics. Biomaterials, 1999. 20: p. 1221-1227.
7. Truijen, I., Studie van de invloed van syntheseparameters op de microstructuur van TiO_2 lagen voor fotovoltaïsche toepassingen. Doctoraatsproefschrift, 2007.
8. Truijen, I., Van Bael, M.K., Van den Rul, H., D'Haen, J., and Mullens, J., Preparation of nanocrystalline titania films with different porosity by water-based chemical solution deposition. J. Sol-gel Sci. Technol., 2007. 43: p. 291-297.
9. Hardy, A., D'Haen, J., Van Bael, M.K., and Mullens, J., An aqueous solution-gel citratoperoxo-Ti(IV) precursor: synthesis, gelation, thermo-oxidative decomposition and oxide crystallization. J. Sol-gel Sci. Technol., 2007. 44: p. 65-74.
10. Wilson, C.J., Clegg, R.F., Leavesley, D.I., and Pearcy, M.J., Mediation of biomaterial-cell interactions by adsorbed proteins: a review. Tissue engineering, 2005. 11: p. 1-18.
11. Bronckaers, A., Hilkens, P., Fanton, Y., Struys, T., Gervois, P., Politis, C., Martens, W., and Lambrichts, I., Angiogenic properties of human dental pulp stem cells. PLoSone, 2013. 8(8).
12. Harrison, R.G., On the stereotropism of embryonic cells. Science, 1911. 34: p. 279-281.
13. Eisenbarth, E., Meyle, J., Nachtigall, W., and Breme, J., Influence of surface structure of titanium materials on the adhesion of fibroblasts. Biomaterials, 1996. 17(14): p. 1399-1403.
14. Clark, P., Connolly, P., Curtis, A.S.G., Dow, J.A.T., and Wilkinson, C.D.W., Cell guidance by ultrafine topography in vitro. Journal of biomedical materials research, 1991. 99: p. 73-77.

15. Teixeira, A.I., Abrams, G.A., Bertics, P.J., Murphy, C.J., and Nealy, P.F., Epithelial contact guidance on well-defined micro- and nanostructured substrates. Journal of cell science, 2003. 116: p. 1881-1892.
16. Braber, E.T.d., Ruijter, J.E.d., Smits, H.T.J., Ginsel, L.A., Recum, A.F.v., and Jansen, J.A., Quantitative analysis of cell proliferation and orientation on substrata with uniform parallel surface micro-grooves. Biomaterials, 1996. 17: p. 1093-1099.
17. Braber, E.T.d., Ruijter, J.E.d., Ginsel, L.A., Recum, A.F.v., and Jansen, J.A., Quantitative analysis of fibroblast morphology on microgrooved surfaces with various groove and ridge dimensions. Biomaterials, 1996. 17: p. 2037-2044.
18. Magdon-Ismail, F.S., Rohanizadeh, R., Atwa, S., Mason, R.S., Ruys, A.J., Martin, P.J., and Bendavid, A., The influence of surface chemistry and topography on the contact guidance of MG63 osteoblast cells. Journal of materials science: Materials in medicine, 2007. 18: p. 705-714.
19. Jiang, L., Lu, X., Leng, Y., Qu, S., Feng, B., Weng, J., and Watari, F., Osteoblast behavior on TiO2 microgrooves prepared by soft-lithography and sol-gel methods. Mater. Sci. Engin. C, 2012. 32(4): p. 742-748.
20. Curtis, A. and Wilkinson, C., Topographical control of cells. Biomaterials, 1997. 18: p. 1573-1583.
21. Lu, X. and Leng, Y., Quantitative analysis of osteoblast behavior on microgrooved hydroxyapatite and titanium substrata. Journal of biomedical materials research, 2003. 66(3): p. 677-687.
22. Scopelliti, P.E., Borgonovo, A., Indrieri, M., Giorgetti, L., Bongiorno, G., Carbone, A., and Milani, P., The effect of surface nanometrre-scale morphology on protein adsorption. Plos one, 2010. 5(7).
23. Brunette, D.M. and Chehroudi, B., The effects of surface topography on micromachined titanium substrata on cell behavior in vitro and in vivo. Journal of biomechanical engineering, 1999. 121(1): p. 49-57.
24. Chehroudi, B., Gould, T.R.L., and Brunette, D.M., Titanium-coated micromachined grooves of different dimensions affect epithelial and connective-tissue cells differently in vivo. Journal of biomedical materials research, 1990. 24: p. 1203-1219.
25. Chehroudi, B., Gould, T.R.L., and Brunette, D.M., The role of connective tissue in inhibiting epithelial downgrowth on titanium-coated percutaneous implants. Journal of biomedical materials research, 1992. 26(4): p. 493-515.
26. Matsuzaka, K., Walboomers, X.F., Yoshinaric, M., Inouea, T., and Jansen, J.A., The attachment and growth behavior of osteoblast-like cells on microtextured surfaces. Biomaterials, 2003. 24: p. 2711-2719.
27. Allouni, Z.E., Hol, P.J., Cauqui, M.A., Gjerdet, N.R., and Cimpan, M.R., Role of physicochemical characteristics in the uptake of TiO2 nanoparticles by fibroblasts. Toxicology in vitro, 2012. 26: p. 469-479.
28. Vasir, J.K., Reddy, M.K., and Labhasetwar, V.D., Nanosystems in drug targeting: opportunities and challenges. Current nanoscience, 2005. 1(1): p. 47-64.
29. Sharma, P., Brown, S., Walter, G., Santra, S., and Moudgil, B., Nanoparticles for bioimaging. Advances in Colloid and Interface science, 2006. 123-126: p. 471-485.
30. Shapiro, E.M., Sharer, K., Skrtic, S., and Koretsky, A.P., In vivi detection of single cells by MRI. Magnetic resonance in medicine, 2006. 55(242-249).
31. Kraitchman, D.L., Tatsumi, M., Gilson, W.D., Ishimori, T., Kedziorek, D., Walczak, P., and al., e., Dynamic imaging of allogeneic mesenchymal stem cells trafficking to myocardial infarction. Circulation, 2005. 112(10): p. 1452-1461.
32. Rejman, J., Oberle, V., Zuhorn, I.S., and Hoekstra, D., Size-dependent internalization of particles via the pathways of clathrin- and caveolae-mediated endocytosis. Biochemical Journal, 2004. 377: p. 159-169.
33. Amiji, M.M., Nanotechnology- improving targeted delivery. Drug Delivery, 2007. Touch Briefings, London, UK: p. 53-56.
34. Xu, Z.P., Zeng, Q.H., Lu, G.Q., and Yu, A.B., Inorganic nanoparticles as carriers for efficient cellular delivery. Chemical Engineering Science, 2006. 61(3): p. 1027-1040.

35. Arbab, A.S., Yocum, G.T., Rad, A.M., Khakoo, A.Y., Fellowes, W., Read, E.J., and al., e., Labeling of cells with ferumoxides-protamine sulfate complexes does not inhibit function or differentiation capacity of hematopoietic or mesenchymal stem cells. NMR in biomedicine, 2005. 18(8): p. 553-559.
36. Soenen, S.J. and Cuyper, M.d., Assessing cytotoxicity of (iron oxide-based) nanoparticles: an overview of different methods exemplified with cationic magnetoliposomes. Contrast media & Molecular Imaging, 2009. 4(5): p. 207-219.
37. National Clinical Practice Cardiovascular Medicin, 2008. Nature publishing group.
38. Thurn, K.T., Paunesku, T., Wu, A., Brown, E.M.B., Lai, B., Vogt, S., Maser, J., Aslam, M., Dravid, V., Bergan, R., and Woloschak, G.E., Labeling TiO2 nanoparticles with dyes for optical fluorescence microscopy and determination of TiO2-DNA nanoconjugate stability. Small, 2009. 5(11): p. 1318-1325.
39. Endres, P.J., Paunesku, T., Vogt, S., Meade, T.J., and Woloschak, G.E., DNA-TiO_2 nanoconjugates labeled with magnetic resonance contrast agents. Journal of American chemical society, 2007. 139(51): p. 15760.
40. Struys, T., Ultrastructural and immunocytochemical exploration of regenerative capacity of the dentin-pulp complex: Morphological characterization of human dental pulp stem cells and their relevance to tissue engineering. Doctoraatsproefschrift, 2011.

Conclusions and outlook

Due to its physical and chemical properties, the semi-conductor titanium dioxide (TiO_2) has gained high interest for its application in photocatalysis, photovoltaics, biomedical applications, batteries, sensors, self-cleaning materials and much more. Since the performance of the TiO_2 material in these photo-induced applications is determined by the efficiency of the device and the interacting media, a high specific surface area of the TiO_2 is desired. This can be accomplished by the synthesis of very small nanoparticles for which the surface-to-volume ratio is very high. On the other hand, high surface area/porosity in TiO_2 films can be introduced by the synthesis method and deposition technique.

Furthermore, other characteristics such as particle size, particle agglomeration, surface defects, hydroxyl groups and crystal phase determine the efficiency of the material. For both the photocatalytic as the photovoltaic applications, anatase TiO_2 is considered as the most active phase.

The aim of this thesis consisted in the development of a stable dispersion of very small (<10 nm) anatase TiO_2 nanoparticles which can be applied as precursor for the controlled synthesis of different/interesting substrate supported TiO_2 morphologies for a wide range of applications.

In chapter 2, the development of a stable aqueous TiO_2 dispersion starting from pre-synthesized nanoseeds is presented. The nanoseeds are prepared via a hydrothermal treatment, followed by a second hydrothermal treatment, in the presence of an aqueous solution of tetraethylammonium hydroxide, to disperse and stabilize the nanoparticles into a stable dispersion. It is demonstrated that the dispersion obtained via this procedure shows a high stability (against sedimentation), contains a solid load of 10 wt% TiO_2 and the particles have dimensions between 5 and 10 nm existing of anatase and brookite in a 4:1 ratio. From the study of the stability of the dispersion against sedimentation and particle agglomeration, it was concluded that particle agglomeration occurs but has no pronounced influence on the dispersions' stability against sedimentation, which is beneficial for the deposition of homogeneous films.

In addition, the parameters of the second hydrothermal treatment were studied in detail since they demonstrate to be crucial for the successful dispersion and stabilization of the particles during the second hydrothermal treatment, compared to alternative conditions. It was demonstrated that the presence of organic residues, ethanol and isopropanol, in the freshly prepared filter cake influences both the dispersibility as well as the stabilization of the nanoparticles. Furthermore, it was suggested that the interaction of the nanoparticles and tetraethylammonium hydroxide is based on electrostatic interactions with the tetraethylammonium cations, indicating also the absence of degradation of TEAH during the hydrothermal processing. The obtained insights from this more in depth study of the parameters contain valuable information which may be used to expand the research towards the stabilization of other oxide nanoparticles.

Chapter 3 demonstrates the versatile application of the concentrated aqueous TiO_2 dispersion in combination with different deposition techniques such as spin coating, dip coating, tape casting, screen printing and soft lithography. For each technique, the parameters are studied in order to obtain smooth, porous or patterned films. It was demonstrated that using optical discs (CD and DVD) as masters in soft lithography, line and square patterned films could be easily obtained with dimension from 900 and 350 nm, showing a small increase in specific surface area compared to the smooth films. Nevertheless, in view of the increase of aspect ratio of the patterns and thus the specific surface area, the height of the prepared patterns showed some limitations. For further research, it would be interesting to study the influence of higher concentrated dispersions on the height of the nanopatterns, as the concentration influences the loss of material in the cavities of the patterns. This implies the study of the concentration TiO_2 nanoseeds on the stability of the dispersion, which was not considered in this work. Another way to increase the specific surface area could be by the introduction of porosity into the patterns, which now consist of densely packed nanoparticles.

Although the patterned films lack high aspect ratio patterns, it may be concluded that the TiO_2 dispersion is a suitable ‘ink’ for the deposition of different nanostructured films, each with its characteristic thickness, porosity and nanomorphology. As one of the shortcomings of previous investigations published in many scientific journal lies in the use of different TiO_2 powders, coming from diverse synthesis routes and different synthesis conditions, for the deposition of various nanostructured films, it is difficult to correlate the characteristics of the prepared films with their potential in a specific application. It this work, the different nanostructured films are prepared from the same dispersion which allows the study of the influence of one characteristic on the performance in a specific application.

Therefore, the photocatalytic activity of the different TiO_2 nanostructures, with different specific surfaces areas, are evaluated in chapter 4. In this comparative, preliminary study, the degradation of Rhodamine 6G is evaluated by both UV-Vis and µTOC analysis, to provide complementary information about both the photobleaching and photomineralization efficiency of the nanostructures. Although the obtained efficiencies are quite low and the differences between the structured and the dense films is not distinctive enough to draw conclusions, it is clear from the results that other factors than only the specific surface area influence the photocatalytic performance. One of the suggested factors is the limited diffusion of dye and/ or intermediates between the patterns which are more expressed in smaller cavities, such as the patterns prepared from the DVD stamp. Furthermore, from this study, it was observed that the deposition of the patterns showed some showed some repeatability problems, which requires further optimization of the nanopatterns.

In view of superhydrophobic coatings, the patterned films showed low contact angles which indicated that the patterning didn’t affect the surface topography towards high contact angles (>90°). Even by the use of hydrophobing agents, no spectacular increase of contact angles was observed. Nevertheless, it is believed that nanopatterns with a higher aspect ratio could have potential as hydrophobic coatings, as also the nanorod arrays, discussed briefly in chapter 3, since they are promising morphologies towards high aspect ratio materials.

In chapter 5, the effect of nanotopography on the cell morphology, cell guidance and osteoblastic differentiation potential is evaluated, in view of the application as implant material. Hereto, human dental pulp stem cells are cultured on the different nanostructured TiO_2 films (dense, line patterned and porous films) which showed a morphology change when cultured on the TiO_2 surfaces, compared to the cells grown on plastic. This observation indicates a successful growth of the stem cells onto the different TiO_2 surfaces. Concerning a guidance effect on the cells, which was expected on the line patterns, only a random growth was observed. It is suggested that the lack of guidance may be attributed to the size difference between de cells (10-15 µm) and the nanopatterns (900 nm), where also the height seems to be a determining factor, as it may influence the protein attachment. The potential of the nanopatterned and porous films towards osteodifferentiation (differentiation into bone cells) is evaluated by the increase of Ca signal in EDX, as Ca is present in bone tissue. The cell growth on the porous films show a two-fold increase of Ca which indicates that these films could have potential as osteoinductive coatings for bone generation. Besides the increase of Ca signal, the Ti signal has increased which may be possible either due to the attachment of the TiO_2 onto the cell membrane, or either due to the uptake of the particles in the cells. When nanoparticles are uptaken in the cells, they can introduce cell death. To evaluate this effect, the cytotoxity of the TiO_2 nanoparticles is studied via the evaluation of the viability of the cells when cultured with different concentrations of TiO_2. It was shown that the viability of the cells was not influenced by the addition of TiO_2 till a concentration of 25 µg/ml, indicating that if the cells were able to uptake the TiO_2 nanoparticles, the particles will not induce cell death. On the other hand, the uptake of TiO_2 by the cells is encouraged for use of TiO_2 in clinical diagnosis, where cell death is undesirable. It was demonstrated that by the addition of a cationic polymer to the dispersion, the cell interactions are enhanced leading to a decreased viability of the cells. The decrease in viability suggests the uptake of the cells. Nevertheless, these preliminary experiments concerning the uptake of the nanoparticles, both in the cells grown on the porous layers as in the 'free' cells, need to be confirmed via TEM or other (more specialized) microscopy techniques in further work.

In conclusion, this work demonstrates the successful development of an aqueous and stable dispersion of very small, anatase TiO_2 nanoparticles. As this dispersion already contains crystallized nanoparticles, it offers a lot a lot of possibilities towards nanostructured film deposition at low temperature, as shown, which is beneficial in view of the use of other substrates such as plastics. Moreover, the preparation of different nanostructures from the same dispersion allows the study of the influence of only one parameter (such as topography) on its performance, since the surface chemistry should be the same for all nanomorphologies. Via the preliminary experiments towards the study of the different morphologies in specific applications, presented in chapter 4 and 5, it can be concluded that this research requires still some work mostly concerning, the increase of aspect ratio (and thus the specific surface area) and the optimization of the repeatability of the film deposition.

List with output

Workshops and conferences

As first author

- ENMIX, workshop, 4-5 oktober 2010, Antwerp (Belgium), no contribution
- ESR meeting of the COST mp0904 Action; "Single- and multiphase multiferroics with restricted geometries", 21-23 maart 2011, Hasselt University (Belgium), no contribution
- Colloids and Materials, 8-11 Mei 2011, Amsterdam (Netherlands), **poster** : "The hydrothermal synthesis of a stable dispersion of TiO_2 nanoparticles with a high anatase content". Presenting author.
- IMO-PV workshop: "Nanomaterials for next generation photovoltaic energy conversion", 13 september 2011, Hasselt University (Belgium), **oral presentation**: " Synthesis of concentrated aqueous dispersions of anatase TiO_2 nanoparticles as building units for nanostructured layers". Presenting author.
- EMRS Fall meeting, 19-23 september 2011, Warsaw (Poland), **poster** " Synthesis of a stable dispersion of TiO_2 nanoparticles for the deposition, of nanostructures" symposium K: " Solution-derived electronic-oxide films, nanostructures and patterning, from material to devices. A. Hardy as presenting author.
- ChemCYS (Chemistry Conference for Young Scientists) organized in Blankenberghe (Belgium), 1st and 2nd March 2012, by Jong-KVCV, **oral presentation**: "Synthesis and deposition of an aqueous TiO_2 dispersion." Presenting author.
- First COST MP0904 Training school: " Nanostructured oxides: from laboratory research to industrial applications", COST 12&13 March 2012, Genoa (Italy). **Poster** "Synthesis of a stable dispersion of TiO_2 nanoparticles for film and pattern formation". Presenting author.
- Materials Science and Technology 2012 Conferences and Exhibition, 7-11 October 2012, Pittsburgh (Pennsylvania). **Poster** "Synthesis of different nanostructures from a stable, aqueous TiO_2 dispersion for photocatalytic and biomedical applications". C. De Dobbelaere as presenting author.
- 5th International Conference on Shaping of Advanced Ceramics, January 29-31, 2013, Mons (Belgium), **Oral presentation** "Hydrothermal synthesis of a stable and aqueous TiO_2 dispersion for the deposition of nanostructures". Presenting author.
- Third International Conference on Multifunctional, Hybrid and Nanomaterials (Hybrid materials 2013), 3-7 March 2013, Sorrento (Italy), **Oral presentation** "Hydrothermal synthesis of a stable and aqueous TiO_2 dispersion for the deposition of nanostructures". Presenting author.
- Annual Meeting of BCERS Belgian Ceramic Society, 19th of April 2013, Hasselt University (Belgium), no contribution.

As coauthor

- Jongerencongres, 25th of may 2011, Belgian Physical Society, Namen (Belgium), **poster**:"Screen-printing a low viscosity TiO_2-dispersion to create uniform thin films for photovoltaic applications", J. Stryckers, B. Souvereyns, T.Vangerven, W. Moons, A. Hardy, M.K. Van Bael, W. Deferme, J. Manca.

- SPIE photonics Europe, 16-19th of April 2012, Brussels (Belgium), **poster**: "Comparison between spin coating and screen printing of mesoporous TiO_2 layers for the use in Dye Sensitized Solar Cells" J. Stryckers, G. Krishna, B. Souvereyns, W. Moons, A. Hardy, M. K. Van Bael, W. Deferme, J. Manca.

Scientific publications

Souvereyns, B., Elen, K., De Dobbelaere, C., Kelchtermans, A., Peys, N., D'Haen, J., Mertens, M., Mullens, S., Van den Rul, H., Meynen, V., Cool, P., Hardy, A., Van Bael, M.K., "Hydrothermal synthesis of a concentrated and stable dispersion of TiO_2 nanoparticles." Chemical Engineering Journal 223 (2013): p 135-144.DOI: 10.1016/j.cej.2013.02.047

Souvereyns, B., Bronckaers, A., De Dobbelaere, C., D'Haen, J., Hardy, A., Lambrichts, I., Van Bael, M.K., "The effect of TiO_2 nano-patterns prepared by soft lithography on the oriented growth of human dental pulp stem cells." Materials Letters (2013), submitted.

Souvereyns, B., Elen, K., Damm, H., Van den Broeck, F., Degutis; G., Martins, J.C., Meynen, V., Cool, P., Hardy, A., Van Bael, M.K., "Hydrothermal dispersion and stabilization of an aqueous, colloidal titania dispersion: a mechanistic investigation". In preparation.

Appendix

A. Hamaker software for the prediction of dispersion stability: theory

In view of the processing of ceramics at nanoscale, the influence of interparticle interactions in the suspended state becomes very important. The Hamaker 2 program has been developed for the rapid prediction of these interactions and the resulting stability of the suspensions [1]. This software is freely available [2] and is aimed to study the interactions between dissimilar particles as a function of any variable system in order to understand the aspects that control the stability (or instability) of the system and how to achieve the required degree of stability.

Theoretical background [1, 2]

The stability of nanoparticles in dispersion and their tendency to agglomerate is considered in the context of electrostatic, steric and van der Waals forces between the particles using the Derjaguin- Landau-Verwey- Overbeek (DLVO) theory [3, 4]. The DLVO theory maintains that the potential energy is the balance of several competing contributions (see chapter 1). The Hamaker software calculates the interparticle interaction within this DLVO theory where also contributions for interactions other than van der Waals and electrostatic interaction such as steric repulsion interactions and others are added. The basic equation describing the total interparticle interaction V in Hamaker 2 is as follows:

$$V = V_{vdW} + V_{electrostat} + V_{steric} + \sum V_{misc}$$

With V_{vdW}, $V_{\mathrm{electrostat}}$ and V_{steric} beeing the contributions of the attractive van der Waals, the electrostatic and steric interactions respectively. The sum over $\sum V_{misc}$ interactions allows adding a collection (through plug-in modules [1]) of other interactions depending on the system in question such as magnetic interactions.

The **stability** of a colloidal suspension is evaluated according to the model published by Israelachvili [5]. The mean Brownian velocity of a particle with diameter d and density ρ_P is given by :

$$\frac{1}{2}mv^2 = \frac{1}{2}\left[\frac{4}{3}\pi(\frac{d}{2})^3\rho_P\right]v^2 \approx kT \Rightarrow v \approx \sqrt{\frac{12k_BT}{\pi d^3\rho_P}}$$

At a given suspension concentration c (in wt%) the number of particles per unit volume (Np) is given as a function of the densities of the particles ρ_p and the medium ρ_m as well as the particle diameter d by dividing the total mass of all particles m_{pT} by the mass of a single particle m_p.

$$N_P = \frac{m_{pT}}{m_p} = \frac{\frac{c}{100}\rho_m}{\frac{4}{3}\pi(\frac{d}{2})^3\rho_P}$$

For a binary system, the number of particles per unit volume is given by the sum of the two particle contributions:

$$N_P = N_{P,1} + N_{P,2}$$

The number of particles along one edge of the unit volume is given by the cubic root of NP, the inverse of which finally gives the spacing between two particles along the edge. This is considered as the closest interparticle spacing d at equilibrium.

$$d = \frac{1}{\sqrt[3]{N_P}}$$

In order for two particles to collide, the particle has to travel the interparticle distance d which will require a time Δt at a mean Brownian velocity v. The collision frequency is then given by:

$$f_c = \frac{1}{\Delta t} = \frac{v}{d}$$

Where for a binary system, the mean velocity is considered:

$$v = \frac{1}{2}(v_1 + v_2)$$

Then, the probability p of two particles having a kinetic energy allowing them to overcome an energy barrier ΔW is given by:

$$p = \exp\left(-\frac{\Delta W}{k_B T}\right)$$

Within a time t, t.f$_c$ collisions will occur and a minimum value for ΔW in order to avoid energetic collisions and thus agglomeration can be calculated as:

$$(\frac{\Delta W}{k_B T})_{min} = -\ln(\frac{1}{t.f_c})$$

For calculating the **van der Waals (dispersion) interactions**, the classical unretarded interaction model by Hamaker [6] or the retarded models by Gregory [7] and Vincent [8] can be choosen. London dispersion interactions originate from the interaction of temporary dipoles resulting from fluctuations of the charge distribution in a material. In macroscopic bodies, these interactions lead to complicated overall interactions. Therefore, Hamaker has approached these interactions in macroscopic bodies by consideration of a pairwise sum over all molecules (atoms) in the bodies. These sums can be decomposed into the Hamaker constant which depends on the interacting materials and the medium separating them. Particle-particle interactions are in general approximated with the case of two interacting spheres. In all following models, $A_{H,eff}$ is the effective Hamaker constant for the system (calculated for a combination of materials), h is the particle surface-surface separation and a_1 and a_2 are the particle radii respectively.

Hamaker model:

$$V_{ham}(h) = \frac{A_{H,eff}}{6}\left[\frac{2a_1a_2}{h^2+2a_1h+2a_2h} + \frac{2a_1a_2}{h^2+2a_1h+2a_2h+4a_1a_2} + \ln(\frac{h^2+2a_1h+2a_2h}{h^2+2a_1h+2a_2h+4a_1a_2}\right]$$

Effective Hamaker constants for different materials and media can be found in the literature [9] or calculated from spectral data [10].

Vincent model:

$$V_{vin}(h) = \frac{A_{H,eff}}{12}\left[a\left(\frac{y}{u(h)} + \frac{y}{u(h)+y} + 2ln\frac{u(h)}{u(h)+y}\right) + \frac{8ba_1^2}{C(h)}(2y + (2u(h)+y)\ln(\frac{u(h)}{u(h)+y}))\right]$$

With a= 1,01; $b = 0{,}14\frac{2\pi}{\lambda}$; λ= 100.10^{-9}; $x = \frac{h}{2a_1}$; $y = \frac{a_1}{a_2}$; $C = a_1 + a_2 + h$; $u = x^2 + xy + x$

This model takes into account the retardation effect, which is the delay in the dipole-dipole interactions at large separations. The Vincent's approach applies a correction for this effect for relative small separations of small particle to the non retarded Hamaker approach.

Further, Gregory applied an empirical method to include the retardation effect, which works well for separations of about one tenth of the particle radius.
Gregory model:

$$V_{gre}(h) = \frac{A_{H,eff}}{6}\frac{a_1a_2}{h(a_1+a_2)}\left[1 - \frac{bh}{\lambda}\ln(1+\frac{\lambda}{bh})\right]$$

With b= 5.32 and λ= 100.10^{-9}

The Hamaker constant can also be calculated based on the dielectric constants and refractive indices and as a function of the separation between the bodies [11]. The Hamaker constant is calculated as

$$A_H = -\frac{4}{3}k_BT\left(\frac{\varepsilon_P - \varepsilon_m}{\varepsilon_p + \varepsilon_m}\right)^2 + \frac{3h\omega\left(n_p^2 - n_m^2\right)^2}{16\sqrt{2}(n_P^2 + n_m^2)^{3/2}}\left\{1 + \left[\frac{\pi n_m}{4\sqrt{2}}\sqrt{n_P^2 + n_m^2}\frac{h\omega}{c}\right]^{3/2}\right\}^{-2/3}$$

Each of these models has its own range of validity. Whereas the Vincent approach work well for small particles about 10 nm, the nonretarded approach gives good results between 10 and 100 nm, the Gregory approach being most appropriate at larger separations.

For the **electrostatic interactions** the model of Hogg-Healy-Fürstenau (HHF)[12] as well as the Linear Superposition Approximation (LSA)[13] is implemented. In all models the ionic strength I_c and the inverse Debye length κ are calculated as

$$I_c = \frac{1}{2}\sum c_i z_i^2$$

$$\kappa = \left(\frac{\varepsilon\varepsilon_0 k_B T}{2e^2 I_c 1000\, N_A}\right)^{-1/2}$$

Where c_i and z_i are the concentration and valence ions in solution respectively, ε and ε_0 the dielectric constant and the electric constant respectively and e the elementary charge.

Further, the surface potential ψ is calculated from the measurable zeta potential ζ via

$$\psi = \zeta \exp(\kappa d_s)$$

d_s being the distance from the surface where the zeta potential is measured. The distance is usually taken as the shear plane, which for an aqueous solution is around 0,5 nm.

HHF model: The interaction potential is based on the linearized Poisson Boltzmann (Debye-Hückel) solved using Derjaguin's method.

$$V_{hhf}(h) = \frac{\pi\varepsilon\varepsilon_0 a_1 a_2}{a_1 + a_2}\left[(\psi_1 + \psi_2)^2 \ln(1 + \exp(-\kappa h)) + (\psi_1 - \psi_2)^2 \ln(1 - \exp(-\kappa h))\right]$$

The validity of this model is limited to small surface potentials, small double layer and particle-particle separation.

LSA model:

$$V_{lsa}(h) = \frac{4\pi\varepsilon\varepsilon_0 a_1 a_2}{a_1 + a_2 + h}\psi_1\psi_2 \exp(-\kappa h)$$

This model has the same limitations as the HHF model but is valid at larger separations.

The **steric interactions** are described by the close to hard wall model introduced by Bergstrom [14].

$$V_{ber}(h) = \begin{cases} h < d_a: & \infty \approx 10^6 \\ d_a \le h \le 2d_a: & \dfrac{2a_2}{a_1 + a_2}\left[\dfrac{\pi a_1 k_B T}{V\varphi^2}\left(\dfrac{1}{2} - \chi\right)(2d_a - h)^2\right] \\ h > 2d_a: & 0 \end{cases}$$

The parameter d_a represents the thickness of the adsorbed layer and φ the volume fraction of adsorbent in the adsorbed layer. V is the molecular volume of the solvent and χ the solvent adsorbent interaction parameter. This model works well for small oligomers but fails for larger molecules.

The figure below (print screen) demonstrates the window in the software program indicating the details needed for the calculations.

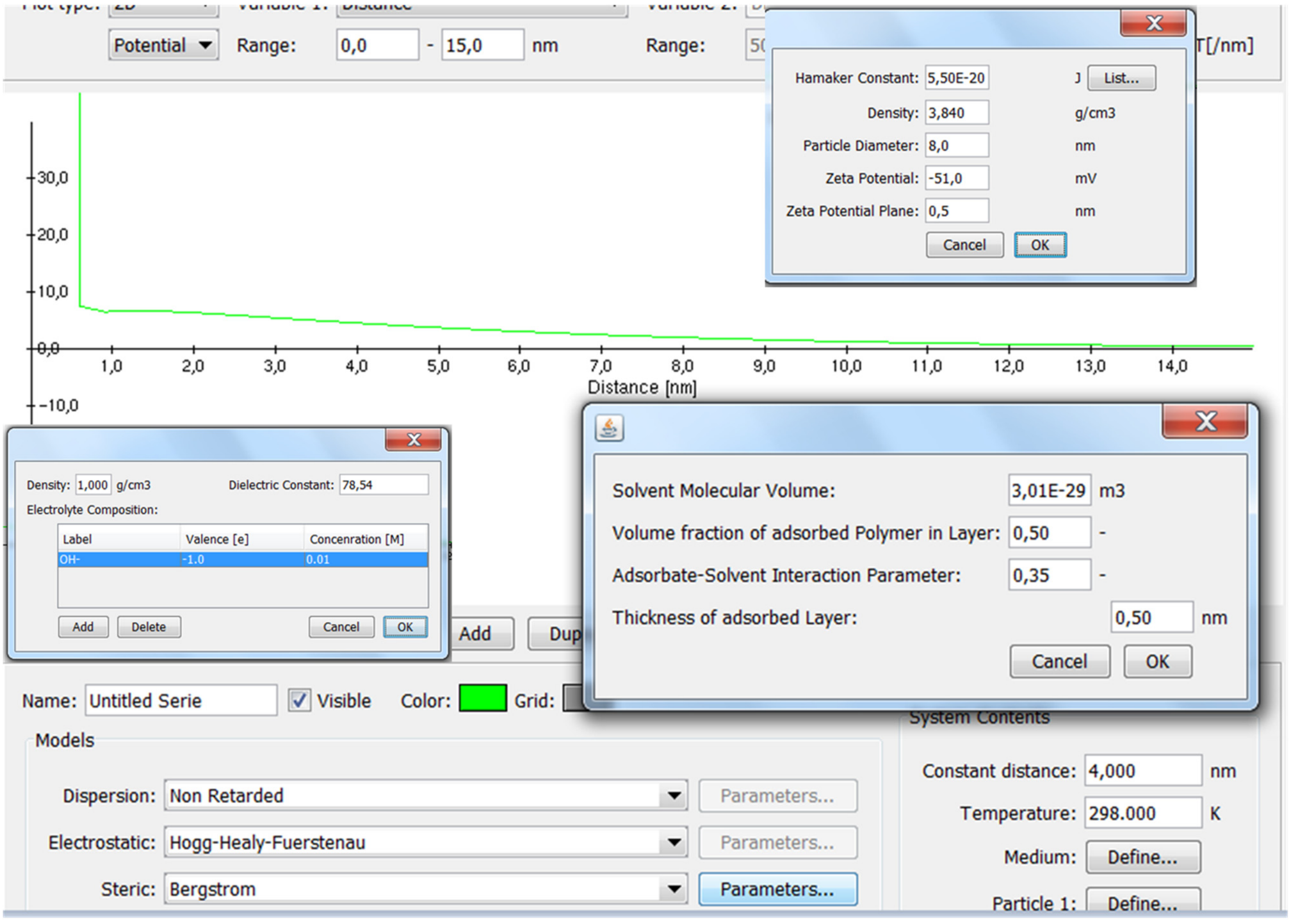

Potential Range: 0,0 - 15,0 nm

Range: 5(

Hamaker Constant: 5,50E-20 J

Density: 3,840 g/cm3

Particle Diameter: 8,0 nm

Zeta Potential: -51,0 mV

Zeta Potential Plane: 0,5 nm

Density: 1,000 g/cm3

Dielectric Constant: 78,54

Electrolyte Composition:

Label	Valence [e]	Concenration [M]
OH-	-1.0	0.01

Solvent Molecular Volume: 3,01E-29 m3

Volume fraction of adsorbed Polymer in Layer: 0,50 -

Adsorbate-Solvent Interaction Parameter: 0,35 -

Thickness of adsorbed Layer: 0,50 nm

Name: Untitled Serie ☑ Visible Color: 🟩 Grid:

Models

Dispersion: Non Retarded

Electrostatic: Hogg-Healy-Fuerstenau

Steric: Bergstrom

System Contents

Constant distance: 4,000 nm

Temperature: 298.000 K

Medium:

Particle 1:

B. Applied characterization techniques

The specifications of the analysis techniques (and sample preparation) applied in this thesis are given below in alphabetic order.

Atomic Force Microscopy

Atomic force microscopy analysis on the TiO_2 nanostructured films and the PDMS stamps are carried out on a Bruker Multimode 8 AFM, applied with a V series controller, used in tapping mode with non contact high resolution tips (length 125 µm, width 30 µm), at a resonance frequency of 204-497 kHz and force constant of 10-130 N/m.

CPS disc centrifuge

The particle size distribution of the particle in dispersion is determined using a centrifugal method (CPS Disc centrifuge, Model DC 20 000) with a rotational speed of 15 000 rpm. The samples are diluted 20 times with milli Q water and shortly (20 s) sonicated with the horn before measurement.

Digital photography

The digital photographs are taken with a Nikon D3 (lens 60 mm, focal point 2.8, sensitivity on 200 ISO), indirect flashed with a Nikon SB900.

Krypton sorption

Physical adsorption experiments were carried out on a Quantachrome Autosorb iQ-MP automated gas sorption system. Film-on-support sample pieces were transferred to a 12 mm diameter glass sample bulb. Prior to measurements, the samples were degassed at 120 °C for 16 h under vacuum. Then the degassed samples were transferred to the measurement station of the Quantachrome Autosorb iQ-MP automated gas sorption system. Adsorption isotherms were obtained at 87 K (by means of liquid argon) with krypton gas as adsorbant. The krypton adsorption isotherms at 87 K were analyzed using the Quantachrome software (ASiQwin version 3.0), which applies a krypton calibration curve traceable to NLDFT pore size analysis [15, 16].

The adsorption isotherm represents the volume of gas (STP at standard time and pressure, i.e 1 mol of gas at 1 atm, at 273K) in function of the relative pressure. For Kr sorption, the surface area is mostly determined at a relative pressure of 0.73, which corresponds to a certain volume of Kr (via the ideal gas law). Via calculations using the Brunauer-Emmet Teller Theory [17], carried out by the software, the surface area is determined, from which the specific surface area is calculated (as shown below).

Calculations of the specific surface area of the porous film (chapter 3, section 3.2), via Kr-sorption:

From the surface area of the coated surface (24.68 cm^2) and the thickness of the layer (600 nm), the volume of the film is calculated, 14.80 10^{-4} cm^3.

Using the density of titania (4.23 g/cm^3), the mass of the layer can be calculated, 63.63 10^{-4} g. The specific surface in case of a dense layer is calculated by multiplying the weight of the sample (7.18 g) by the calculated surface area (5 10^{-2} s/g, from measurement), resulting in 0.366 m^2, followed by dividing by the mass of the layer (63.63 10^{-4} g). The specific surface area of a dense layer is then 58.5 m^2/g.

Then, the pore volume (calculated by the ideal gas law) for pores smaller than 14.4 nm (each relative pressure corresponds to a pore size) being 2.77 10^{-5} cc/g at a relative pressure of 0.73, is multiplied by the weight of the sample (7.18 g) which result in a total pore volume in the sample cell of 19.89 10^{-5} cm^3 (for pores till 14.4 nm). In order to calculate the specific surface area of the porous layer (not taken into account the pores larger than 14.4 nm), the absolute surface in the sample cell (0.366 m^2) is divided by the mass of the porous layer (obtained from the density of titania multiplied with the difference between volume of the dense layer, 14.80 10^{-4} cm^3, and total pore volume, 19.89 10^{-5} cm^3) resulting in a specific surface area of 67,6 m^2/g.

Lumisizer- PSD and stability analyzer

The particle size distribution and stability analysis is carried out on a LUMiSizer 651 with a light source of 470 nm and at 25°C. A rotation speed of 4000 rpm (2300g) is applied and the measurement is stopped after 120 minutes (time interval of 30 sec). The samples are measured undiluted in a polycarbonate cuvette of 2 mm diameter.

Micro-volume TOC analysis

µ-volume TOC measurements are carried out with a computer guided Shimadzu TOC-V$_{CPH}$ equipment with manual injection kit using the 250µL Hamilton 1725 gas-tight syringe RN type 2 [18].

N_2 sorption

The nitrogen sorption measurements have been performed on a Quantachrome Autosorb-1-MP gas sorption system at 77 K. Prior to the measurements, all samples have been degassed under high vacuum conditions for a duration of 16 h at 473 K. The Barret-Joyner-Halenda (BJH) method has been applied on the **desorption branch** of the isotherm to achieve the pore size distribution. The micropore volume has been calculated based on the t-plot method, while the Brunauer-Emmet-Teller (BET) method has been applied to determine the apparent specific surface area. The total pore volume has been defined at 0.98 P/P_0.

Optical Microscopy

The TiO_2 dispersion is analyzed with a Zeiss Scope A.1 microscope using a magnification of 400.

Photon Correlation Spectroscopy

The zeta potential of the particles in dispersion is measured with a ZetaPALS90Plus/BI-MAS Particle Sizing Option (Brookhaven Instruments Corporation, refractive index of 1.00, angle of 90°, wavelength of 660 nm, 35 mW solid state laser) equipped with an electrode.

Proton NMR

Proton NMR analysis on the dispersion is carried out with a Bruker 500 MHz AVANCE III spectrometer, equipped with a 5mm ^{1}H, BB BBI-Z-probe. Temperature was set to 298 K. 1D 1H and 2D NOESY were measured using standard pulse sequences from the Bruker library. 2D NOESY mixing time was set to 300 ms.

Raman analysis

Micro-Raman spectroscopy is carried out with a HORIBA Jobin_Yvon T64 000 equipped with confocal microscope operating with a quartz cell for liquids and monochromator working in subtractive mode. Excitation of the samples is performed with the (488 nm) Ar^+ ion laser lexel SHG-95 (power of 200mW). Before measurements, the machine is calibrated using Si (520,7cm^{-1}) mode.

Scanning Electron Microscopy

The SEM images are recorded with a FEI Quanta 200FEG SEM equipped with secondary electron backscattered electron detectors. Element analysis in section 5.1 is carried out by energy-dispersive X-ray spectroscopy (EDX).

The sample preparation for the Cross-SEM image 3.38 is performed by cryogenic breaking (breaking after dipping in liquid N_2)

TGA analysis

Thermogravimetric analysis are recorded on a TA Instruments 951-2000 apparatus (100 ml dry air, 5°C/min).

Thermogravimetric analysis coupled with mass spectrometry are carried out on a TA Intsruments TGA Q 5000 coupled with a Pfeiffer Vacuum ThermoStar^{TM} MS, heating from room temperature to 300°C at a heating rate of 10°C min^{-1}. Fragments formed during ionization (with energy of 70 eV) of the evolving gas molecules are scanned in the m/z = 5-145 mass range in a 50 mL min^{-1} dry air flow. The balance chamber is flushed with nitrogen with a flow of 10 ml min-1. The temperature in the capilair is preset on 240°C.

Transmission Electron Microscopy

Transmission Electron Microscopy (TEM) is carried out on a Tecnai spirit (120 kV). For this purpose, a small amount of the dried powder is redispersed in ethanol and a drop of the obtained dispersion is dried under an IR-lamp on a coated grid (Formvar Carbon 200 Mesh

Cu). Dark field TEM images are obtained using an electron beam tilt angle of 0.55° while focusing on the (101) diffraction ring of the anatase phase.

Using the dark field image, the Feret's diameter of the crystallites is calculated using the image processing program Image J (free available at http://rsbweb.nih.gov/ij/) . The TIFF image can be loaded in the program and by differences in contrast, the particles can be selected and the dimensions are measured for a selective amount of particles. For estimating the size of a particle, one must choose the best size characteristic which is easy for smooth spherical particles. For other shapes it is important to choose a method of size measurement which is likely reflect the aspect ratio of the particles which is of most interest. The most commonly used measurements are: Martin's diameter (B), Feret's diameter (A) and the projected area (C), represented Figure 1.

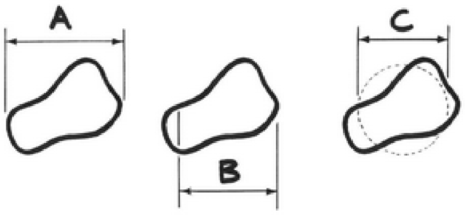

Figure 1 Illustration of different diameters used in calculations.

UV-Vis Spectroscopy

The UV-Vis analysis at the UHasselt is carried out on UV-Vis-NIR Varian Cary 500 spectrofotometer .

For the photocatalytic experiments on the nanostructured TiO_2 layers, the degradation of Rhodamine 6G is measured via UV-Vis using an equipment from Thermo Electron evolution 500 with a double beam UV-vis spectrometer [19].

Viscosity measurements

The viscosity measurements are carried out on a HAAKE Rheometer MARS thermo Electron Corporation measuring geometry double GAP DG41.

Water Contact Angle Measurements

The water contact angles in chapter 4 are measured on an equipment of type OCA15PRO from Dataphysics, provided with the software program SCA20. The contact angle was measured statically with a water drop of 3µL and calculated according to the Young's equation.

X-Ray Diffraction

The crystal phase of the particles is determined at room temperature by X-Ray Diffraction (XRD) using a Siemens D-5000 diffractometer with Cu-$K_{\alpha 1}$ radiation. The peaks are indexed according to the (h k l) values reported in JCPDS card No 21-1272 for anatase and No 29-1360 for brookite. Crystallite sizes are derived from broadening of X-ray diffraction peaks using the Scherrer formula [20] applied to the (101) reflection for anatase (at $2\theta = 25°$).

Quantitative XRD analysis

For quantitative analysis, a X'Pert Pro apparatus from PANalytical is used and the spectrum was refined by applying Rietveld analysis using the High- Score Plus software of PANalytical.

References

1. Aschauer, U., Burgos-Montes, O., Moreno, R., and Bowen, P., Hamaker 2: A Toolkit for the Calculation of Particle Interactions and Suspension Stability and its Application to Mullite Synthesis by Colloidal Methods. J. Dispersion Sci. Technol., 2010. 32(4): p. 470.
2. Aschauer, U., Hamaker 2.1: A colloidal stability toolkit (version 2.1) [computer software]. Laboratoire de technologie des poudres, Ecole polytechnique fédérale de Lausanne, Switserland, Princeton University, USA, Retrieved May 2010: p. Available from http://hamaker.epfl.ch/.
3. Derjaguin, B.V. and Landau, L.D., Theory of the stability of strongly charged lyophobic sols and the adhesion of strongly charged particles in solutions of electrolytes. Acta Physico Chim. URSS, 1941. 14: p. 733-762.
4. Verwey, E.J.W. and Overbeek, J.T.G., Theory of the stability of lyophobic colloids. Elsevier Amsterdan 1948.
5. Israelachvili, J.N., Intermolecular and Surface Forces. Academic press: San Diego, 1991.
6. Hamaker, H.C., The London-van der Waals attraction between spherical particles. Physica 1937. IV(10).
7. Gregory, J., Approximate expressions for retarded van der Waals interaction. J. Colloid Interf. Sci., 1981. 83(1).
8. Vincent, B., The van der Waals attraction between colloidal particles having adsorbed layers II Calculation of interaction curves. J. Colloid Interf. Sci., 1973. 42(2).
9. Bergström, L., Hamaker constants for inorganic materials. Advances in Colloid and Interface science, 1997. 70: p. 125-169.
10. French, R.H., Cannon, R.M., DeNoyer, L.K., and Chiang, Y.M., Full spectral calculation of non-retarded Hamaker constants for ceramic systems from interband transition strengths. Solid State Ionics, 1995. 75: p. 13-33.
11. Russel, W.B., Saville, D.A., and Schowalter, W.R., Colloidal dispersions. Cambridge Press: Cambridge U.K., 1985.
12. Hogg, R., Healy, T.W., and Fuerstenau, D.W., Mutual coagulation of colloidal dispersions. Transactions Faraday Society, 1966. 62: p. 1638-1651.
13. Ohshima, H., Healy, T.W., and White, L.R., Accurate analytic expressions for the surface charge density/surface potential relationship and double-layer potential distrribution for a sphericle colloidal particle. J. Colloid Interf. Sci., 1982. 90(1).
14. Bergstrom, L., Schilling, C.H., and Aksay, I.A., Consolidation behavior of flocculated alumina suspensions. J. Amer. Ceram. Soc., 1992. 75: p. 3305-3314.
15. Thommes, M., Nishiyama, N., and Tanaka, S., Aspects of a novel method for the pore size analysis of thin silica films based on Krypton adsorption at liquid argon temperature (87.3K). Recent progress in mesostructured materials, 2007. Ed D. Zhao, S. Qui, Y. Tang, C. YU.

16. Thommes, M., Physical Adsorption Characterization of Nanoporous Materials. Chemie Ingenieur Technik, 2010. 82(7).
17. Brunauer, S., Emmet, P.H., and Teller, E., Adsorption of Gases in Multimolecular Layers. Journal of American chemical society, 1938. 60(2): p. 309.
18. Kus, M., Ribbens, S., Meynen, V., and Cool, P., Microvolume TOC analysis as useful tool in the evaluation of labscale photocatalytic processes. Catalysts, 2013. 3.
19. Rehg, T.J. and Higgins, G., Spin coating of colloidal suspensions. AlChE Journal, 2004. 38(4): p. 489-501.
20. Cullity, B.D. and Stock, S.R., Elements of X-ray diffraction. Pearson Education International, 2001. third edition.